DEVELOPMENT OF SODIUM-SULFUR BATTERIES FOR UTILITY APPLICATION

EPRI EM-266
(Research Project 128-3)

Annual Report

December 1976

Prepared by

Electrochemistry Branch
General Electric Company
Research and Development Center
Schenectady, New York 12301

Principal Investigator
D. Chatterji

Prepared for

Electric Power Research Institute
3412 Hillview Avenue
Palo Alto, California 94304

Project Manager
James R. Birk

LEGAL NOTICE

This report was prepared by General Electric Corporate Research and Development, as an account of work sponsored by the Electric Power Research Institute, Inc. (EPRI). Neither EPRI, members of EPRI, General Electric Corporate Research and Development, nor any person acting on behalf of either: (a) makes any warranty or representation, express or implied, with respect to the accuracy, completeness, or usefulness of the information contained in this report, or that the use of any information, apparatus, method, or process disclosed in this report may not infringe privately owned rights; or (b) assumes any liabilities with respect to the use of, or for damages resulting from the use of, any information, apparatus, method or process disclosed in this report.

ABSTRACT

This report describes the results obtained during the past year of a multi-year program which has as its goal the development of a sodium-sulfur battery system for bulk storage of energy. The emphasis of the program has been to demonstrate that the necessary long life, high capacity, and high efficiency can be obtained from the sodium-sulfur system using economical materials and practical fabrication methods. During the past year, while accelerating work on testing and study of small cells, new programs were initiated on module and system design.

Two initial cell/module/system designs are discussed. The cell in these preliminary designs consists of many individual beta-alumina tubes used as the separator between single sodium and sulfur compartments. Heat conduction experiments were made and a complete thermal analysis of the system is given. Progress on construction of a 45 tube cell is given. A comparative cost analysis of the above multi-tube designs with designs consisting of bundles of cylindrical single tube cells indicated that the latter approach would probably have a cost advantage. The summary of the work of two studies which will be necessary for a final system design is described. These are (a) a statistical analysis of the effects of failure or change in performance of individual cells or modules on the reliability of the modules and system, and (b) a study on optimization of the system cost in terms of cell performance parameters and the required system operational parameters.

The results of the year's ceramic development program and the small 4-watt cell testing program are given in detail. Improvements in the microstructure, grain boundary resistance, and surface uniformity of the ceramic electrolyte have resulted in cells with lower resistance and no sign of ceramic degradation after more than six months of continuous charge and discharge at constant current. In the previous year there was a surface resistance and the electrolyte life was limited to about 100 Ah/cm^2. This year over 300 Ah/cm^2 has been obtained with no limit evident, and the surface resistance problem has been solved. Improvements in the design of the graphite current collector has resulted in consistently high cell capacity. The utilization of sulfur achieved has increased up to a value of 95% as

compared with last year's 80%. A few cells using stainless steel containers have shown no decrease in either cell capacity or cell resistance up to the present extent of testing (190 cycles for one cell) or to the time of failure due to seal failures.

The work in several areas of supporting research is presented. These include corrosion studies on container materials, sodium motion and defect structure in beta alumina, pressure-temperature stability of beta and beta" alumina, and the effects of grain orientation on the electrical properties of beta-alumina. A summary of a fundamental beta alumina sintering study at the Massachusetts Institute of Technology is also given.

The results of this year's work have considerably strengthened our previous opinion that the sodium-sulfur battery will meet all technological requirements of a successful load-leveling and peaking system.

FOREWORD

This report describes work performed between May 1, 1975 and April 30, 1976 under Electric Power Research Institute Project RP128-3, "Sodium-Sulfur Battery Development For Bulk Power Storage", and the work of a parallel program on beta alumina and sodium-sulfur batteries which is supported by the General Electric Company. The work was principally carried out by the Electrochemistry Branch in the Power Systems Laboratory of General Electric Corporate Research and Development in Schenectady, New York. Dr. D. Chatterji, Manager--Electrochemistry Branch, has management responsibility for the program. Dr. J.R. Birk of the Electric Power Research Institute is Project Manager. Major contributors during this reporting period were:

Dr. Manfred W. Breiter
Mr. Vincent J. DeCarlo
Mr. Robert R. Dubin
Mr. Donald L. Hollinger, Corp. Manufacturing Engineering
Ms. Deborah Kaminski, Thermal Branch
Mr. Randall N. King
Mr. Michael H. McLaughlin, Thermal Branch
Dr. Stephan P. Mitoff
Dr. Louis Navias, Consultant
Dr. Wayne B. Nelson, Automation and Control Laboratory
Mr. R. Hosmer Norris, Consultant
Mr. Henry T. Plant, Corporate Manufacturing Engineering
Dr. Robert W. Powers
Dr. Walter L. Roth

TABLE OF CONTENTS

TABLE OF CONTENTS (Cont'd)

TABLE OF CONTENTS (Cont'd)

LIST OF ILLUSTRATIONS

LIST OF ILLUSTRATIONS (Cont'd)

LIST OF TABLES

Section A

INTRODUCTION AND SUMMARY

Technologies for bulk storage of electric energy are required to make optimum use of the alternatives available for the generation of electricity and to provide flexibility in the delivery of electric energy. Because of the rapid growth of the electrical segment of the nation's energy economy, such technologies are receiving increasing attention. A number of technology options ranging from thermomechanical to electrochemical to electromagnetic energy storage systems are presently being considered. It is clear, however, from a recent EEI/EPRI survey[A-1] of a large segment of the domestic utility industry that battery energy storage commands a very high Research & Development priority.

The major role of bulk energy storage in an electric system is to increase the use of high-efficiency, low-operating-cost base load generating equipment. Battery energy storage appears to offer, in addition, a combination of operational, economic and environmental benefits unmatched by most other storage technologies. These benefits include: (a) siting freedom and transmission credits resulting from the ability to locate storage facilities away from generation sites and closer to load centers, (b) improved ability to load follow and meet peak demand, (c) potential for increasing overall system reliability and stability, (d) modular construction and attendant flexibility in size, (e) short lead time for construction, and (f) environmental acceptability.

Although the potential benefits of bulk energy storage are substantial, advanced battery systems will not find utility applications unless their economics are competitive with gas turbines and other methods of generating peak and intermediate power. According to an EPRI estimate[A-2], battery

systems must achieve certain technoeconomic characteristics to be cost competitive with gas turbines. For an off-peak energy cost of 12 mils/kWh and T&D credits of $60/kW, battery systems could become more economical than gas turbines and combined cycle machines for peak/intermediate power generation up to ∿ 2500 hours of annual operation, provided the following cost and performance goals are met:

Maximum Battery Cost (to the Load-Leveling System Manufacturer):

	$80/kW plus $20/kWH
Minimum Life:	10 years (250 cycles/yr)
Minimum Energy Efficiency:	70%
Maximum Operation/ Maintenance Cost:	1.0 mils/kWh

A number of advanced battery systems are being developed with funding from EPRI, ERDA and the industry. Appraisal of the alternatives by General Electric Corporate Research and Development have led to the selection of the sodium-sulfur system as the most likely of the advanced batteries to meet the requirements of utility load-leveling[A-3]. Since 1957, work on the generic materials and design problems of high temperature batteries and fuel cells has been underway at the General Electric Company. Around 1967, investigations aimed at understanding the structure-composition-property relationships for the solid electrolyte beta-alumina were launched. In 1970, the effort in the area of solid electrolytes was consolidated within the Electrochemistry Branch of the General Electric Corporate Research and Development, and the effort focused on demonstrating the scientific feasibility of a sodium-sulfur battery for bulk energy storage. In April 1973, a program was undertaken by the General Electric Company under sponsorship of the Electric Power Research Institute, that has as its long range objective the development of a practical sodium-sulfur battery system for utility load-leveling application. In late 1975, the program base was broadened by securing technical assistance from many other organizations within and outside Corporate Research and Development.

A-1 LONG RANGE PLAN FOR SODIUM-SULFUR BATTERY DEVELOPMENT

Recent research on prototype sodium-sulfur cells at General Electric and other laboratories has demonstrated that the required life and performance for load-leveling use is possible using practical and economical materials of construction. Having achieved these results, it is believed that the development of the sodium-sulfur cell has progressed to the stage of seeking to demonstrate engineering feasibility.

The overall approach is to base programs of cell design, fabrication methods development, and materials identification on experience gained in building and testing prototype sodium-sulfur cells. Previous cell testing has focused on the problems limiting cell life, on the performance of cells under cycling conditions, and to a limited extent, on their safety. It has been concluded that if the electrical performance already obtained in General Electric tests can be achieved in mass produced cells with adequate cycle life, then the sodium-sulfur cell can serve as the working element in a practical load-leveling battery.

The following program phases must be accomplished to establish the engineering feasibility of the sodium-sulfur load-leveling battery system:

A-1.1 Prototype Cell

The objective of this program has been to provide a sodium-sulfur prototype cell that is safe and controllable in the event of a failure or at the end of life and that possesses the electrical characteristics required for the load-leveling mission. This cell serves as the means of testing, under conditions simulating those required for load-leveling, the performance of cell components and fabrication methods. By applying suitable analytical techniques, experiments with this cell allow evaluation of theoretical predictions with regard to electrochemical and thermal behavior of the cathode and anode. The effects of design and material changes on electrical and life characteristics can be evaluated realistically employing this test cell. The prototype test cell program will continue as the most efficient way to test major design and material variations. The program is scheduled to continue with appropriate changes to keep these cells abreast with current

thinking. For example, the current cell geometry will be changed to conform with the electrolyte tube size required for BEST cell designs.

A-1.2 Cell Development

The overall objective of this program is to provide an economical, long lived, efficient cell that can serve as the working cell of the BEST Facility and can either serve itself as the cell of the demonstration storage facility or can provide the necessary performance and manufacturing information to develop the cell needed for that facility.

Early objectives of the BEST cell design and evaluation have been to determine the number and size of electrolyte tubes per cell and to decide whether the cell will consist of a number of tubes in the same reactant compartment or consist of parallel arrays of sub-cells with individual reactant compartments. Cell development of test type units will be continued until sufficient construction and test experience permit development of a final BEST Facility cell.

The major effort will be development of tubular designs for BEST and a demonstration plant; however, a parallel effort is in place to evaluate an alternative nontubular design for a sodium-sulfur cell for load-leveling.

A-1.3 Module Development

The overall objective of this phase will be to provide a module that can serve as the integral unit in the BEST Facility and can either serve itself as the cell of the demonstration storage facility or can provide the necessary performance and manufacturing information to develop the module needed for that facility. According to the present concept of the BEST battery system, modules will be made by connecting multi-tube cells in series which are placed within a truckable housing. It is anticipated that material and electrical and thermal control problems will be identified in this module design. It is necessary that the concept of a system with very large numbers of modules in series, without interconnection, be modeled to test its practicality. Alternate system designs may need to be developed based on the outcome of this work and on the direction that the cell development tasks take.

A-1.4 Best Facility

The overall objective of this phase of the program will be to provide the sodium-sulfur battery system for the BEST Facility for competitive evaluation of the General Electric sodium-sulfur battery. The system will consist of series/parallel arrays of modules developed in the preceding phase. The number of modules will depend on a judgement of the minimum size necessary to provide meaningful test results and of the minimum number of units that will be economical to manufacture. The BEST Facility program will include, besides the construction of battery modules, the entire system of controls, safeguards, test probes and analysis procedures, and complete installation and maintenance procedures.

A-1.5 Demonstration Plant

At this time, it is not clear whether an intermediate demonstration plant will be required or whether a full-size demonstration plant can be built directly. The proposed program envisions the latter alternative because of the need to provide the load-leveling technology at the earliest practical date. A positive decision to proceed with the construction of this plant will require not only successful performance in the BEST Facility, but also development of the fundamental understanding of the phenomena connected with the life of sodium-sulfur cells that will limit the risk in such a decision.

A-2 PROGRAM ACCOMPLISHMENTS

In April 1973, under the sponsorship of the Electric Power Research Institute, the scope of the General Electric sodium-sulfur battery development program was expanded considerably. The General Electric-Electric Power Research Institute program has completed its third year. A brief review of what has been accomplished so far is given here.

The emphasis during the first two years of the program was on design, construction, testing, and analysis of numerous prototype cells and on desired electrical characteristics through optimization of materials and design. The past fifteen months saw a gradual shift in the emphasis towards the BEST cell and module designs and overall systems analysis. For the purposes of

this review of major accomplishments, the work on prototype cell development will be summarized first, followed by an overview of the work on the BEST cell/module/system design and engineering.

A-2.1 Prototype Cell Development

The program has made use of a 16 Ah capacity sodium-sulfur battery of tubular design, shown schematically in Figure A-1. This "prototype" cell has served as the research tool for the program, has allowed systematic investigation of the effects of design, material and operational variables on the cell performance, and has led to identification of performance-limiting problems.

Cell Design and Fabrication. The design shown in Figure A-1 is evolutionary in origin and was arrived at after evaluating alternative designs. The major design/construction features which underwent significant changes during the program are: (a) the container-to-alpha alumina header seal, (b) the method of filling the electrode chambers with active materials, (c) the configurational details of the cathode which led to excellent cell capacity without sacrificing cell conductivity (details not shown in Figure A-1). Originally glass seals were used to join alpha-alumina to the container material. This was subsequently replaced by more reliable mechanical seals. Similarly, the cathode and the anode were formed by filling with molten sulfur and molten sodium, respectively; now the anode is filled electrolytically and the cathode is formed by using pre-cast sulfur graphite cylinders.

Ceramic Development. Since the most critical component in a sodium-sulfur battery is the beta-alumina electrolyte, considerable effort has been spent in understanding structure-composition-property relationships in this class of materials and in extending such knowledge to develop reliable processing techniques capable of producing high quality ceramic.

Cell Construction Materials. A study of the corrosion behavior of many metallic and nonmetallic materials in sodium and in sodium polysulfide melts has identified promising candidates for use as cathode and anode containers and as current collectors. The study has been extended to include coated materials and composites. Accelerated tests in special corrosion

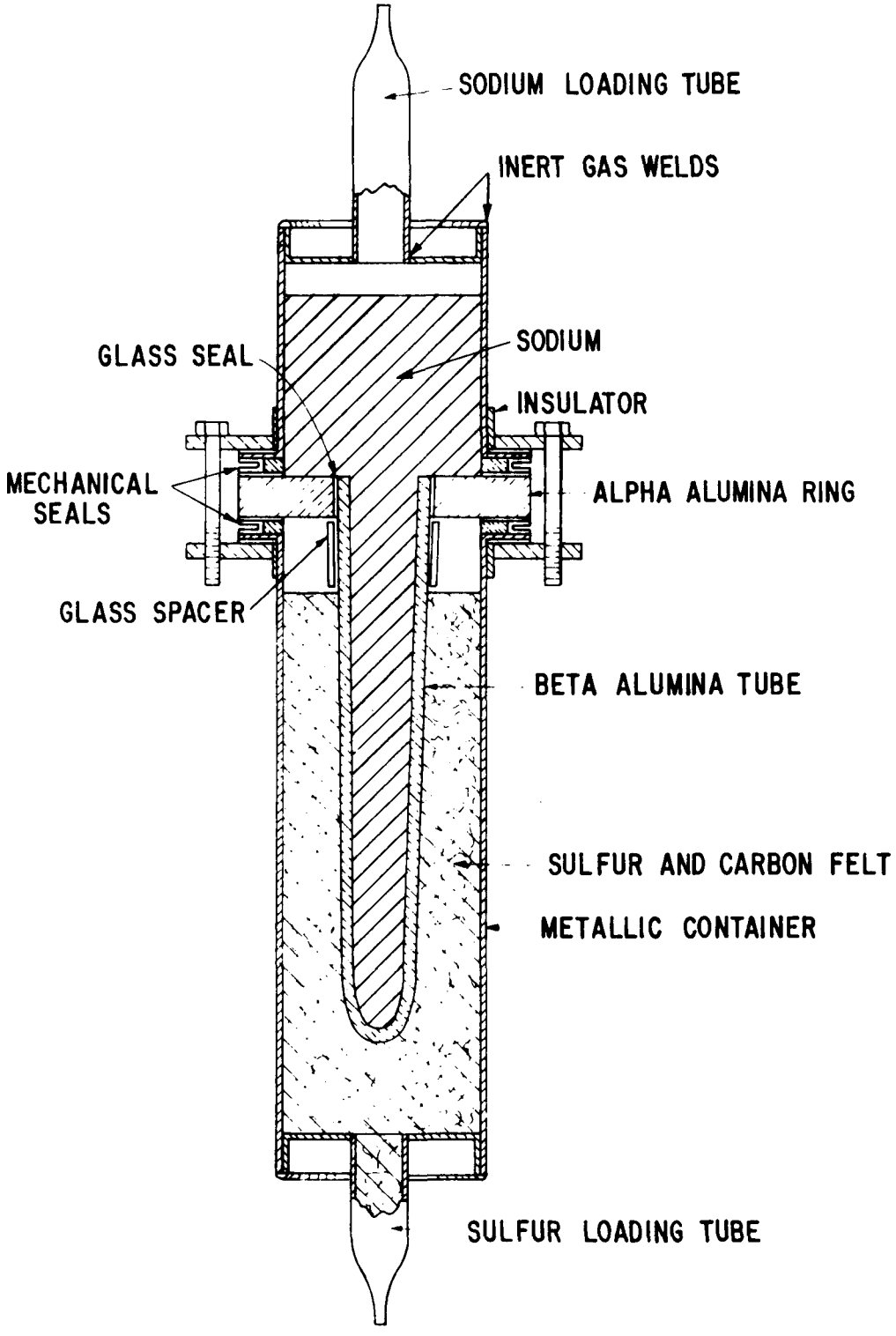

Figure A-1. Prototype Sodium-Sulfur Cell of 16 Ah Capacity

rigs simulating the electrochemical environment within the sodium-sulfur battery have been supplemented by real-time in-cell tests. The subject of current collection has also received some attention. Many forms of graphite (sponge, mat, felt, cloth, etc.) have been evaluated. The selected variation of graphite mat combines excellent conductivity with low cost.

Cell Cycling. A facility for automatically cycling up to 50 cells has been designed, built, and placed in operation. The cell testing facility directly enters the cycling data in a central computer and the performance charts are routinely obtained through the computer to monitor the cell performance. The test area is also equipped with many alarm and safety devices to warn the operator or the attendant of equipment and/or power failures.

Failure Analysis. Malfunctions in sodium-sulfur cells can arise for many reasons, including improper assembly, insufficient charge of reactants, leaks in seals, cracks in the ceramics, gross heterogeneities within the sulfur electrode, and chemical reactions of cell components with sodium and sulfur. The causes of cell failure have been (a) inferred from the electrical performance, (b) assessed from microscopic examination, chemical analysis and other destructive testing methods, and (c) observed rather directly by x-radiography in a non-destructive manner. A new experimental apparatus has been installed to allow real-time x-radiography of cells at operating temperature.

Cell Performance. Four interrelated characteristics -- life, efficiency, capacity, and cost -- will determine the ultimate acceptability of sodium-sulfur batteries to the utilities. Consequently, the major thrust of the program has been aimed at continually improving electrical performance of the prototype cell in a cost-effective manner. The chronology of progress in these and other areas of the sodium-sulfur program is presented in Table A-1.

A-2.2 Best Cell/Module/System Design and Engineering

Beginning in mid-1974, preliminary design work was initiated on the 10 MWh BEST battery system. The study, "Conceptual Battery Design for BEST

Table A-1

CHRONOLOGY OF PROGRESS IN THE DEVELOPMENT OF SODIUM-SULFUR PROTOTYPE CELL

	April 1973	April 1974	April 1975	April 1976	Long Range Goal† For Load-Leveling Battery Systems
1. Solid Electrolyte					
Composition	7.2%Na_2O 0.5%Y_2O_3 1.0%MgO 1%ZrO_2	7.2%Na_2O 1%MgO 1%ZrO_2	7.2%Na_2O No additives	8.4%Na_2O No additives	
Density gm/cc	3.22	3.22	3.20	3.29	3.29
Size, diameter/length	1cm/7cm	1cm/7cm	1cm/7cm	1cm/7cm 1cm/15cm 2cm/15cm	1.5cm/24cm 2.4cm/37cm
Resistivity at 300°C	——— 17Ωcm ———		26Ωcm	15Ωcm	5-10Ωcm
2. Ceramic Life in Test Cells	3Ah/cm^2	70	115	300+	1700
3. Single Cycle Capacity per unit area (mAh/cm^2/discharge cycle)	250	365	598	633	700
4. Sealing Technique					
Beta to alpha alumina	Glass	Glass	Glass	Glass	
Cathode to anode containers	Glass	Glass	Mechanical	Mechanical	
5. Filling Techniques					
Sodium	Molten	Molten	Electrolyte	Electrolyte	
Sulfur	Molten	Molten	Precast	Precast	
6. Cell Testing & Analysis					
Test stations	<5	∿10	∿20	∿50	
Data Logging/reduction	Manual	Manual	Computerized	Computerized	
Failure Analysis Methods	Post-mortem	Post-mortem	Post-mortem + x-ray	Post-mortem + in-situ x-ray	
7. Utilization of Cell Capacity	∿30%	45%	80%	up to 90%	Highest possible
8. Change in Cell Resistance During Life (1.0 x refers to no change)	2.5x	2.3x	1.2x	1.0x	1.0x
9. Energy Efficiency (estimated average at 73 mA/cm^2)		73%	61%	77%	80%

*The numbers quoted to not refer to one individual cell, i.e. no one cell has exhibited maximum favorable values for all parameters.

†Long range goals for a Na/S system, based on current densities and duty cycle given in the report, "Conceptual Battery Design for BEST Facility."(A-4)

Facility" (A-4), was the first systems study for the General Electric-Electric Power Research Institute program and was restricted to one conceptual design.

A number of systems aspects have been examined during the past year or so. A detailed thermal engineering study for a 10 MWh system (consisting of 144 modules of 28 cells each where each cell contains 100 tubes) has been completed. Work has started on the statistical analysis of system reliability, capacity and life. A detailed cost and manufacturing study is in progress for alternate battery designs and ceramic processing methods. This study should culminate in a general layout for the battery manufacturing facility, identification of manufacturing methods, establishment of firm figures for the battery production cost, and identification of critical materials and processing steps where cost improvements would be needed. Computer calculations have been initiated to arrive at a new design for the load-leveling battery system, optimized for performance, cost, manufacturability, and reliability. The coming years will see a concerted effort to produce a viable design for the BEST battery through iterative interaction between the various task groups.

A-3 ORGANIZATION OF THE PROGRAM AND REPORT

The sodium-sulfur battery R&D at General Electric Corporate Research and Development has been performed under two parallel programs; one supported by the Electric Power Research Institute and the other by the General Electric Company. This report covers accomplishments of both programs. In consideration of the readability of the report it was not organized in an Electric Power Research Institute and General Electric task sequence. Therefore work from both programs is often discussed in the same sections. The separation of work will instead be given in this section.

A.3.1 Tasks of the May 1, 1975 to April 30, 1976 Program

During the past contract year the program was divided into six tasks, with support and the nature of the work as identified below.

Task A -- Design and Tests of Multi-tube Cell (EPRI Supported). The work of this task was to provide the information needed and to carry out analyses of

designs for a multi-tube 2.5 kWh cell, to select the most promising options, and to build and start testing of single tube cells employing the geometry, materials, and construction techniques of the options selected.

Task B -- Development of Alternative Cell Designs (GE Supported). The work of this task consisted of design and initial testing of an alternative ceramic construction to cells consisting of tubular arrays.

Task C -- Development of Ceramic Electrolyte (GE Supported). The development of the ceramic electrolyte tubes has been carried out under this task. This includes all the ceramic related research as well as the production of tubes for test cells and studies of economics of cell production.

Task D -- Evaluation of Cell Performance (EPRI Supported). Single tube cells are evaluated including the following aspects of cell design and performance.

- Factors limiting cell life, capacity and resistance
- Results of design changes
- Effects of operating variables
- Performance of materials and
- Safety

Task E -- Module Design and Testing (EPRI Supported). The purpose of this task was to conduct preliminary cell/module/system designs. This included statistical modeling studies; evaluation of cell parameters (size, shape, current density, number of cell required/kW) in relation to cell and operational variables; and finally the evaluation of materials and fabrication methods.

Task F -- Supporting Research (GE Supported). Supporting research included studies and experimentation on those aspects of sodium-sulfur development which are best carried on apart from the ceramic and cell/module/system programs. Examples are corrosion testing, and fabrication and testing of coatings and sealing materials.

A.3.2 Arrangement of the Report

The report on the sodium-sulfur battery development is presented in the following sequence.

Section B -- Cell/Module/System Designs and Experimentation. This section will cover the approach being followed to arrive at a load-leveling battery system, the system design established to date, system thermal studies, size and performance studies, multi-tube cell construction, and preliminary cell cost analysis.

Section C -- Ceramic Development. In this section ceramic development from this year's program is presented along with some work from last year's program which was not previously reported. Topics covered in this section include ceramic composition, homogeneity, surface properties, grain boundary resistivity, and production of larger sized tubes.

Section D -- Single Tube Cell Performance. This section includes all the work and results related to single tube cells, namely life, effects of different cycling modes, cell component evaluation, current collectors, cell examination, safety, and complex impedance measurements.

Section E -- Supporting Research. Areas of supporting research covered in this section include pressure/temperature stability of beta-alumina, defect structure of beta alumina, effects of crystal orientation on conductivity and container material corrosion and coatings.

Section F -- Plans for Future Work. A brief description is given on the program plan for the next contract period.

A-4 REFERENCES

A-1 Birk, J.R. "Batteries for Energy Storage: Potential Applications and Alternative Technologies," Presented at the Engineering Foundation Conference on Energy Storage, Pacific Grove, California, February 8-13, 1976.

A-2 Anon., "Battery Storage," EPRI Journal, February 1976, pp. 33-34.

A-3 Mitoff, S.P. and Bush, J.B. Jr., "Characteristics of a Sodium-Sulfur Cell for Bulk Energy Storage," Paper No. 749141, Proc. of the Ninth Intersociety Energy Conversion Engineering Conference, San Francisco, California, August 1974.

A-4 "Sodium-Sulfur Battery Development for Bulk Power Storage--Conceptual Battery Design for BEST Facility," EPRI Contract No. 128-2 Addendum, General Electric Company, Schenectady, New York, December 27, 1974.

Section B

CELL/MODULE/SYSTEM DESIGNS AND EXPERIMENTATION

The present objective of the sodium-sulfur battery program is to develop a battery system for the BEST Facility for the purpose of determining its suitability as the major component of a commercial load-leveling system.

During previous years the program was almost exclusively focused on evaluating the performance of small cells made with practical materials. This work has been continued as will be discussed in other sections of this report, but in addition a substantial effort has been initiated to design and test concepts leading to construction of BEST Facility sized cells. The cells must be incorporated into a module/system design, therefore module and system studies were initiated simultaneously. Thus all BEST cell design work is intimately tied in with the module and systems studies, and it is appropriate to discuss all cell/module/systems studies and experimentation together.

The first phase of the approach used toward obtaining a system design was to start with the performance records of our small test cells and expand the size of the cell by increasing the number of tubes in a common container. Starting from this building block, modules and then a system were designed in considerable detail to evaluate its practicality. A preliminary multi-tube cell design was given in an earlier report[B-1]. The refined version of this cell will be given in this report.

The second phase of the approach was the evaluation of the system involving manufacturability, cost, efficiency, and the developments required to improve the above. The evaluation also included consideration of starting from a new type building block cell.

The third phase will be to redesign the system, taking into account the things learned from the evaluation, and the improvements in small cell performance which have occurred since the first design.

At the end of this contract period the first two steps have been in the most

part completed and considerable ground work has been done for the continuation of the last step of designing a more sophisticated and practical system.

The organization of this section of the report is according to the three design phases given above, and will be given as:

- B-1 Initial Designs and Experiments
- B-2 Evaluation of Design and Alternative Single-tube Cell
- B-3 Basic Studies for Final Design

B-1 INITIAL DESIGNS AND EXPERIMENTS

The design and experimental work which has been performed on a multi-tube cell for the BEST Facility is given in this section. The work started with a preliminary study[B-1] of a conceptual BEST Facility battery in December 1974. The elements of this design were discussed in last year's report and the details in Reference B-1, so it will only be briefly discussed as background material in this section.

During the present contract year the design was modified and refined using experimentally determined heat transfer values and more detailed thermal calculations. The satisfaction of thermal and electrical requirements led to a design for the cell, module, and system which is presented in this section.

The successful construction of a multi-tube cell depends on being able to seal many beta-alumina tubes to a single insulating header. Every one of these seals must be impervious or the entire cell will be shorted. Experimental work on multi-tube cells was concentrated on the seal problems, and the successful construction of a 45 tube cell will be described.

B-1.1 Preliminary BEST Facility Cell/Module/System Design

The first General Electric Company battery design study was described in the report, "Conceptual Battery Design for BEST Facility[B-1]." The cell in this design study was conceived as a one hundred tube unit with all the beta-alumina tubes sealed to a single insulating header between the sodium and sulfur compartments. The header was about 3.3 cm by 80 cm with two rows of

50 tubes as shown in Figure B-1. The long flat construction was chosen so that the heat generated during operation could be removed from the side by natural convection. This design suffers from the following problem: the insulating header material found satisfactory in prototype cells is made of alpha-alumina, but it would be impractical to make a 3.3 cm x 80 cm x about 0.4 cm header of this brittle material, so that material and construction details could not be specified in the above report. Metal-non-metal laminates were considered as a more flexible header, but had not been tested. A thermal study was performed in the current contract year, which shows that it is possible, in fact more desirable, to remove the heat through the sodium-filled beta-alumina tubes. This led to a second generation design which is discussed below.

B-1.2 Refined BEST Facility Cell/Module/System Design

The development of a refined design of the BEST Facility system will be given in this section. The design is based on thermal considerations because heat removal while maintaining set maximum and minimum temperature limits is so very dimensionally dependent that it sets the geometry of the entire system.

Two improvements were required to be made on the previous study: (a) the elimination, if possible, of the long thin insulating header, and (b) a more exact thermal analysis. The design of a cell with a more symmetrical geometry, for instance a 2 by 50 arrangement of tubes, requires that all the heat be removed along the axis of the tubes. Besides a study of geometry and cell design, some experimental work was required to determine the heat flow rate through the sodium in the tubes and the heat flow rate through the graphite-sulfur-polysulfide matrix. The thermally-based design will be presented by first giving a brief description of the cell geometry followed by the experimental work and the thermal analyses.

B-1.2.1 Multi-tube Cell/Module/System Design. The BEST Facility battery system size chosen was 10 MWH, to operate 10 hours on discharge and five hours on charge. This size and rate are arbitrary and were only chosen to be consistent with the previous study[B-1]. The same performance base was also used, which refers to performances of test cells at the end of 1974.

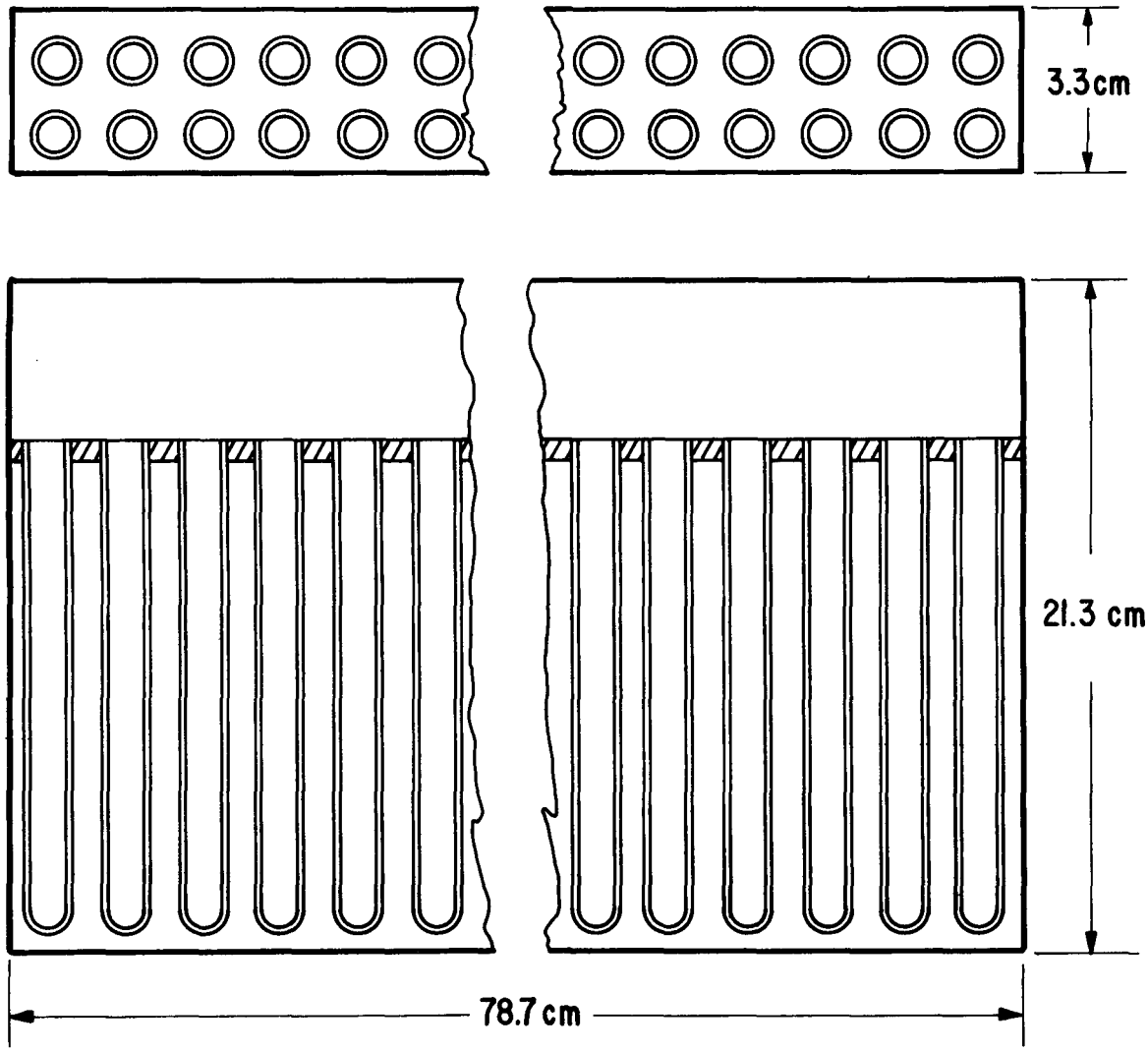

Figure B-1. Preliminary Header Design for the Multi-tube Cell with Common Na- and S- Compartments

This results in using 100 tubes, 1 cm x 15 cm, in each 2.5 kWH cell. There would be 20 cells per module, and 200 modules per system. As will be evident later, these parameters are yet to be determined by studies of cell optimization, cell reliability, statistical analysis, and cost analysis. It is evident that statistical studies must be combined with performance and construction variable studies which will be major tasks of future work. Therefore, the second generation design is not visualized as necessarily being the BEST design in detail, but work planned for this cell will be applicable to the general class of cells in which tubes are in parallel in a common compartment.

A cutaway drawing of the cell is shown in Figure B-2. The method of heat transfer through the top of the tubes allows the cells to be arranged in a 10 by 10 array. This header could be made of a 17 cm x 17 cm x 0.4 cm plate of alpha-alumina, permitting the use of mechanical seals to the sodium and sulfur compartments as currently used in the prototype cells. Heat is removed by forcing low pressure ambient temperature gas through a flat duct, the bottom portion of which is an aluminum slab. The temperature of each cell is controlled by a thermostatic valve which regulates the coolant gas flow rate. If safety considerations require it, the coolant could be nitrogen in a closed cycle with a central heat exchanger. Complete thermal calculations show that cell modules of this design could operate at 80 percent efficiency, requiring no auxiliary heat during daily load-leveling with the coolest portion of the cell never dropping below 310^{o}C nor the hottest portion exceeding 365^{o}C. Current collection is to be performed by metal wire/graphite mat devices designed for the purpose which are welded to the bottom of the aluminum can used as the sulfur container. The sodium compartment is also to be made of aluminum.

The insulation is only on one side of the cell because of its stacking in a module. A module is shown in Figure B-3, which shows insulation at top and bottom, and at the end of a string. Twenty-five such modules stacked in a row would form a 1.25 MWH, 1000 V string, if all the cells were connected in series. The exhaust ducts and space between the cells and insulation at top and bottom (not shown) are available for electrical connections. The series/parallel arrangements will depend on results of statistical reliability

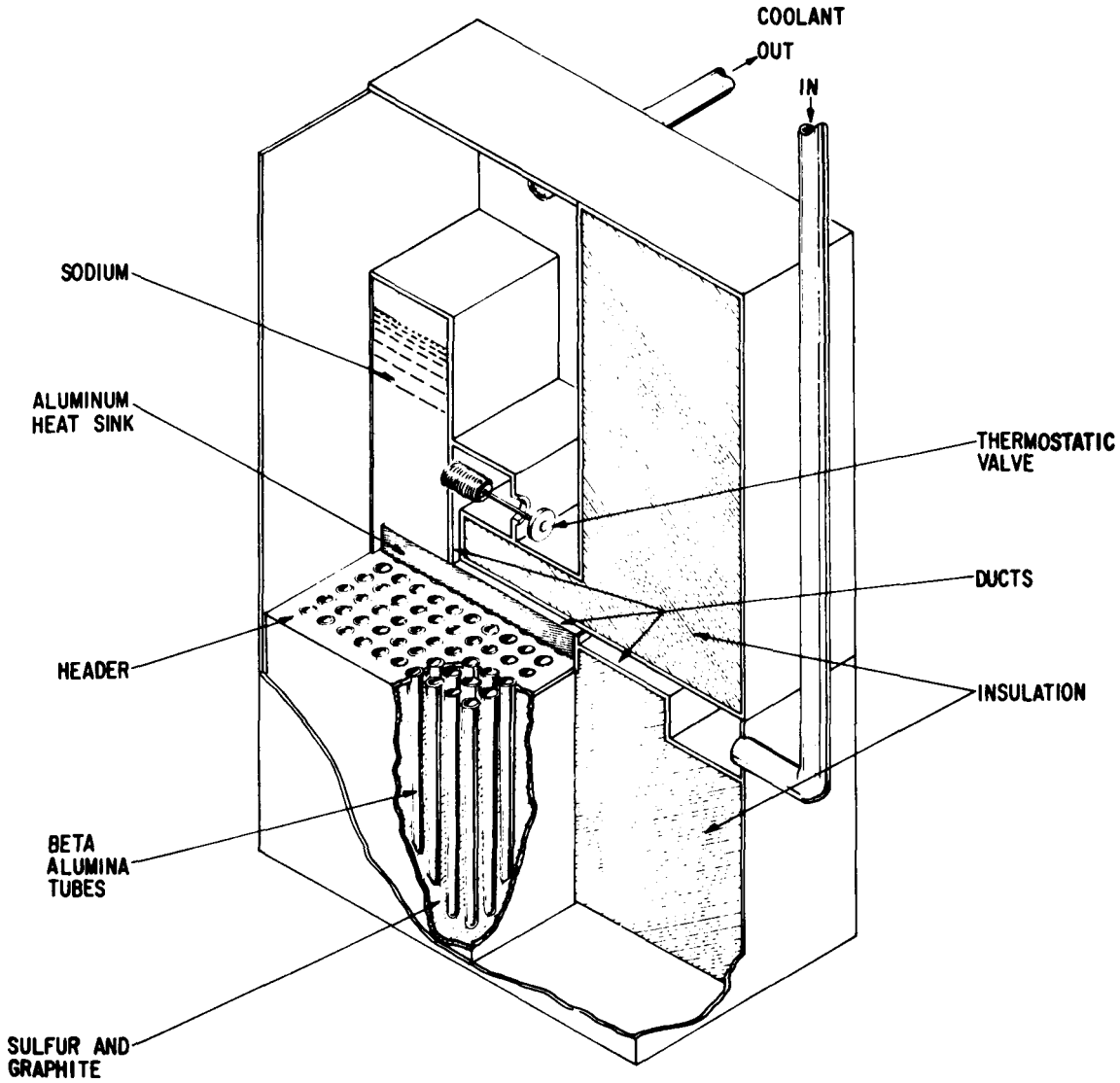

Figure B-2. Cut-away View of a Multi-tube Cell with Common Na- and S- Compartments

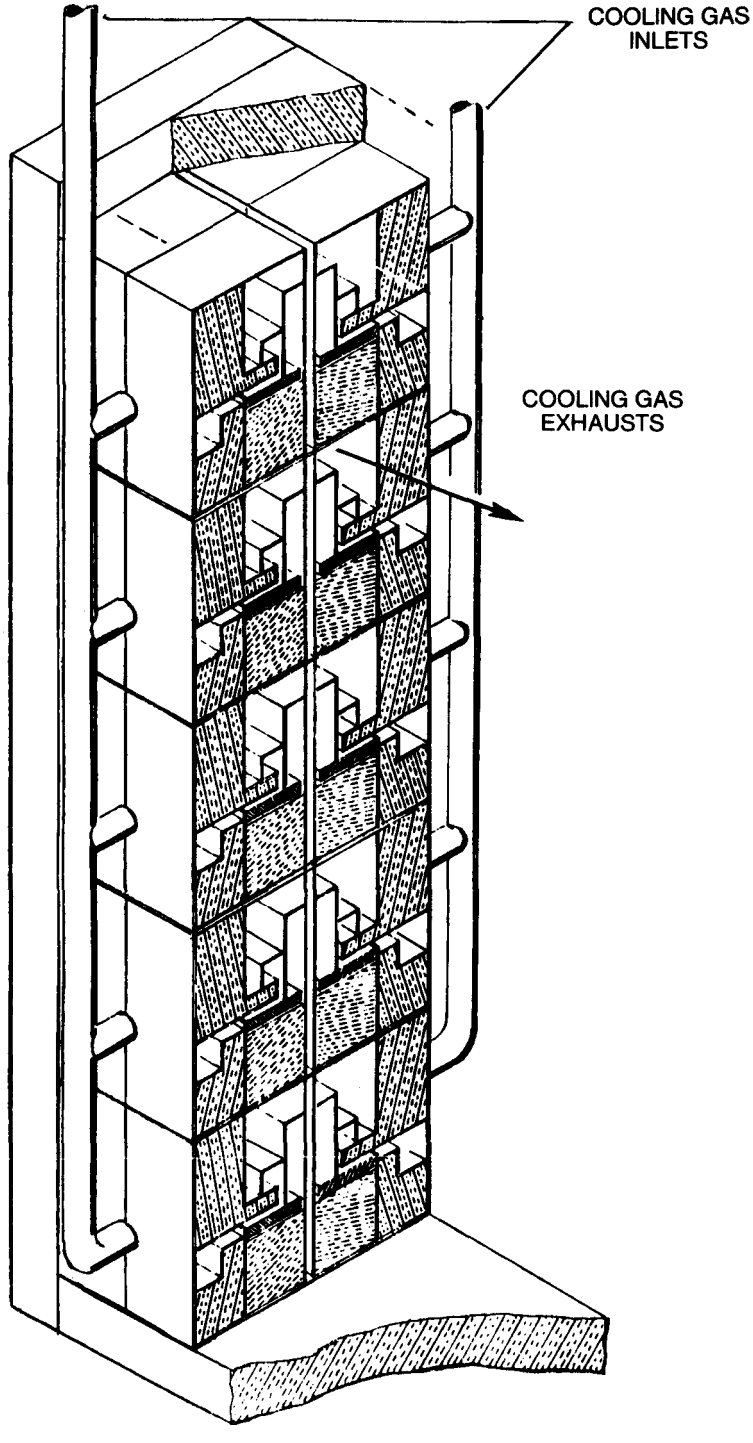

Figure B-3. Twenty Cell Module

studies which are in progress. A complete description of the cell module/system design and the thermal analysis is given in Appendix I-1.

The remaining four sections on the multi-tube design will cover:

- The experiments and results of heat flow through molten sodium.
- The results of the thermal conductivity of the cathode materials.
- A summary of the thermal characteristics of the cell/module/system.
- Results of seal development for a multi-tube cell.

B-1.2.2 Heat Flow Through Molten Sodium. The best cooling method for a multi-tube cell would employ cooling through the sodium inside the beta-alumina tubes. This would then prevent overheating of the tubes near the center of the array which would certainly occur if cooling were attempted from the sides of the cells. There are certain problems with respect to heat flow-through liquids which are discussed below. It was necessary to build an apparatus to experimentally determine the best flow characteristics of tubes filled with molten sodium, in order to obtain accurate values for the thermal design calculations.

There are several possible mechanisms of heat transfer in a closed-end tube. For geometries with low length to diameter ratios, the heat convects upward in a boundary layer flow and cool fluid returns down in the core. The cool core is essentially at a constant temperature. If the length to diameter ratio is increased sufficiently, the boundary layer grows thicker relative to the tube diameter and the return of the cool fluid is impeded. In this regime, self-sustaining temperature oscillations have been observed[B-2]. For a very large L/D ratio, the boundary layers on the walls merge at the center and choke off the return of cool fluid down the center of the tube. Stable natural convection is halted and the heat transfer is by conduction alone.

In this regime of large L/D ratios, a third heat transfer mechanism has been postulated. Maintaining a negative temperature gradient against gravity is an inherently unstable process. The hotter fluid near the bottom of the

tube is spurred upward by buoyancy forces and restrained by viscous forces. If the temperature gradient becomes sufficiently steep, the buoyancy force becomes strong enough to overcome the viscous effects. The result can be either a sudden upward surge of fluid to relieve the instability or the generation of a series of insulation cells. After the vertical temperature gradient is relieved by this mixing process, the system can again fall back to a nonconvective conduction mode and subsequently repeat the cycle.

The possibility of such a periodically unstable phenomenon is certainly cause for concern in the overall module design. The main purpose of the experiment is to determine what heat transfer mechanisms occur for the geometries and heat flux rates currently envisioned and, specifically, whether an unstable convection effect must be dealt with.

Previous Work. The main body of work relevant to this study deals with free convection in closed-end tubes--the so-called closed thermosyphon. This process was investigated experimentally by Bayley and Dzekanski[B-2] and Larsen and Hartwett[B-3], for liquid mercury, as a possible cooling technique for rotating turbine blades. Bayley and Czekanski's data are in the region of impeded convection, where they observed the violent temperature oscillations referred to above. The relevant thermal parameter (the Grashof-Prandtl number parameter, $GrPr^2 \frac{r}{L}$) in their study is several orders of magnitude higher than in the present case. Therefore it is reasonable to assume that the convection process in the sodium is impeded and quite possibly choked. Unfortunately, Bayley and Czekanski do not indicate a choking limit.

A more recent study by Pucci and Gerretsen[B-4] extends the range of $GrPr^2$ down to 3×10^2. This is about one order of magnitude higher than the present case. Pucci and Gerretsen's correlation encompasses three orders of magnitude (up to 2×10^5), but they also report no lower choking limit.

Apparatus and Experimental Procedure. The design of the apparatus used for this study is shown in Figure B-4. The sodium is contained in a 15 cm long, 0.8 cm diameter stainless steel tube which opens into a sodium-filled reservoir. The tube is wound with four separately-controllable Nichrome wire heaters. The wall temperature is monitored by thermocouples TIG welded into

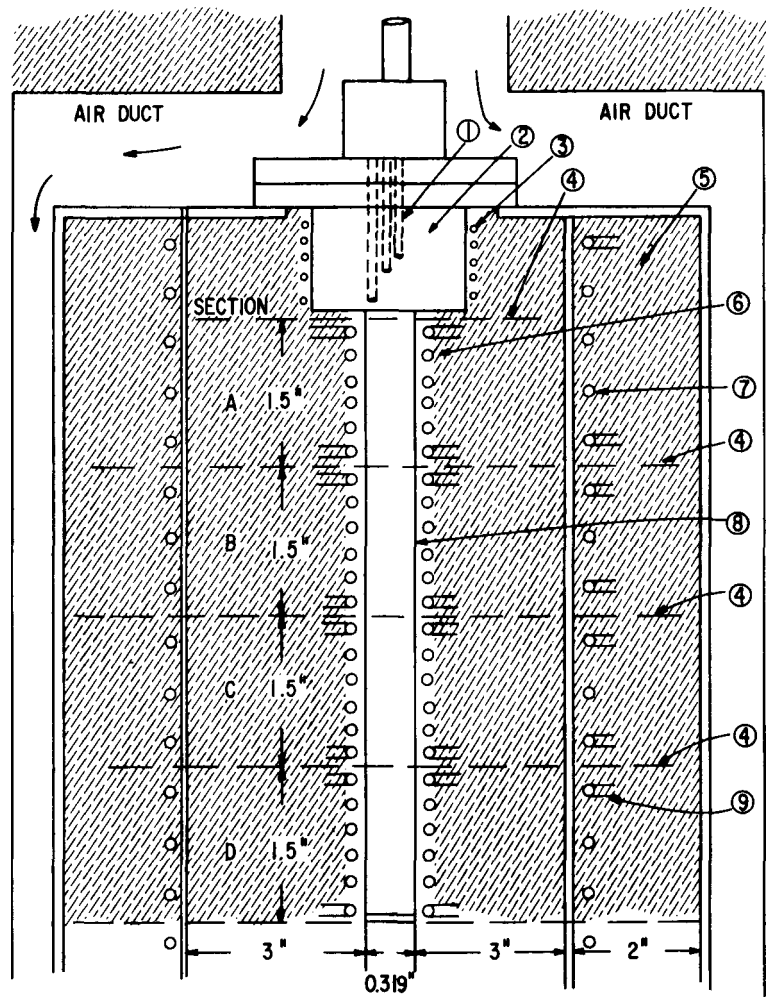

1. Reservoir thermocouples
2. Reservoir
3. Reservoir heater - wound Nichrome wire
4. Wall thermocouple plane
5. Fiberfax insulation
6. Test section heater - wound Nichrome wire
7. Guard heater
8. Stainless steel tube - 0.76 mm wall thickness
9. Section D guard heater - extends 7.6 cm beyond lower end of test section

Figure B-4. Sodium Heat Flow Apparatus

wells on the outer surface of the tube in five axial locations. Thermocouples were also placed in the sodium on the tube centerline 7.6 cm from the bottom and in the reservoir. Heat was supplied to the reservoir by a separate wire-wound heater. The reservoir could also be cooled or heated by an air stream of adjustable temperature and velocity.

At the elevated temperatures of the tube (250° to 400°C), heat losses to the surroundings must be minimized. For th is purpose, the insulated tube was surrounded by independently controllable guard heaters. In the course of the experiment, power to these heaters was adjusted until the guard heater temperatures matched the tube temperatures in corresponding axial locations. This minimized radial heat leaks.

The magnitude of the heat loss was measured by adjusting the power on the heaters to obtain a flat temperature profile in the tube. This test indicated appreciable heat losses down the heater wires. After the heater leads were wrapped with a woven resistance heater, the losses were considerably reduced.

Due to the high temperatures and low heat flux rates (a maximum of 6.5 W/cm^2 was attainable without jeopardizing the apparatus), the heat losses were on the order of 25% of the total heat input. However, this heat leak was measured and the data reduced to within a 10% error band.

Observations. In all cases studied, the heat transfer process was by conduction alone. The reservoir temperature was varied between 250° and 350°C, to approximate the range of battery operation. The heat flux rate on the inside tube diameter was held constant at values up to 6.5 W/cm^2. The maximum heat flux rate expected during a possible emergency discharge such as given in Reference B-1 might be 2.8 W/cm^2, while under normal operating conditions, the rate does not exceed 0.84 W/cm^2.

The data is compared with a one-dimensional conduction profile in Figure B-5. The value of the thermal conductivity of sodium was taken as the average from three independent investigations[B-5]. The conduction in the stainless steel tube accounted for about 7% of the total thermal resistance to heat flow.

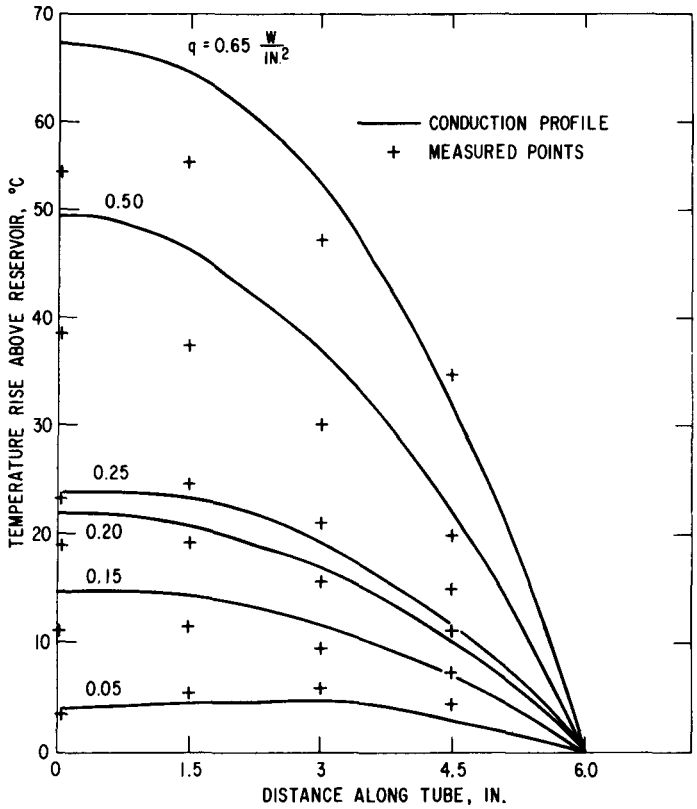

Figure B-5. Axial Temperature Profiles -- Comparison Of Conduction Profile With Data

At high values of heat flux rates the difference between theory and measurement is relatively large. This may be due to the heat losses containing a significant radiative component at the elevated temperatures associated with higher heat flux rates. As the figure shows, the temperature profiles are sufficiently close to those calculated, assuming conduction alone, to indicate that no unstable convective phenomena are expected. All thermocouple readings were steady and non-oscillatory, further indicating no convection. The data were reproducible over a range of reservoir temperatures.

Conclusions. In the range of temperatures from 250° to 300°C and heat flux rates up to 6.5 W/cm^2, the heat transfer process was conduction alone. The length to diameter ratio of the apparatus was approximately 19, and the maximum $GrPr^2$ value was 32. At higher values of these parameters the danger of unwanted oscillations may still exist. At lower values, the process may be assumed to be conduction controlled. Current conceptual designs call for a

scale-up of the tube size maintaining the same L/D ratios. As the diameter is increased, the Grashof number will increase as D^3. Therefore, any design which includes a larger diameter than that tested must be investigated. It is now known that for $GrPr^2$ less than 30, the mechanism is conduction and for $GrPr^2$>300 the mechanism is impeded convection[B-4], but no data are yet available for the intermediate range.

The thermal calculations used in Appendix I were based on heat transfer through the sodium based on conduction alone.

B-1.2.3 Thermal Conductivity of Sulfur-Polysulfide-Graphite Matrix. The thermal conductivity of the graphite mat and sulfur/polysulfide mixtures is necessary information for thermal analysis of sodium-sulfur cells. This parameter is a function of the state of charge of the cell, the sulfur loading fraction in the cathode, the temperature and the orientation of the graphite fibers. Five sulfur/polysulfide samples were prepared which were sufficient to obtain thermal conductivity values or estimates for each of the variables as required for operating conditions of a cell.

The conductivity measurements were performed by Dynatech R/D Company, Cambridge, Massachusetts.

Experimental Procedure. The samples were made by casting disks (50 mm diameter x 13 mm thick) of VCAR VM0032 Mat and three different sulfur/polysulfide compositions in graphite molds with a dry nitrogen cover gas. The samples were sealed in polyethylene bags for shipping. The three compositions were pure sulfur, Na_2S_{10} (corresponding to a two-phase mixture near the normal fully charged state, and Na_2S_3 (corresponding to the fully discharged state). An attempt was made to have a random orientation of the graphite fibers, but one sample was made with a preferred orientation in the conduction direction. Loading fractions corresponded to those in our test cells, i.e., five weight percent graphite and ten percent void space in the fully discharged condition. Two samples had one-half of the polysulfide loading.

The Comparative Method was chosen to measure the thermal conductivity. The sample was placed within an insulating containment ring and then between two pyrex 7740 reference standards of known thermal conductivity with thermocouple instrumentation at the interfaces. The composite stack was placed between the plates of an upper heater, an auxiliary heater and a lower heat sink. A reproducible load was applied to the top of the complete system. A guard tube which could be heated or cooled was placed around the system and the interspace and surroundings filled with an insulating powder. The system was then evacuated and backfilled with argon. By means of adjustments to the power in the various heaters and of the heat sink temperature, a steady temperature distribution was maintained in the system and undue radial loss prevented by keeping the guard tube at a temperature close to the average temperature of the sample. At equilibrium conditions the temperatures at various points in the system were evaluated from the thermocouple readings.

The thermal conductivity was calculated from

$$\lambda = \frac{1}{2}\left(\frac{\Delta\chi}{\Delta T}\right)_{\text{sample}}\left[\left(\frac{k\Delta T}{\Delta\chi}\right)_{\text{top reference}} + \left(\frac{k\Delta T}{\Delta\chi}\right)_{\text{bottom reference}}\right]$$

where λ = thermal conductivity

$\Delta\chi$ = thickness

ΔT = temperature difference

k = thermal conductivities of references at temperature

The results are given in Table B-1 for the three different states of charge, loading of sulfur, and graphite orientation. Conductivity was measured on all of the samples at 300°C. In addition it was measured on three of the samples at 350°C with no change observed in values.

TABLE B-1

Thermal Conductivity of S, Na_2S_x, C Composites

	Sulfur/Side Loading	Thermal Conductivity (Random Graphite)	$Wm^{-1}\ {}^oK^{-1}$ (Oriented Graphite)
Sulfur (as filled)	Design Value	0.17	0.35
Na_2S (as charged)	Design Value	(0.17)	(0.35)
Na_2S_3 (as discharged)	Design Value	0.27	(0.45)
Sulfur	One Half Design Value	(0.13)	(0.31)
Na_2S_{10}	One Half Design Value	0.13	(0.31)
Na_2S_3	One Half Design Value	0.22	(0.40)

The above conductivity values were those used in the thermal analysis presented in the following sections of this report.

B-1.2.4 Summary of Thermal Analysis of Cell/Module System. A complete thermal analysis of the design shown in Figures B-2 and B-3 is given in Appendix I. A summary of the findings is given here.

Temperature Control. An imposed restriction on the design was that the maximum and minimum temperature of any part of any cell in the system never exceeds 365°C or falls below 310°C. The results of the thermal calculation for the design shown resulted in maximum and minimum temperatures of 360°C and 313°C, respectively.

Cooling Gas Flow. The cooling gas (air was assumed) flow must be reasonable with respect to rate, temperature, pressure, and power consumption. The resulting calculations show very reasonable requirements 0.74 ft^3/min, per cell, inlet air temperature can be warmer than any expected ambient, and the fan power is only 0.036 W/cell.

Time Lag For Sudden Heat Removal or Sudden Heat Generation. If the time lag to reach 90% of the steady-state condition is comparable with the duration of a cycle interval the steady-state temperature calculations given would be far from the transient values. The time constants are less than 0.2 hours which is an acceptable situation.

Auxiliary Power Requirements For a Daily Cycle. The cells generate i^2R and $T\Delta S$ ($\pm$) heat during the operating cycles. The duration of the operating times will depend on the most economical utilization of storage batteries as determined by the utilities' requirements. In every application there will be appreciable idle periods when the system is neither on charge nor discharge. Some auxiliary heat generally will be required to keep the cells in the operating temperature range. For the 10 hour discharge and 5 hour charge cycle the thermal analysis shows that this auxiliary heat requirement will be less than 2% of the energy stored per cycle on a daily basis. This figure is quite dependent on the particular duty cycle requirements.

In general, the multi-tube cell design shown on Figures B-2 and B-3 meets all the thermal requirements for efficient operation without exceeding normal temperature limitations. Just as important, the thermal requirements do not impose obviously uneconomical or impractical manufacturing restrictions.

B-1.2.5 Multi-tube Cell Construction. The cell design shown in Figure B-2 presents a number of significant sealing problems which are different enough from the small single tube cells to have called for some early experiments to see if scale-up were feasible. The square header design made the use of alpha-alumina and the usual glass alpha-to-beta and mechanical alpha-to-metal seals. It was decided that the first tests should be done on a fairly large size header, because the problems increase with the size and the number of tubes. The anticipated problems were: (a) cracking the alpha-alumina plate by the mechanical pressure of the exterior seals, (b) obtaining the large number of alpha-to-beta seals all of which must be leak-tight in one sealing operation, (c) getting precise alignment of the tubes, and (d) obtaining leak-tightness on large exterior seals.

The following test was carried out to evaluate the feasibility of producing a relatively large mechanical seal between the metal cans and alpha-alumina header. The diameter of a recrystallized alpha-alumina disk with a thickness of 0.72 cm was reduced from 15.2 cm to 14.3 cm. This adjustment allowed the use of an Inconel 0 ring with C shape cross section of a stock production size (14 cm outer diameter). The alpha-alumina disk had to be ground to obtain a sufficiently smooth surface. Cans with flanges of suitable size were spun from aluminum, and polished. A pair of stainless steel collars (18.5 cm outer dia., 12.3 cm inner dia.) with a thickness of 0.7 cm were machined. Twelve holes (0.5 cm dia.) were drilled in a symmetric fashion into each of the collars to hold the screws. The center of these holes was at a distance of 7.9 cm from the center of the collar. The final assembly of the mechanical seal was the same as for the single tube cell. Subsequent testing revealed that the mechanical seal between an alpha-alumina header without beta-alumina tubes and the two aluminum cans became helium-leak tight after appropriate adjustments for the width of the stainless steel collar. Owing to the bigger size of the metal cans the transition region between flange and straight can portion is larger than in the single tube cell. The pressure on the flange must be concentrated in the correct area by the collars; otherwise the inner aluminum spacer behind the 0 ring is pushed slightly inwards. In the latter case the achievable leak tightness is about 10^{-5} mm Hg.

The second test gave a positive answer to the question of whether an array of holes can be drilled into the alpha-alumina without cracking. The array which was chosen is illustrated in Figure B-6. It attributes about the same portion of the total volume of the sulfur compartment to each of the beta-alumina tubes. The portion corresponds to the volume of the sulfur-carbon plug per unit of electrolyte area of the design given in the previous section on thermal design. The 15.24 cm size header can accommodate a maximum of 45 tubes. Countersunk holes were also drilled since they are helpful in the actual sealing of the beta alumina tubes to the alpha-alumina header by glass.

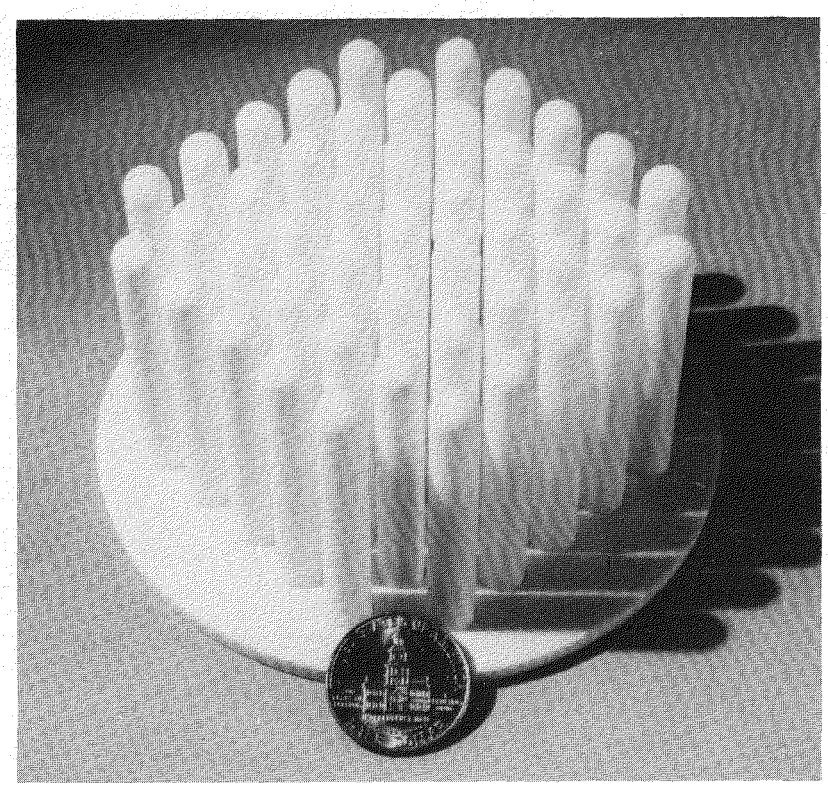

Figure B-6. Arrangement of Tubes in 45-Tube Cell Header

Since the header is large, the sealing process between the header and beta-alumina tubes was carried out in a large furnace. A series of sealing experiments with a small alpha-alumina disk and a beta-alumina tube were run to establish the sealing procedure. The available furnace was large, and uniform heat distribution took a long time necessitating many experiments. FN sealing glass was chosen because its sealing temperature was within the temperature limitations of the furnace.

A special holder was constructed from parts formed of alpha-alumina to guarantee the alignment of the beta-alumina tubes during the sealing. The completed header with 45 tubes sealed to it is shown in Figures B-6 and B-7. Figure B-6 demonstrates that the tubes are parallel to each other. It should be mentioned that satisfactory seals were obtained for 44 tubes by the first execution of the sealing procedure in the furnace. However, one of the tubes was only partially sealed to the header. After adding more FN glass to the

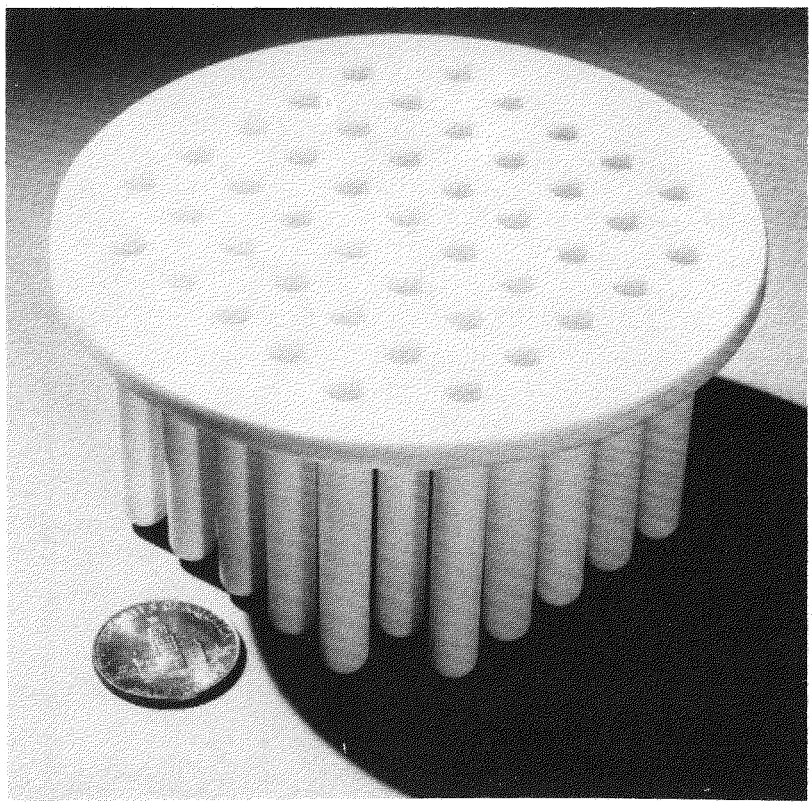

Figure B-7. 45 Tube Cell Header, Alpha to Beta-Alumina Seals

hole of this tube, a second run was made. The second heating resulted in repair of the faulty seal and did not prove detrimental to the other seals. This was an encouraging experience because the success of repeated application of the sealing operation to the same header is important to the overall statistical reliability and cost of the process.

The use of alpha-alumina instead of a metal as header material eliminates the need to develop a beta-alumina-to-metal seal and to find an insulating coating for the seal area. Some experiments were carried out in this direction with aluminum. However, satisfactory seals between beta-alumina tubes and aluminum could not be produced in vacuo with low melting aluminum alloys as a sealing medium. Since the above results were not promising, the effort was dismissed in favor of the described work with alpha-alumina as a header material.

Metal-to-metal exterior seals are routinely produced for our single tube cells. Aluminum-to-aluminum or steel-to-steel welds are used to seal the end caps on the containers. The procedures can be directly transferred to the construction of a multi-tube cell.

A multi-tube cell was assembled with the header, shown in Figure B-7 using an aluminum can as sodium compartment and a stainless steel can as sulfur compartment. Both cans were machined by spinning. A stainless steel can was chosen because it can be produced with a sharp angle between flange and straight part of the can. This sharp bend leads to a better use of the space than one which is rounded. In an earlier attempt the rounded flange area of aluminum cans allowed only 37 beta-alumina tubes to be sealed to a header of the same size. In general, the assembly steps are the same for the multi-tube cell as they are for the single tube cells used for life testing.

The completed cell is shown in Figure B-8. As shown, a filling tube is welded to the stainless steel (cathode) can. A lid with filling tube was not attached to the aluminum can to allow for the possibility of checking individual glass seals for helium leak tightness. The header did not crack when the pressure was applied through the collars by tightening the screws. Separate testing demonstrated that the mechanical seal between header and aluminum (anode) can was helium leak tight. The best seal between header and stainless steel corresponded to 10^{-5} mm Hg vacuum obtained on the helium leak detector. It is anticipated that the latter value can be improved by adjustments of collar width, flange and spacer. The results are satisfactory to proceed with plans for the filling and testing of the experimental multi-tube cell.

B-2 DESIGN ANALYSIS AND ALTERNATIVES

The first stages of the design process have been completed. That is, a cell/module/system design has been obtained which could be built and expected to perform satisfactorily for the load-leveling application. It would meet the electrical, thermal, and efficiency requirements which have been projected for sodium-sulfur batteries. Its performance is based on actual small cell data, and such a system could be constructed today. However some

Figure B-8. 45 Tube Cell, Containers Attached

critical design criteria given only brief mention so far in this report are economic analysis and design optimization. These are critical to any complete design. The second part of the study has been to explore the economics of the design and to compare them with alternative approaches, which could use the same economically practical materials but offer a cost advantage in the manufacturing process. The major alternative design which has been studied for the BEST Facility and succeeding production models is a larger single tube cell approach, rather than many tubes in a single cell. This was at first avoided because of the obvious increase in the number of exterior seals and increased materials cost for containers, in comparison with placing several ceramic electrolyte tubes of the same size in a single cathode container.

In this section an alternative single tube cell will be described and its characteristics will be compared with those of the multi-tube cell. A summary of the results of a manufacturing cost comparison of the multi-tube cathode vs the single tube cathode approach will be given.

B-2.1 Alternative, Single Tube Cell

Cells made with bundles of subcells, each with a single beta-alumina tube and individually sealed reactant compartments could offer some cost and performance advantages over the common container design if manufacturing costs are low enough to supersede increased materials and seal number costs. An individual container-type design may result in improved safety, less pronounced effects of individual failures on performance of the whole cell, and adaptation to assembly-line mass production. Furthermore, the knowledge we have generated in the past years on how to increase sulfur utilization is directly applicable to single tube container construction, and can directly be transferred from the prototype cell work.

Subcells of this type would look very much like the test or "prototype" cells which are currently being made and tested. The size of an individual subcell depends on an analysis of the cost of the system as a function of many size dependent variables such as cost of container materials, cost and manufacturability of the ceramic, cost of the seals, and cell efficiency. The most critical ingredient for the success of this approach is the ceramic-metal seal between the insulator and each container. A sealing method is required which is adaptable to a short manufacturing time cycle and assembly-line construction method.

Cells would be made by bundling the tubular subcells in parallel, connecting all the cathodes and anodes to single metallic plates. The number of subcells per cell is, like the optimum subcell size, a subject which must be analyzed in detail. In this case the analysis is not as stongly based on economics as it is on system reliability. The parallel connection of subcells to form larger cells which are connected in series is one of the examples (crossover system) which is discussed in the section of this report on statistical studies of system reliability.

The parallel plate connectors can serve double use as heat sinks. These are necessary in the thermal design for the purpose of utilizing ambient temperature cooling gas without developing cold spots. A preliminary thermal analysis of a subcell type design of subcell bundles showed that the method of cooling through the sodium side could also be successfully employed with this arrangement. A complete thermal analysis will be repeated when the final size of the cell/subcell is determined.

B-2.2 Comparative Cost Analysis of Multi-Tube and Single-Tube Designs

The multi-tube and single tube designs each have their advantages. The multi-tube design is more compact, uses less material (particularly containers) and has fewer seals. The single tube approach would have more flexibility for electrical series/parallel arrangements, is similar in cathode geometry to test cells which have demonstrated satisfactory performance, possibly could simplify safety controls, and may be adaptable to assembly line production. A comparative cost analysis was undertaken to clarify the situation. Unfortunately no cost analysis could be very precise because there are aspects of both designs which had to be left rather vague at the present stage of development.

The costs determined in the study are not complete cell costs but only those costs which are not common to both designs. For example the cost of the reactants and the beta-alumina are not included. Of those steps and materials which are not common to both designs, every attempt was made to make the analysis complete. That is, each such manufacturing step was considered in detail to include all the time, materials, and other production costs.

The basis of comparison was to take a multi-tube design with 100 electrolyte tubes 1 cm x 15 cm in size, and compare the costs to those of a paralleled bundle of 100 single tube cells using beta-alumina tubes of the same 1 cm x 15 cm dimensions. It is important to note that this size single tube cell would certainly be too small to be economical, so this is a comparison only, and not to be construed as an estimate of the cost of a part of an economical Na/S system. For example, recall that the power and energy density design

base has not been updated from 1974 data to current cell performance data which has significantly improved since 1974. Therefore absolute costs may not be extracted from these figures.

The summary costs for the compared portions of the multi-tube and single tube designs are shown on Tables B-2 and B-3, respectively. These costs will of course be changed when an economic optimization is made, and obviously excessive cost items will be changed to reduce cost. An example of an excessive cost is heat transfer plate (heat sink) which appears in both designs. As shown in Table B-4 the multi-tube incremental cell cost is $46 more than that of the single tube cell of the same size. The major difference is in the exterior seal ($36 for the clamping device and "C" rings). The multi-tube design is more expensive even if the cost of the clamping device is reduced to $4, the header to $16, and the "C" rings to $6, which would be a very inexpensive seal for this size and header.

Another cost consideration not taken into account in Table B-4 for the multi-tube cell design is the yield of successful tube/header assemblies. The seals between every one of the 100 tubes and the header must be good to produce a good assembly. Figure B-9 shows the calculated percent yield of good cell assemblies vs the percent of tight individual seals for different numbers of tubes per header. Examining the figure for 100 tubes and an acceptable yield of assemblies chosen to be 90%, less than one in one thousand defective seals could be tolerated. This is probably a most unrealistic yield to expect, and points to another problem of the multi-tube design.

Barring the quite real possibility that some construction step in the single tube design turns out to be impracticable or more costly than anticipated, it appears that the multi-tube design cell would be less economical and emphasis will be placed on single tube cells in the foreseen future.

B-3 BASIC STUDIES FOR FINAL DESIGN

The first design studies detailed above have been carried out as far as was profitable. The next design studies will work toward a system which will be close to a final BEST Facility and demonstration plant stage. The earlier

TABLE B-2

PARTIAL MANUFACTURING COSTS

100 TUBES IN COMMON HEADER W/COMMON RESERVOIRS

		Labor	Material	Total
Aluminum reservoirs (2)	Sheared, rolled, welded	$ 1.73	$ 5.73	$ 7.50
Heat transfer plate	Cut, grind edge	2.00	4.00	6.00
Sodium reservoir to plate weld	Tungsten Arc	.30	--	.30
Alpha-Alumina 100 hole header/separator	Purchase	--	32.00	32.00
Clamping device		12.75	11.25	24.00
"C" rings (2)	Purchase	--	12.00	12.00
Assembly labor		3.00	--	3.00
Filling & closure, 2 reservoirs	2-stage, EB Weld	2.00	--	2.00

"COST" PER 100 TUBE UNIT = $86.80

TABLE B-3

PARTIAL MANUFACTURING COSTS

SINGLE TUBE CELLS IN 100 CELL BUNDLE

		Costs per 100 tube unit Labor	Material	Total
Sodium reservoir Sulfur reservoir	Tube spinning & cut-off	$ 1.11	$15.34	$16.44
Heat transfer plate	(Saw & de-burr)	1.50	6.29	7.79
	(Drill 100 holes)	1.68	--	1.68
Alpha-Alumina separators	Purchased from Manufacturer	--	6.00	6.00
Aluminum to alumina sealing	Bonding metal to ceramic	3.50	--	3.50
Filling & closure	(Fill in vacuum)	5.00	--	5.00
	(EB weld closures)			

"COST" PER 100 CELL BUNDLE = $40.41

TABLE B-4

PARTIAL MANUFACTURING COST COMPARISON

	Bundle of 100 Single Tube Cells	100 tubes w/common separator & reservoirs
Reservoirs	$16.44	$ 7.50
Heat transfer plate	9.47	6.30
Alpha-alumina separator(s)	6.00	32.00
Sealing system	3.50	39.00
Filling & closure	5.00	2.00
	$40.41	$86.80

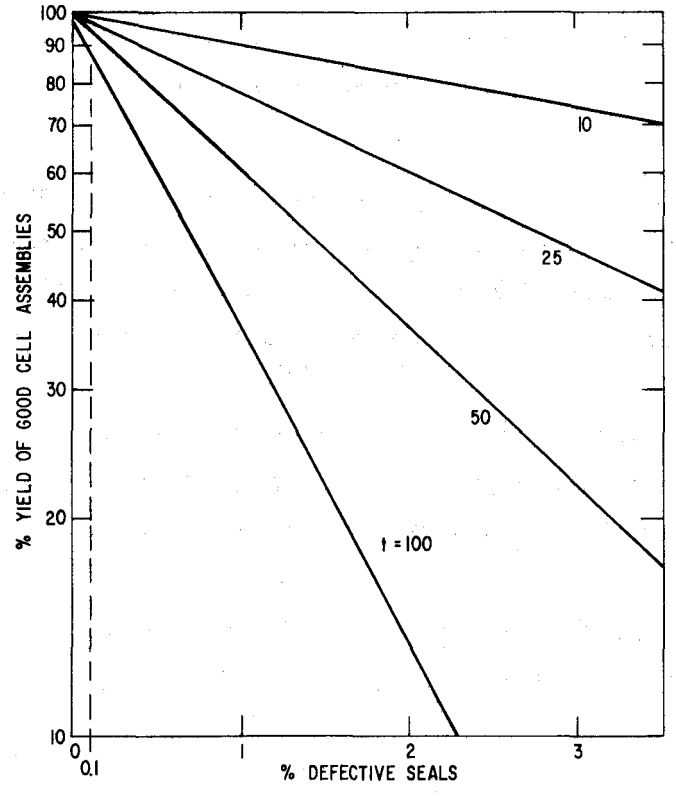

Figure B-9. Yield of Cells as a Function of Seal Unreliability and Seals per Cell

designs have shown the engineering feasibility of the system. Now with test cell performance coming close to the original optimistic predictions for the Na/S battery a design can be started which will be a realistic representation of a load-leveling system. Required are many design optimization studies, and experiments and evaluations. Some of the groundwork for this long term work was accomplished during the contract year and will be given in this section and Appendix I. In particular, one is a statistical analysis of cell/module/system networks which relates the performance of individual components to the performance of the entire system, and the other is the beginning of an analysis to optimize system cost in relation to cell parameters and application duty cycles.

B-3.1 Statistical Study of System Reliability and Performance

In proceeding from the stage of having cells on test, which give a certain known level of acceptable performance to the stage of building a battery system to a required level of performance, a great deal of statistical analysis is required. Examples of this are:

- How much redundancy must be built into the system?
- What is the best combination of series and parallel connections?
- How is cell reliability related to system reliability?
- In a given configuration what is the probability that the system will fail during a cycle?

In order to have a way to answer these questions as the system design proceeds, we have undertaken a statistical study of system reliability and performance to serve as groundwork for the cell/module/system design.

The text of the study is given in Appendix I. The approach of the work is to evaluate system reliability with respect to

- voltage
- capacity/energy discharge
- current
- resistance

as a function of module failure probability per cycle of system operation.

The output of this task is design curves for the relationship between system performance and module reliability for various system configurations. Such curves can be used two ways: (1) given a module reliability, one can determine the system performance of the different configurations; and (2) given a desired system performance, one can determine the needed module reliability. A complete text of this study is given in Appendix I-2, which is the first of a series of studies to guide the cell/module/system design on a well-founded statistical basis.

B-3.2 Cell Parameter and Cost Optimization

A study of cell size optimization has been partially completed. Its purpose has been to choose the optimum dimensions of the ceramic electrolyte tube

for the most economical load-leveling system. The basis for such an analysis can begin with the physical properties of ceramics. The manufacturability of a ceramic tube depends on its dimensions. The wall thickness cannot be too thin in proportion to tube diameter or it will be too fragile to manufacture and handle. The tube length cannot be too long in proportion to tube diameter because of curvature and subsequent alignment problems. Some rough practical limits can be set for the above ratios. If one sets these limits, the tube size can be completely defined in terms of a single variable, for instance, tube diameter. Given the specific resistivity of the ceramic, experimentally determined expressions for the cathode losses as a function of size and other more readily determined performance variables, it is possible to determine curves of system performance and cathode volume for different tube sizes. There are different sets of curves for different operational variables. When these sets of system performance curves are used as input variables for cost and reliability analyses, the optimum tube size is obtained in terms of cost, performance, and the operational requirements of the specific system application.

The extent of this study so far has been to devise a computer program which determines the number of single tube cells required for a system with a specified duty cycle and individual cell performance.

In the program three beta-alumina ceramic parameters are set: (1) the electrical resistivity which is known for each of our ceramic compositions; (2) the ratio of outside tube diameter to wall thickness which is generally about 10 to 1 in ceramics independent of the absolute values; (3) the ratio of the tube length to tube diameter which was conservatively set at 15 to 1 because very small curvature along the length can be tolerated especially as the cell size increases.

The resistivity of the sulfur compartment is also set. The sulfur compartment resistivity is taken as all the resistive losses, other than those due to the beta-alumina, which we measure on the prototype test cells. It is certainly not strictly correct to scale this in size as a specific resistivity, but if the thickness of the cathode of the resulting computer designed cell is close to that of the test cells (0.7 cm) the error will be very small.

The final fixed input parameter is the cell capacity per unit volume. This is calculated from the density of Na_2S_3 (complete discharge condition) allowing for the graphite volume, a 10% intentional void space, and assuming 80% utilization of theoretical capacity.

When the system parameters, watts delivered, hours of discharge, hours of charge, and efficiency, are supplied as inputs to the program, it can be used to calculate the number of cells, the cell resistance, current density, etc. The iterative method employed is to find a sulfur compartment size which will use all the available sulfur present (80% of total) while satisfying the equation for cell efficiency (also set at 80%). In terms of the discharge current, i, this equation is:

$$Eff = (O.C.V. - iR)/(O.C.V. + iRH_d/H_c)$$

where H_d and H_c are the times for discharge and charge.

An example of how the program can be used is given as follows to determine the effects of changing the resistivities of the ceramic and of the cathode (sulfur) compartment on the number of cells required for a 10 MWH system with a 10 hour discharge, a 5 hour charge, and an efficiency of 80%. The results are shown on Table B-5 for single tube cells with a diameter of 1 cm (15 cm long, 0.1 cm wall) and on Table B-6 for 2.5 cm diameter tubes (37.5 cm long, 0.25 cm wall). The cathode resistivities are normalized to a value of one for a cell presently being tested (Cell No. 195). It is interesting to note that large improvements (reductions) in either cathode resistance or ceramic resistance alone are not too effective in reducing the number of cells required for the system, but that the simultaneous reduction of both is more effective. This of course is a simple consequence of the resistances being used in series.

The eventual purpose of the computer program will be its future use as part of a study for quantitative cost evaluation. Another part of this study which has not yet started will be to evaluate cell manufacturing cost as a function of cell size. Combining both will result in a determination of system cost as a function of ceramic tube size and other parameters in the program presented above.

TABLE B-5

SINGLE TUBE CELLS* REQUIRED FOR 10MWH SYSTEM

(1 CM TUBE DIAMETER)

Ceramic Resistivity (OHM-CM)	Relative Cathode Resistivity (Present Value = 1.0) 1.23	0.62	0.31	0.12
30	400	347	314	290
20	331	267	228	203
15	294	226	186	159
10	258	188	145	115
5	224	151	106	73

*In Thousands

TABLE B-6

SINGLE TUBE CELLS* REQUIRED FOR 10 MWH SYSTEM

(2.5 CM TUBE DIAMETER)

Ceramic Resistivity (OHM-CM)	Relative Cathode Resistivity (Present Value = 1.0) 1.23	0.62	0.31	0.12
30	128	120	115	111
20	96	86	80	76
15	80	69	63	58
10	66	54	46	41
5	52	39	30	24

*In Thousands

B-4 REFERENCES

B-1 "Sodium-Sulfur Battery Development For Bulk Power Storage - Conceptual Battery Design For BEST Facility", EPRI Contract RP128-2 Addendum, General Electric Company, Schenectady, New York, Dec. 27, 1974.

B-2 Bayley, F.J., and Czekauski, J., J. of Mech. Eng. Sci., Vol. 5 No. 4, p. 295, 1963.

B-3 Larsen, F.W., and Hartwett, J.P., ASME J. of Heat Transfer, p. 87, Feb., 1961.

B-4 Pucci, P.F. and Gerretsen, J.C.R., ASME J. of Eng. for Power, Series C., Vol. 94, p. 202, July 1972.

B-5 Thermo Physical Properties Research Center Data Book, Purdue University, Lafayette, Indiana, 1964.

Section C

CERAMIC ELECTROLYTE DEVELOPMENT

Major progress was made during the report period in improving the properties of the beta-alumina ceramic electrolyte required for utility load-leveling. This is shown in Table C-1 where recent year-to-year changes in the most important properties are presented. The operating life of the ceramic no longer limits cell life. Ceramic degradation is not evident even after hundreds of deep cycles. Over the period, the ceramic resistivity has been reduced and the mechanical strength increased somewhat. Some reduction in fabrication costs was also achieved although this was not a major objective of work in this contract period. Photomicrographs of fifth generation ceramic can be compared in Figure C-1 with that first used on this program. Grains of exaggerated size are absent in current ceramics. Porosity, indicated by dark roundish spots on the photomicrographs, is much lower and the pores are smaller. As a result of this lower porosity, there is a marked increase in translucency. External surfaces of current beta-alumina ceramic have a smooth, almost waxy, feeling. This section describes how these improvements were brought about.

The framework of a processing scheme described in previous interim reports has nonetheless been retained[C-1,C-2]. The major elements of this scheme involve: 1) the use of a commercial alumina, rather than high purity alumina, as the powder source; 2) the use of electrophoretic deposition from an amyl alcohol suspension as the forming technique; and 3) the use of the stoker sintering method for firing the green beta-alumina tubes. Over the

TABLE C-1

PROGRESS TOWARD PROPERTY GOALS

Property	1973	1974	1975	1976	Goal
Maximum Operating Life in Cells	3	70	115	300+*	1500-2500 AH/cm^2
Electrolyte Resistivity At 300°C	17		26	16**	5-10Ωcm
Fracture strength			20	24*	40-50 kpsi

past year, use of XB-2 beta-alumina from Alcoa as the powder base had been continued. The main processing changes made in this report period include first the use of a higher soda content in the ceramic. An increase of the soda concentration from 7.2% to the range, 8.4 to 9.6%, has resulted in higher fired density with less exaggerated grain growth, with a lower grain boundary resistivity at 300°C, and with a lower sintering temperature. The elimination of flaws in greenware associated with removal from forming mandrels has led to a great decrease in the number of cracked tubes after firing. A better control of the furnace atmosphere during sintering has also contributed to the higher fired density and in addition has given rise to less surface porosity, greater surface smoothness, lower surface resistivity, as well as to straighter tubes with less out-of-roundness. This control involves, but is not limited to, use of dry oxygen in place of the ambient atmosphere within the furnace.

More fundamental studies on tortuosity (described in Section E) and an exploitation of the temperature comparison method for separating measured resistivities into grain boundary and crystal components have given quantitative answers to a number of questions on relationships between processing,

*Fifth generation ceramic

**Sixth generation ceramic

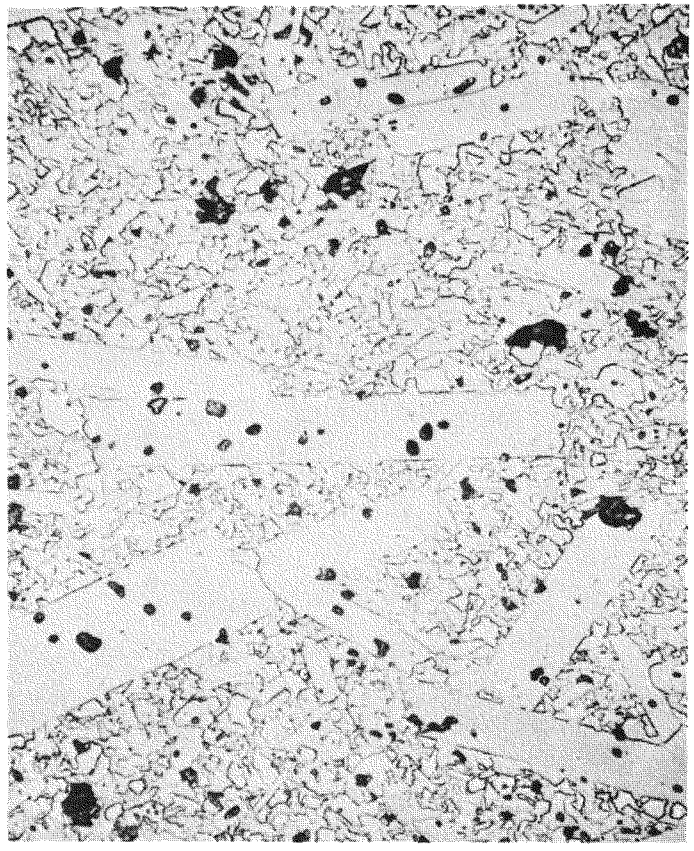

FIRST GENERATION BETA-ALUMINA CERAMIC
1.40 $Na_2O \cdot 11Al_2O_3$ WITH 1% MgO, 1% ZrO_2
AND 0.5% Y_2O_3 (10/1973)

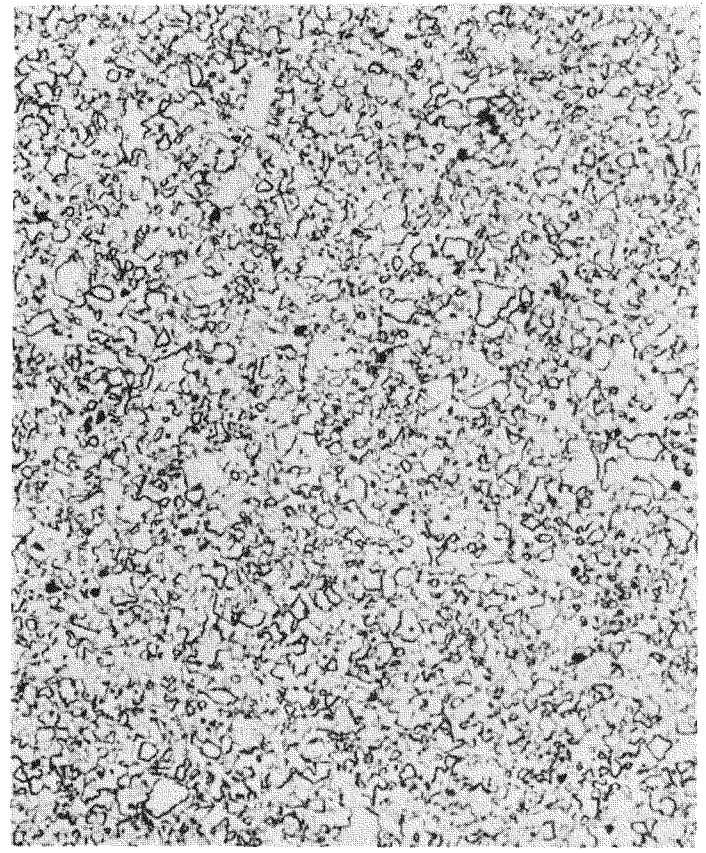

FIFTH GENERATION CERAMIC
1.66 $Na_2O \cdot 11Al_2O_3$ WITHOUT ADDITIVES
(4/1976)

Figure C-1. Improvements in Ceramic Microstructures

structure, composition, and properties. Tortuosity refers to the elongation of the conduction path in polycrystalline beta-alumina, over that in single crystals, arising from the random orientation of the individual grains. Recall that in beta-alumina, transport of sodium ions occurs only in certain planes perpendicular to the c-axis of the crystal. In addition to providing a value for the tortuosity constant, this study also shows the effect of preferred orientation on crystal resistivity and provides some insight on field enhancement effects around exaggerated size grains. Using the temperature comparison method, the variation with temperature of both the grain boundary and the crystal components of resistivity have been determined for seven different ceramic compositions. Certain trends in the variation of these component resistivities with composition can be discerned. The relevance of this new information to the problem of longer ceramic operating life and to the problem of reducing the resistivity is discussed below.

C-1 APPROACH TO IMPROVED CERAMIC ELECTROLYTE PROPERTIES

Over the first two years and even throughout a portion of the third year of work under contract with EPRI, major emphasis was given to extending the operating life of the beta-alumina electrolyte. However, since ceramic operating life is no longer limiting, major emphasis has shifted to reduction of the ceramic resistivity. In previous years, this property was carefully monitored and techniques for separating the measured resistivity into grain boundary and crystal components were developed. Over the past year, mechanical strength of the ceramic was monitored more closely. This latter property will be accorded increased attention in the immediate future. The very important property, leak tightness to helium, has been achieved as a matter of course. Experience has indicated that if beta-alumina ceramic is crack-free, it is also leak-tight.

The approach taken to extend ceramic operating life has been described in previous interim reports; however, to make this report more self-contained, it will be briefly described again. The approach is closely related to a model of the electrical properties of beta-alumina ceramic shown in Figure C-2. In that figure, r_c represents the specific resistivity associated with the interior of the grains. This component is usually referred to as the crystal resistivity. On the other hand, r_b represents the extra resistivity

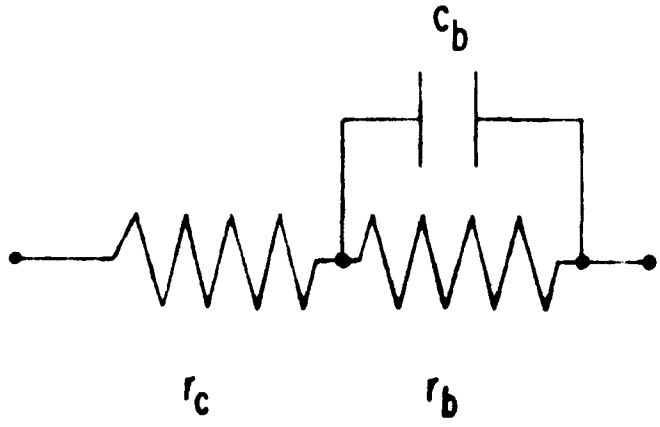

Figure C-2. Simplified Model of Electrical Properties of Polycrystalline Beta-Alumina

in the ceramic associated with the presence of grain boundaries. The capacitor C_b models the dielectric properties of these grain boundaries. Extended discussions of the evidence supporting this model are given elsewhere[C-3,C-4]. The model is really a voltage divider for direct current, apportioning a part of the voltage drop associated with current flow across the grain interiors and a part across the grain boundaries. Since the two resistivity components are very roughly of the same size at 300°C and since the grain boundaries are very thin, electric fields at grain boundaries are very high. Assuming grain boundary thicknesses to be 10 A°, typical fields are computed to be about 10^5 V/cm. Such large fields cause concern about the acceleration of decomposition processes that might occur at boundaries, particularly at those close to electronic conductors. For example, breakdown might occur in sodium sulfur cells near the electrolyte surface in contact with sodium and then propagate across the wall of the beta-alumina tube to the other external surface. The tube would then be electronically shorted. Because sintering aids, materials used to increase densification or reduce the sintering temperature, often congregate at grain boundaries and conceivably might be reduced there, one aspect of the effort to improve operating life involves learning to sinter beta-alumina to high density without use of such aids. The high average fields at grain boundaries can be further enhanced if local current densities through portions of the ceramic greatly exceed average values. Consequently, the second aspect of the approach to improved operating life involves reducing field enhancement wherever feasible. It can arise from heterogeneous

features in the ceramic itself as well as from details associated with the shape of the beta-alumina tube. Both aspects of the approach to better operating life are discussed in more detail below.

The approach to reducing the electrical resistivity involves a knowledge of the effects of ceramic composition and processing history on the components of resistivity and thence on the total ceramic resistivity. As mentioned above, the temperature comparison method for obtaining the grain boundary and crystal components of resistivity was sufficiently exploited over the past year that some trends in the effects of ceramic composition now appear discernible. The sixth ceramic generation constitutes an attempt to lower the ceramic resistivity while retaining other features considered responsible for extended operating life.

C-2 EXPLOITATION OF THE TEMPERATURE COMPARISON METHOD

The circumstances leading to the development of the temperature comparison method for separating measured resistances of beta-alumina ceramics into grain boundary and crystal components were discussed in a previous interim report[C-2]. A preliminary description of the operational basis was also given there. A more detailed description is in preparation[C-5]. Only a brief account is presented in this report with primary emphasis given to the effects of composition on the components of resistivity.

The method involves 4-probe measurements of the resistivity from room temperature to a little over 400°C on a set of specimens of different grain size, and consequently of different grain boundary resistivity. For convenience, measurements are usually made at low frequencies, e.g., 10 and 100 hz. The method is based primarily on a plot of resistivity at a higher temperature, e.g., 300°C vs the corresponding resistivity at a reference temperature, usually 26.8°C, for the specimens in the set. As illustrated in Figure C-3 for ceramic with 8.4% Na_2O, these plots are usually prepared for temperatures between 150° and 400°C at 50° intervals. They have been called resistivity distribution plots because they can show at a glance the distribution of total specimen resistivity between crystal and grain boundary components.

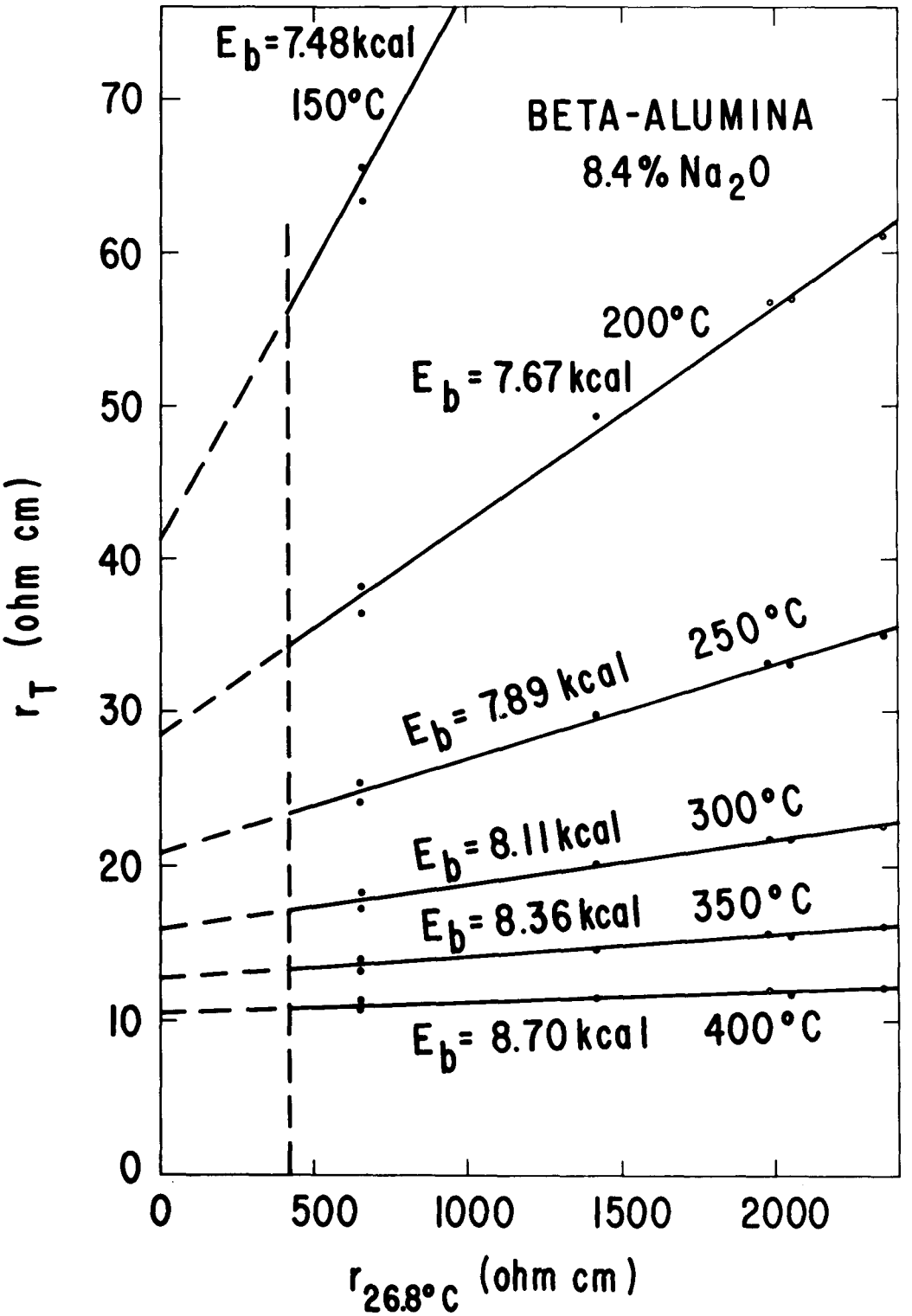

Figure C-3. Resistivity Distribution Plots for Ceramic with 8.4% Soda

These plots should be linear if:

- $r_{measured} = r_c + r_b$, i.e., if the model is valid.
- r_c is the same for all specimens in the set at any fixed temperature.
- r_c varies with the absolute temperature T as $T/r_c = \sigma_{oc} \exp(-E_c/RT)$ where the activation energy, E_c, is a constant.
- the grain boundary activation energy, E_b, is the same for all specimens in the set. It need not remain invariant with temperature however.

The grain boundary activation energy, E_b, can be derived from the slope of the resistivity distribution plot using the expression $E_b = \frac{R \ln (mL/T)}{(1/T-1/L)}$ where m is the slope, T is the upper temperature, and L is the reference temperature. Values of E_b obtained in this way are averaged over the temperature interval from L to T. As illustrated in Figure C-3, such activation energies can and often do increase somewhat with temperature.

There is still one other very important property of such a plot. The intersection with the dashed vertical line representing the value of the crystal resistivity at the temperature L determines the value of the crystal resistivity at T. This value is indicated by the vertical distance from the axis of abscissae to the point of intersection. Crystal resistivity values at 50° intervals from 150° to 400°C can be read from Figure C-3 in just this manner.

Resistivity distribution plots for the third generation ceramic, that with 7.2% Na_2O and 1.0% ZrO_2, were presented in the previous interim report[C-2]. Those for fifth generation ceramic with 8.4% Na_2O appear in Figure C-3. Plots for five other ceramic compositions are also available. The most important information for all seven beta-alumina ceramic compositions is condensed in Table C-2. It should be emphasized that all the ceramics on which data are given in this table are beta-alumina, not beta"-alumina. To illustrate some trends more readily, the variation in the crystal resistivity with temperature for three of these compositions is presented in Figure C-4.

The parameters given in Table C-2 for ceramic with 7.2% Na_2O and 1% ZrO_2 differ slightly from the data given in the previous interim report[C-2]. The

TABLE C-2

RESISTIVITY PARAMETERS FOR VARIOUS BETA-ALUMINA CERAMIC COMPOSITIONS

PARAMETER	Low Soda Ceramic	Generation IV	Generation V	Generation III	1% MgO Ceramic	Generation VI	Generation I
Composition %Na_2O %Other Additives	6.2	7.2	8.4	7.2 1.0% ZrO_2	7.2 1.0% MgO	9.6 0.25% Li_2O	7.2 1.0% MgO 1.0% ZrO_2 0.5% Y_2O_3
R_c Crystal (Intragrain) Resistivity At 300 C - OHM CM	22.8	17.0	17.0	13.1	11.0	11.8	5.87
R_c At 26.8°C	266	391	418	284	327	552	103
σ_0 Pre-Exponential Factor	761	2151	2294	2613	4288	6626	4486
E_c Activation Energy For R_c' KCAL/MOLE	3.88	4.73	4.81	4.66	5.04	5.61	4.38
E_b Grain Boundary Activation Energy Averaged Between 26.8°C and							
150°C (KCAL/MOLE)	7.19	7.23	7.48	7.05	7.60	8.09	6.95
200	7.49	7.36	7.67	7.20	7.78	8.28	7.07
250	7.87	7.41	7.89	7.23	7.92	8.47	7.18
300	8.5	7.47	8.11	7.27	7.99	8.70	7.29
350		7.49	8.36	7.26	7.99	8.96	7.34
400		7.47	8.70	7.23	7.99	9.27	7.40

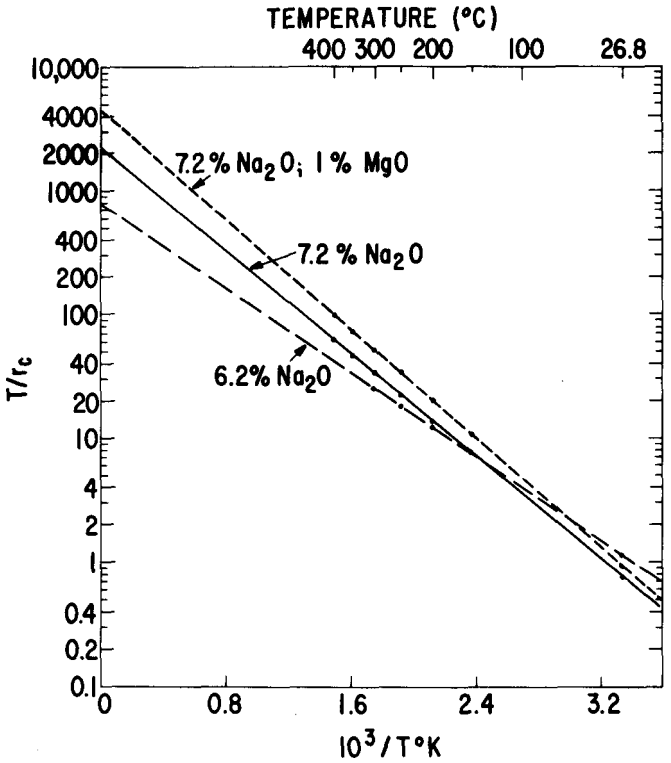

Figure C-4. Variation in the Crystal Resistivity with Temperature for Three Ceramic Compositions

discrepancies arise from use of different values for the geometric constant, the cross-sectional area of the specimen divided by the distance separating the voltage probes. This constant is used to convert measured resistances into specific resistivity values. Previously the cross-sectional area was determined from caliper measurements on the outer diameter and on the wall thickness of the tubular specimens. It was found subsequently that a more accurate value could be obtained from the measured mass of the specimen, its density, and its overall length, the closed end having been cut off. The scatter in resistivity distribution plots was noticeably reduced by the new procedure. For example, the average variance for the six resistivity distribution plots for third generation ceramic was reduced 35 percent using the better values for the cross-sectional areas.

At low levels, the soda content of the ceramic can be seen to have very marked effects on the resistivity of the crystal component. An increase from 6.2 to 7.2% Na_2O concentration leads to an increase in both the pre-exponential

constant and the activation energy with the result that the resistivity with 7.2% Na_2O is less than that with 6.2% Na_2O above 150°C and greater below this temperature. A further increase in soda concentration from 7.2% to 8.4% has an almost negligible effect. The presence of magnesia at the 1.0 wt percent level also gives rise to an increase in both the pre-exponential constant and the activation energy. These trends are accentuated in ceramic with 0.25% Li_2O. As expected, zirconia appears to have but a small effect on r_c. The crystal resistivity for the first generation ceramic, that with three additives, is surprisingly low, a result not understood at this time.

The activation energy found for r_c in ceramic with 6.2% Na_2O, 3.88 kcal/mole, does not differ greatly from the single crystal values of 3.77 kcal/mole found by Yao and Kummer and the value 3.79 reported by Whittingham and Huggins[C-6, C-7]. If the r_c value at 25°C for ceramic with 6.2% Na_2O is divided by 1.34, the tortuosity factor as calculated recently in this Laboratory, an equivalent single crystal resistivity of 205 ohm cm is obtained. This can be compared with values of 75 ohm cm reported by Whittingham and Huggins and 33 ohm cm, by Yao and Kummer. The result of the present work exceeds that of Whittingham and Huggins by roughly the same factor as that of Yao and Kummer is lower. Admittedly, data on resistivity distribution plots are much more scattered for the ceramic with 6.2% Na_2O than those from any other ceramic composition--a fact consistent, however, with the rapid change in resistivity parameters between 6.2% and 7.2% soda. Still the differences are much greater than any likely measurement error. These probably result from differences that arise in specimen preparation. The single crystals, on which results were cited above, were large grains removed from cast blocks of a commercial beta-alumina designated as Monofrax H by the manufacturer, the Carborundum Corporation. They contain about 6.0% Na_2O. On the other hand, specimens used in the present study were made from an Alcoa semi-commercial beta-alumina powder, designated as XB-2. The soda-content of the powder was 7.2%. After forming and sintering as indicated above, tube specimens were heated in air at 1575°C for about one day to reduce the soda content to approximately 6.2%. These results do raise questions about the possibility of changing the crystal resistivity by process variations.

In Table C-2, the average activation energies for the grain boundary resistivity are shown to increase with temperature. While the increase may be of marginal significance in the fourth generation ceramic and that with 1% MgO, it is regarded as real for the other ceramics. A change in an apparent activation energy with temperature is often attributed to heterogeneities in the rate controlling process. In the present case, these might be compositional variations within the grain boundaries. It is interesting that the increase of activation energy with temperature is least in the ceramic with 7.2% Na_2O, one in which no additives were incorporated and in which the soda content was not altered from that of the as-received powders. The incorporation of additives gives rise possibly to a small increase in activation energies with temperature. However, the largest effects appear associated with alterations in the soda content from that of the as-received powders. Additional work will be needed to determine how sensitive are values for the activation energies for grain boundary resistivities to details of specimen preparation.

C-3 WORK OF THE PREVIOUS YEAR

This portion of the section on Ceramic Electrolyte Development describes some work carried out between May 1, 1974 and April 30, 1975 which previously was given but very restricted distribution. It provides background and perspective to the work carried out in this report period. The most important part of sintering work carried out in the previous period was on "liquid phase" sintering. Briefly discussed also is a furnace modification to permit firing of ware in dry O_2 instead of ambient air. These activities were prompted by the need to compensate for the absence of sintering aids, particularly of zirconia. The "liquid phase" scheme involves adding and intimately mixing with the beta-alumina powder a small amount of Na_2O/Al_2O_3 material relatively rich in soda[C-8]. Its purpose is to promote liquid phase sintering as the composition of the material corresponds to a liquid on the phase diagram at the sintering temperature. The material should disappear into the beta-alumina during the later stages of sintering.

A preliminary evaluation of this stimulating idea was carried out with very promising results, which are presented in Table C-3. Actually, two different Na_2O/Al_2O_3 mixes were investigated. Mix A was 2.1 Na_2O.11 Al_2O_3. It

TABLE C-3

DENSITY DATA FOR VARIOUS CONCENTRATIONS
OF SODA ENRICHED MIXES

POWDER	CONTROL SUPERGROUND XB-2		SUPERGROUND XB-2 +10 PERCENT MIX A		SUPERGROUND XB-2 +5 PERCENT MIX B		SUPERGROUND XB-2 +10 PERCENT MIX B	
OVERALL COMPOSITION	1.40 $Na_2O \cdot 11 Al_2O_3$		1.47 $Na_2O \cdot 11 Al_2O_3$		1.56 $Na_2O \cdot 11 Al_2O_3$		1.73 $Na_2O \cdot 11 Al_2O_3$	
1750°C Sinter, 1/2 In./Min Traverse Rate	8J1-1	3.191 g/cc	8J2-1	3.214 g/cc	8J5-1	3.239 g/cc	8J3-1	3.241 g/cc
	-3	3.187	-4	3.193	-4	3.243	-4	3.249
	-5	3.208						
	8J4-1	3.200						
	-3	3.186						
	-5	3.207						
Average Density		3.1965		3.2035		3.241		3.245
Standard Deviation		.0099		.0148		.0028		.0056
1700°C Sinter, 1/2 In./Min Traverse Rate	8J1-2	3.137 g/cc	8J2-2	3.162 g/cc	8J5-2	3.229 g/cc	8J3-2	3.242 g/cc
	-4	3.091	-3	3.172	-3	3.208	-3	3.247
			-5	3.151	-5	3.221		
	8J4-2	3.127						
	-4	3.122						
Average Density		3.1192		3.1617		3.2193		3.2445
Standard Deviation		.0198		.0105		.0106		.0035

corresponds approximately to the phase boundary between beta- and gamma-alumina below 1400°C. Mix A is in the beta/liquid field at 1700°C. Mix B had the composition 4.7 Na_2O•11 Al_2O_3. It corresponds to the eutectic composition for Na_2O•Al_2O_3 and beta-alumina. XB-2 beta-alumina has the approximate composition 1.4 Na_2O•11 Al_2O_3. Both Mix A and Mix B were prepared by tumble mixing superground XB-2 beta-alumina powder with anhydrous sodium carbonate powder and calcining in air at 1100°C.

As indicated in the table, three different proportions of these mixes were added to superground XB-2 powder. Suspensions of these plus two controls were vibratory milled with beta-alumina grinding media for 48 hours. Five closed end tubes were electrophoretically formed from each suspension with no difficulties. About half of the greenware was sintered at 1750°C and the other at 1700°C. From the density data presented, it is apparent that densification is promoted by addition of the soda rich material. Nearly theoretical density was achieved with 10% of Mix B at 1700°C. Very acceptable values of electrical resistivity were obtained on the sintered specimens. The only concern was with the possible presence of sodium aluminate in these specimens. However, x-ray diffraction indicated the presence of beta-alumina only.

Examination of the microstructure of these compositions revealed an unexpected and important consequence of the use of this particular method of sintering. It results in an unusually small grain size, while obtaining near theoretical densities. It had long been the goal to obtain this combination for the highest mechanical strength and homogeneity of electrical fields in beta-alumina for the purpose of obtaining long cycle life.

Because water vapor and sodium oxide react at high temperature to form very stable sodium hydroxide vapor, it is important to avoid a large content of water during the firing process. The water vapor present in ambient air did not appear high enough to cause detectable amounts of alpha-alumina formation due to soda loss, but because ambient humidity is not constant, an apparatus was constructed to permit controlled humidity firing. Shown in Figure C-5 is the new addition to the exit end of the sintering furnace. The sintered ware enters a fused silica tube which acts as a holding chamber. The other end of this holding chamber is attached to a portion of a vacuum coupling. The

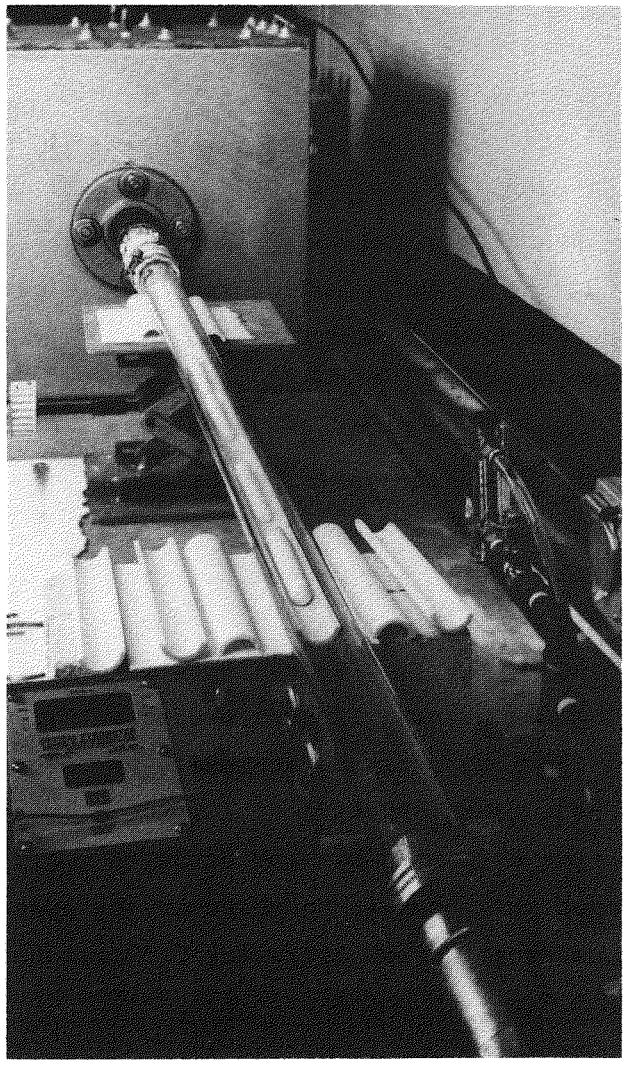

Figure C-5. Exit End of Sintering Furnace

other portion of the coupling contains a connection for introducing oxygen and a viewing port for observing the interior of the furnace. Dried oxygen flows through the silica tube at an average speed of 1/2 in/sec in a direction opposite to that of the ware. With this arrangement, water either present in the ambient atmosphere at the entrance end of the furnace or formed by oxidation of residual organic matter in the beta-alumina tubes tends to be swept from the furnace before the ware enters the sintering zone.

C-4 MAKING A MORE HOMOGENEOUS CERAMIC ELECTROLYTE

At least eight sources of heterogeneities in beta-alumina ceramics have now been identified, their origins determined, and actions taken to eliminate them either totally or partially. A summary of this information is presented in Table C-4. Four of the more important -- flaws in greenware, pores, exaggerated size grains, and surface non-uniformity -- were subjects of serious attention over the contract period.

C-4.1 Flaws in Greenware

Probably most important of all were flaws in greenware arising from sticking of the ware to the forming mandrels. The force needed for removal of the

TABLE C-4

CERAMIC HETEROGENEITIES LEADING TO FIELD ENHANCEMENT

Heterogeneity	Source(s)	Actions to Remove
1. Flaws in greenware	Force needed to remove tubes from mandrels.	Avoid exposure of suspensions and deposited tubes to humid atmosphere. More thorough evaporation of vehicle.
2. Pores	Insufficient sintered density.	Change ceramic composition. Change sintering conditions.
3. Exaggerated size grains	Ceramic composition. Sintering temperature too high. Sintering arrangements.	Increase soda content. Reduce temperature. Change sintering conditions.
4. Surface non-uniformity	Surface porosity.	Change saggers, bedding, and furnace atmosphere.
5. Second phase particles	Tramp contamination from calcining kilns.	Sieve beta-alumina powder.
	Contamination from containers.	Filtration of suspensions.
	Wear from grinding media, e.g., ZrO_2	Use other media, e.g., beta- or alpha-alumina.
6. Gas strings at inner wall of tube	Electrolysis of vehicle due to high electric field at mandrel surface during tube deposition.	Reduce electric fields during electrophoretic deposition.
7. Stress gradients	Excessive traverse rate through furnace.	Reduce traverse rate.
8. Soda gradient across tube	Ceramic composition.	Change composition to reduce sintering temperature.
	Other sintering conditions.	Control furnace atmosphere. Use proper saggers and bedding.

deposit introduced cracks which often did not disappear during the subsequent sintering operation. Such flaws not only affected the distribution of current but also compromised the ceramic integrity.

In the development of the presently used electrophoretic forming process four to five years ago, little or no difficulty was encountered in removal of deposits from mandrels after the importance of thorough removal of the amyl alcohol vehicle was recognized as well as the need for keeping the concentration of aluminum stearate anti-foaming agent in the suspension less than about 0.25%[C-9]. At that time the additives yttria and magnesia (and sometimes zirconia) were incorporated in the beta-alumina powder. The sticking problem became difficult following deletion of magnesia from the formulation. It was ameliorated by shrinkage of the mandrels by chilling in an ice brine mixture prior to deposit removal and by use of a special jig developed in the previous contract year. Despite use of these techniques, the problem appeared to get worse again during the humid late spring and early summer of 1975. This observation suggested the use of dry air for evaporation of the amyl alcohol in the deposit. The use of a dehumidifier for this purpose in the laboratory hood into which the amyl alcohol was permitted to evaporate was partially successful. Tubes deposited within about an hour before beginning evaporation of the amyl alcohol were easily taken off forming mandrels. However, other tubes left exposed to the laboratory atmosphere for longer periods of time were still hard to remove. The problem was finally solved using a dry box for storage of deposits after forming but before beginning vehicle evaporation. The relative humidity in this storage chamber is usually kept less than 10% by passage of nitrogen gas through a column of "Drierite" desiccant before admission to the chamber. The combined use of this holding chamber and of the dehumidifier has almost completely solved the problems of difficult removal and cracking. It was later established that the dehumidifier serves mainly as a source of rapidly moving air warmed about 10°C above ambient. It provides for more thorough evaporation of amyl alcohol than possible with use of the hood draft alone.

Table C-5 presents some experimental data on twenty-five additive-free tubes which were formed electrophoretically. Approximately one-half were stored in the dry holding chamber after forming while the other half were allowed to

TABLE C-5

CORRELATION OF DRYING CONDITIONS WITH EASE OF REMOVAL OF DEPOSITS FROM MANDRELS AND WITH SUBSEQUENT CRACKING UPON SINTERING

Specimen No.	Drying (1) Conditions	Ease of (2) Removal	Tendency to Crack
9D1-1	CD	No effort	OK
-2	AD	Quite difficult	Cracked
-3	CD	No effort	OK
-4	AD	Very difficult	Cracked
-5	CD	No effort	OK
9D2-1	AD	Very difficult	Cracked
-2	CD	No effort	OK
-3	AD	Very difficult	Cracked
-4	CD	No effort	OK
-5	AD	Very difficult	Cracked
9D3-1	CD	No effort	OK
-2	AD	Very difficult	Slight crack at top
-3	CD	No effort	OK
-4	AD	Broke on removal	----
-5	CD	No effort	OK
9D4-1	AD	Very difficult	OK
-2	CD	No effort	OK
-3	AD	Very difficult	OK
-4	CD	No effort	OK
-5	AD	Slightly difficult	OK
9D5-1	CD	No effort	OK
-2	AD	No effort (3)	Broke after Density Meas.
-3	CD	No effort	OK
-4	AD	No effort (3)	OK
-5	CD	No effort	OK

(1) CD indicates tube kept in dry nitrogen chamber until dried by dehumidifier discharge while AD indicates tube exposed to atmosphere until dried with dehumidifier.

(2) No effort means tube readily pushed off mandrel by hand. Otherwise, degree of difficulty in pulling off with wooden block indicated.

(3) These tubes were the last deposited and were exposed to the atmosphere for only a short time.

remain in contact with laboratory air. All were later dried using the dehumidifier. Those left exposed to the laboratory atmosphere, apart from a few exposed for only a short time, were difficult to remove from the forming mandrels and usually appeared cracked following sintering. On the other hand, those kept in the dry holding chamber after forming were very easily removed from the mandrels and were not cracked after sintering.

Some conditions have been found where it becomes difficult to remove deposits from mandrels despite use of the dry holding chamber and the dehumidifier. These relate to the pick-up of water by amyl alcohol suspensions before electrophoretic forming. For example, removal difficulties were encountered after suspensions were vigorously stirred in contact with a humid atmosphere for an extended time, e.g., 1/2 to 1 hour. However, no difficulties were encountered with deposits from suspensions similarly stirred but capped against the atmosphere. Removal troubles were also met with suspensions filtered out in the laboratory atmosphere to remove small quantities of second phase particles. This problem was overcome by carrying out the filtration in a dry box.

C-4.2 Pores and Exaggerated Size Grains

Pores and exaggerated size grains are extermely important sources of ceramic heterogeneities. They are perhaps better discussed together as there is somewhat of a "trade-off" between them. As documented rather thoroughly in the previous interim report, exaggerated size grains appear at a critical density which depends on the ceramic composition as well as other factors[C-2]. Higher densities (lower porosity) can only be achieved by accepting larger and larger amounts of grains of exaggerated size. Consequently, a compromise is required between the amounts of these two heterogeneities.

As discussed in the previous subsection, a very important finding in the course of work on "liquid phase" sintering was that exaggerated grain growth tends to be suppressed in beta-alumina augmented in soda content over that as received from Alcoa. Sintering can be carried out to a higher density before the onset of formation of large grains. While the onset is very sharp, it is also very reproducible as partially documented in Figure C-6. Here low magnification

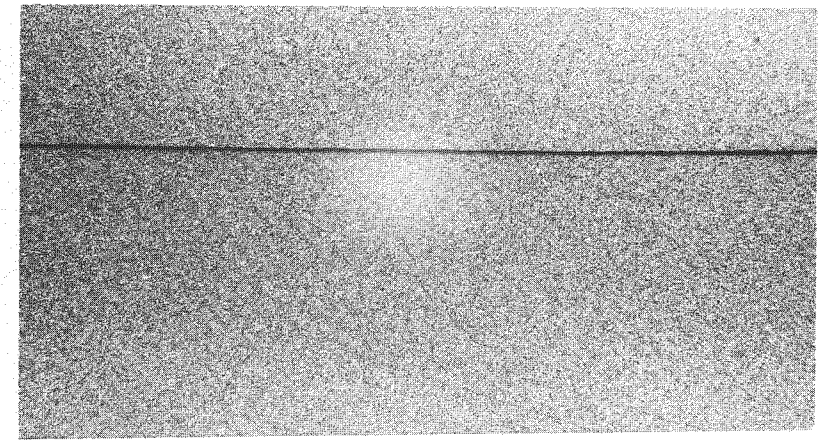

SPECIMEN AQ2-4
1700° SINTER
3.289 g/cc

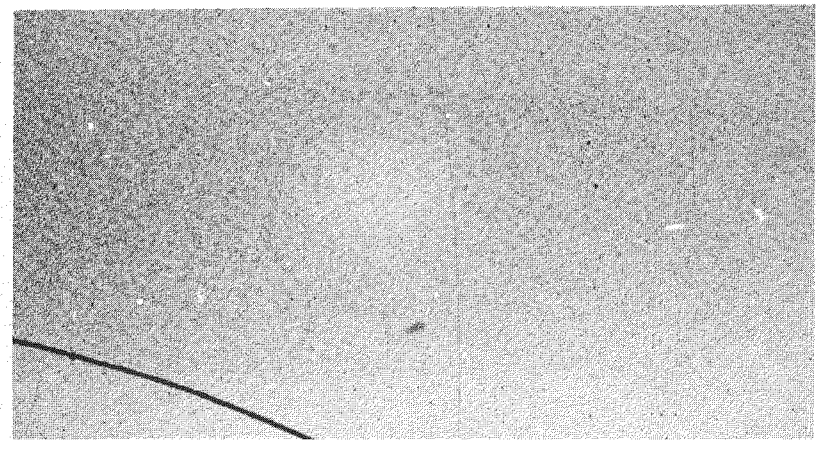

SPECIMEN AQ2-3
1712° SINTER
3.289 g/cc

1 mm

SPECIMEN AQ2-2
1725° SINTER
3.296 g/cc

Figure C-6. The Effect of Sintering Temperature on Microstructure

microstructures are presented for generation V ceramic in which the soda content was increased to 8.4% soda for maximum sintering furnace temperatures of 1700, 1712, and 1725°C. There are few, if any, large grains evident at 1700° while several can be discerned in the field at 1712°. A much larger number can be seen at 1725°C. A goal of this program is to prepare microstructures as shown for specimen AQ2-4. At this time, however, portions of ceramic are found moderately often with microstructures as shown for AQ2-3.

The heavy black lines crossing the field shown on Figure C-6 are consequences of the way the specimens were arranged on the metallographic mount to obtain a field of nearly maximum effective width. Such a line demarcates the position of the inner wall of the tube specimen. Figure C-6 also illustrates an important limitation of high magnification micrographs, such as shown on Figure C-1 for generation V ceramic, in providing accurate information on the amount of large grains present. Since even for specimen AQ2-2 sintered at 1725°C, only a small fraction of the field is covered with large grains, a representative high magnification micrograph would show no large grains.

As discussed in Subsection C-4, the first soda-enhanced compositions were prepared by electrophoretic co-deposition of two powders. One was XB-2 beta-alumina powder and the other was very high in soda. Usually the soda-alumina eutectic composition was employed for the second powder. The higher densities achieved upon sintering, over controls not containing a second powder high in soda content, was taken as evidence for liquid phase sintering. However, new information has suggested an alternative interpretation. If ware is formed using a single powder of the same overall composition as achieved by use of the two powder route, nearly the same densification kinetics are obtained. This is shown in Table C-6 where the density of ware is given following sintering at different temperatures using a furnace traverse rate of 1/2 in. per minute. Some greenware had been formed using the single powder route while others were formed with two powders. Data on generation V ceramic are given in A in the table and for generation VI in B. With the latter, lithia was incorporated in the XB-2 for the two-powder route. The new interpretation given these results is simply that the more rapid densification achieved with the two-powder route over controls not containing the second powder is a consequence of the higher overall soda content, not of the use of two powders

TABLE C-6

COMPARISON OF DENSITIES ACHIEVED AT DIFFERENT SINTERING TEMPERATURES FOR THE TWO-POWDER VS THE SINGLE POWDER ROUTE

A. Ceramic Generation V Material with 8.4% Na_2O

Sintering Temperature - °C	Two-Powder Route Density g/cc	Single Powder Route Density g/cc
1675	3.220	3.220
1700	3.243	3.239
1725	3.259	3.256
1750	3.273	3.268

B. Ceramic Generation VI Material with 9.6% Na_2O and 0.25% Li_2O

1575°C	3.104	3.122
1600	3.238	3.248
1625	3.246	3.257
1650	3.254	3.266
1675	3.271	3.277

per se. Sintering temperatures are lower for beta-alumina of higher soda concentration. Very likely at temperatures near those used for sintering, soda diffusion is so rapid that significant soda gradients cannot be sustained and rapid compositional equilibration occurs.

The somewhat higher sintered density indicated on Figure C-6 over those shown in Table C-3 is evidence of other factors affecting densification. One is the use of dry oxygen in the sintering furnace instead of ambient air. Controlled atmosphere sintering has been made possible by use of the holding chamber attached to the exit end of the furnace as discussed at the end of the previous subsection. In Table C-7, soda concentrations are shown for four tubes of the 8W series, two of which were sintered in a dry oxygen atmosphere and two others, serving as controls, sintered in the ambient atmosphere. These tubes were of generation III ceramic and contained 1% zirconia. The soda content before sintering was 7.2%. Apart from the furnace atmosphere, the fabrication of these tubes was as similar as possible. The soda loss was

TABLE C-7

EFFECT OF FURNACE ATMOSPHERE ON SODA CONTENT OF BETA-ALUMINA TUBES

SPECIMEN DESIGNATION	COMPOSITION	SINTERING TEMPERATURE	FURNACE ATMOSPHERE	% Na_2O FOUND
8W3-1	1% ZrO_2	1688°C	Ambient Air	6.68
8W3-5	1% ZrO_2	1688°C	Ambient Air	6.52
8W4-3	1% ZrO_2	1688°C	Dry Oxygen	6.77
8W5-2	1% ZrO_2	1688°C	Dry Oxygen	6.73
8X4-1	Additive-free	1750°C	Ambient Air	6.62
8X4-2	Additive-free	1750°C	Dry Oxygen	6.90
8X4-5	Additive-free	1750°C	Ambient Air	6.68
8X5-1	Additive-free	1750°C	Dry Oxygen	6.97

somewhat less in those tubes sintered in a dry oxygen atmosphere. It was likewise less in dry oxygen in experiments with additive-free generation IV ceramic tubes. In this latter series, the 8X, the original soda content before sintering was also 7.2%.

Comparative densification data for sintering in dry oxygen versus the ambient air atmosphere for both generation III and IV ceramics are given in Table C-8. Again densities are only compared between ware fabricated as similarly as possible except for the furnace atmosphere used. The significance of the density difference for the two atmospheres depends on its magnitude compared with a measure of the scatter in the data. This comparison is quantified in the statistic called t. Assuming the data to be normally distributed, from the value of t and the number of specimens employed in the experiment, the likelihood that the density difference came about by chance alone can be read from a statistical table. For the experiment carried out on May 19, 1975 with generation III ceramic, the probability is less than 0.001 that the density difference observed occurred by chance. An experiment was carried out on May 23 and May 27 with generation IV ceramic in which dry oxygen and ambient air atmospheres were alternated. The purpose was to exclude the possibility that the difference in observed average difference for the two atmospheres was due to some other sintering condition such as drift in the furnace temperature. The reproducibility in the average density for the first

TABLE C-8

EFFECT OF FURNACE ATMOSPHERE ON DENSIFICATION

SINTER DATE	SUSPENSION NO.	CERAMIC COMPOSITION	SINTERING CONDITIONS TEMPERATURE RATE, ATM.	AVERAGE DENSITY g/cc	DENSITY RANGE	STANDARD DEVIATION	NO. OF SPECIMENS
19 May 1975	8W3 8W4 8W5	1% ZrO_2	1688°C, 0.5 in/min, Ambient Air	3.180	3.143-3.206	.0104	9
	8W3 8W4 8W5	1% ZrO_2	1688°C, 0.5 in/min, Dry Oxygen	3.219	3.213-3.225	.0049	6
23 May	8U, 8X	No additive	1750°C, 0.5 in/min, Ambient Air	3.222	3.209-3.227	.0116	5
	8U, 8X	No additive	1750°C, 0.5 in/min, Dry Oxygen	3.249	3.247-3.251	.0018	5
	8U, 8X	No additive	1750°C, 0.5 in/min, Ambient Air	3.225	3.211-3.233	.0092	5
27 May	8U, 8X	No additive	1750°C, 0.5 in/min, Dry Oxygen	3.254	3.249-3.260	.0039	5
10 June	9A6 9A7 9A8	1% ZrO_2	1688°C, 0.5 in/min, Dry Oxygen	3.256	3.250-3.262	.0037	8
	9A6 9A7 9A8	1% ZrO_2	1688°C, 0.5 in/min, Dry Air	3.235	3.277-3.251	.0083	7
11 June	9A9 9A10	1% ZrO_2	1688°C, 0.5 in/min Dry Oxygen	3.249	3.242-3.254	.0045	5
	9A9 9A10	1% ZrO_2	1688°C, 0.5 in/min Wet Oxygen	3.249	3.238-3.257	.0071	5
14 May	8W1 8W2	1% ZrO_2	1650°C, 0.5 in/min, Ambient Air	3.084	3.071-3.094	.0097	5
	8W1 8W2	1% ZrO_2	1650°C, 0.5 in/min, Dry Oxygen	3.084	3.067-3.100	.0130	5
5 June	8Z4 9A1	1% ZrO_2	1650°C, 0.5 in/min, Dry Oxygen	3.107	3.091-3.136	.0170	5
	8Z4 9A1	1% ZrO_2	1650°C, 0.5 in/min, Dry Air	3.096	3.083-3.107	.0086	5

and third sets of five tubes sintered in ambient air and between the second and fourth sintered in dry oxygen definitely eliminated this possibility. The likelihood that the average density difference between the first and second sets of five tubes and between the third and fourth sets came about by chance is each less than 0.01. Since the three comparisons cited can be viewed as independent events, the overall probability, that the higher average density obtained with dry oxygen is an accident, is very remote. The experiment of June 10 shows a very significant difference in average density between firings in dry oxygen and dry air. By inference then the density difference is attributed to nitrogen rather than to small amounts of water vapor in the ambient air. This conclusion was supported by the results of the experiment of June 11 which indicated no significant density difference for firings in dry oxygen compared with those in oxygen saturated with water vapor.

It may seem strange at first that no significant density difference was found between firing in dry oxygen and ambient air for densification up to about 3.10 g/cc in contrast to about 3.20 g/cc in the experiments discussed above. This fact was first discovered on May 14 and confirmed on June 5. However, the experiments comparing densification of beta-alumina in air and in oxygen atmospheres were prompted by knowledge of the sintering behavior of alpha-alumina. As pointed out to us by Dr. J. E. Burke, the higher densification achieved in oxygen with the latter is associated with the higher solubility and diffusion coefficient of oxygen over those for nitrogen. Presumably a similar situation occurs in beta-alumina. The trapping of nitrogen in pores just would not be expected to be reflected in the density until a majority of the pores were of the closed variety, i.e., not connected to external surfaces.

The demonstration of the better sintering achievable in an oxygen atmosphere was facilitated by the good reproducibility in density values. Experience in this laboratory has indicated much better reproducibility using the stoker method than with conventional batch sintering. This is attributed to the fact that with stoker sintering, all specimens are subjected to the same thermal history provided the furnace temperature is held constant. On the other hand, with batch sintering, ware at different positions within the furnace may experience somewhat different temperatures as it is difficult to hold a furnace at the same temperature throughout.

C-4.3 Surface Heterogeneities

Surface heterogeneities were largely eliminated from beta-alumina ceramic during this contract year through changes in the saggers, bedding, and furnace atmosphere. This problem had been made manifest by a number of observations: a higher cell resistivity than expected from bulk resistivity measurements, sometimes a localized spalling of the electrolyte during cell operation leading to pit formation, surface porosity as indicated by dye adsorption, and sometimes a surface spotting.

C-5 FEATURES OF TUBE SHAPE RELATED TO FIELD ENHANCEMENT

Local current densities can also exceed average values and thereby give rise to field enhancement because of features associated with details of the tube shape. Table C-9 contains a listing of such features along with brief explanatory comments. Probably the most important involves the shape of the closed end of the tube. The other features have but minor effects on field enhancement. Their elimination does facilitate cell assembly or cell operation however.

The tubes used in cells during the first contract year had rather pointed tips as shown to the right of Figure C-7. However, during the second year and third years, tubes with hemispherical ends were mainly employed, such as shown to the left of the figure. Much less field enhancement occurs with the latter because of its larger radius of curvature. A spiral type of crack, apparently originating at the tip, was often observed with the older style tubes. However this has not been seen on tubes with hemispherical ends. At one time a rather pointed tip was thought necessary to provide longitudinal rigidity during removal of greenware from mandrels.

The first mandrels used in this Laboratory for electrophoretic forming of beta-alumina tubes had a 0.57 degree taper to facilitate removal of greenware. Actually, tubes can be taken from mandrels without any taper whatsoever if thoroughly dry. However, they must be pulled off over the entire mandrel length with greater risk of flaw introduction. In contrast, for mandrels with some taper, force needs to be applied for only a short removal distance. With tubes of 0.029 degree taper, a partial vacuum tended to be created on

TABLE C-9

FEATURES ASSOCIATED WITH TUBE SHAPE LEADING TO FIELD ENHANCEMENT

Feature	Comments
1. Pointed tip on tube	Tube mandrels initially pointed to facilitate satisfactory removal of greenware. Cell failure due to spiral cracks in beta tubes associated with pointed tips. Tubes with hemispherical closed ends now fabricated.
2. Taper	Initially 0.6 degree taper used on tubes to facilitate removal from mandrels. Removal just as easy with 0.06 degree taper now used.
3. Non-uniformity in wall thickness along length	Can arise from particle settling in electrophoretic plating bath. Suitable stirring arrangements required.
4. Ellipticity in tube cross-section	Can arise from sintering conditions.
5. Tube not straight	Can arise from excessive traverse rate of greenware through sintering furnace, from warped saggers, and from sintering conditions.

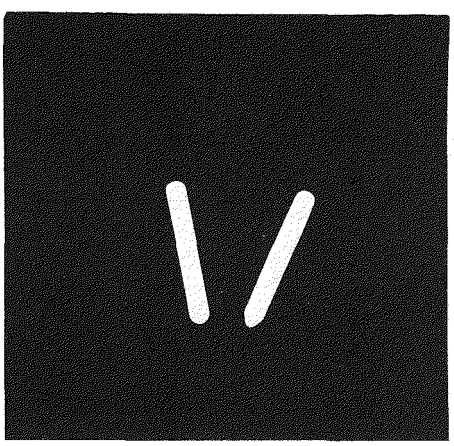

Figure C-7. Tubes with Different Types of Closed Ends

removal. Here also it seemed there was risk of introducing flaws. With the 0.06 degree taper currently used, both of the problems with lesser degrees of taper are avoided.

A non-uniformity in the wall thickness of a beta-alumina tube along its length can arise from concentration gradients in the electrophoretic deposition bath. This condition can come about from excessive settling of the particles prior to deposition. It is readily avoided by an adequate stirring arrangement.

Crooked tubes can arise from an excessive traverse rate through the sintering furnace as well as by the use of warped saggers. Another factor is the sintering arrangements. Tubes can be made straighter and with less ellipticity (out-of-roundness) by appropriate sintering conditions.

C-6 EFFECTS OF CHANGES IN CERAMIC COMPOSITION ON OPERATING LIFE, RESISTIVITY, AND FABRICATION PROBLEMS

Beta-alumina tubes of two new compositions, ceramic generations V and VI, were fabricated and incorporated into sodium-sulfur cells for testing purposes during the report year. Life testing experience with generation VI ceramic, however, was still limited at the end of the contract period. For perspective, it is interesting to list the composition, maximum operating life obtained in metal-cased cells subjected to deep discharge, and component resistivities at 300°C for these new compositions as well as for the other compositions studied in previous years. This information is given in Table C-10. Component resistivities at 300°C were readily calculated using typical measured values of the resistivity at room temperature and information from pertinent resistivity distribution plots. The first generation ceramic contained 0.5 weight percent yttria, 1.0% magnesia, 1.0% zirconia, and 7.2% soda. The sintering aids were eliminated one-by-one. For reasons given above, the soda concentration was increased in generation V and again in generation VI. A small concentration of lithia was also incorporated in generation VI ceramic.

Operating life has risen steadily with each succeeding ceramic generation. The elimination of additives and an increase in the soda concentration has also had a beneficial effect in reducing the grain boundary resistivity. It

TABLE C-10

COMPOSITION, COMPONENT RESISTIVITIES, AND MAXIMUM OPERATING LIFE OF THE CERAMIC GENERATIONS

Generation	Additives	% Na_2O	Resistivity Components at 300°C (Ω cm) r	r_c	r_b	Maximum Operating Life, AH/cm^2
I	0.5% Y_2O_3 1.0% MgO 1.0% ZrO_2	7.2	16.8	5.80	11.0	3
II	1.0% MgO 1.0% ZrO_2	7.2				70
III	1.0% ZrO_2	7.2	23.5	13.7	9.8	100
IV	---	7.2	25.5	16.8	8.7	115
V	---	8.4	21.6	17.0	4.6	373 on 5/13/76
VI	0.25% Li_2O	9.6	15.7	12.3	3.4	No data

should be noted that as a consequence operating life has increased as r_b at 300°C, an operationally definable ceramic property, has decreased. Stated otherwise, operating life can be correlated with a property of the ceramic electrolyte. If it can be assumed that the effective grain boundary thickness is not affected by composition, then r_b can be shown to be proportional to the average electric field at the grain boundaries. This average field, F_{av}, is given by the total voltage drop across the tube wall divided by the total thickness of the grain boundaries across which sodium cations must migrate. Thus

$$F_{av} = \frac{(i/A)\ r_b t}{(t/\overline{gs})\ \tau} = \frac{(i/A)\ r_b\ (\overline{gs})}{\tau}$$

Here i is the constant test current passing through A cm^2 of tube wall area; t is the wall thickness; $\overline{gs}$ is the grain size or the receiprocal of the number of grain boundary intersections per unit length across which sodium cations

must migrate, and τ is the grain boundary thickness. It has been shown for generation I ceramic that the product of $\overline{gs}$ and r_b is constant, at least to a rough first approximation. This correlation observed between operating life and r_b at 300°C, along with the relationship between r_b and average electric fields at grain boundaries, provides at least some support for the working hypothesis underlying this development, that high electric fields at grain boundaries are deleterious.

In contrast to the grain boundary resistivity, the crystal resistivity increased at 300°C as additives were deleted. An increase in the soda concentration from 7.2% to 8.4% affected the crystal component hardly at all. The introduction of a small amount of lithia has effected a substantial decrease. As a result of these complex effects, the overall ceramic resistivity was maximum in generation IV ceramic and has been reduced in generation VI to a value slightly less than obtained with generation I. In contrast to the first ceramics, however, the grain boundary resistivity in current ones is very substantially smaller than that of the crystal. Further substantial reduction of overall resistivity obviously must come out of the crystal component.

The additive yttria was deleted from the first ceramic generation without complications. After the second ceramic generation, however, special fabrication problems appeared with each succeeding ceramic generation. Fortunately it was possible to solve each problem without adding greatly to the cost or complexity of the fabrication procedure. Some of these difficulties were discussed in conjunction with ceramic heterogeneities. For example with generation III ceramic, on deletion of magnesia, there appeared the sticking of green tubes to forming mandrels. With generation IV, two fabrication difficulties were encountered. There was a need to mill with either alpha-alumina or with beta-alumina grinding media instead of with zirconia, a more efficient media. And furthermore to compensate for the absence of the zirconia sintering aid, the beta-alumina powder required a finer particle size. A localized exaggerated grain growth problem showed up with generation V ceramic. With generation VI, the presemce of lithia was found to affect adversely the particle mobility during electrophoretic deposition. To carry out satisfactory forming, changes in the powder and suspension preparation steps were required.

C-7 FABRICATION OF LARGER CERAMIC TUBES

Over the contract period, tubes of 1 cm diameter and of 15 cm length were fabricated for the multi-tube cell without special difficulties. Ceramic electrolyte tubes of 2 cm diameter by 15 cm in length were also made without encountering special problems. The latter were made, however, on mandrels of obsolete design. Some samples of larger tubes are shown in Figure C-8 along with a sample of the smaller size used in test cells during the contract period.

C-8 COST STUDIES FOR FABRICATION OF BETA-ALUMINA TUBES

A study of the cost of fabricating beta-alumina tubes in a manufacturing pilot plant which is a conceptual scale-up of laboratory procedures was carried out by staff members of the General Electric Manufacturing Engineering Consulting Services. A production rate was assumed sufficient to construct within one year a sodium-sulfur battery meeting BEST specifications. The purposes of this study were to obtain realistic cost information, to identify costly steps in the present processing scheme, and to identify problems likely to be encountered in volume production which can be overlooked in laboratory scale operations.

While the production cost of a 2.5 cm diameter by 37 cm long beta-alumina tube turned out to be about eight dollars for a production rate of 40,000 tubes per year and on amortizing capital equipment over one year, the best present estimate is that the ultimate mass production cost for this size tube will lie between one and two dollars. Surprisingly, saggers and bedding material as used in present processing were identified as major material costs. Scaling problems, both as to tube size as well as regarding production rate, will require primary attention in the immediate future.

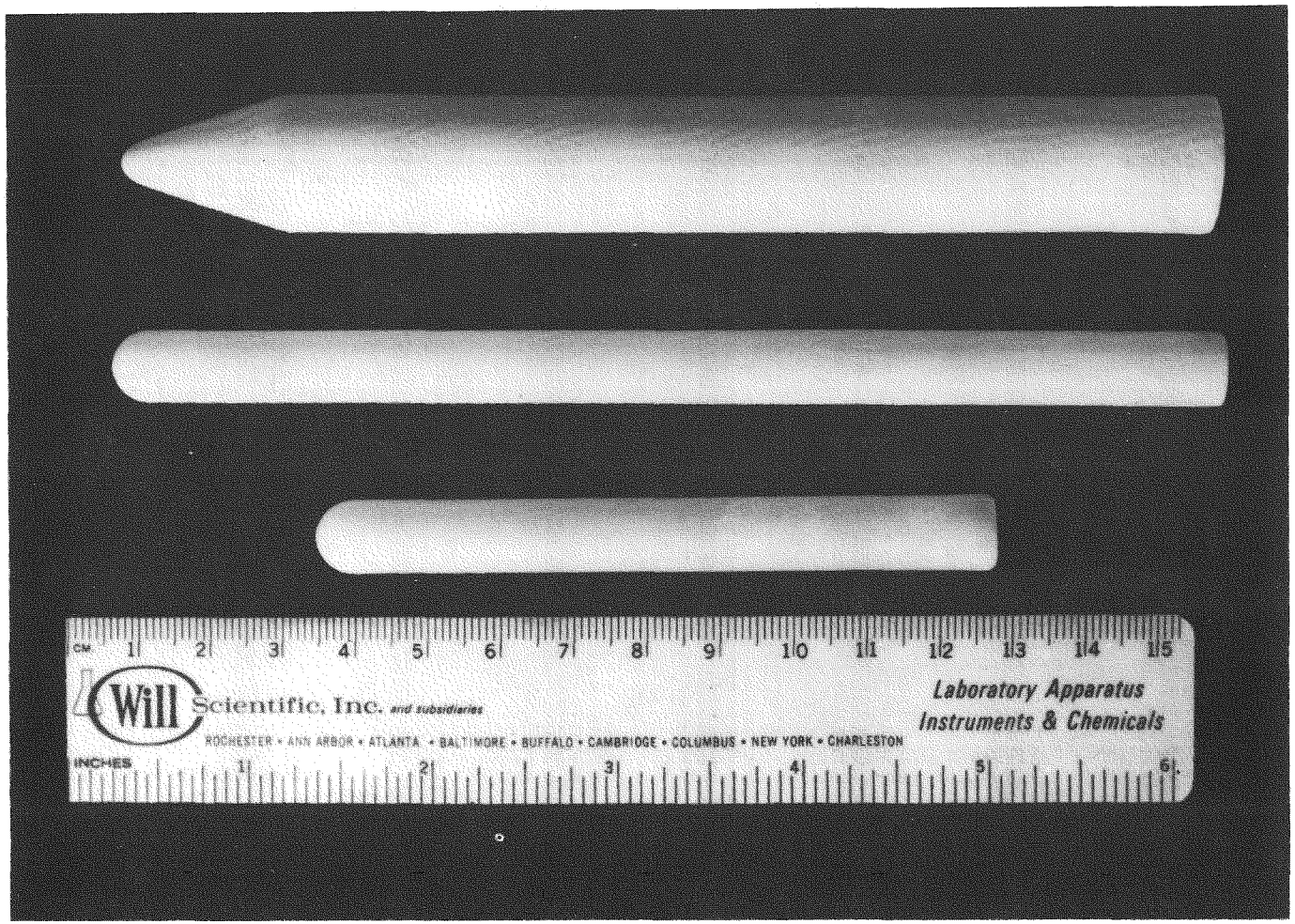

Figure C-8. Examples of Different Tube Sizes Fabricated During Contract Period

C-9 REFERENCES

C-1. "Sodium-Sulfur Battery Development," EPRI Report 128-0-0, July 1974.

C-2. "Sodium-Sulfur Battery Development," EPRI Report 128-2, Sept. 1975.

C-3. Powers, R.W. and Mitoff, S.P., J. Electrochem. Soc. Vol. 122, 266 (1975).

C-4. Powers, R.W., Proceedings of International Conference on Superionic Conductors: Chemistry, Physics, and Applications. Schenectady, N.Y. May 10-12, 1976. Published by Plenum Press.

C-5. Powers, R.W., to be submitted to J. Am. Ceramic Soc.

C-6. Yao, Y.F. and Kummer, J.T., J. Inorg. Nucl. Chem. 29, 2543 (1967).

C-7. Whittingham, M.S. and Huggins, R.A., J. Chem. Phys., 54, 414 (1971).

C-8. DeJonghe, L.C. and Chandan, J., Am. Ceramic Soc. Bull. 55, 312 (1976).

C-9. Powers, R.W., J. Electrochem. Soc. 122, 490 (1975).

Section D

SINGLE TUBE CELL PERFORMANCE

In this section all of the work related to single tube cells will be presented. In last year's report it was reported that considerable improvement was made in overall cell performance, mostly by virtue of obtaining higher cell capacity, but that ceramic life was still limiting the cells short of the load-leveling requirements. High cell resistance caused by a surface resistance on the ceramic was also identified as a problem. It was stated that improvements in ceramic processing during the coming year were expected to overcome these performance limitations. As detailed in Section C on Ceramic Development, the expected improvements in the ceramic electrolyte have been achieved, and the improved cell life and resistance resulted. In addition, further improvements in cell capacity and understanding of the construction methods to achieve high capacity have been made during the year.

The first cells made with improved ceramic electrolytes were put on test about six months ago, and since that time none of these cells has failed as a result of the ceramic electrolyte, except where it was found that the cell was discharged at constant current to the point of nearly emptying the tube of sodium, or where the cell was charged at up to 6 volts repetitively. Presently the usual failure mode is due to seals. The exterior mechanical seals often develop leaks on cells made with aluminum containers after several months of testing. The other problem which also takes three to six or more months to occur is sodium attack of the glass seal between the alpha and beta-alumina. A more sodium-resistant seal is now being developed. It

is therefore not presently known what the life limit, if any, of the present ceramic will be but it certainly far exceeds the ∿100 AH/cm^2 of last year's material, and the 300 AH/cm^2 of this year.

The high cell resistance has been identified as resulting from a porous surface layer on the beta-alumina which was eliminated by changes in the saggers, bedding, and furnace atmosphere during firing of the ceramic tubes.

Cell capacities of up to 95% (based on the lower limit of discharge shown by each cell, which is usually near Na_2S_3, as complete discharge and pure sulfur as full charge) have been obtained on single cycles and over 80% on sustained cycling at a constant current of 108 mA/cm^2. It is also significant that while peak utilization of material increased from 80% to 95% during the last year, typical values have increased from about 50% to 80%. This has been accomplished by using layers of different grades of carbon mats in the cells. The higher resistance grades are used closest to the beta-alumina and the lowest resistance near the container wall.

In some cells it has been possible to sustain the low resistance and high capacity to about 200 cycles. An example of the performance of such a cell is shown in Figure D-1. The cathode container for this cell is 347 stainless steel. The figure shows the performance up to the end of the contract period. The cell is being cycled at a constant current of 2 A. The sodium capacity to the top of the beta-alumina tube in this cell is 14.2 Ah, so it is sodium limited. The capacity per unit area of this cell for each half cycle over the first 190 cycles recorded to date was 633 mAH/cm^2.

The first four parts of this section summarize the results of studies related to construction and performance of cells as tested in the standard procedure, that is the cells are all of the same approximate geometry, and they are all cycled at constant current (54 mA/cm^2 or 108 mA/cm^2). In Section D-1 cell life, failure modes, and factors which contribute to extended life are summarized. In Section D-2 the current collector designs and their effect on cell capacity are discussed. The materials used in cell construction and their suitability are discussed in Section D-3 and the examination of cells in Section D-4.

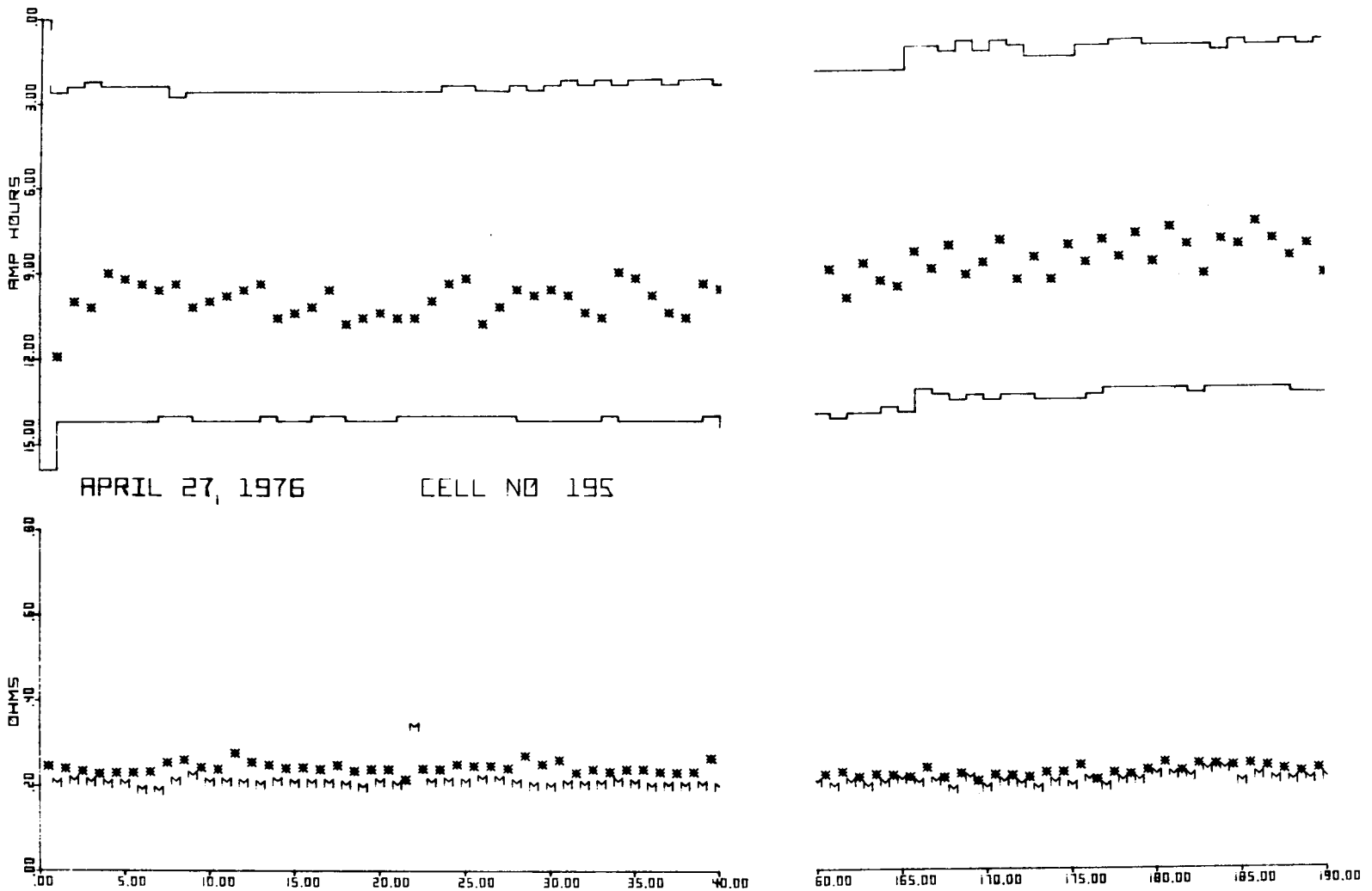

Figure D-1. Cell 195 Cycling Record, Showing Upper and Lower Limits of Capacity and Resistance from 1st to 190th Cycle

The last four sections are related to special tests performed on certain of the same type of cells. In Section D-5 the method, results, and a discussion are given on initial complex impedance measurements on the single tube cells. The complex impedance of a battery system is of importance to power conditioning design. Alternative cycling procedures which may be employed in the use of the cells in load-leveling are examined in sections D-6 and D-7. Thermal cycling (Section D-6) may be a required mode of operation because of the more efficient use of waste heat which can be made by allowing the cells to heat to a maximum temperature at the end of each working half-cycle. Higher cell capacity can be achieved, especially on poorer cells by trickle or taper charging at the end of this cycle (Section D-7). Finally a few comments are made concerning evaluation of cell safety (Section D-8).

D-1 CELL LIFE

The main testing mode for the life of the cells consists in discharging and charging cells at constant current to fixed upper and lower voltage cutoffs, followed by current reversal. An automatic cycling device which is being gradually expanded to its full capacity of 50 cells, currently permits testing of 20 cells simultaneously. Another ten cells were cycled by means of mechanical cycling devices in the same or in different cycling modes. The data obtained with the automatic device are stored on magnetic tape. The tapes are periodically transmitted to the Corporate Research and Development computer. Plots of cell resistance versus time, ampere hour limits of each discharge and charge cycle, and the ampere hour position of the single-phase/two-phase boundary at each discharge cycle are produced by the computer (e.g. Figure D-1).

Ten cells are operated at 1 A and ten cells at 2 A by the automatic device. Cycling at 2 A (108 mA/cm^2) was made feasible by the decrease of the cell resistance to below 0.2Ω during the past year. As a result, life testing could be accelerated by a factor of two. Another change was necessitated by the smaller cell resistance. The cut-off voltages were changed from 1.2 V to 1.3 V for discharge and from 3.0 V to 2.8 V for charge. Since a rapid increase of cell voltage from relatively flat portions during most of the time of charge or discharge occurs towards the end of discharge and charge

response, the new cut-off voltages result in the beneficial effect of smaller voltage drops across the solid electrolyte.

A summary of the considerable improvement in cell life achieved during the contract year is presented in Table D-1. For comparison similar data are also shown for the preceding two contract periods in Table D-1. The total number of cells, evaluated between April 29, 1975 and March 17, 1976 was 112, in contrast to a total of 104 during the first two periods. The cut-off date of March 17, 1976 was chosen to allow enough time to accumulate a life of at least 50 AH/cm^2 by May 12, 1976. The actual number of cells put on test during the past contract year was 125. The improvement in cell life at 50 mA/cm^2 becomes evident from the comparison of the respective figures for the combined two periods and for the last contract year under "Number of Cells with More than 200 AH/cm^2" and "Best Life". Two cells with more than 200 AH/cm^2 were still cycling on May 12, 1976, and the best life corresponded to 288 AH/cm^2. A comparison for 100 mA/cm^2 is not available. However, five cells with more than 200 AH/cm^2 were still in operation on May 12, 1976, and the best life was 377 AH/cm^2. The number of hours of operation for the cells with longest life, obtained by dividing the number of AH/cm^2 by A/cm^2 are: 5750 hours at 0.05 A/cm^2 and 3770 hours at 0.1 A/cm^2.

A summary of the failure modes is provided in Table D-2. On one occasion a sudden power loss led to cooling of the furnaces in which the cells were cycled. Twenty cells were lost. They happened to be largely discharged. The contraction of the polysulfide during solidification cracked the beta-alumina tube. In contrast, the cells which were largely charged, survived the cooling. Several additional circuits which monitor the temperature of the furnaces and give a warning in case of cooling were installed in the meantime to greatly reduce this failure mode in the future. Cells which developed a high resistance with time because of an inadequate performance of the sulfur electrode were removed since their cycles became too short to be practical. Failure due to handling is minor. Short circuiting of cells was the result of three different causes: cracking of alpha-alumina disc, cracking of beta-alumina tubes and seal failure. The improvement in the quality of the beta-alumina tubes is clearly reflected by the data in Table D-2. Cell failure due to the solid electrolyte alone has been reduced to

TABLE D-1

CELL LIFE

PERIOD	NUMBER OF CELLS	CURRENT DENSITY IN mA/cm^2	NUMBER OF CELLS WITH MORE THAN 50 AH/cm^2	NUMBER OF CELLS WITH MORE THAN 100 AH/cm^2	NUMBER OF CELLS WITH MORE THAN 200 AH/cm^2	BEST LIFE AH/cm^2	BEST LIFE NUMBER Of Cycles
8/9/73 to 3/15/75	104	50	21	3	0	120	100
4/29/75 to 3/17/76	112	50	21	4	2	288	260
					2 Still Cycling	Still Cycling	
		100	16	10	5	377	647
					4 Still Cycling	Still Cycling	

5/12/76

5/12/75

about 1/3 of the total number of failures and only two or three of the electrolyte failures occurred in cells put on test during the last four months. When the beta-alumina tube cracks directly below the glass seal to the alpha-alumina ring it is difficult to decide if compression by the seal or the beta-alumina are responsible for the failure. Compression by the seal may lead to mechanical failure. On the other hand, composition changes may occur with time in the region of the beta-alumina tube below the seal and introduce cracking.

At present, three factors which contributed to the extended cell life can be identified:

- Improved uniformity of current distribution at the surface of the beta-alumina tube
- Lower ceramic surface resistivity
- Improved uniformity of contact at the graphite/ceramic interface

Satisfactory current distribution as well as low surface resistivity were achieved by improved processing techniques of the beta-alumina tubes. Essentially, the formation of a porous layer, which was responsible for an inhomogeneous current distribution because of regions with different resistivity, was overcome. The absence of a porous film was verified by determinations of the resistivity of the beta-alumina tubes in the direction of the current flow. Such determinations were routinely carried out during the electrolytic charging of half cells with sodium in molten sodium nitrate. Although these measurements do not yield an absolute value of the resistivity, they supply relative values for a comparison of different ceramics. The resistance of half cells obtained under equivalent experimental conditions did not vary by more than 10% within a good batch of beta-alumina tubes and was lower than 0.2Ω.

Improved uniformity of the contact at the carbon fiber/ceramic interface and of the current distribution inside the sulfur electrode was achieved by several changes in the production procedures of the carbon fiber/sulfur plug. These changes are discussed under "Evaluation of Current Collector Designs".

TABLE D-2

STATISTICS OF CYCLED CELLS

Number of Cells Tested from May 1975 to end of April 1976.	125
Number of Cells Failed by end of April 1976.	98
Failed due to:	
Equipment Breakdown	20
High Resistance	19
Handling	2
Cracked Alpha-Alumina	4
Cracked Beta-Alumina	31
Seal Failure	14

D-1.1 Statistical Analyses of Prototype Cell Data

Statistical analyses of the performance of all test cells was initiated during the last half of the contract year. The purpose of these analyses was to determine the factors that improve cell performance.

A list of four operating variables (current, voltage cut-offs, etc.), twenty-two design variables (construction details, amounts of reactants, types of materials and seals, etc.) and seven performance variables (life, capacity, etc.) was prepared for each cell. The variables are used for fitting models to the data for the purpose of estimating life distributions and predicting life of designs not tested.

A variety of analyses were carried out on the data by means of the STATPAC program for data analysis. The analyses included:

- Graphical displays of the data, including histograms of each variable and crossplots of all pairs of variables.

- Stepwise regression analyses to estimate the relationship between each performance variable and the significant design and operating variables.
- Residual analyses to assess the effect of qualitative variables not included in the regression analyses. The residuals were cross-plotted against all other variables to search for correlations, and the residuals were subjected to a one-way analysis of variance for each variable not in the regression analysis.

So far forty-two cells have been analyzed in the computer programs; however, many of these cells had just started performance testing. Also, a large fraction of the cells were made to test some experimental current collector designs which were unsuccessful, and many of the cells were one of a kind. Thus the sample is too small for accurate statistical analysis. Most of the results were anticipated, e.g. high cell resistance with experimental current collectors. Some of the results were not anticipated: (a) the cell resistance correlated with small changes in the amount of sulfur used in filling the cell (lower resistance with more sulfur), and (b) there was no correlation found between the cell resistance and the cell capacity. The latter is surprising in that the cells are cycled at constant current to fixed voltage cut-offs (between 1.2 and 3.0 volts for 41 of the 42 cells analyzed). The value of the statistical analysis will increase as the obvious cell problems, such as the alpha to beta seal, are improved.

D-2 EVALUATION OF CURRENT COLLECTOR DESIGNS

Three basic designs (See Figure D-2) were evaluated:

- Wrapped electrode configuration
- Bonded electrode configuration
- Brush electrode configuration

The bonded electrode configuration proved difficult to make, and it is unlikely that the cost goal can be met with this design. When brush electrode configurations were tested it was found that the cell resistance was large (between 0.5 and 1Ω). The large cell resistance is due to the relatively small surface area per volume of the brush electrode configuration when compared with the wrapped electrode configuration. It is difficult to produce

brush mandrels which contain enough carbon fibers for a comparable surface area. The effort was successfully concentrated on the improvement of the wrapped electrode configuration during the contract year.

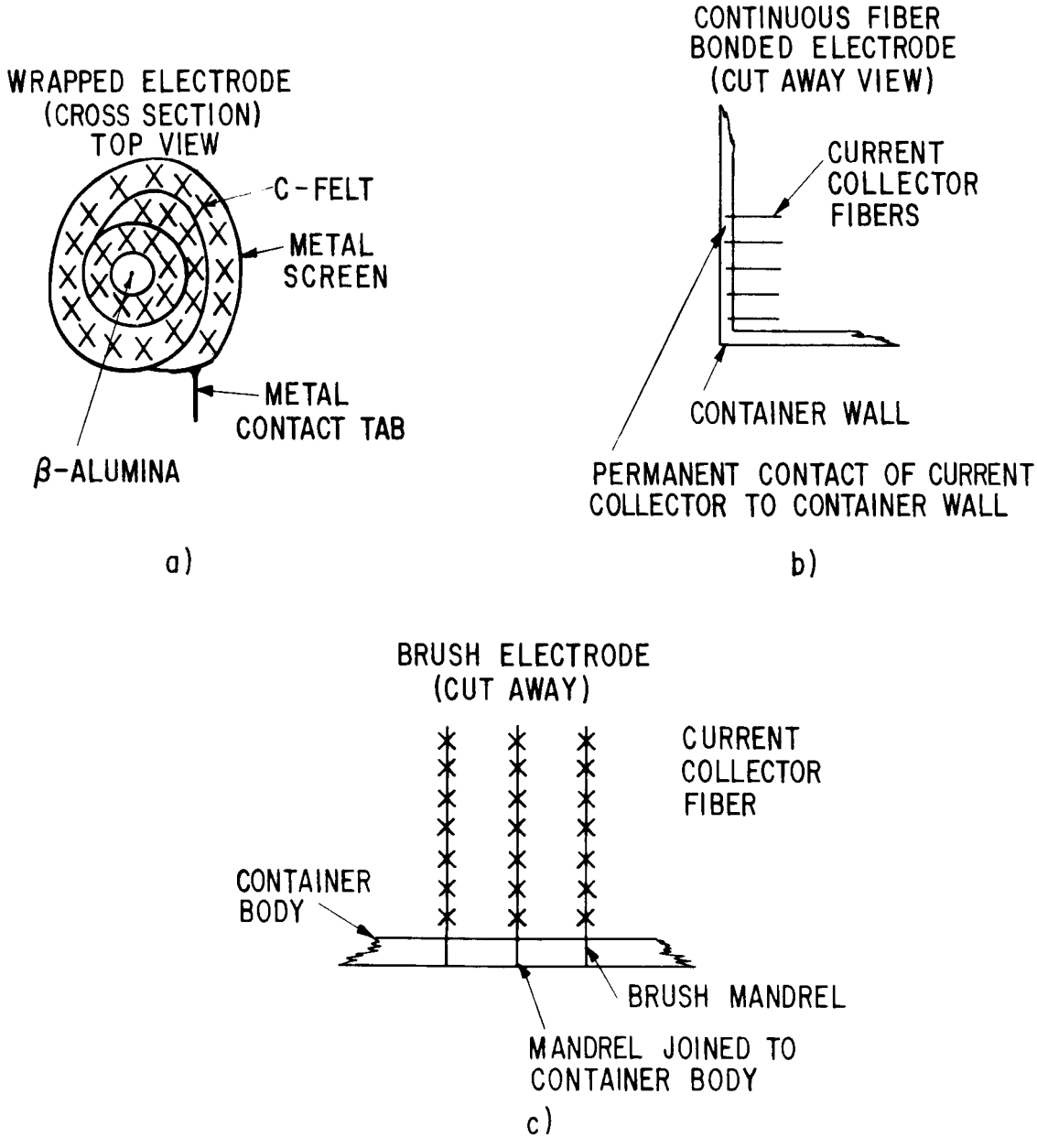

Figure D-2. Basic Electrode Designs

As mentioned, a significant cost improvement was achieved by the replacement of WDF-grade carbon felt by Thornel Mat Grade VM0032 in the carbon fiber/sulfur plug of the wrapped electrode configuration. A better fit of the beta-alumina tube in the center hole of the plug was obtained by casting a solid plug and drilling the hole. The direct casting of plug with hole in a Teflon polymer mold did not yield holes which are well-centered.

Cycling of cells with carbon fiber/sulfur plugs of the above type in stainless cathode containers revealed that the cell capacity decreased with the number of cycles and became too small for an economical operation. Frequently the cell resistance increased also.

The situation is similar to that with WDF-grade carbon felt. Numerical values for the declining performance are presented as an example for Cells No. 138 and Cell No. 162 in Table D-3. This table contains values of the cell resistance in ohms and the cell discharge capacity in AH during the 10th, 100th and 200th cycles for different cells operated at either 50 or 100 mA/cm^2. The cells were manufactured in the sequence of increasing cell number.

The column which gives the cell resistance during the 10th cycle reflects the improvement in cell resistance achieved during the contract year with the wrapped electrode configuration. The most recent cells operate with a cell resistance between 0.15 and 0.2Ω. It should be mentioned that some short-lived cells with chromium coated aluminum as cathode material had resistances between 0.15 and 0.2Ω. The most significant data in Table D-3 relate to the long-lived cell No. 195. This cell fulfills the requirements[D-1] with respect to cell resistance and cell capacity for sodium-sulfur batteries in the BEST Facility. It operated with a constant efficiency of about 80% and constant cell resistance.

The design of the wrapped electrode configuration which led to the good performance of cells with stainless steel cathode containers is illustrated in Figure D-3. Additional small holes (four or six) were drilled into the carbon fiber/sulfur plug. The arrangement of the small holes around the center hole was symmetrical. The space between plug and beta-alumina tube was

TABLE D-3

CELL CAPACITY AND RESISTANCE

Cell No.	Sulfur Can	Current Density in mA/cm^2	Cell Resistance in Ohms			Cell Discharge Capacity in AH		
			10th	100th	200th	10th	100th	200th
138	Stainless Steel	50	0.43	0.44	0.42	12	11.7	8.7
162	Stainless Steel	50	0.44	0.55	0.57	13.7	9.9	5.5
195	Stainless Steel	100	0.21	0.20	0.21	11.6	12.4	12.2
231	Stainless Steel	100	0.17	-	-	11.4	-	-

Figure D-3. Cathode Construction

stuffed with another grade of Thornel MAT. Taken in equal volumes, the latter material possessed a larger electronic resistance than Thornel MAT grade VM-0032, used in the plug.

The improvement in cell resistance and cell capacity is attributed to a gradient of the electronic resistance inside the sulfur electrode. The resistance increases towards the beta-alumina surface and prevents the preferential formation of sulfur layers close to the beta-alumina tube during

charging. Both the holes in the plug and the stuffing in the space between plug and beta-alumina produce the resistance gradient. The latter statement need not be verified with respect to the stuffing since the resistance of a matrix of this material is larger than that of the equivalent matrix of MAT VM-0032. Experimental verification of the role of the small holes in the plug was obtained by filling them with solid glass rods in some cells. The performance of cells, constructed with the same materials and beta-alumina tubes of equivalent properties, was independent of the presence of glass rods in the small holes. This result represents experimental proof that convection of polysulfide or sulfur inside the small holes is not responsible for the better performance of the cells. The latter conclusion is confirmed by the visual observation that sulfur or polysulfide was not discovered inside the small holes of failed cells which had been opened.

D-3 EVALUATION OF CELL COMPONENTS AND REACTANTS

The general problem of cell component evaluation is separated into the following five subdivisions:

- Anode container materials
- Header and seal materials
- Cathode container materials
- Current collector materials
- Reactants

Tests of sodium containers, spun from aluminum, revealed no evidence for corrosive attack by liquid sodium at the operating temperature of 300°C after prolonged cycling of the test cells. Aluminum is a satisfactory anode container material. In contrast, strong attack with gradual development of leaks was caused by sodium in the region where the filling tube of soft steel containers had been pinched off. Further work with soft steel as anode container material was abandoned.

Pure alpha alumina (Lucalox® type) rings had been used as headers in the first test cells. Radial cracking of the beta-alumina tube directly below the glass seal occurred frequently. Therefore an attempt was made to reduce the compression exerted by the alpha-alumina ring onto the beta-alumina tube

in the sealing area by a better match of the expansion coefficients of these two ceramics. Silica containing alpha-alumina rings were found during the preceding contract your to possess the same expansion coefficient as beta-alumina. While the said solution reduced the number of radial cracks below the seal, it introduced a new problem for cells with longer life. Sodium reacted with the silica and slowly penetrated the rings. Eventually the rings cracked. This type of failure was not observed in short-lived cells. The choice of 99.5% pure alpha-alumina rings during the past contract year led to satisfactory glass seals between ring and beta-alumina tube. The number of cell failures due to cracking of the ring was greatly reduced (Table D-2).

Another problem observed only in the cells with long life of the past contract year is the gradual deterioration of the sealing glass exposed to sodium. The glass seal loses strength, probably as a result of the penetration by sodium, and eventually fails. Clear evidence for failure of the glass seal became available during the last quarter of the contract year. Attempts are under way to find sealing glasses with a better resistance to sodium. One type of such a glass was prepared, but the mismatch of expansion coefficient between glass and beta-alumina led to the development of visible cracks in a glass seal that otherwise proved helium-leak tight. The glass composition is being varied now to obtain a better match. Other approaches are being explored.

While the mechanical seal between header and cans proved satisfactory for aluminum as an anode can material and 347 stainless steel as a cathode can material, it developed leaks with some, but not with all of the aluminum cathode cans. (The latter cans often have a protective layer on their inner wall). The cause for this type of failure has not been elucidated. More work is required.

Two materials have been mainly used for the cathode container in the past contract year: 347 stainless steel and aluminum, coated with a protective layer. Corrosive attack by polysulfides of the stainless steel containers of cells with long life was negligible in some cases and small in other cases. Cells with aluminum cathode containers have not achieved a sufficiently long

life to assess the corrosion resistance. Work on other container materials like silicon carbide or composites was carried out with reduced effort because it is unlikely that the cost goal can be met. The first use of cathode cans made of these materials in test cells did not reveal corrosive attack after cycling.

A significant cost improvement by about a factor of 10 was made during this contract year by the replacement of WDF-grade carbon felt by Thornel MAT Grade VM-0032 in the carbon fiber/sulfur plug. The replacement did not result in a reduction of performance of the test cells. Visual examination of the carbon material after removal from cycled cells has not revealed a noticeable degradation so far. In contrast, the incorporation of carbon foams into the sulfur electrode proved detrimental to the cell performance. A rough estimate indicates that the real surface area is much smaller than that of carbon felts or Thornel MAT of equal volume. The difference in surface area is considered responsible for the performance decline with carbon foam.

Electrolytic filling of the cells with sodium from molten sodium nitrate guarantees that the sodium is very pure. The potassium content is low. Since potassium may be incorporated into the sodium beta-alumina during cycling and thereby reduce the stability of the ceramic, electrolytic filling is advantageous for small test cells. A noticeable improvement in cell performance (capacity and resistance) was achieved by purifying the inexpensive 99.5 percent pure grade sulfur by the Bacon-Fanelli technique. Hydrocarbons, the major impurities, are removed by this technique. It is likely that cell life is also extended.

D-4 EXAMINATION OF CELLS

A number of techniques were applied to obtain the following types of information:

- Diagnosis of the causes of failure or unsatisfactory operation
- Presence of blocking or insulating films
- Deterioration of ceramics, current collector, or container materials
- Distribution of sulfur and polysulfide in the carbon fiber matrix

D-4.1 X-Radiography

The application of x-radiography for diagnosing causes of malfunction and assessing reasons for poor performance in cycling sodium-sulfur test cells was reported in EPRI 128-2 Report, September, 1975. Typical problem areas found at that time were:

(1) non-symmetrical centering of the beta-alumina separator in the cathode compartment,
(2) physical displacement of the carbon current collector when cells are filled,
(3) occasional poor wetting or lack of contact of sulfur and sodium polysulfide with the beta-alumina interface,
(4) voids which inhibited flow of active material through the carbon felt-sulfur extended electrode,
(5) corrosion of the cathode container.

Wicking in the carbon felt was shown to be a significant factor for mass transport of reactants in the cathode reservoir. Poor performance frequently was due to the non-uniform distribution of sulfur in the carbon current collector. An important source of capacity loss was shown to be loss of reactants by corrosion of the cathode reservoir.

These causes of cell malfunction and poor performance have been virtually eliminated by improved cell assembly and filling methods. The application of the x-radiography technique has taken two new directions: a) improvement of resolution of fine detail and small contrast differences to extend its range of application for post-mortem analysis of failed or discontinued cells, b) development of high temperature real-time radiography to observe the distribution and flow of active material in the interior of test cells as they are discharged and recharged.

The previous radiographic studies were made on an occasional use basis with an x-ray unit which was used primarily for a medical x-ray project. Equipment dedicated to this project has been obtained and modified to extend its range of capability for studying sodium-sulfur test cells. The basic apparatus is a "Faxitron" X-Ray Unit that is manufactured by Hewlett-Packard.

With this unit it is possible to make radiographs of specimens with x-ray voltages from 10 kV to 130 kV. The x-ray energy, target to specimen distance, and spectral filtration can be controlled to optimize exposure for specimens with different x-ray absorption coefficients, density and thickness.

D-4.1.1 Modification of X-Ray Unit for Horizontal Operation. An intended advanced application of x-radiography is observation of sodium-sulfur test cells at high temperature. This will make it possible to examine the contents when they are liquid without subjecting the cell to the distortions and strains that occur when sodium, sulfur, and sodium polysulfides solidify, and to observe changes in the components and active materials as cells are charged and discharged. These experiments required modification of the x-rays, and provision for cooling the system so x-ray film can be placed close to the test cell.

The x-ray unit comprises two functional components: a unit for generating and controlling an x-ray beam, and a dual-cabinet for radiographing specimens. The dual-cabinet facilitates radiography of specimens at either ambient or high temperature. The cabinets are lined with lead and have several radiation-tight access ports for manipulation of apparatus and introduction of control and sensing equipment to the raidation enclosure.

The generator and cabinets are housed in a single unit which is designed to operate with vertical orientation of the x-ray beam. Real-time radiography of sodium-sulfur cells in which reactants and products are liquid requires operation with a horizontal x-ray beam. The transformers, rectifiers, and x-ray tube are immersed in oil and operate at high voltage. An auxiliary oil reservoir has been added for the unit to function horizontally. The additional oil is required to keep the x-ray generator components immersed and allow for thermal expansion. Figure D-4 is a photograph of the modified unit with a test cell in position for radiography at ambient temperature.

Modification for horizontal operation has occasioned difficulties. After the initial conversion, a series of radiographs were taken but work was discontinued when a high voltage breakdown developed in the x-ray generator. A short was found in one of the high voltage transformers, which was

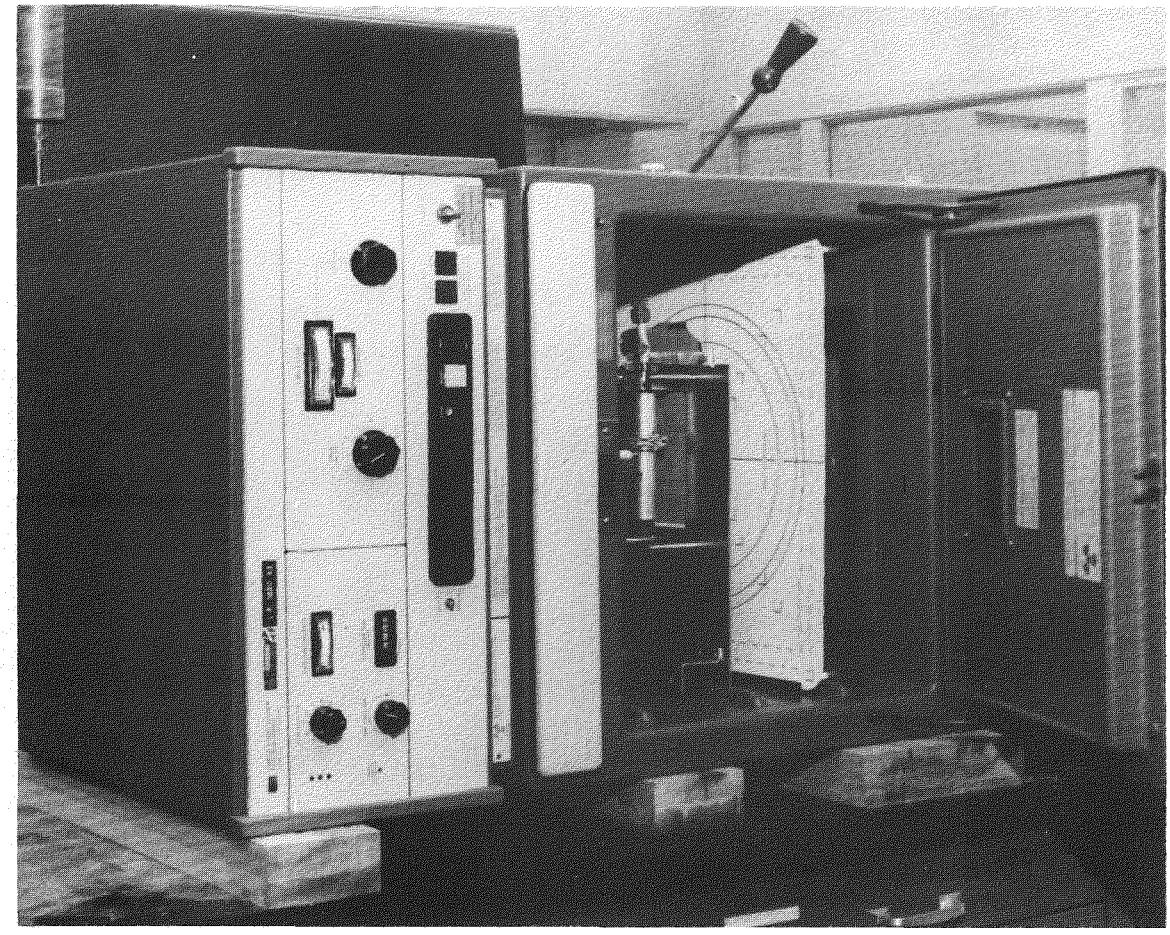

Figure D-4. X-ray unit rotated to horizontal position. The auxiliary oil reservoir is at upper left above the x-ray generator. A test cell is shown in place in the upper cabinet. It is backed by x-ray film and a sensor for determining the exposure

replaced. The manufacturer does not believe the short was caused by operation in the horizontal mode. The unit was repaired, turned to horizontal position, and immediately developed an oil leak. The equipment weighs in excess of 900 pounds and undue stress probably was applied where the x-ray generator is attached to the cabinet. At the time of this writing, the extent of the damage is not known.

Apparatus has been built for cycling and radiographing test sodium-sulfur cells at operating temperature. Figure D-5 is an overview of the equipment in place in the x-ray cabinet. Figure D-6 is a close up view of the cell

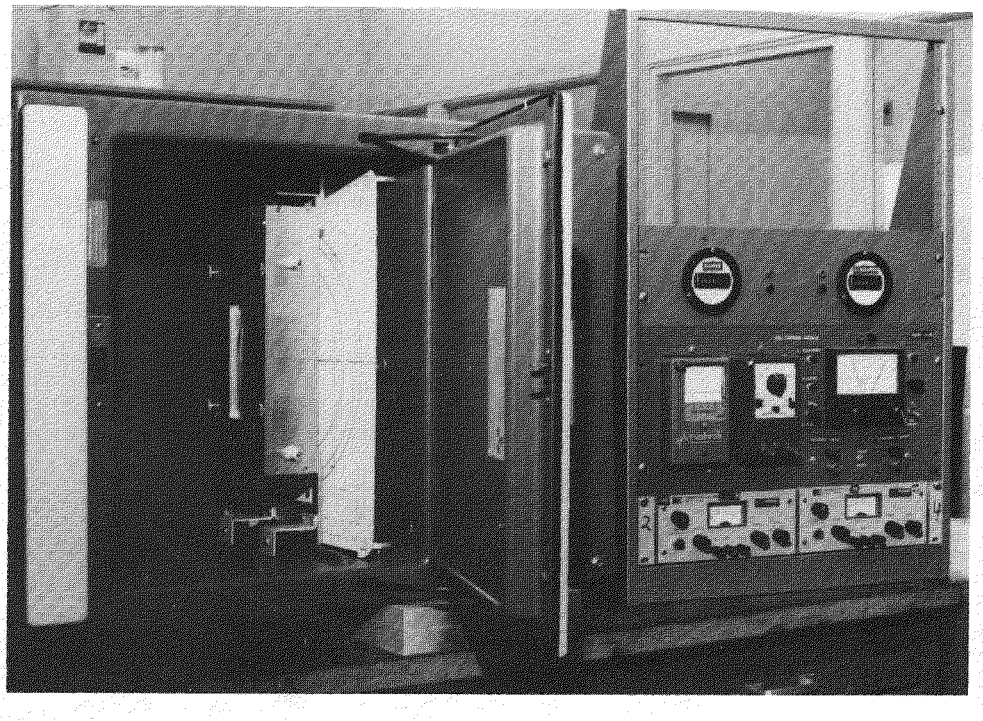

Figure D-5. Furnace for radiographing sodium-sulfur cells installed in lower cabinet of x-ray unit. The entrance aluminum window, connections for circulating cooling water, and bushings for electrical contact to heaters are visible. The apparatus for cycling test cells is at right.

furnace. The cell is clamped in an enclosure which contains two quartz heaters and reflectors which focus heat on the cell. The enclosure has thin aluminum windows on both sides to transmit the x-ray beam over a 1 1/2" by 5 1/2" area. The radiograph can be made with either Polaroid or regular x-ray film. The furnace is insulated on the inside, and water is circulated through the outer jacket to remove heat in excess of that required to maintain the cell at 350°C. Provision has been made for rotating cells to radiograph the contents from different directions. A rack of equipment for cycling and monitoring the performance of the cell is next to the x-ray cabinet. It is identical with that used for evaluating test cells. Portions of this apparatus have been used to make radiographs at room temperature, but the system has not been operated at high temperature.

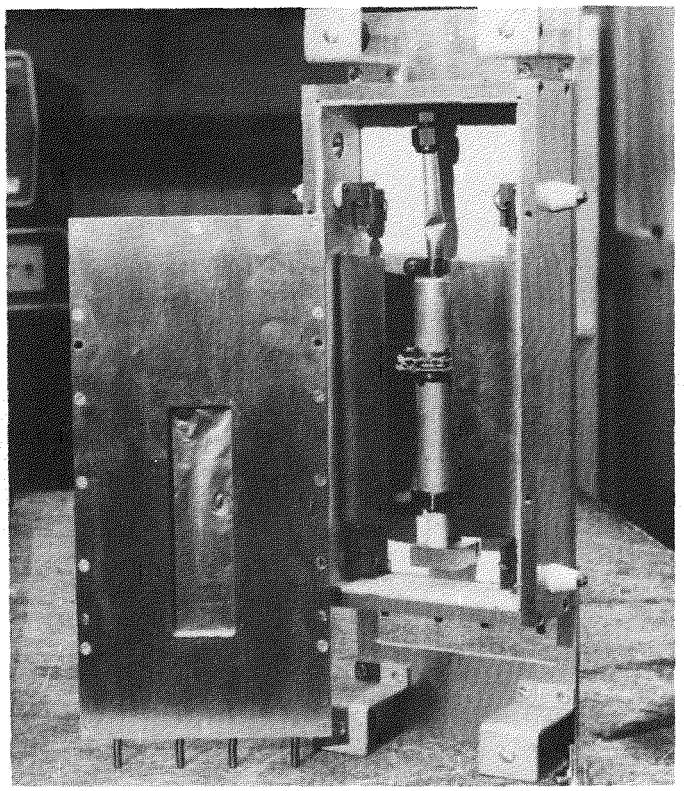

Figure D-6. Close up view of furnace with cover removed and a test cell in place for radiography. The heaters are behind reflectors which focus radiation on the cell. Connections in the cover are for circulation of cooling water.

D-4.1.2 Examination of Cycled Cells. Radiographs made with this equipment of recent versions of sodium-sulfur cells are shown in Figures D-7 through D-13. Most important cell components and active materials can be seen. Particularly to be noted is the precision with which cell components are assembled and the homogeneity of the sulfur and sodium polysulfide in the carbon felt current collector. The current collector for the initial electrolytic charging with sodium is nickel sponge near the bottom of the beta-alumina tube. It is attached by nickel wire to a nickel tab that is spot welded to the anode compartment. The anode and cathode reservoirs are aluminum. The O-rings which seal the cathode and anode compartments are Inconel and can be seen between steel clamps that hold the cell together. The individual components of the glass seal which joins the beta-alumina separator to alpha-alumina can be distinguished between the O-rings.

Several features of interest are seen in these radiographs. Cells No. 165 and No. 166 are examples for the use of uncoated aluminum cathode cans. Electrical contact between the carbon fibers and the can is made by clamping carbon fibers between two coated aluminum foils. The aluminum foils are spot welded to the cell wall. These cells frequently have high resistance, either initially or after relatively short cycling. It is possible that the high resistance is caused by corrosion at the spot welds. Comparison of Figure D-7 and Figure D-8 demonstrates welds between the aluminum foil and aluminum can be examined by rotating the cell to place the x-ray beam parallel to the interface. It may be possible to observe corrosion in the welds after cells have undergone extensive cycling.

Another potential problem area is the beta-alumina/glass/alpha-alumina seal. Degradation may be due to thermal strain or changes in composition due to diffusion across the interfaces. Considerable detail can be seen in these joints when the steel clamps are removed and the seal is examined at an angle to the cell axis (Figure D-9). The 1013 glass that joins beta-alumina to alpha-alumina contains barium and is easily distinguished from the other components in the seal.

The distribution of active material in the carbon felt-sulfur electrode is relatively homogeneous in the test cells. Small void volumes are found in some cells whose shape and size can be estimated from radiographs taken at several angles (Figures D-10 and D-11). The large void at the bottom of each beta-alumina tube is introduced purposely to reduce current gradients near the tips of the separator.

Figures D-12 and D-13 are examples of aluminum cells protected with a thin coating. The thickness of the coating tapers from the top to the bottom of the can.

Cells No. 192 and 193 were slightly over-filled with sulfur and the pressure of the reaction products upon discharge deformed the bottom of the cell. There is a thin layer of x-ray opaque material on the surface of the sulfur-sodium polysulfide melt whose extent can be estimated from radiographs taken at 90° angles.

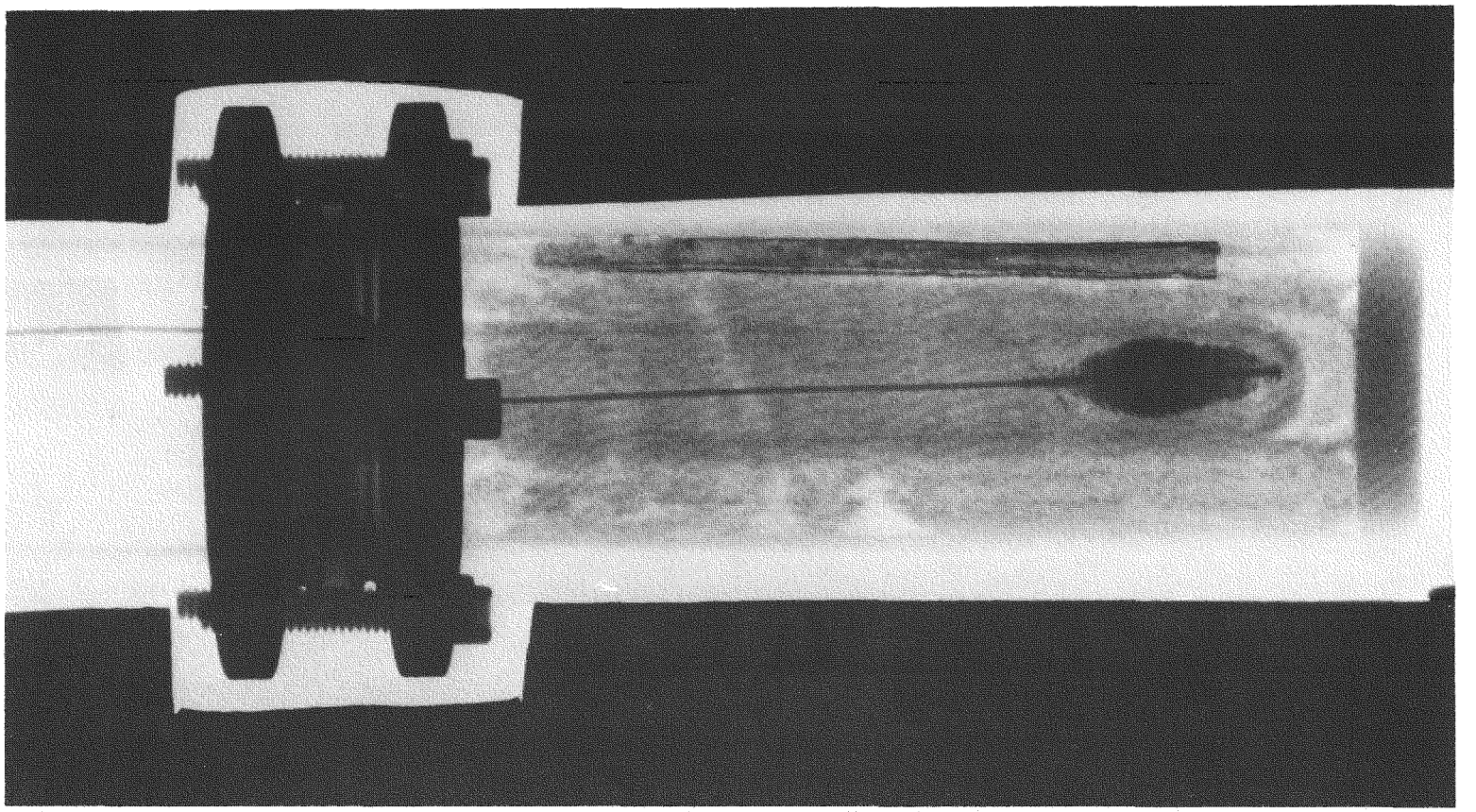

Figure D-7. Cell No. 165 after 39 cycles. The square tab in the sodium reservoir is nickel; the dense strip in the sulfur reservoir is coated aluminum foil, spot welded to the aluminum can. The resistance of this cell was high, probably because of high resistance at the interface.

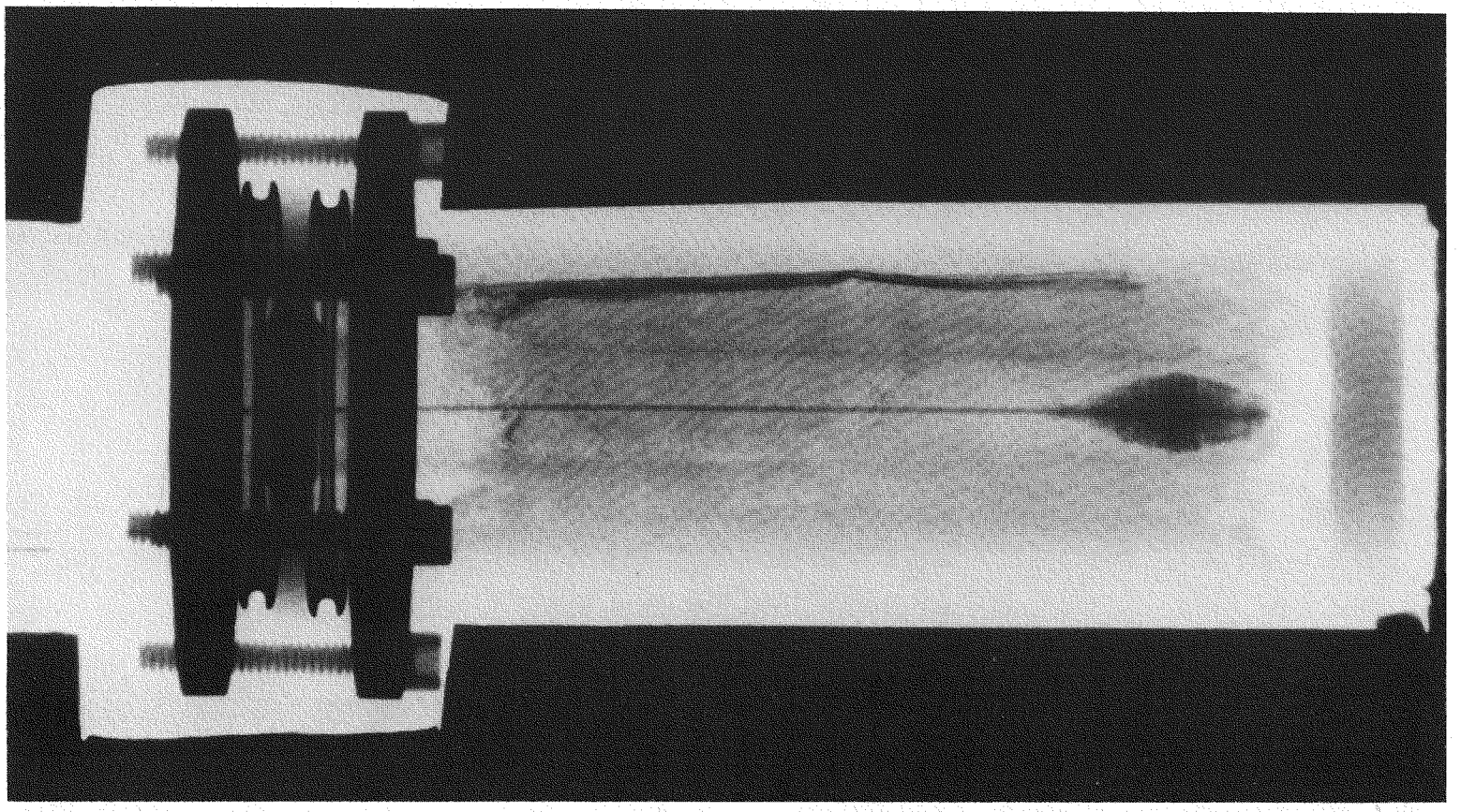

Figure D-8. Cell No. 166 after 72 cycles. This cell is similar to 165, but had slightly lower resistance. The coated aluminum tab is welded to aluminum near the top of the sulfur reservoir.

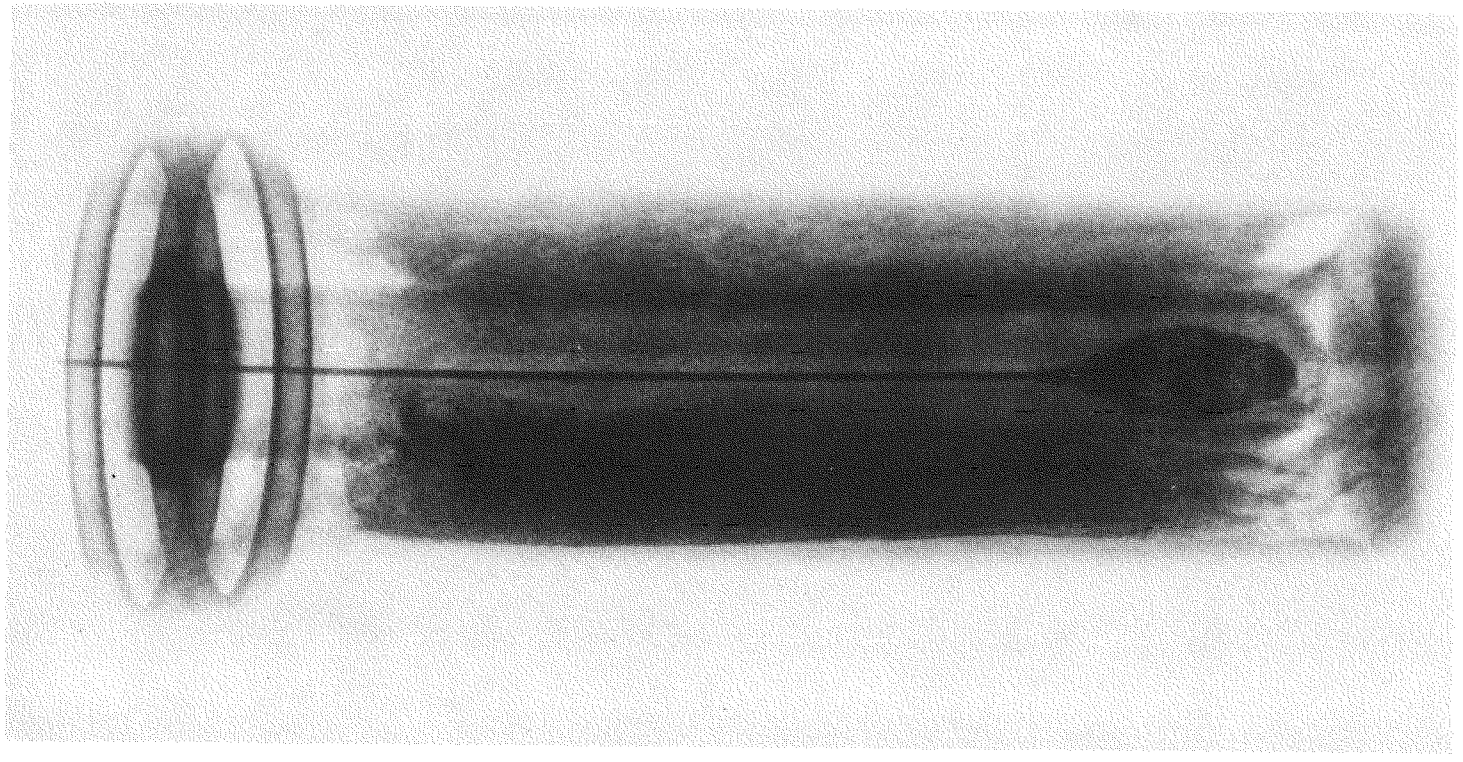

Figure D-9. Cell No. 166 viewed at an angle to the cell axis after removing the clamps which attach the sodium and sulfur compartments.

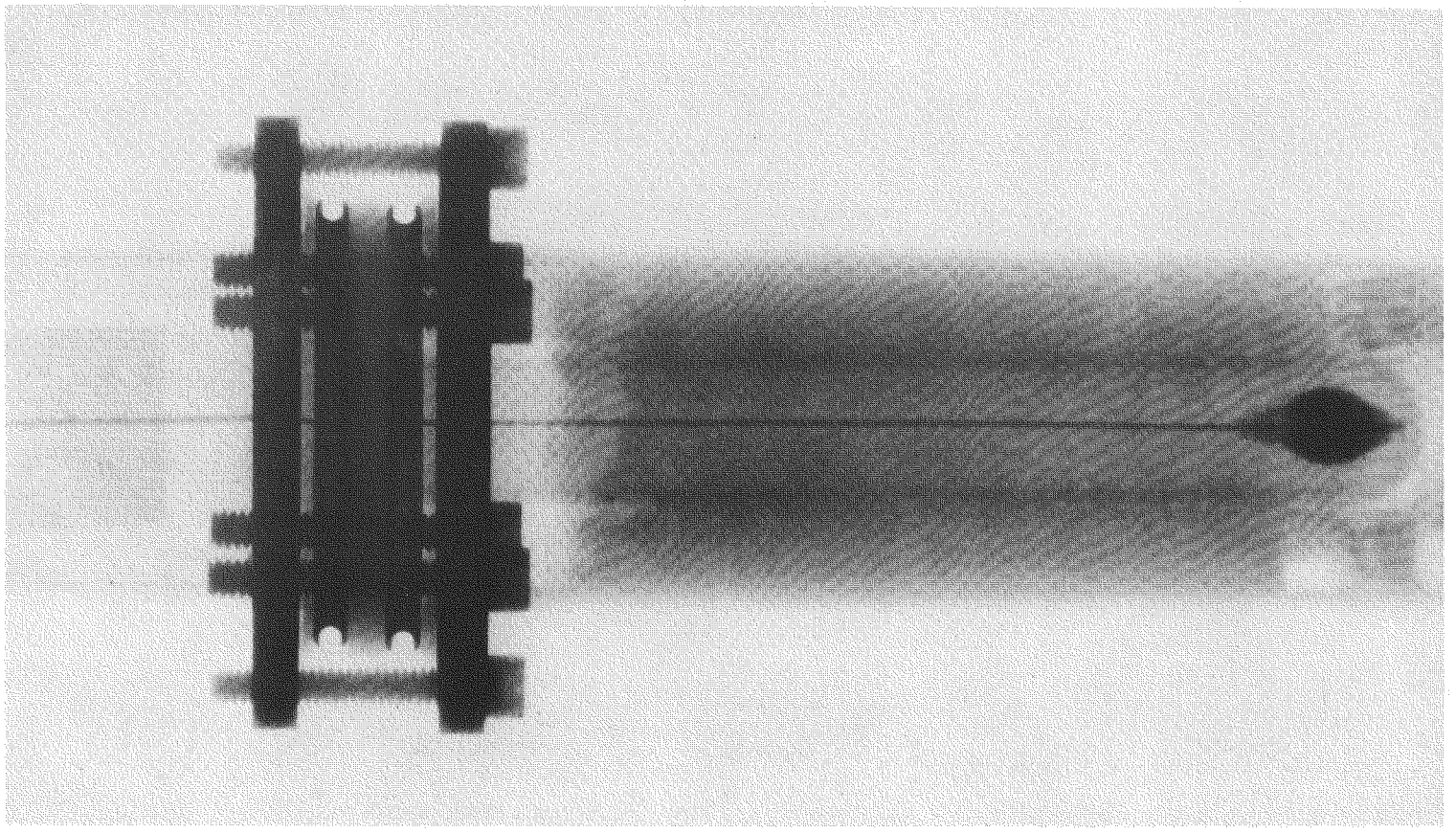

Figure D-10. Cell No. 205. Figure D-8 is the same, but viewed at 45° to show the dimensions of the void near the bottom of the carbon-sulfur electrode. The void at the tip of the beta-alumina separator is introduced purposely.

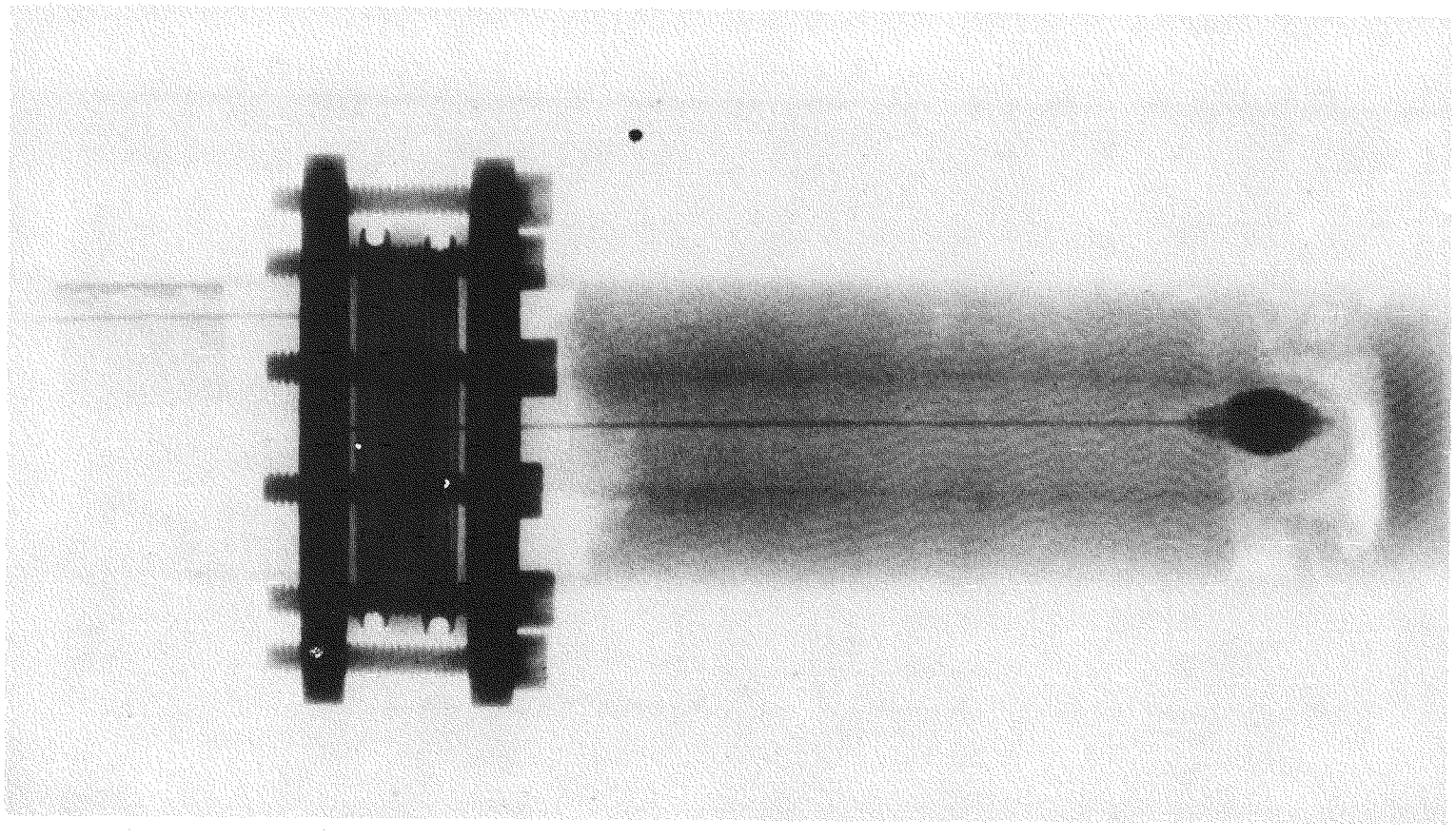

Figure D-11. Cell No. 205 radiographed at 45° to Figure D-10.

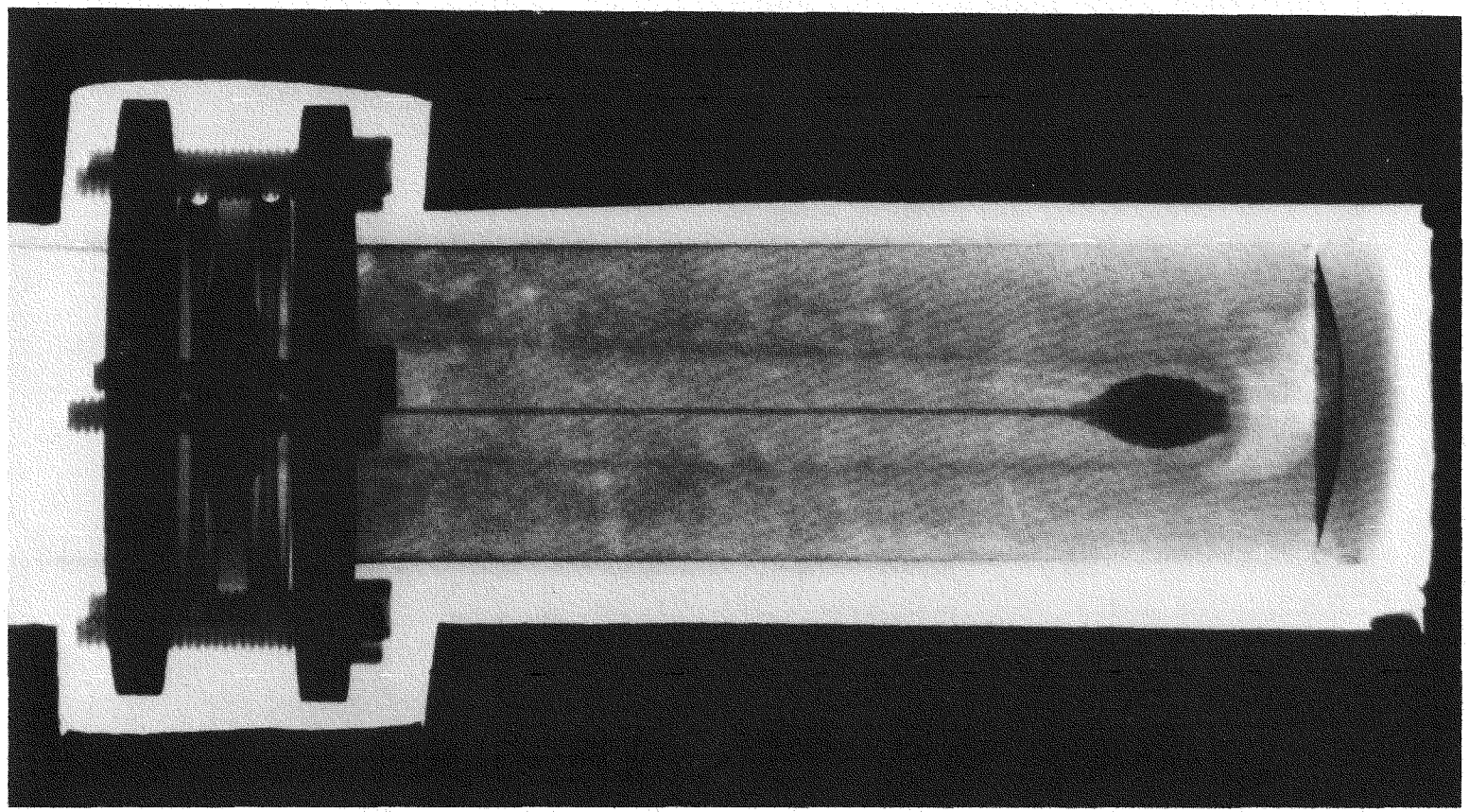

Figure D-12. Cell No. 193. The dark line at the cell edge is molybdenum applied to the aluminum by plasma spraying. The thickness of the coat decreases from top to bottom of the reservoir. Note the absence of free volume in the sulfur compartment and the deformation of the aluminum can at the bottom of the cell.

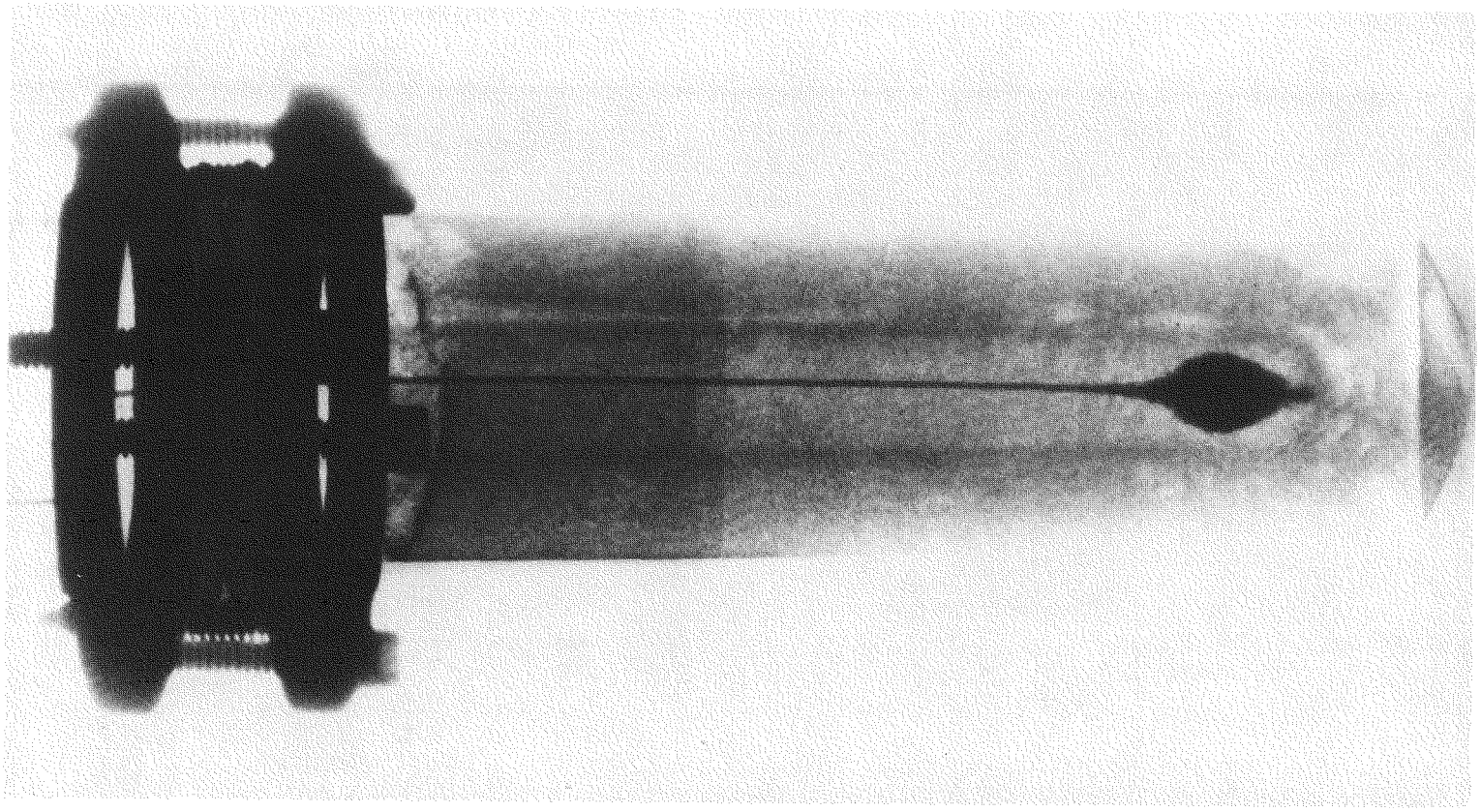

Figure D-13. Cell No. 192. This cell is similar to 193 (Figure D-12). Its performance was inferior to 193, probably because of poor transport of sodium across the void space that is visible on one side of the beta-alumina separator. Also note the corrosion product on the surface of the sulfur melt.

The behavior of sodium-sulfur test cells confirms the importance of sulfur wicking for good performance. Cells No. 192 and No. 193 were identical except for carbon loading (Figures D-12 and D-13). No. 192 has less carbon felt and its performance was markedly inferior to that of No. 193. Its resistance was higher and increased with cycling. The comparison radiographs demonstrate that the density of active cathode material in the cell with superior performance was continuous to the beta-alumina surface, whereas in the cell with poor performance there were voids and regions of low sulfur content at the interface.

D-4.1.3 Dismantling and Sectioning of Cycled Cells. The dismantling of cycled cells in air has been continued. The procedure gives direct information on cell failures resulting from the cracking of the alpha-alumina ring, the cracking of the beta-alumina tube or the degradation of the glass seal. Examination of the interior walls of the cathode compartment allowed the assessment of corrosive attack by polysulfides. The location of cracks in the beta alumina or the alpha alumina ring was identified, and local regions of interest underwent microscopic examination. The data for statistical failure analyses are largely derived in this way. Specific results obtained by dismantling of cycled cells have already been described in other sections dealing with cell testing.

An attempt was made to section cycled cells in air to reduce the cost of this procedure which is relatively expensive to carry out in a dry nitrogen atmosphere. Identification of inhibiting films in the vicinity of the beta-alumina surface was attemped; however, the attempts proved futile. The rapid reaction of polysulfide with water vapor in the air did not allow for visually distinguishing between different types of films by their color.

D-5 CELL IMPEDANCE

Although the impedance of sodium sulfur cells is usually considered to be entirely ohmic, small capacitive and inductive components can become very important when switching, faults, and power conditioning are considered. Therefore some experiments were performed to determine the elements of an R-C-L equivalent circuit.

Measurements[D-2] of the AC impedance of telephone-type lead-acid batteries were previously made in a Wheatstone Bridge as a function of the battery charge between 60 and 5000 Hz. The interpretation of the results was based on the equivalent circuit in Figure D-14. The resistances R_M, R_A and R_C result from the metal resistance, the acid resistance and polarization resistance respectively. The polarization resistance R_C is shunted by the capacitance C_C. The effect of the inductance L is correctly stated to assume a major importance for large batteries. The number of internal connections and possible loops increases with the battery size.

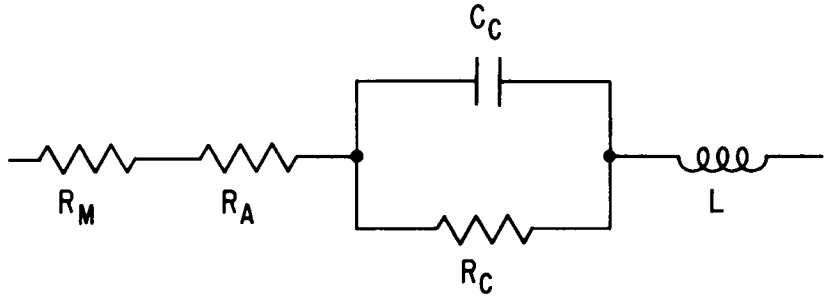

Figure D-14. Equivalent Circuit of a Battery

To separate the inductive and capacitive components, the bridge was first balanced for resistance and inductance at 5000 Hz, with the capacitance omitted. The inductance setting was then left unchanged while the bridge was balanced for resistance and capacitance at 1000 Hz and lower frequencies. This procedure assumes either

$$R_C << \frac{1}{6.28 \cdot 5000 C_C}$$

or

$$R_M + R_A >> \left| \frac{1}{R} + 6.28 \cdot 5000 C_C \right|$$

The experimental result that the resistance at 1000 Hz is identical with the resistance, read from pulse oscillograms, suggests that the second inequality is fulfilled. The method of separately obtaining the capacitive and inductive component appears justified for the batteries studied. However, the correctness of such a procedure has to be established for other types of batteries.

The impedance of the sodium-sulfur cell was determined at different states of charge at frequencies between 10 and 10,000 Hz by a phase-sensitive device which has been developed [D-3, D-4] for studies of electrode kinetics and double layer measurements on solid electrodes. The measurements were made with a small AC signal (below $3mV_{eff}$) across the cell which was held inside a furnace at 300°C. The resistance in the leads to the cell was eliminated. The use of a phase-sensitive device allowed to easily measure small impedances and gave direct information about the sign of the phase shift (capacitive or inductive). This is an advantage over a bridge in which a complex impedance may be compensated by either a suitable combination of inductance and resistance or capacitance and resistance, the latter combination being preferred in commercial bridges.

Two sodium-sulfur cells with different performance were studied. Owing to an insufficient design of the sulfur electrode, Cell No. 120 only cycled in the one-phase region with capacity of about 40%. In contrast, the second cell (No. 129) could be charged into the two-phase region and cycled with a capacity of about 75%. Measurements of the cell impedance of both cells at frequencies between 10 and 10,000 Hz demonstrated that the cells behaved like an ohmic resistance during most of discharge and charge within the accuracy of the phase-sensitive device ($\pm 1°$). In a series circuit of resistance R_S and capacitance C_S it was found that $R_S \geq 0.02\ 1/W\ C_S$ at frequencies between 10 and 3000 Hz.

Figure D-15 shows a plot of the ampere-hour limits and the resistance R_S at 1000 Hz for cell No. 129 during the first cycles. The change of R_S with time during every cycle corresponds to the charge of the DC resistance obtained from the cell voltage-time curve. The resistance changes relatively little during most of the discharge cycle. The transition from the two-phase region to the one-phase region is recognizable by a small decrease of R_S during discharge. In contrast, the transition from two-phase region to one-phase region is marked by a considerable increase of R_S during charge. Figure D-15 also demonstrates that the changes of R_S are the largest towards the beginning and end of every cycle.

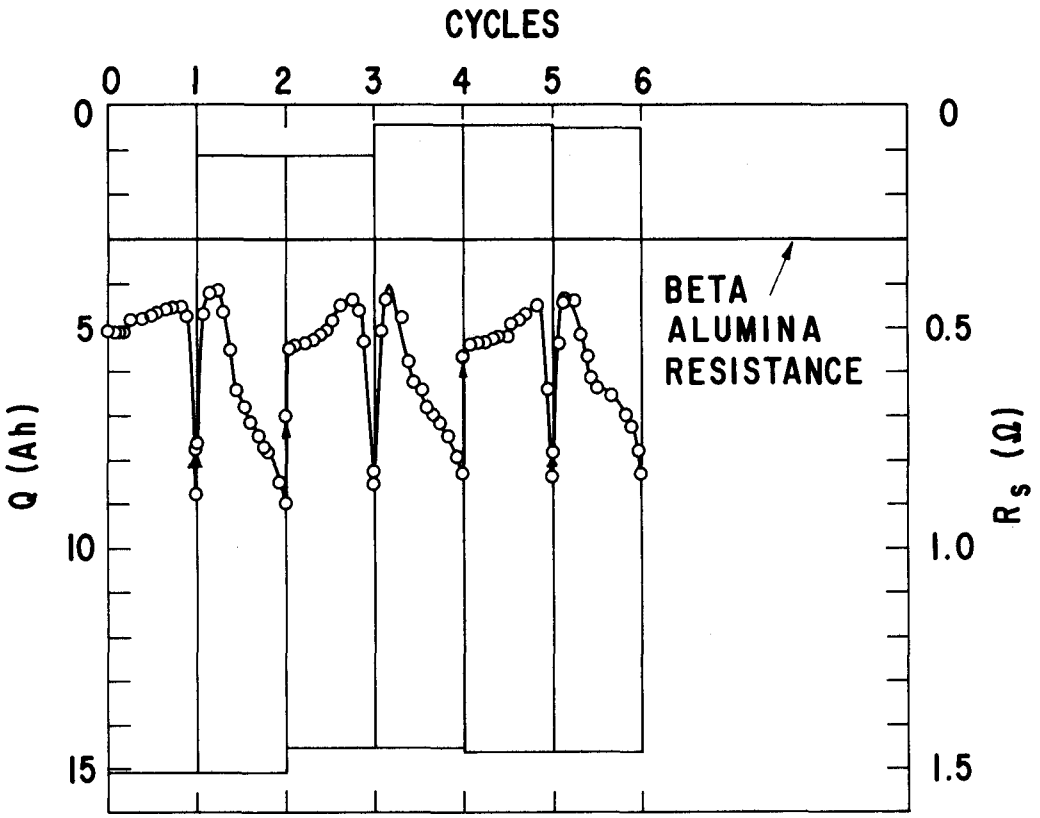

Figure D-15, Ampere-Hour Limits and Resistance for Cell 129

The presence of an inductive component could not be detected in cells 120 and 129. This result is understandable since our sodium-sulfur cells with a single beta-alumina tube do not contain internal connections like the telephone-type lead-acid batteries. Bigger sodium-sulfur cells with a larger number of tubes or bundles of single-tube cells may possess an inductive component in their impedance because of many connections and loops. The question of an inductive component should be evaluated for such systems in the future after the final design of larger units has been developed.

D-6 EFFECTS OF THERMAL CYCLING ON CELL PERFORMANCE

To evaluate the effect of temperature changes, four cells were thermal cycled while being tested at 50 mA/cm^2 with cut-off voltages of 1.3 V for discharge and 3 V for charge. The temperature was kept at 300°C for one day, and at 350°C for the next day during the working week. Over the weekends or holidays the cells remained at the same temperature as that of the preceding workday.

The test results for cell 219 which had a stainless steel cathode container were printed out on June 9, 1976 (see Figure D-16). The cell construction employed an improved design of the sulfur electrode which is described in in detail under "Evaluation of Current Collector Designs". Periodic temperature changes were initiated after the 13th cycle. The abscissa in Figure D-16 is the same for both plots. The upper plot gives the ampere-hour limits for every electrical cycle. The marked fluctuations in the ampere-hour limits after the 13th cycle are due to the temperature changes. The cell operates at a larger capacity at 350°C than 300°C. It should be pointed out that every temperature change was not introduced at the end of a discharge or charge cycle since a synchronization of thermal and electrical cycle is not to be expected in practical applications. The mismatch between thermal and electrical cycle leads to the somewhat irregular pattern of the ampere-hour limits in the upper plot of Figure D-16. The transition from the two-phase region to the one-phase region during discharge is marked by asterisks in the upper plot.

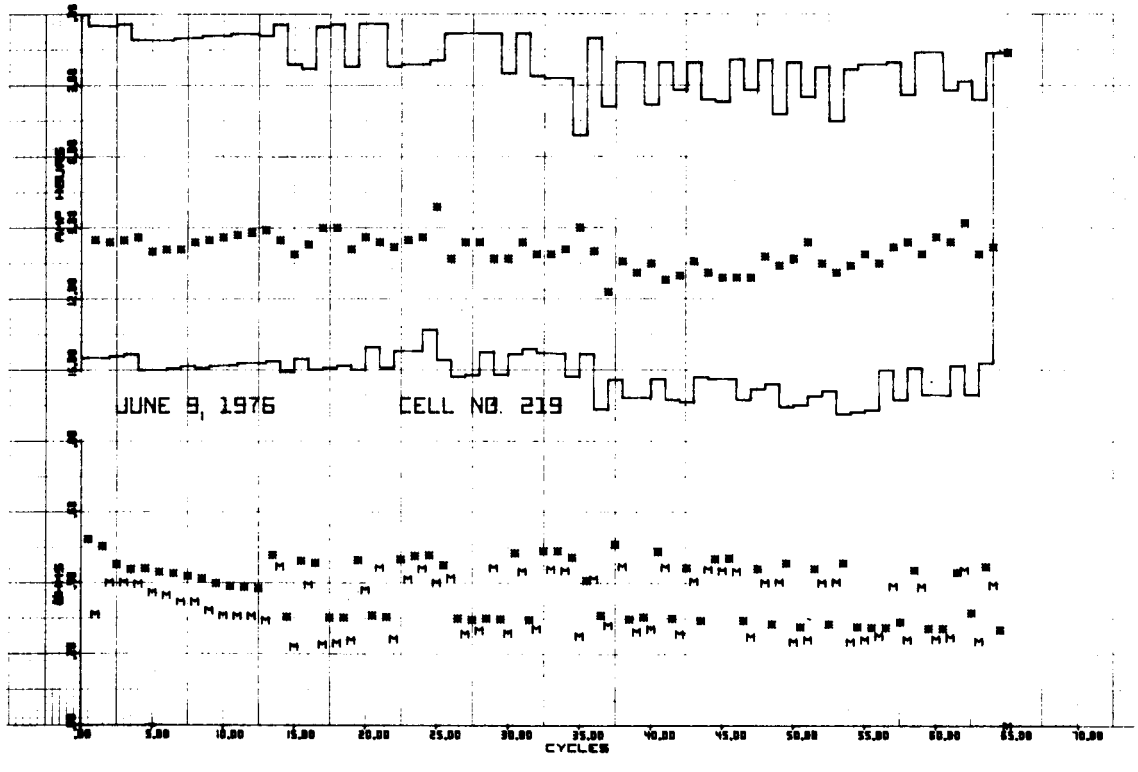

Figure D-16. Performance of Cell 219 While Being Thermally Cycled

The lower plot in Figure D-16 gives the cell resistance as a function of cycle. The asterisks denote the cell resistance at the beginning of each discharge. The symbol M corresponds to the middle of discharge. The two values differ somewhat. The absolute difference depends upon the design of the sulfur electrode. The resistance of cell 219 had decreased to about 0.4Ω at the beginning and to about 0.3Ω in the middle of discharge at the end of the 12th cycle at 300°C. These relatively large values of the cell resistance were found with beta-alumina tubes from a certain batch. Probably a surface resistance of the beta-alumina tubes was mainly responsible for them.

The effect of temperature on the cell resistance at the beginning and in the middle of discharge is clearly demonstrated by the lower plot in Figure D-16. Each of the two resistances is about twice as large at 300°C than at 350°C in cell 219. In addition, the values of the two resistances at 300°C have been increased over the respective values at the end of the 12th cycle by the periodic temperature changes. It is likely that the larger cell capacity at 350°C (see upper plot) is caused by the lower cell resistance.

At present the limited time of cycling with periodic temperature changes does not allow quantitative conclusions on the effect of temperature changes on the cell life. In a qualitative sense the test results do not indicate any detrimental effects so far.

D-7 EFFECTS OF ALTERNATE ELECTRICAL CYCLING MODES ON PERFORMANCE

In the last quarter of the contract year another cycling mode was introduced to cell testing. The cells are discharged at 75 mA/cm^2 for 7 hours. Then they stay at open circuit for 6 hours. Finally a taper charge is applied for 11 hours. The charging commences at 100 mA/cm^2 until a cell voltage of 3 V is reached. It is completed with decreasing current at constant voltage of 3 V.

The above cycling mode approximates conditions which could be used in load-leveling. It should be easier on the cells than charging at constant current. The preferential formation of a resistive layer of sulfur at the interface carbon fibers/ceramic is greatly reduced by a taper charge. If formed, resistive sulfur layers lead to a lower cell capacity with higher

local current densities through the ceramic during charging at constant current.

The above cycling mode promises to be life-prolonging and economical. At present, four cells are being operated in this way. Although the four cells perform satisfactorily, it is too early to derive conclusions on cell performance and cell life.

D-8 SAFETY STUDIES

More than 125 cells were tested during this contract period and no incidents of explosion or uncontained fire occurred. The one cell which did exhibit container melting was made with an aluminum container. A fire occurred which was confined to the cell furnace interior.

No specific safety experiments were conducted during this contract period since such experiments were done on a similar cell design during the previous contract period. General observations were made during cell testing and are summarized here:

(1) Rapid cooling to room temperature followed by rapid heating of cells may cause electrolyte failure, but normally does not lead to container melting.

(2) Electrolyte failure has been associated with "bulging" of the cathode container in some cases.

(3) Current collector designs can influence cell safety. The graphite "brush" current collector design may be less desirable from a safety standpoint than the conventional graphite felt "plug" design. The cell which failed and burned was constructed with this design. This is probably a consequence of the lower fiber density used in the "brush" design and its inability to immobilize the sulfur.

(4) System design work shows that a closed loop cooling system of inert gas or ambient air should be possible. This would be beneficial from a safety standpoint by reducing fire hazards and containing hazardous gases evolved within the system.

D-9 REFERENCES

D-1 "Sodium Sulfur Battery Development for Bulk Power Storage--Conceptual Battery Design For Battery Energy Storage Test (BEST) Facility," Electric Power Research Institute, Contract No. 128-2 Addendum, General Electric Co., Schenectady, N.Y., Dec. 27, 1974.

D-2 Willihnganz, E. and Rohner, P., AIEE Trans. Vol. 78, Part 2, 259 (1959).

D-3 Breiter, M.W., J. Electroanalyt. Chem. 7, 38 (1964).

D-4 Breiter, M.W., J. Electrochem. Soc. 113, 1071 (1966).

Section E

SUPPORTING RESEARCH

A load-leveling system employing sodium-sulfur batteries requires economical solutions to a variety of problems, many in areas of new technology for which new materials and novel processes must be developed. Solutions are found primarily by an iterative approach in which overall performance of test cells is optimized by varying design parameters and component materials under conditions approximating the final configuration. To assure long range success, however, supporting research is needed to provide a body of knowledge for scientifically interpreting the results of tests, to generate information for identifying new solutions, to develop new skills and methodologies for problem-solving, and to maintain a defensive strategy and awareness of alternative approaches.

This Section provides an overview of the supporting research carried out during the reporting period; the work described herein was solely sponsored by the General Electric Company. Two broad classes of supporting work are described in this Section: those directed specifically toward already identified problem areas, and those designed to improve understanding of materials and processes likely to be critical elements in the operation of a successful system. Thus, for example, Section E-1 (Corrosion Behavior of Container Materials) and E-2 (Performance and Development of Alpha-To-Beta-Alumina Seal) describe supporting research in already identified problem areas, whereas the subsequent sections discuss the work carried out to improve understanding in areas that appear to be peripheral now but may prove critical to the long range success of the entire technology. For this

reason a brief report on the International Conference on Superionic Conductors (held in Schenectady, May 10-12, 1976) is included at the end of this section. Major breakthroughs in this area will almost certainly influence the future of all solid electrolyte batteries and it is extremely important to keep ourselves abreast of the developments in this field.

It may be useful to point out at this stage that the terminology "supporting research" is being used in a restricted (and probably confusing) sense. Obviously, in order to succeed in the developmental tasks described in preceding sections, a considerable amount of supporting research had to be carried out. Thus, ceramic development is intimately associated with research aimed at improving ceramic quality through a better understanding of structure/property/composition/processing relationships. It has been chosen, somewhat arbitrarily, not to distinguish such sharply focused "research" from the "developmental work". On the other hand, studies of beta-alumina at high pressure and temperature are viewed as supporting research. Similarly, prototype cell development has routinely made use of different alloys as container materials and various coatings for direct evaluation purposes. This again, is viewed as developmental work whereas corrosion experiments in simulated environments carried out to understand the phenomenology and thus identify new solutions are classified as supporting work.

E-1 CORROSION BEHAVIOR OF CONTAINER MATERIALS

The successful development of a long life Na/S battery for load-leveling depends on the selection of suitable cell container materials. In particular, the reactive chemical environment found in anode and cathode compartments strictly limits the choice of satisfactory container and/or electrode materials.

Work during the present contract period was aimed at identification, development and study of materials suitable for use as container, electrode or dual function container/electrode materials in Na/S batteries.

E-1.1 Approach

Results of materials investigations from the previous contract period were used to guide materials studies and provide a unified approach with respect to past and present work. Work on promising materials investigated during the previous contract period was extended.

Investigations in the anode (sodium) environment included studies on metals and non-metals. Those in the cathode environment (S, Na_2S_x) dealt with metals, metals with protective coatings (coated metals), and non-metallic materials. The need for extensive work on protective coatings was clear from results of previous work since most unprotected metals had degraded severely in the cathode environment. In addition, corrosion products were observed to adversely influence cell performance.

Two types of materials stability were evaluated. The first type, chemical stability, refers to materials stability in molten chemical reactants, such as sodium, sulfur or Na_2S_x. The second type, called electrochemical stability, refer to materials stability as an electrode under cycling. Both types of stability are essential for satisfactory, long life performance of Na/S battery container and electrode materials.

Stability experiments were carried out both in a laboratory cycling apparatus and in prototype cells. The cycling apparatus, described below, was developed during the previous contract period and provided a quick method to qualitatively evaluate performance of candidate materials under cycling in molten Na_2S_x. Materials evaluation in prototype cells was selectively used as a follow-up technique to establish electrochemical stability in actual cells.

Metallographic cross-sectioning, scanning electron microscopy (SEM), and electron beam microprobe techniques were used to characterize and study the corrosion of candidate materials. These techniques were especially useful in evaluating the effectiveness of protective coatings.

The specific materials mentioned under Section E-1.3 have been grouped according to the classifications mentioned earlier and are presented in a way

to maintain continuity with earlier work. Representative results from the previous contract period have been briefly stated to provide background while the work of the present period is described in some detail.

E-1.2 Experimental Techniques

Seven different types of sample tests were used to investigate materials stability. The various tests are listed in Table E-1 and were applied to materials as indicated in Table E-2. A description of each test follows.

Four types of chemical stability tests were available. Type I and Type II tests were done by reacting polished samples of the candidate material in either molten sulfur (Type I) or molten Na_2S_x (Type II) at 350°C. Samples were placed in sealed glass ampules with high purity reactants. The glass ampules were evacuated for one hour at 5×10^{-5} torr and sealed off at room temperature after a short bake-out period to eliminate gaseous impurities from the reaction ampule. After various reaction times penetration results were determined by microscopic examination of specimen cross-sections. Weight change determinations were made when appropriate.

Type III sample testing consisted of continuous oxidation of the candidate material in a circulating air furnace at 350°C. Oxidation was interrupted periodically to determine weight change.

Type IV testing was used to determine the stability of sintered SiC and hot pressed Si_3N_4 (Norton) in molten sodium. Six millimeter square specimens ($\sim$ 2 mm thick) were sealed into individual glass (Corning 7052) ampules and filled with triply distilled sodium under high vacuum. Samples were reacted at 350°C for 750 hours or for 500 hours at 500°C. Weight change measurements and microscopic examination were also employed.

Electrochemical stability was determined by Type V and Type VI testing. These two tests were equivalent except for small changes in the apparatus. These tests provided an effective method for qualitative screening and comparison of numerous samples.

TABLE E-1

MATERIALS EVALUATION TESTS

TEST TYPE		TEST DETAILS
A.	CHEMICAL STABILITY	
	TYPE I	Sample stability in molten Sulfur at 350°C. Vacuum apparatus.
	TYPE II	Sample stability in molten Na_2S_x at 350°C. Vacuum apparatus.
	TYPE III	Sample stability in air oxidizing atmosphere at 350°C. Air furnace.
	TYPE IV	Sample stability in triply distilled molten sodium. Exposure for 750 hrs. or 500 hrs. at 350°C as specified.
B.	ELECTROCHEMICAL STABILITY	
	TYPE V	Laboratory cycling under N_2 in Na_2S_x at 350°C with reference electrode. Standard conditions of 30 mA/cm^2 for 100 hrs. Apparatus shown in Figure E-1.
	TYPE VI	Laboratory cycling under N_2 in Na_2S_x at 350°C.
C.	PROTOTYPE CELL	
	TYPE VII	Cycling in laboratory test cell. Standard discharge at 1A. Nominal container dimensions: O.D. = 1 inch, length = 2.9 inches, wall thickness = .060 inches.

Table E-2

EVALUATION OF CANDIDATE CONTAINER MATERIALS

MATERIALS	TEST TYPE: CHEMICAL STABILITY I	II	III	IV	ELECTROCHEMICAL STABILITY V	VI	PROTOTYPE CELL VII
Uncoated Metals							
Rodar Alloy	X	X			X		X
Molybdenum	X	X			X		
SX-10 Alloy	X						
Coated Metals							
Chromium Coated Rodar Alloy					X		
Mo Coated Rodar Alloy					X		
Resin Coatings					X		X
Graphite Bonded Rodar Alloy					X		X
Graphite Bonded Aluminum					X		
Non-Metallic Materials							
Sintered SiC	X	X		X		X	X
Si-SiC Composite	X					X	X
Graphite (Speer 580)			X				
Pure Silicon	X						
Silicon Nitride (Si_3N_4) (hot pressed)				X			

The Type V test was run using the apparatus of Figure E-1. A polished specimen was attached to the end of an insulated lead wire and immersed in molten Na_2S_x (of nominal composition Na_2S_4) opposite a molybdenum counter electrode. The Na_2S_x was protected from oxidation by a flow of dry N_2 gas. Samples were cycled at various current densities and frequently removed for microscopic examination and evaluation. Fiducial scratchmarks were made on the polished sample surface. Microscopic observations were focused on the area adjacent to these marks. A molybdenum reference electrode was included for monitoring changes in the cycling potential. This gave a gross indication of sample cycling performance.

The Type VI cycling apparatus was similar to the apparatus shown in Figure E-1; except that no reference electrode was included and the samples were in the form of glass coated rods instead of disks. The test procedures were identical to those described above for Type V testing.

Prototype cell testing constituted the Type VII test. The candidate cell material was used to form a cathode container suitable for testing in a laboratory cell. Nominal cathode container dimensions (O.D. = 1 inch, length = 2.9 inches, wall thickness = .060 inches) and standard clamp seals were used throughout. Cycling was at 300°C at 1 A using an automatic cycling apparatus. Precision mass determinations, cathode container cross-sectioning, and electrical cycling data were used to measure the performance of candidate materials in actual cells.

Protective coatings intended to prevent scale formation on steels were tested on Rodar substrates since this substrate material is easily degraded in molten Na_2S_x.

Chromium coatings were applied by electroplating to a final thickness of about 1 mil. Molybdenum coatings were 5 μm thick and applied by sputtering.

Phenolic and polyphenylene resin coatings were applied by spray techniques. Graphite bonded metal structures were formed using phenolic resin binders and graphite cloth or graphite paper (Grafoil).

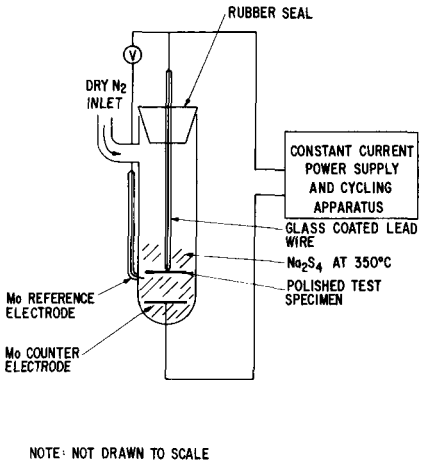

Figure E-1. Type V Test Apparatus

E-1.3 Investigation

E.1.3.1 Uncoated Cathode Container Materials.

Rodar Alloy. Rodar alloy was reported on in some detail during the previous contract period. This Fe-Ni-Co alloy represents the class of corrodable substrate materials which forms a somewhat protective corrosion product scale under cycling. It was noted that the dissolution of metal sulfide corrosion products adversely influenced cell performance. This demonstrated the need for protective coatings to be applied to corrodable substrates.

SX-10 Alloy. The SX-10 (iron - 3 percent silicon) alloy is a low cost iron alloy commonly known as transformer iron. Type I and Type II tests showed corrosion rates as high as 32 mils per year with no protective scale formation.

Sintered SiC. SiC is a highly stable semiconducting ceramic which has been known for many years. Prochazka, of this laboratory, has developed a method to form dense articles of SiC without employing costly hot pressing techniques[E-1]. This development now makes it possible to use conventional mass production forming techniques such as die pressing, slip casting, injection molding, extrusion or prefired machining to form dense articles of the sintered SiC product.

The chemical stability of sintered SiC was determined adequate for use as a cathode container in Na/S cells; however, the final cost of this material may still limit its use as a container material in Na/S cells. Discussion of corrosion experiments with sintered SiC in the cathode environment follows.

Table E-3 shows weight change results after Type I, II and VII corrosion testing of sintered SiC samples. No significant weight change was noted except for the data point at 120 hours which is believed to reflect a measuring error. No evidence of surface reaction was noted even after 14,540 hours exposure to molten Na_2S_x. Scanning electron microscopy and x-ray emission analysis of cross-sections were unable to identify reaction products within 1 μ of the sample surface.

Figure E-2 shows the SiC rod face surface appearance at different times during Type VI testing. Figure E-2A was taken prior to melt exposure. Figures E-2B and E-2C were taken after cycling at a constant current density of 30 mA/cm^2 for 250 hrs. and 675 hrs., respectively. Figure E-2D shows the surface after 100 hours of cycling at 80 mA/cm^2. Careful examination showed no alteration of the surface under any of these conditions.

The first ten cycles of the capacity cycling diagram for a sintered SiC Type VII test are shown in Figure E-3. The total test ran for 79 cycles over 3 weeks with a total 406 AH passed. The diagram shows that cycling in the two-phase region was routine and full discharge capacity was reached. The loss in cell capacity with time was linked to a faulty clamp seal which eventually caused cell failure. This cell test experiment was continued to a total of 1100 hours of actual cycling by reuse of the sintered SiC cathode container in a new cell after replacement of current collector and reactants.

Observations of the SiC cell body after cycling and removal of the carbon felt, Na_2S_x and sulfur by washing and acid reaction showed no evidence of corrosion at the interior or exterior surfaces of the container in either experiment. No pitting, scale formation, or cracking associated with cycling or melt exposure could be detected. Precision mass determination of the container before and after melt exposure showed no differences beyond

Table E-3

WEIGHT CHANGE RESULTS ON SiC

I. Uncycled Samples

Environment	Test Type	Exposure Time	Sample	Thickness Change	Weight Change	Percent Wt. Change
Sulfur	I	120 hrs.	S-15	<.5%	+36.3 mg	+6.7%
Sulfur	I	360 hrs.	S-13	<.5%	-.08 mg	-.01%
Sulfur	I	864 hrs.	S-5	<.5%	-.02 mg	-.03%
Na_2S_x	II	1360 hrs.	NS-14	<.3%	-.31 mg	-.1%
Na_2S_x	II	14,540 hrs.	NS-16	<.3%	+.14 mg	+.05%
II. Cycled Samples						
Cell Cathode (Na_2S_x, S,C ...)	VII	600 hrs.	Cell #106	-		-
Cell Cathode (Na_2S_x, S,C ...)	VII	500 hrs.	Cell #125	-		-
Total (Cell #106 + Cell #125)		1100 hrs. cycling at ≈ 20 mA/cm^2 + 1.05 mg + .003%				

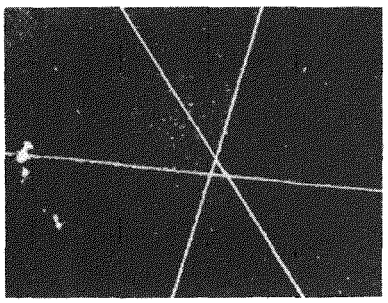

T = 0 HRS. 15X

(A)

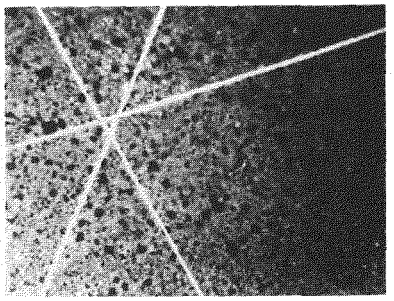

T = 250 HRS. 30 MA/CM^2 15X

(B)

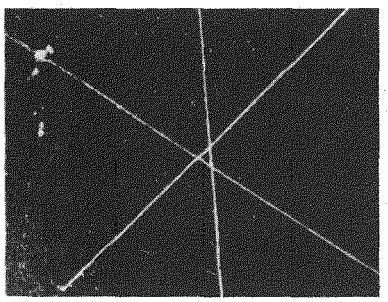

T = 675 HRS. 30 MA/CM^2 15X

(C)

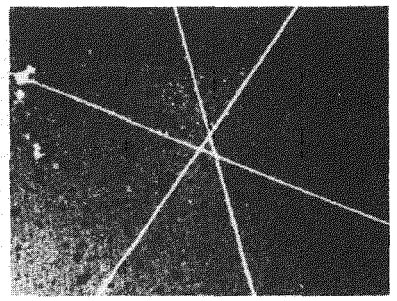

T = 100 HRS. 80 MA/CM^2 15X

(D)

Figure E-2. Sintered SiC Test Results

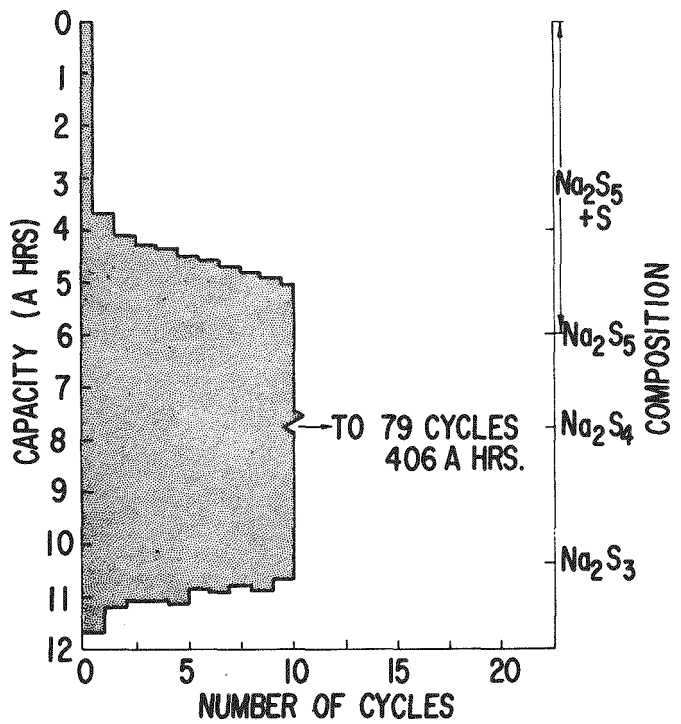

Figure E-3. Capacity Cycling Diagram

experimental measuring error. This is shown in Table E-3. Three sets of interior surface fiducial scratch marks made prior to melt exposure were unchanged by cycling and melt exposure.

Si-SiC Composite. The formation of composite articles of silicon, SiC and carbon has been shown by Hillig et al[E-2]. These composites can be formed by the reaction of molten silicon with carbon filaments at about 1450°C. The molten silicon reacts with the carbon filaments to partially convert them to SiC.

Adjustment of fabrication parameters allows one to vary the ultimate composition and distribution of the composite components. Complex shapes can be fabricated using this technique, with virtually no shrinkage. The final articles are highly chemically stable, electrically conductive, and of low density (less than 3 g/cc).

Samples of Si-SiC composite showed excellent chemical corrosion stability in Type I tests. Samples exposed for over 1000 hours showed no scale formation, pitting, cracking, weight change, or other signs of physical degradation. Scanning electron microscope (SEM) and x-ray emission analyses were unable to detect corrosion products within 1 μ of the surface.

Type VI testing (640 hours at 50 mA/cm^2) of Si-SiC composite revealed extensive leaching of silicon from between the SiC-C fibers. No chemical attack of the SiC-C fibers was noted; however, the fibers were prone to breakage in the absence of the silicon reinforcement. A modified container design was developed to prevent Si leaching. It is presently undergoing Type VII testing and incorporates an interior graphite sleeve intended to act as a barrier to the diffusion of free Si. This design should minimize the dissolution of free Si into the catholyte under cell cycling.

Graphite. Weight change results with time after Type III testing of an Airco Speer 580 graphite rod are shown in Figure E-4.

The rate of material loss due to oxidation corresponds to at least 1 mil/yr and appears to be constant with time. The result indicates that the

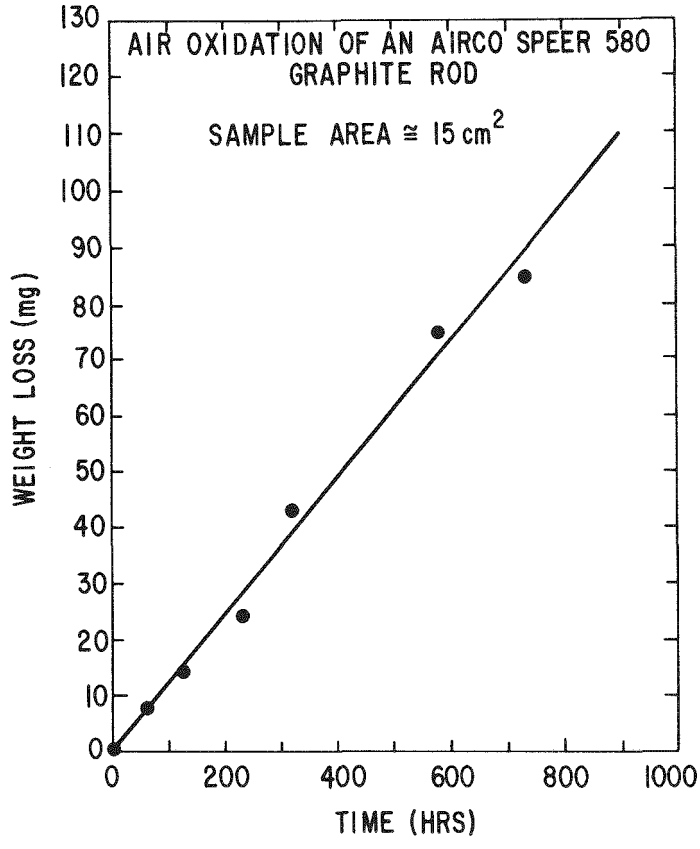

Figure E-4. Type III Testing of Graphite

oxidation rate of graphite in air at 350°C is non-negligible, and graphite or carbon cathode containers will require oxidation protection if used for long-term service in an oxidizing atmosphere.

Molybdenum. Molybdenum underwent Type I, II and V testing for extended times (1000 hours or more). Discoloration of the sample surface was common; however, this was not accompanied by physical degradation of the surface. X-ray diffraction analysis revealed the formation of a 1 μm thick layer of MoS_2. It is presumed that this skin protects the bulk sample from further attack. The protective skin is electrically conductive. Samples typically exhibit good electrode performance even an high current density for long times.

The high volumetric cost of Mo prohibits its use as a cathode container in Na/S cells. However, the chemical and electrochemical stability demonstrated by this material indicated that thin (several microns thick) coatings of

molybdenum should effectively protect steel substrates from corrosion. Work with protective Mo coatings was begun and is described under Section E-1.3.2.

Pure Silicon. Silicon has shown excellent chemical stability in Type I tests, however, other experiments have shown silicon unstable in Na_2S_x under applied electric fields. Siliconized metals might then have some usefulness if restricted to non-electrode applications.

E-1.3.2 Coated Cathode Container Materials

Chromium Coating. Figure E-5 shows the cross-section of a Cr coated Rodar alloy disk after Type V testing for 170 hours at 30 mA/cm^2. Cracking of the coating is apparent along with substrate reaction and corrosion product build up. Subsurface corrosion was extensive enough to disrupt the Cr coating and force it loose from the substrate surface. Attack of the coating was less extensive and included blistering, light scaling, discoloration, and direct chemical reaction. Fiducial scratchmarks at the sample surface were attacked or obliterated. An identical experiment with shorter exposure time indicated similar results with less extensive attack. This shows that degradation of substrate and coating advances with time.

Localized attack of coating and substrate also occurred. Vertical channels formed perpendicular to the sample surface during cycling and were spaced about 40 μm apart. Typical channel dimensions were 3 μm width and 5-15 μm length. Penetration of the channels extended well into the substrate in many cases.

Some information on composition and structure of corrosion products was obtained by scanning electron microscopy, x-ray mapping and point x-ray spectroscopy.

Three distinct surface layers were noted. The outermost layer was a chromium sulfide (most likely Cr_2S_3) formed by chemical reaction of the surface layer with Na_2S_x. The middle layer was unreacted Cr. This layer was reduced to less than half its original thickness. The third layer was a 1/2 mil thick Ni coating electrodeposited prior to Cr deposition and intended to prevent cracking in the Cr and promote adhesion of the Cr to the substrate.

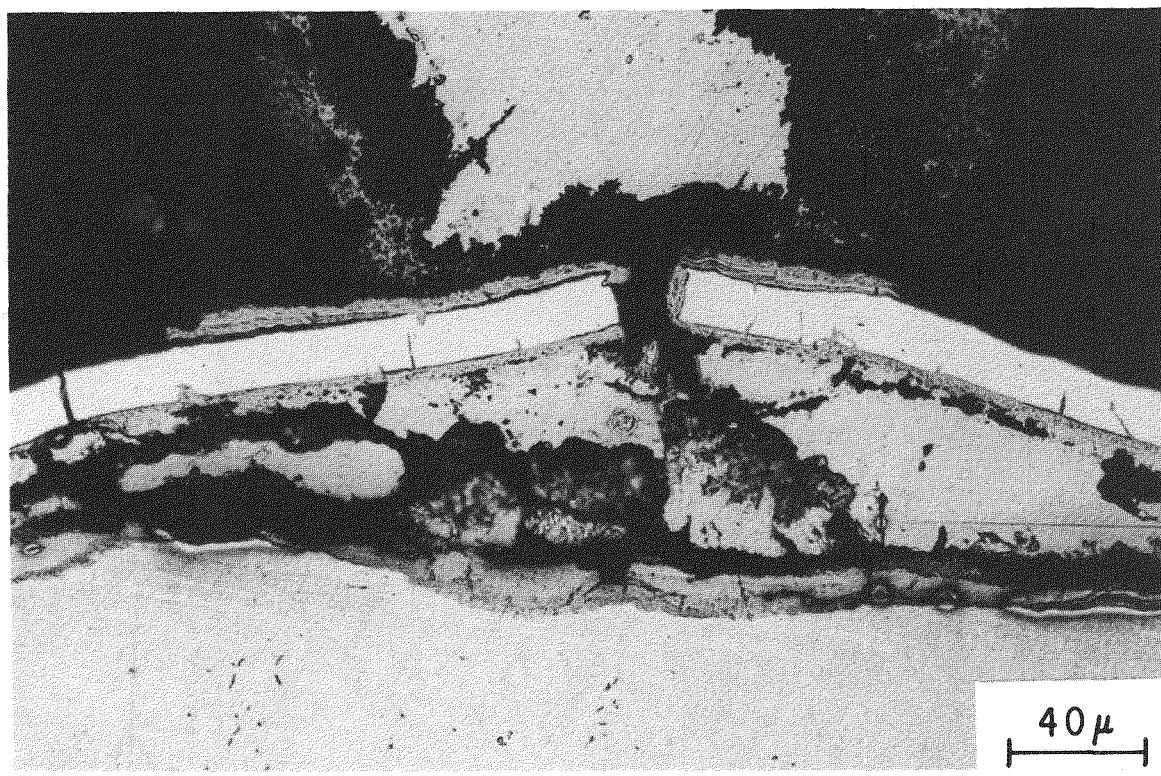

Figure E-5. Sub-surface Corrosion of Chromium Coated Rodar Alloy

The corrosion product channels mentioned earlier advanced from the outermost layer into and through the Cr and Ni layers and terminated in the substrate material.

No sodium was detected in any of the corrosion products. This implied the formation of simple Cr, Fe and Ni sulfides. Examination of the Ni and Cr platings at 1500X showed uniform, dense coatings. Porosity, poor adhesion or flaws were not typically observed in the coating. This is evidence that channel formation was caused by preferential chemical or electrochemical (presence of dissimilar metals) attack and not physical flaws.

The results of this investigation demonstrate that Cr electroplated in the above manner will probably not offer long term corrosion protection for corrodable substrate electrode materials. Moreover, Cr exceeds the raw material cost target by a factor of 12 making it economically feasible only as a very thin coating.

Molybdenum Coating. The effectiveness of an Mo coating applied to a Rodar alloy substrate can be seen in Figure E-6. Figure E-6A shows the specimen surface before testing and E-6B the same surface after Type V testing for 336 hours. After 100 hours of cycling the coating showed characteristic darkening but no cracking or scaling. In contrast, the uncoated face was badly attacked and showed a uniform corrosion product. Base metal attack of the coated face occurred at discrete points. Prolonged cycling to 336 hours produced localized cracking of the film (center point Figure E-6B) at such points. It is suspected that as corrosion products build beneath the surface they stress the Mo coating and cracking results.

Separate experiments demonstrated that substrate corrosion occurs at defects in the Mo coating. Note the line attack in Figure E-6B (lower right) and its counterpart defect in the uncycled specimen shown in Figure E-6A. A second example is the obvious depression at the center of both micrographs.

Corrosion products were observed to trail along the scratchmark grooves. Examination of the corrosion product (Figure E-7) showed well-crystallized mixtures of $FeNiS_2$, $NiCO_2S_x$, FeS_2 and Fe_2O_3. These are characteristic Rodar alloy (substrate) corrosion products. No Mo containing corrosion products were detected. These results verify localized base metal attack. The absence of Mo in the corrosion product establishes the inertness of the Mo coating.

High magnification scanning electron micrographs showed no physical cracking or scaling of the coating away from regions of pinhole attack. X-ray diffraction from the surface of a cycled Mo specimen revealed a 1 μm thick MoS_2 film. Presumably, this protective film prevents most of the base metal from attack.

The most probable explanation for localized attack is that shadowing effects at surface scratches or pinholes produce inadequate coating densities for substrate protection.

The limitation of Mo as a protective coating lies in the quality and cost of the applied coating and not its chemical stability. Economic considerations

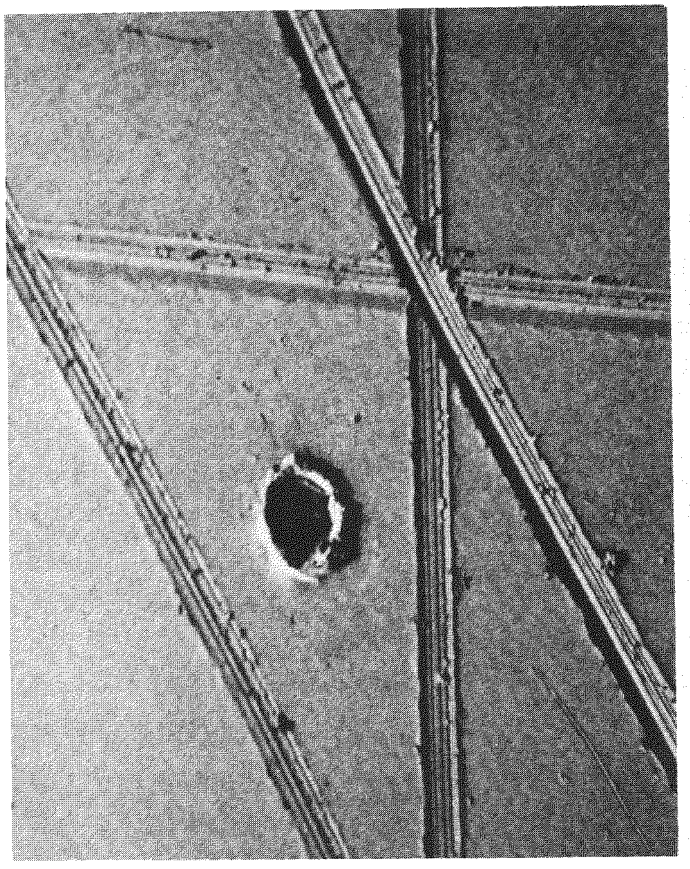

(A)

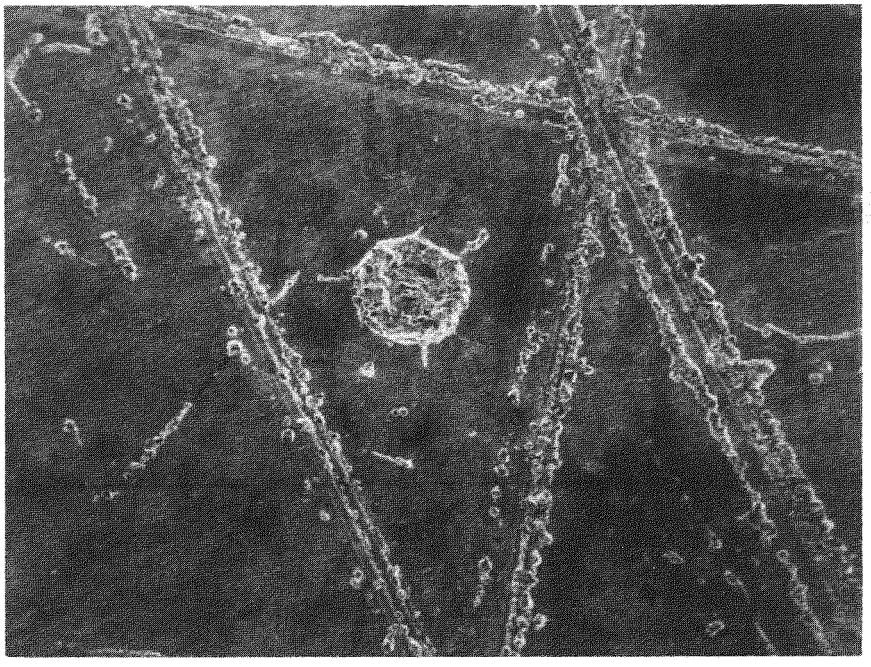

(B)

Figure E-6. Molybdenum Coated Rodar Alloy Test Results

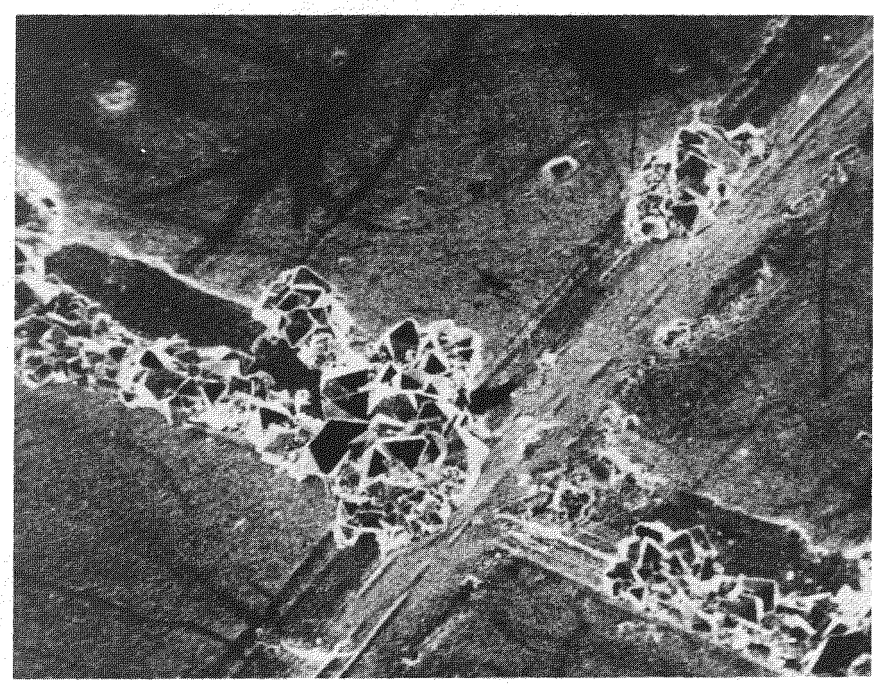

Figure E-7. Attack of Mo-Coated Rodar Alloy

rule out thick coatings and demand very inexpensive methods of applying thin coatings. The final coating must be defect free or else ultimate degradation of coating and substrate will occur. This suggests that Mo coated substrates could be employed for limited uses (spacers, headers), but not for general use in cathode container protection.

Resin Coatings. As an outgrowth of work begun in the previous contract period different commercially available resin coatings were evaluated. These included phenolic resin and polyphenylene resin coatings. The phenolic resin coatings proved most effective.

Degradation of the coatings and substrates always occurred when steel substrates were used. Results were different using aluminum substrates. The differences appear to be caused by differences in corrosion mechanism.

Steels degrade under cycling by forming a thick surface scale which tends to grow thicker with time and flake off. Porous coatings, such as resin coatings, allow pinhole attack which leads to progressive subsurface corrosion and flaking of the coating. In contrast to steels, aluminum forms a densely packed, thin layer of corrosion product which prevents further reaction of the surface. Therefore, areas of the aluminum substrate exposed by pinholes in the coating do not lead to extensive subsurface corrosion and flaking of the coating. The protective reaction product formed on aluminum during cycling is electrically insulating. This requires the application of an electrically conductive coating to the metal surface if aluminum is to function as an electrode in molten Na_2S_x. A graphite filled phenolic resin coating was identified which met this goal.

Examination of a resin coated sample after Type V testing for 160 hours at 30 mA/cm^2 showed good adhesion of the coating to the aluminum surface and no signs of physical degradation except that the coating had darkened a bit. Electrode performance was stable during the cycling period.

Type VII test results showed that the coating remained intact; however, cycling was restricted to the single phase region.

The use of this coating in cells requires improvements in electrical conductivity and appropriate modifications to promote cycling in the two phase region. The resin coatings studied are ineffective as protective coatings for steels and must be restricted to use as conductive coatings for aluminum.

Bonded Structures. A special structure was developed to improve the effective electronic conductivity of resin coatings. This class of structure was named a resin bonded structure and was formed by bonding a chemically inert structure, with good electronic conductivity, to an aluminum substrate.

Two types of resin bonded structures were evaluated under Type V testing. Both structures demonstrated adequate electrode performance under cycling; however, one structure showed very poor wetting by Na_2S_x. Evaluation of these structures under cell cycling terminated because of a furnace breakdown. No conclusive results regarding cell cycling with these structures could be gathered under these conditions.

E-1.3.3 Visual Summary

The relative stability of many of the materials studied is shown in this section by a series of photographs (Figure E-8). Specimen surfaces are shown before and after Type V testing in Na_2S_x.

The conclusions drawn from the preceding text and the photographs are:

- Of the uncoated container materials studied, only molybdenum and SiC showed satisfactory results in the corrosion tests, while aluminum, nickel, and 347 and 430 stainless steel did not.
- Metal coatings of Mo and Cr were tested on a Rodar base; only the molybdenum coating was satisfactory.
- Non-metallic coatings of various resins and MoS_2 were tested on aluminum; only the phenolic resin withstood attack.
- Graphite cloth and Grafoil graphite paper were resin bonded to aluminum and low carbon steel. These were satisfactory on aluminum but not steel.

It must be appreciated that the tests refer to materials and coatings of specific types and that entirely different results and conclusions may result from coatings applied in a different manner or from subtle differences in test conditions.

E-1.3.4 Metallic Anode Container Materials

Engineering Materials. Aluminum has demonstrated satisfactory performance as a sodium container in laboratory cells. It is presently used as standard equipment in all prototype cells. A literature search has verified laboratory experience that sodium corrosion of common engineering materials does not occur at 350°C. Temperatures in the 600°C range are high enough to promote metal attack by sodium under certain conditions.

E-1.3.5 Non-Metallic Anode Container Materials

Ceramics. The stability of sintered SiC and hot pressed Si_3N_4 was evaluated in molten sodium by Type IV testing.

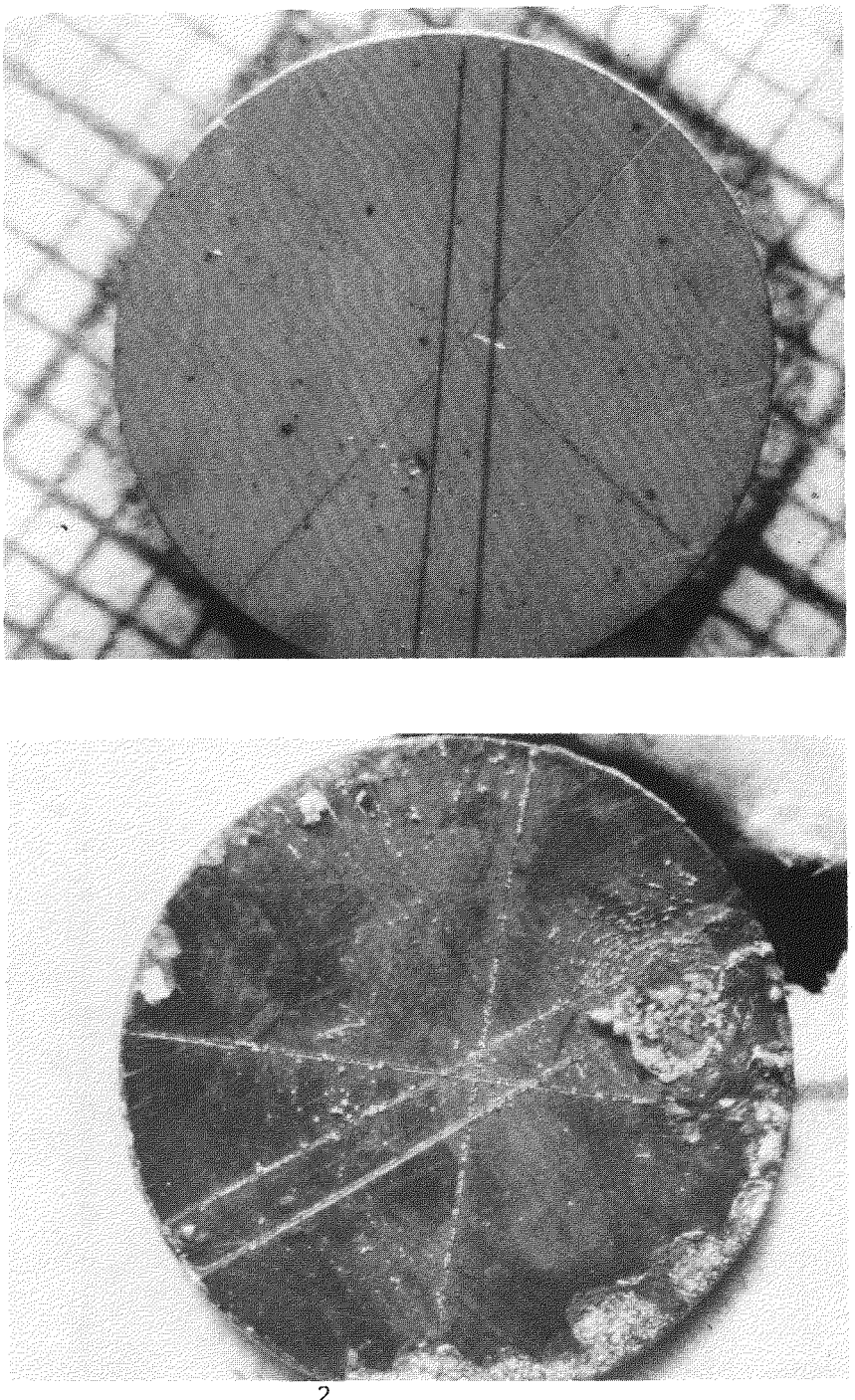

T=115 hrs. @ 30 ma/cm^2 7.5X

Figure E-8A. Mo Coated Rodar Alloy

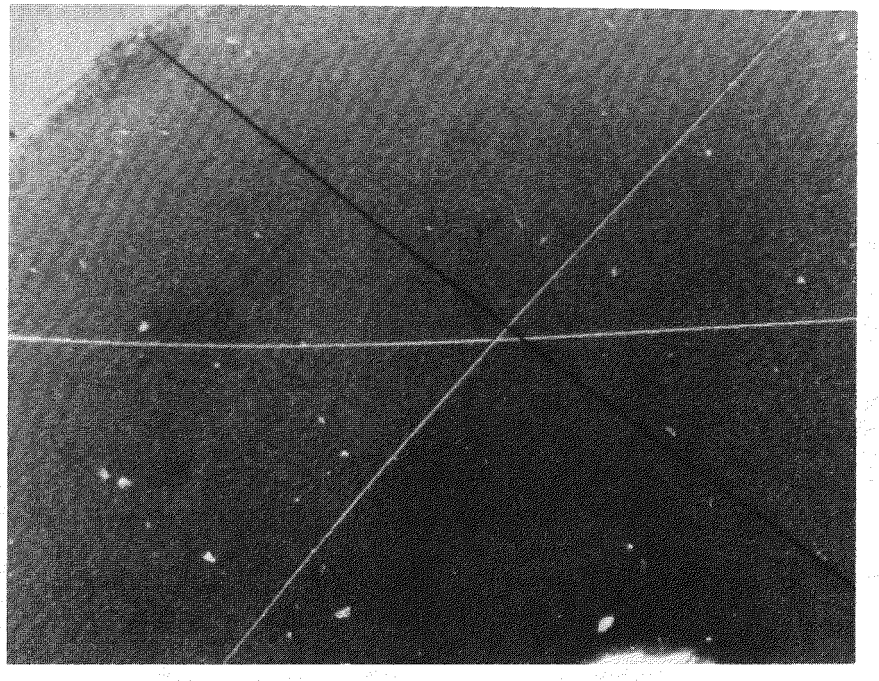

T=0 15X

T=100 hrs @ 30 ma/cm^2 15X

Figure E-8B. Cr Plated Rodar Alloy

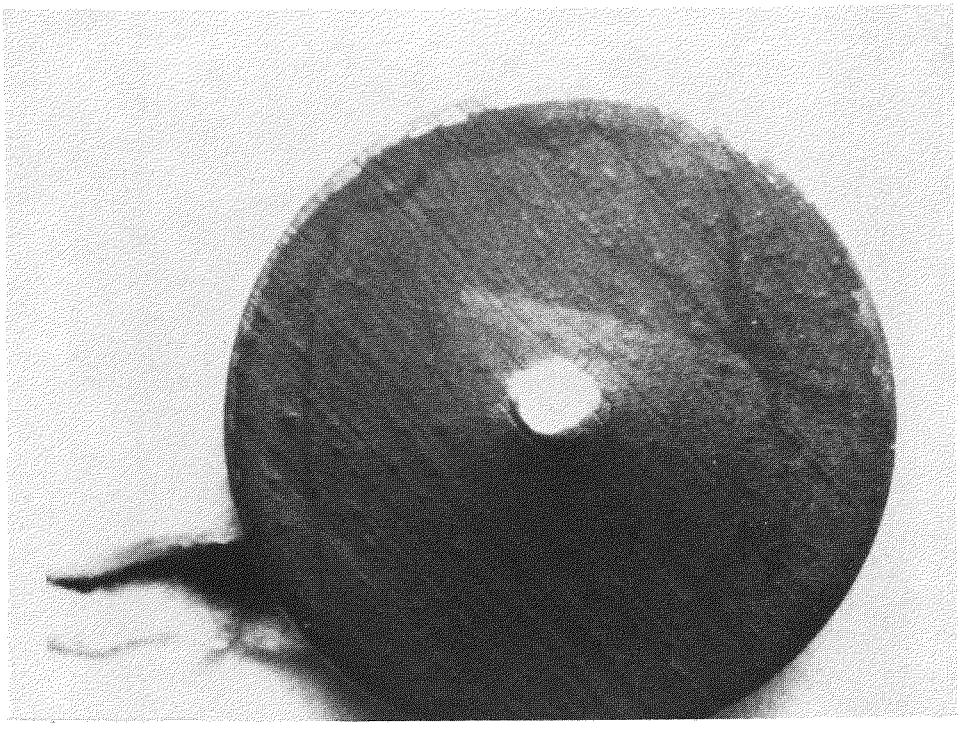

T=0 7.5X

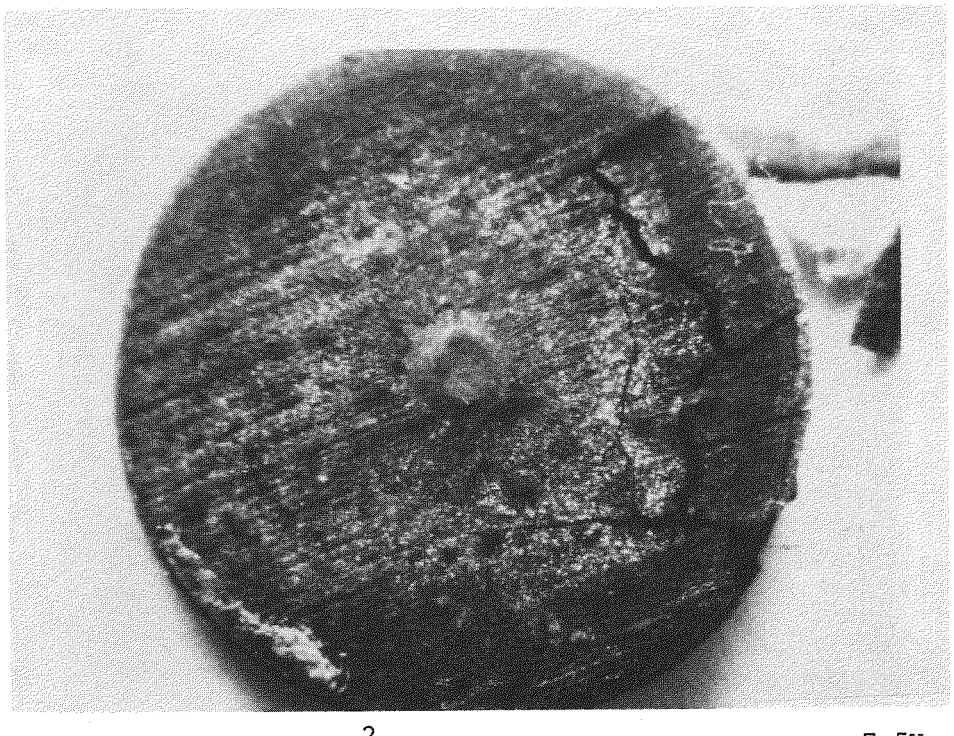

T=120 hrs. @ 30 ma/cm^2 7.5X

Figure E-8C. Resin Coated Steel

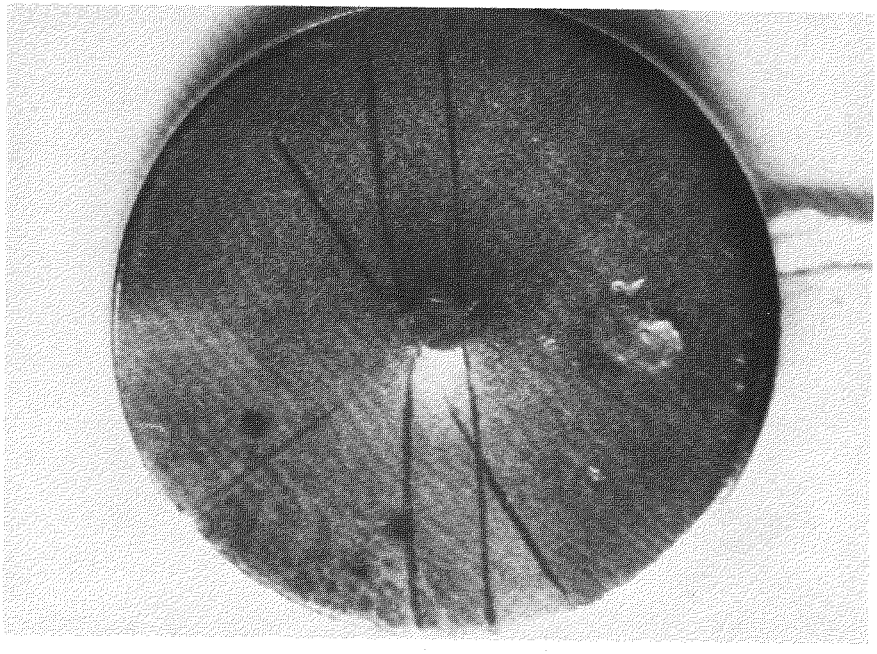

T=0 7.5X

T=120 hrs. @ 30 ma/cm^2 7.5X

Figure E-8D. Nickel

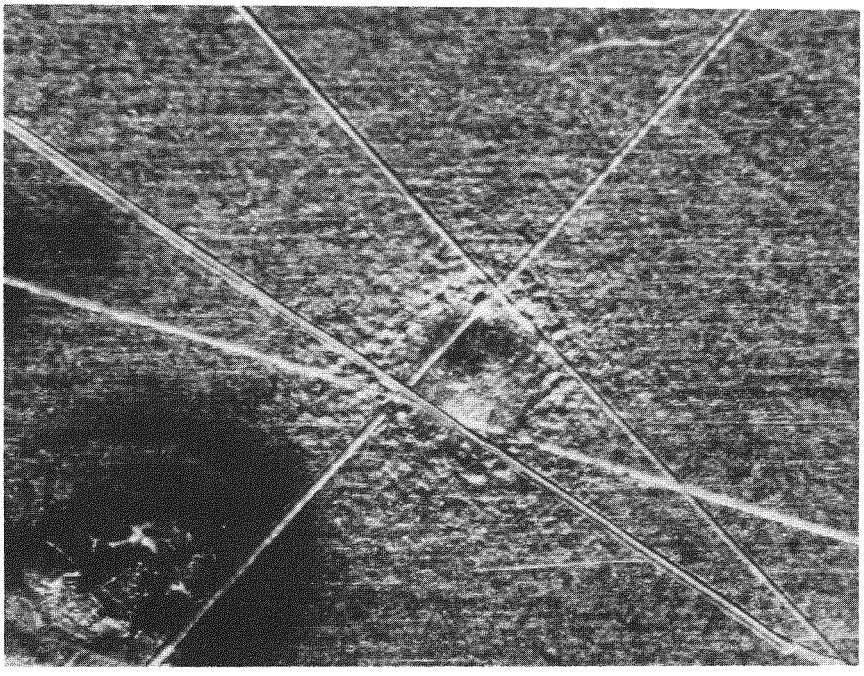

T=0 15X

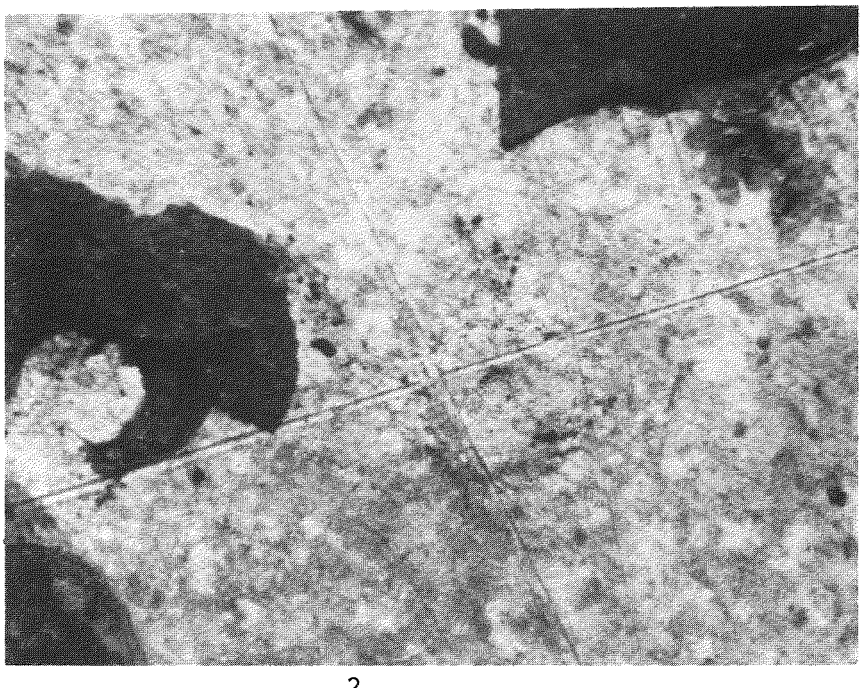

T=120 hrs. @ 30 ma/cm^2 15X

Figure E-8E. Stainless Steel 430

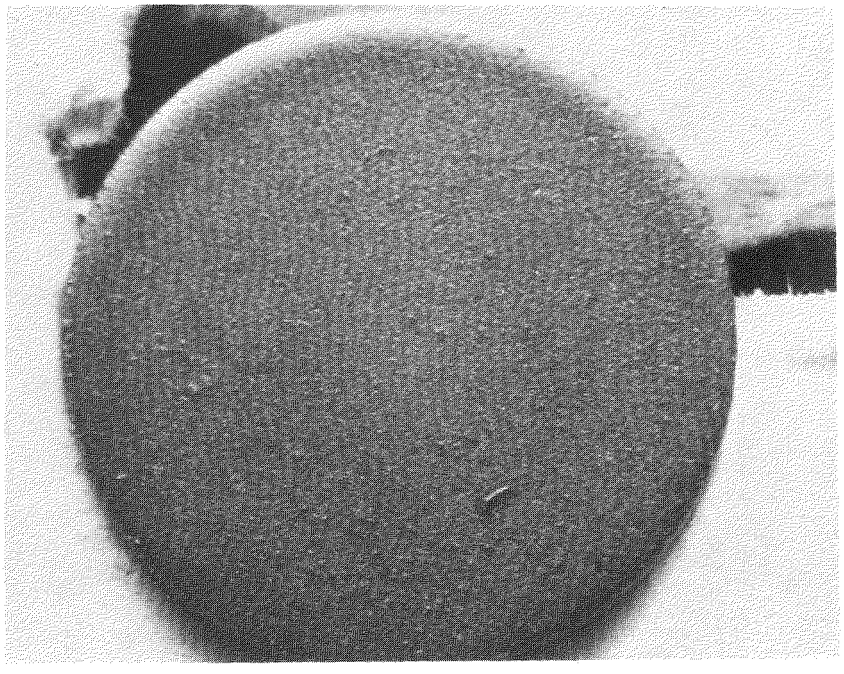

T=0 7.5X

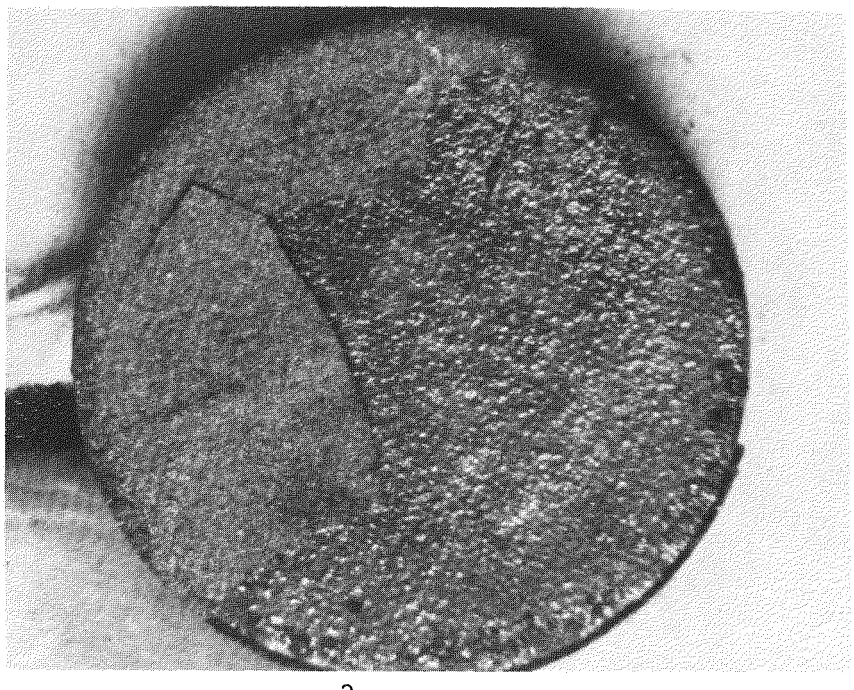

T=100 hrs. @ 30 ma/cm^2 7. 5X

Figure E-8F. MoS_2 Coated Aluminum

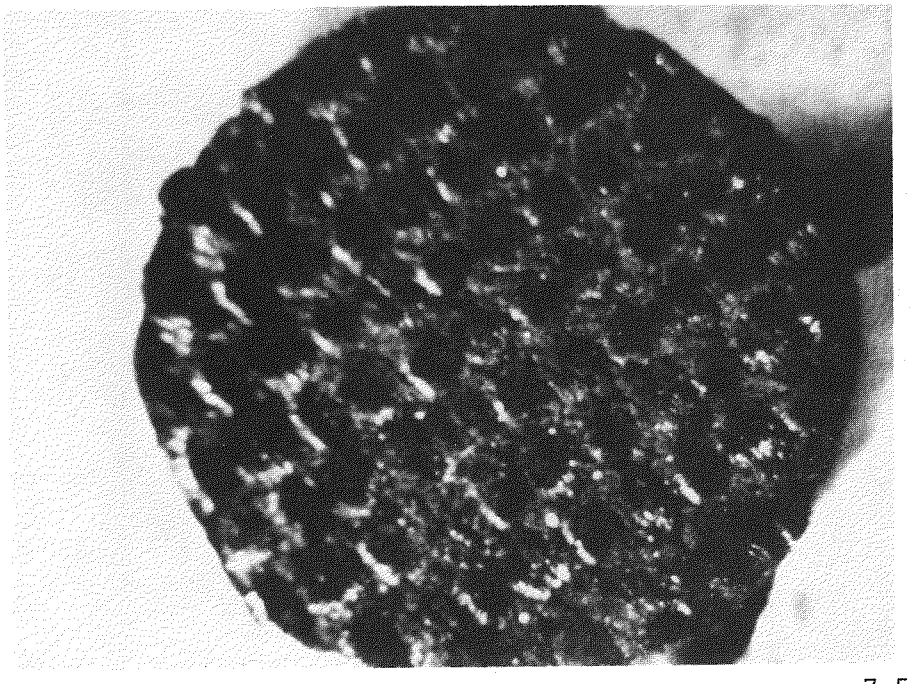

T=0 7.5X

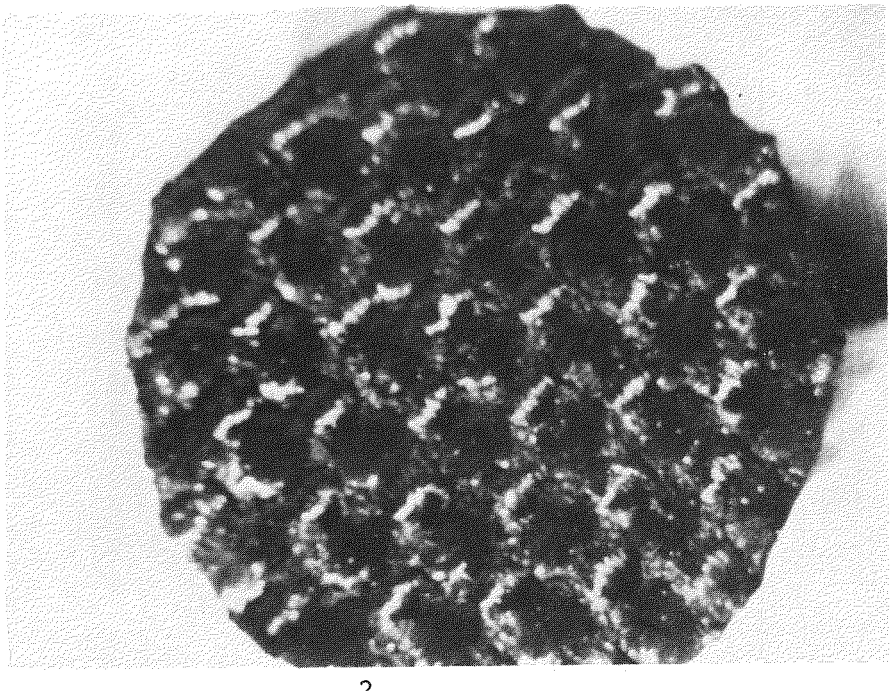

T=120 hrs. @ 30 ma/cm^2 7.5X

Figure E-8G. Graphite Cloth Bonded Aluminum

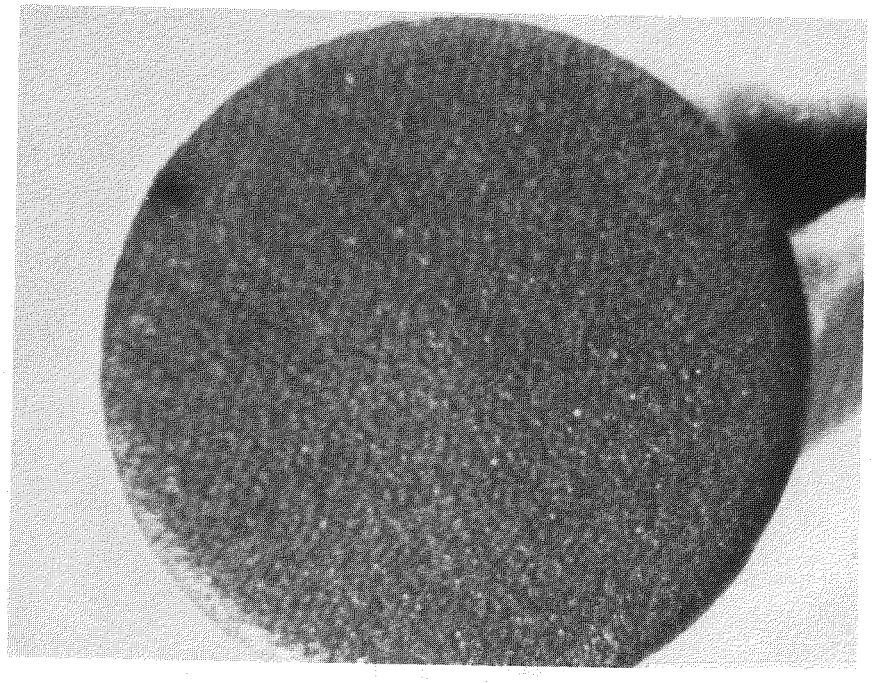

T=0 7.5X

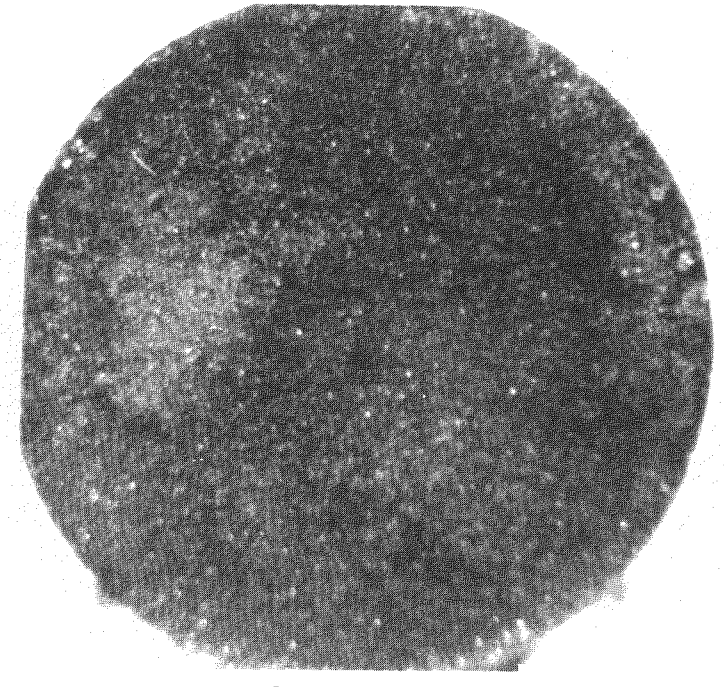

T=160 hrs. @ 30 ma/cm^2 7.5X

Figure E-8H. Resin Coated Aluminum

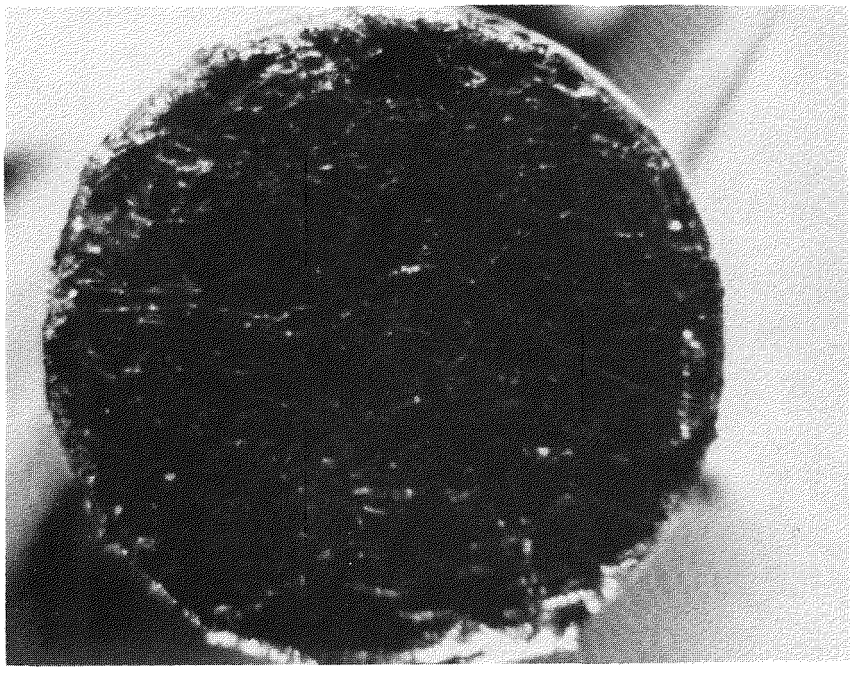

T=0 7.5X

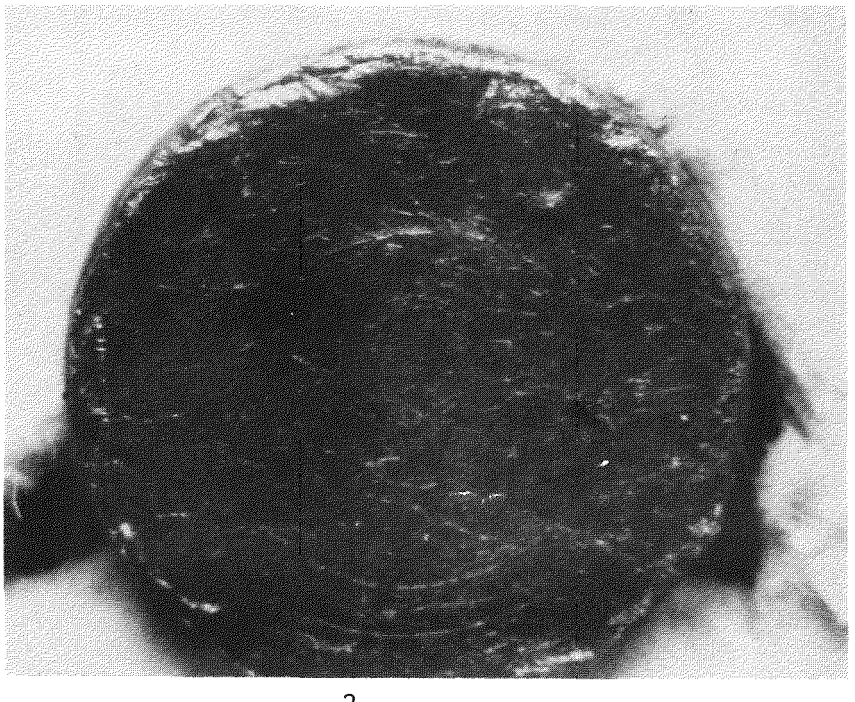

T=210 hrs. @ 30 ma/cm^2 7.5X

Figure E-8I. Grafoil Bonded Aluminum

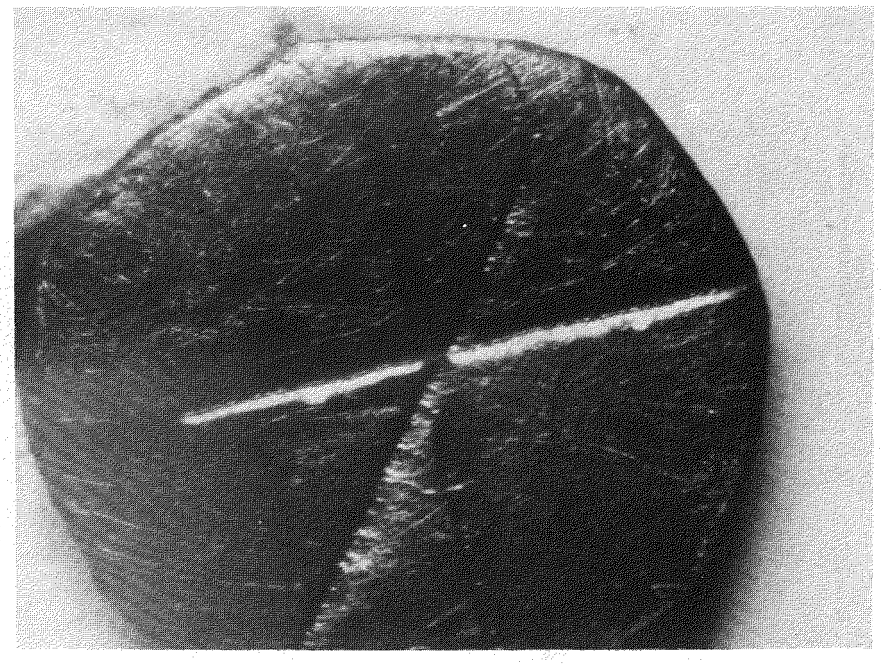

T=0 7.5X

T=300 hrs. @ 30 ma/cm^2 7.5X

Figure E-8J. Grafoil Bonded Steel

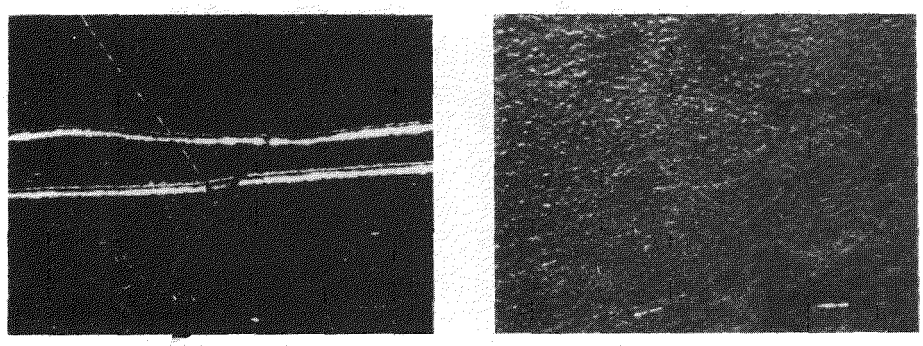

T=0 15X T = 20 HRS. AT 30 MA/CM^2 15X

Figure E-8K.

S.S. 347

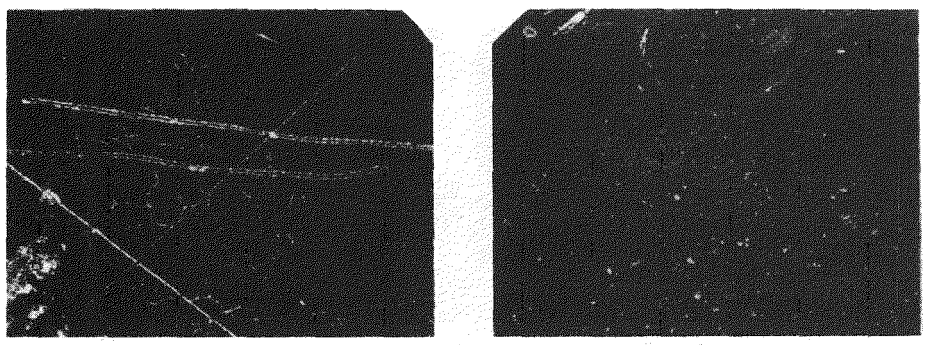

T = 0 15X T = 100 HRS. AT 30 MA/CM^2 15X

Figure E-8L.

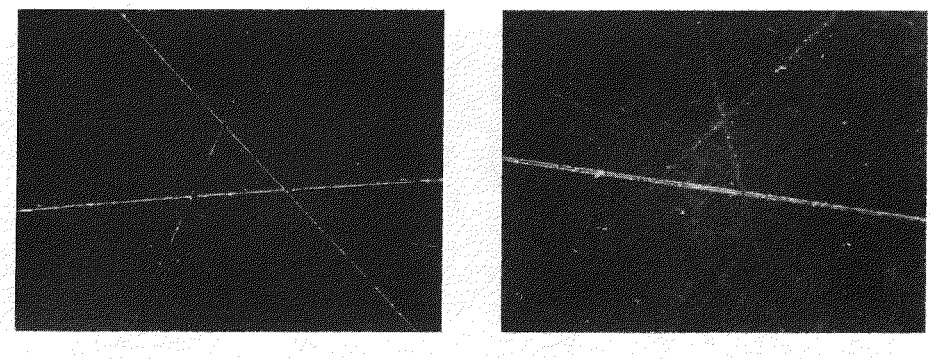

T = 0 15X T = 190 HRS. @ 30 MA/CM^2 15X

Figure E-8M.

SINTERED SiC

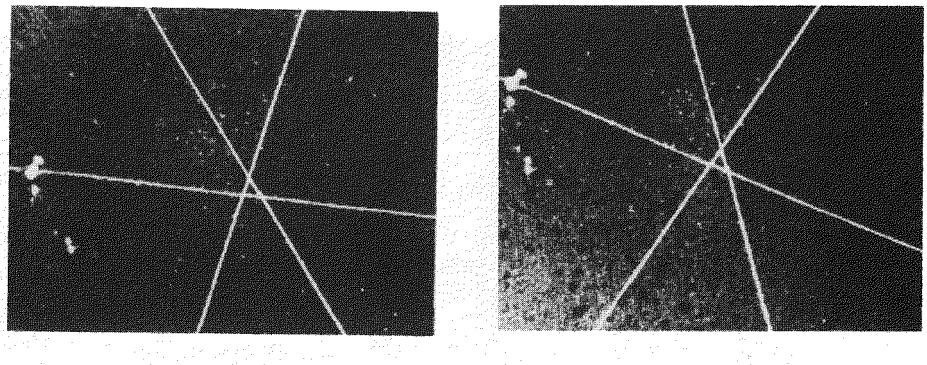

T = 0 15X T = 110 HRS. @ 80 MA/CM^2 15X

Figure E-8N.

Table E-4 summarizes sample treatment and weight loss data. Those samples (SCP-1, SN-1) exposed to molten sodium at the lower temperatures (350°C) showed no weight loss beyond experimental error. However, those samples (SCP-2) reacted for shorter times at the higher temperature (500°C) did show weight loss beyond experimental error.

No physical signs of surface degradation were observed in any of the samples studied. This was true for those samples which did exhibit weight loss as well as for those which did not exhibit weight loss.

Surface pores were prominent in high magnification (1000X) scanning electron micrographs for sample SCP-1; however, no evidence for cracking, flaking, grain boundary attack, or formation of surface reaction products was found. Low magnification optical micrographs for the Si_3N_4 sample also showed no evidence of attack; however, magnifications were too low to absolutely substantiate this point. In contrast, Singh and Tuohig[E-3] have reported cracking of Si_3N_4 under similar conditions.

Conclusions based on the data collected were that sintered SiC and HP Si_3N_4 are stable in contact with molten sodium for extended times at 350°C. Some degradation of these materials appears to take place at higher temperatures; however, further work is needed to clarify this point. Stability experiments with hot pressed SiC were terminated because of experimental problems. This prevented any comparison of the stability of the hot pressed and sintered SiC materials.

E-2 PERFORMANCE AND DEVELOPMENT OF ALPHA-TO-BETA SEAL

Factors which influence seal life become more important as the average cycle life of Na/S cells improves. The three different types of seals used in prototype Na/S cells are the mechanical clamp seal (header to container), the fill tube pinch seal (cold weld), and the header to beta-alumina seal. An investigation of failure modes associated with the standard hermetic header to beta-alumina seal was completed. Initiation of at least two common types of seal failure was found prior to cycling or exposure of the seal components to the cell reactants.

Table E-4

MATERIALS EVALUATION IN MOLTEN SODIUM

Sample No.	Sample Description	m_o	m_f	Treatment and Comments	Δm Wt. loss	$\frac{\Delta m_{\%}}{m_o}$
SCP-1	Sintered SiC	.29593g	.29588g	750 hrs./350°C/Na	.00005g	.02%
SCP-2	Sintered SiC	.29415g	.29391g	500 hrs./500°C/Na	.00024g	.08%
SC-1	Norton HP-SiC	.28133g	--	Ampule Cracked on Heating Experiments Terminated	--	--
SC-2	Norton HP-SiC	.28456g	--	Ampule Cracked on Heating	--	--
SN-1	HP Si_3N_4	.29412g	.29411g	750 hrs./350°C/Na	.00001g	.003%
SN-2	HP Si_3N_4	.29694g	.29432g	500 hrs./500°C/Na Oxidized Sodium	.00262g	.88%

E-2.1 Procedure

Several typical alpha-to-beta-alumina header seals were examined. A sketch of the seal details are shown in Figure E-9. Treatment ranged from cycling in a sodium sulfur cell for 190 cycles and 1250 hours to evaluation prior to cycling. Seal cross-sections were polished metallographically and examined by optical or scanning electron microscopy.

All seals examined had passed the standard mass spectrometer helium leak test during routine assembly. Seals were fabricated using Grade AL-995 (Western Gold and Platinum Co.) or A1075 (G.E.) alpha alumina, G.E. 1013 sealing glass and beta-alumina tubes of 1 cm O.D. Table E-5 shows nominal compositions and other pertinent properties of these materials. The methods and details of seal fabrication are described elsewhere[E-4]

E-2.2 Seal Examination

Table E-5 summarizes the various types of seal failure noted in this investigation. Widespread degradation of the glass and beta-alumina were observed after sodium exposure and is shown in the polished anode contact surface of Figure E-10. The crack network shown can be separated into radial and circumferential crack components. Radial cracks run roughly along diameters of the anode contact surface and may terminate at bubbles in the sealing glass or continue to run through the glass and into the alpha-alumina header.

Circumferential cracks run circumferentially about the beta-alumina and have not generally been observed in the alpha-alumina header. Circumferential cracks have been observed in sealed and unsealed portions of the electrolyte tube. This suggests that circumferential cracking of the beta may be related either to layering of the green deposit during electrophoretic deposition or else firing of the beta-alumina.

Polished seal cross-sections (uncycled) have shown massive cracks in the electrolyte tube wall. These planar (cross-sectional) cracks run either part or all the way through the electrolyte as seen in Figure E-11. Secondary cracks can appear in the glass seal between header and electrolyte as shown by the lower arrow in Figure E-11. Planar cracks may extend completely

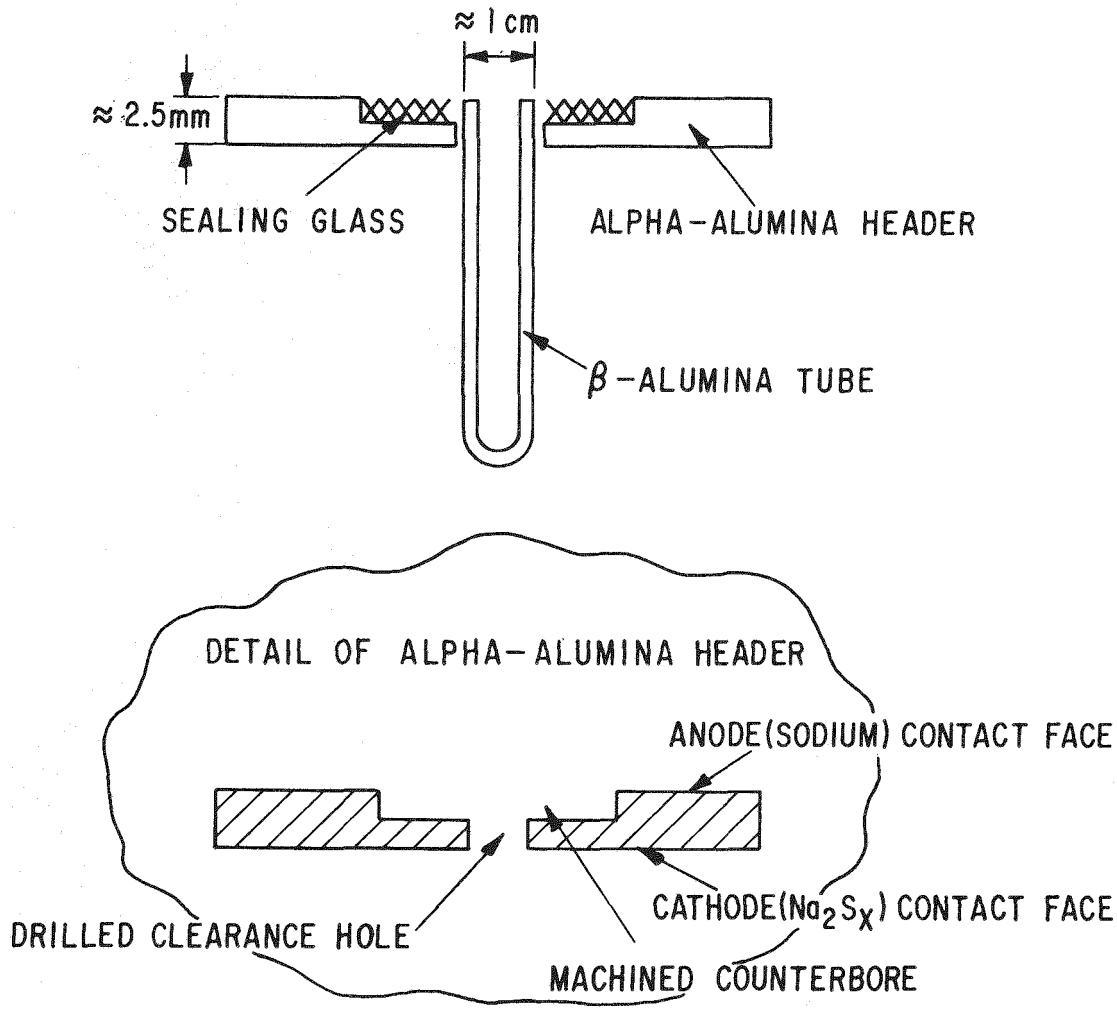

Figure E-9. Header Seal Geometry

Table E-5

COMPONENT FAILURE

Failure Mode	Header		Glass		Beta-Alumina	
	Cycled	Uncycled	Cycled	Uncycled	Cycled	Uncycled
Discoloartion	✓	X	✓	X	✓	X
Flaking	X	X	✓	X	✓	X
Radial Cracks	✓	✓	✓	✓	✓	✓
Circumferential Cracks	Infrequent		✓	✓	✓	✓
Planar Cracks	X	X	✓	✓	✓	✓
Bubble Formation	X	X	✓	✓	X	X
Chemical Reaction	X	X	X	X	✓	✓

Legend: ✓ ≡ Observed

X ≡ Not Observed

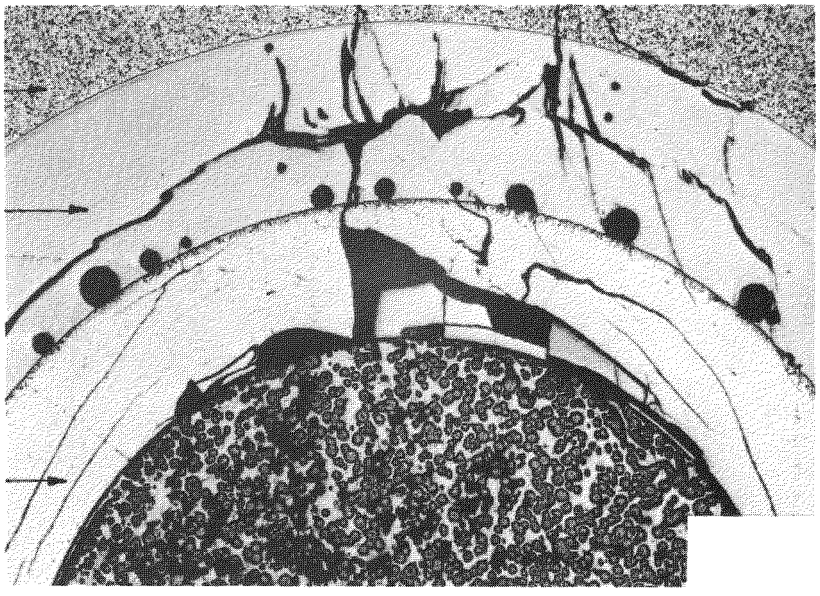

Figure E-10. Header Seal Failure

through the electrolyte and into or through the glass seal. Those planar cracks which penetrate the glass normally exit from the glass without extending into the alpha-alumina header. The abrupt change in direction of the crack tail circled in Figure E-11 is consistent with this observation.

Planar cracking can be explained by thermal expansion mismatch. During cool down the alpha-alumina header forces the β-alumina tube into compression (Table E-6). The tube wall thickness is inadequate to withstand the bend stresses at the cathode contact surface and therefore, cracking results.

The planar cracking phenomenon is undoubtedly a precursor for a commonly observed cell failure mechanism which results from a crack in the beta-alumina tube parallel to the seal area. In view of the previous discussion and the observation that these cracks can occur in uncycled cells one concludes that the above crack failure is related more to improper seal component geometries than to actual cycling.

Table E-6

SELECTED PROPERTIES OF HEADER SEAL COMPONENTS

	Header	Glass	β-Al_2O_3
Composition (Wt. Percent)	AL-995 99.5% Al_2O_3 ≃.2% SiO_2 Balance: CaO, MgO	GE #1013 SiO_2 50% B_2O_3 10% Al_2O_3 10% BaO 30%	Na_2O 7.2%, 7.2% MgO 1%, --- ZrO_2 1%, --- Al_2O_3 Balance, Balance
	A 1075 96% Al_2O_3 4% Additives (SiO_2, MgO)		
Thermal Expansion (cm/cm°C) 25°C - 300°C	AL-995 7.4×10^{-6}	5.4×10^{-6}	6.1×10^{-6}
	A-1075 $\simeq 6.1 \times 10^{-6}$		
Sealing Temp.	----------	1250°C+	----------

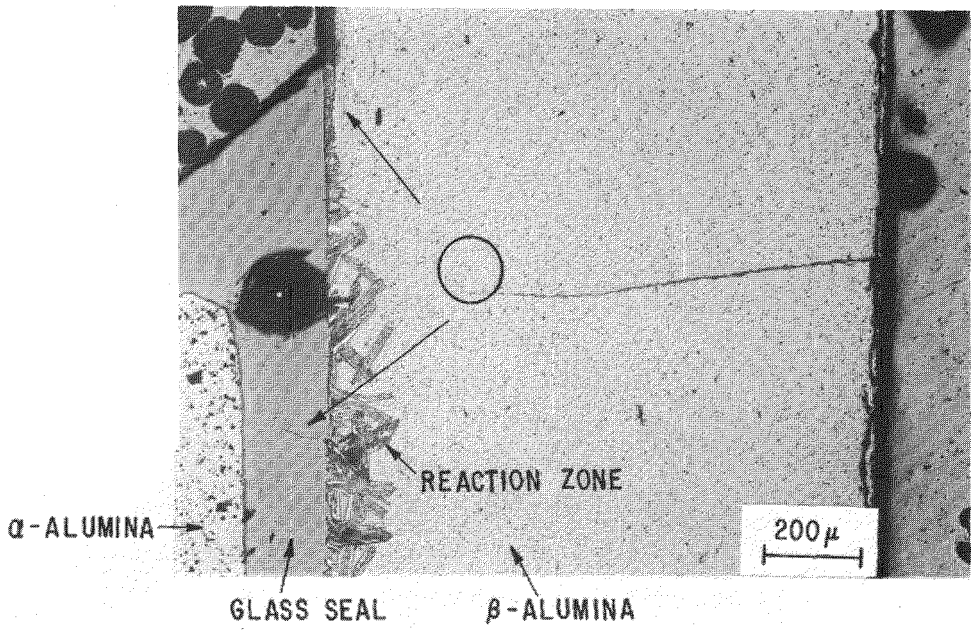

Figure E-11. Planar Cracking and Reaction Zone

Examination of seal cross-sections revealed the formation of a reaction zone between sealing glass and beta-alumina. Needle-like crystals as large as 20 μm x 150 μm form regularly where the sealing glass contacts the ceramic surface. This is shown in Figure E-11. The crystal size tapers at the edges of the reaction zone (Figure E-11, upper arrow). No reaction zone was noted between the sealing glass and alpha-alumina header.

Investigation of the chemical nature of the interfacial reaction zone was carried further by Navias[E-5] using microprobe analysis. The findings indicate that the needle-like crystals formed are α-Al_2O_3.

Figure E-12 shows a seal cross-section scanned with the microprobe. Each dot on the photograph corresponds to a data point shown in the composition profile of Figure E-13. The plot shows clearly that barium and silicon, present in the sealing glass, have diffused into the reaction zone. Barium

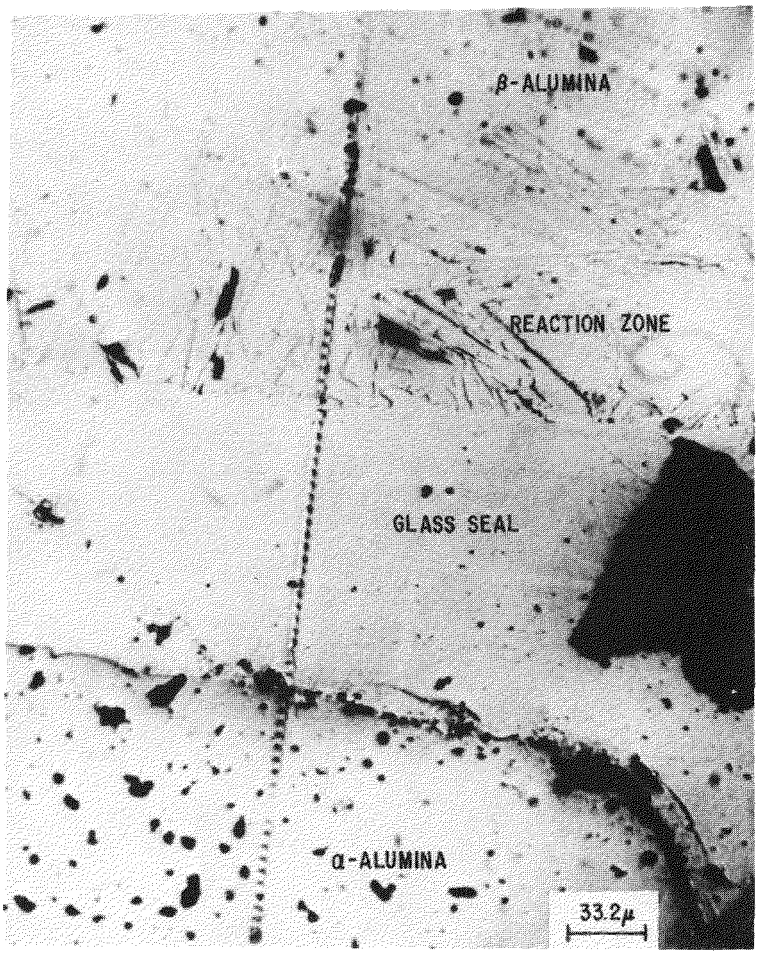

Figure E-12. Microprobe Scan of Header Seal Cross-Section

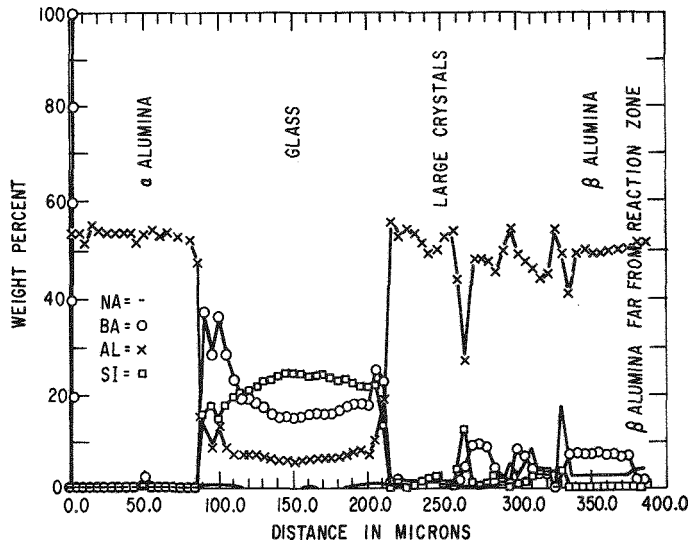

Figure E-13. Composition Profile of Header Seal Cross-Section

diffusion continued through the reaction zone and well into the beta-alumina. No barium was found in the reaction zone α-Al_2O_3 crystals.

Cracking of the header seal can occur previous to cell assembly while ultimate seal failure is generally determined by the anode (sodium) environment under cycling. It is clear that the production of long-life header seals (ten years) will require the development of a new sealing glass and component parts with better matched thermal expansion or else a new type of improved header seal.

E-3 EFFECTS OF CRYSTAL ORIENTATION ON ELECTRICAL PROPERTIES OF POLYCRYSTALLINE BETA-ALUMINA

The following is a computer study performed to estimate the relationship of the resistivity of single crystals and that of randomly oriented polycrystals, the effect of preferred orientation on resistivity, and the magnitude of the electric field enhancement due to adjacent crystal misorientation and exaggerated size grains.

There is essentially no conductivity in beta-alumina in the direction perpendicular to the crystallographic c-axis. Therefore, for optimum conductivity the ideal configuration for an electrolyte of beta and beta"-alumina would be a single crystal or polycrystals with the c-directions perpendicular to the flow of current. Because of the difficulties in fabricating single crystal beta-alumina and its tendency to cleave along the c-plane, this approach appears impractical. Therefore the electrolytes are generally composed of fine grained ceramics consisting of randomly oriented crystals.

Two major sources of increased electrical resistance result from employing polycrystalline material. One is resistance at grain boundaries, which has been considered separately[E-6], and the other is the effect of random orientations and interconnections called the tortuosity. The quantitative determination of all these resistance losses is basic to the problem of ceramic electrolyte life in applications such as Na/S batteries. For instance, if a major fraction of the ceramic resistance is at grain boundaries, the electric fields can locally be extremely high, resulting in breakdown and failure of the ceramic. If excessively large fields exist near exaggerated size grains in the microstructure, the same electric failure could result.

The work presented here is a Monte Carlo computer study of current flow in simple geometric models of a polycrystalline ceramic with conducting planes such as beta-alumina. The first problem was to determine the expected resistivity of a polycrystal in comparison with that of oriented single crystals. This was undertaken so that the crystal resistivity of an assembly of randomly oriented grains determined in the previous studies[E-6] could be compared on an absolute basis with experimental single crystal resistivity

values. The second purpose of the work was to obtain a quantitative value for the effect of any preferred orientation in our ceramics on the electrical resistivity. Normally our ceramic is in the shape of closed end tubes and resistivity is measured in the longitudinal direction. However in Na/S cells, the resistivity of importance is that in the radial direction, it is important to assess the magnitude of any preferred orientation effect. The third purpose of the study was to gain some insight as to the effects of large or exaggerated size grains within the ceramic, because during firing beta-alumina is prone to develop some very large crystalline grains in a matrix of fine grains. This is often called bimodal or duplex microstructure.

E-3.1 Approach

The first step in obtaining a mathematical solution for the effects of random orientation of grains is to assume a geometrical model which fills space. Figure E-14 is the simplest of such models, in which each grain is a cube in simple cubic packing. An exact solution for the resistivity of such a three dimensional matrix is prohibitively tedious, being approximately an n^{th} order equation where n is equal to the number of grains. On the other hand it is very simple to set a lower limit to the resistivity through any plane of a random distribution of orientations, independent of the model for the grain shape. This is illustrated in Figure E-15, which represents an infinitely thin cut through a conductor such as beta-alumina. The resistivity through such a plane can be shown to be equal to $4/\pi$ times the resistivity of the crystals in the direction of the conducting planes. This can only be a lower limit however, because the infinitely thin plane avoids the problem of one crystal blocking the contribution of the next crystal "down stream", when such slabs are placed on top of each other.

The solutions obtained in this work were based on two different three-dimensional resistor networks in the following two sections.

E-3.1.1 Simple Cubic Model Random Orientation

Figure E-14 shows a two dimensional representation of simple cubic packing with the resistor network for the x and y coordinates of two of the cubes. Each, which represents an oriented grain, consists of six resistors radiating

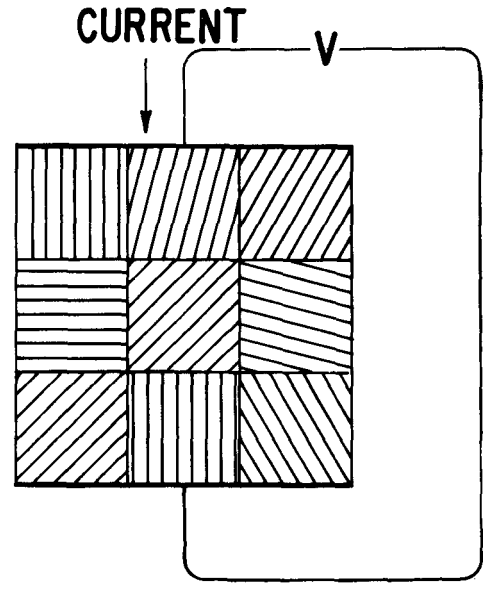

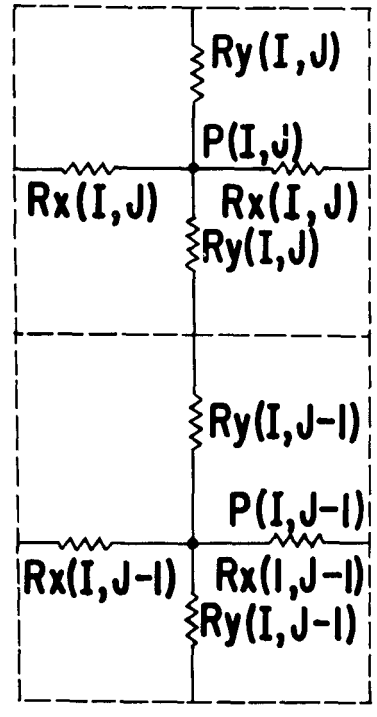

$$\frac{r_{POLY}}{r_{SINGLE}} = 1.356 \pm .014$$

Figure E-14. Resistor Network for a Square Array

from a point in orthogonal directions. The crystal property of conduction only along planes was simulated by the values assigned to each resistor. For example, if the conducting plane is perpendicular to the z direction, Rz would be set equal to infinity and Rx and Ry equal to unity. For other orientations, the values of Rz, Rx, and Ry are chosen by the relationship, $R^i = 1/\text{Sin}A^i$, where A^i is the angle between the crystallographic c-axis and the x,y, and z directions of the model. These resistors are connected at the free ends to other resistor networks representing adjoining cubes to make "polycrystals". In this study polycrystals up to 11 x 11 x 11 cubes were studied.

In order to assign values for each cube, points were placed within a box at random. X,Y, and Z coordinates were chosen for each point using a random number computer subroutine retaining only those points falling within a hemisphere of unit radius. The projection from the center through each point was taken as the c-axis for each of the random crystals. The value of each resistor in the network model was then set by the size of the angle between the corresponding resistor directions and the c-axis.

With the resistor value determined, boundary conditions were imposed with fixed potentials at the two ends in contact with hypothetical electrodes. Zero current in or out the other four sides was assumed. The equilibrium potential of each crystal point (six resistor junction) was determined by an iterative process which involved scanning each point and setting the net current in equal to the current out. After about one hundred iterations for a 9 x 9 x 9 matrix, potential values differed by less than a few tenths of a percent from those obtained with 500 iterations. With sufficiently accurate potentials, all the pertinent parameters such as potentials at each points, currents through each branch, and overall resistance were readily determined.

While the results will be discussed later, it is important to point out an obvious deficiency of this model. In Figure E-15, the center square is illustrated with the conducting planes inclined at 45° to the electrodes. If the overall current is from top to bottom, current would be diverted to the left in the central grain; however, the resistor network of the model would set each segment of the center cube at a value of 1/cos 45°. Therefore the

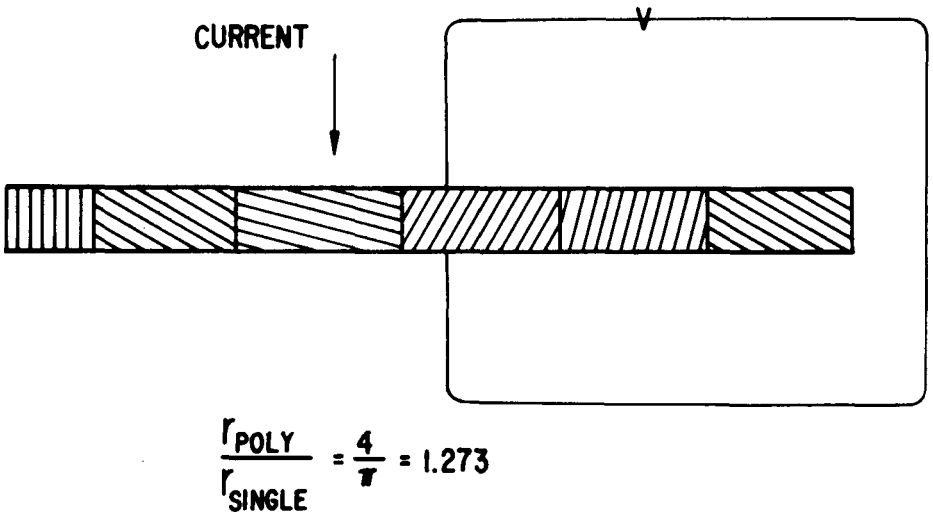

Figure E-15. Infinitesimally Thin Cut Through a Polycrystal

impedance and resultant current from the top to the right is the same as it is to the left. Because of this lack of assymmetry, a second geometrical model was considered.

E-3.1.2 Duodecahedral Model

Figure E-16 shows a two dimensional close-packed structure of hexagons and a corresponding two dimensional resistor network for one of the hexagons and its neighbors. A packing of duodecahedrons is an extension of the two dimensional hexagonal arrangement into three dimensions. This corresponds to the face-centered close-packed crystal structure. In this structure the resistor network consists of twelve resistors, rather than six for the simple cubic case, emanating from the central potential point of each crystal or grain in the model. Figure E-17 shows the resistor network representing two adjacent duodecahedrons. Resistor network Maxwell solutions for individual twelve membered units showed that the directional properties lacking in the simple cubic model were inherent in the duodecahedral model. The method used in the computer solution was similar to the cubic model, but algebraically more complex.

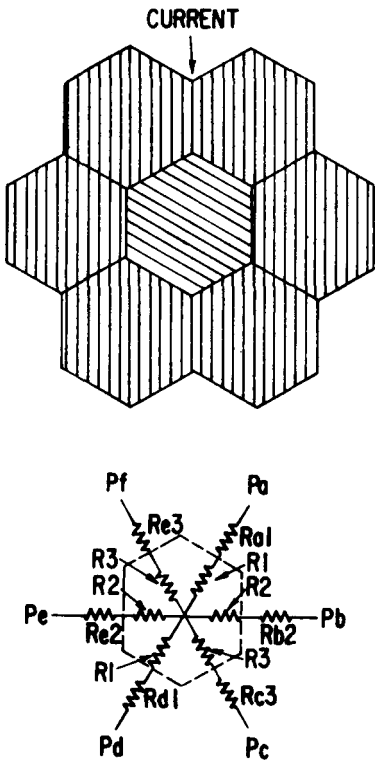

Figure E-16. Resistor Network for a Hexagonal Array

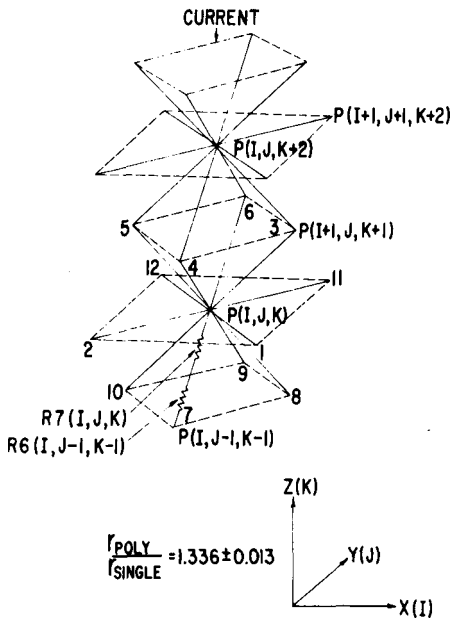

Figure E-17. Resistor Network for Two Adjacent Duodecahedrons

E-3.1.3 Preferred Orientation

The method of expressing preferred crystallographic orientation as determined by x-ray pole figure analyses is basically very similar to the technique employed here to synthesize a preferred orientation for the computer model. For the random models, the points in a box which were chosen were those which fell within a sphere and that generated the random directions for the c-axis. A bias can be imposed by choosing only those points which fall within a spheroid. Therefore, for example if a ceramic tube has a larger than random number of crystals parallel to the tube axis, the x-ray results may be expressed as a 10% excess orientation in this direction. This is equivalent to choosing intensities which vary as the axes of a prolate spheroid with the major axis 10% longer than the minor axis, the former being perpendicular to the surface. This is also equivalent to choosing random numbers which fall within a prolate spheroid; the method used for the computer programs simulating preferred orientation. No other modifications to the computer programs were required.

E-3.1.4 Large or Exaggerated Grains

The approach to simulate exaggerated grains within the structure was merely to allow the program to choose random orientations, and then "manually" change a slab of the units to an aligned orientation. Because, as will be seen, the resistivity for an array of randomly oriented crystals is only a little larger than that of perfectly oriented single crystals, the most significant studies were those with slab oriented in the non-conducting direction, thus blocking the current path.

E-3.2 Results and Discussion

All three approaches to fixing the tortuosity factor, the ratio of the resistivity of randomly oriented crystallites to that of a single crystal oriented in its conducting directions, led to surprisingly low values. The calculated lower limit for the above ratio is $4/\pi$ or 1.27. The simple cubic model gave

1.36*, and the face centered cubic (duodecahedron) model, 1.34. When the cubic model calculation, which was done first, resulted in such a low value, it was thought that the lack of directionality was responsible. Work on the duodecahedronal model was pursued when it was determined that the directional property was inherent in it. After this model led to an even lower value, it appeared that the directionality element is not very important. Therefore the best estimate of the tortuosity factor lies between 1.34 and 1.36.

Another significant result from both random orientation models relates to the maximum potential difference between adjacent crystals. In a sample of 4 runs on the simple cubic model with 11 x 11 x 11 cubes, the largest potential difference between any two cubes was only 40% greater than if the resistivity were completely homogeneous (three dimensional conductors). Since each of the computer runs requires a considerable process time, it was judged that a sample of over 5000 potentials was sufficient to give a good estimate of the maximum potential difference between uniform size crystals.

The results of the preferred orientation study were obtained by correlating the excess x-ray intensity, in reference to the ceramic tube geometry, to the eccentricity of the spheroid used to choose random numbers for the computer program.

The simple cubic model was chosen over the face centered cubic (duodecahedron) model for the preferred orientation study because it yields the exact correct limits for the extreme case of a single crystal. Note for the hexagonal model on Figure E-16 that resistor network requires a zig-zag current flow in certain directions even when the conducting planes are perfectly aligned or perfectly misaligned to the potential direction. Therefore the correct limiting

* The results for the simple cubic and face-centered cubic models were obtained with ten computer runs, each on 11 x 11 x 11 matrices, using different sets of random numbers for each run. The precise values obtained for the tortuosity factor were 1.36 with a standard deviation of 0.014 for simple cubic model and 1.336 with a standard deviation of 0.013 for the face centered cubic model.

values of unity or infinity cannot be expected for extremes of preferred orientation with this model. On the other hand when complete orientation of the crystals is given as input to the program for the simple cubic model, the results are the same as for a single crystal oriented in the preferred direction.

The comparison of interest as pointed out earlier is that between the resistivity in the longitudinal direction of a ceramic tube and that for the radial direction which is the direction of importance when the tube is used in a cell. X-ray results showed an excess intensity of 10% basal poles in the radial direction with a maximum undertainty of $\pm$300%. The preferred orientation is such to lead to an underestimate of radial resistance from longitudinal resistivity measurements. The proper comparison to be made for this situation is that for the longitudinal resistance perpendicular to the major axis of porlate spheroids, and radial resistance parallel to the major axis of prolate spheroids.

Figure E-18 shows two curves for the ratio of polycrystalline ceramic resistivity to oriented single crystal resistivity as a function of the preferred orientation.* The latter quality is expressed as the spheroid axis ratio. It can be seen that the two curves approach the proper limits. The upper curve corresponds to the relative resistivity in the high resistivity direction. As the axis ratio of the spheroid increases, log of the resistivity ratio linearly approaches infinity. The lower curve represents the resistivity perpendicular to the preferred c-direction. The log of the resistivity ratio approaches zero asymptotically. The difference in resistivity ratios obtained at any c-axis/a-axis value represents the difference in resistivity to be expected between the longitudinal and radial directions. The vertical

*Each of the points on the graph represents between 5 and 10 separate computer runs on the 11 x 11 x 11 simple cubic model. The bar widths given for each point represent values of plus and minus one standard deviation computed for the number of determinations made.

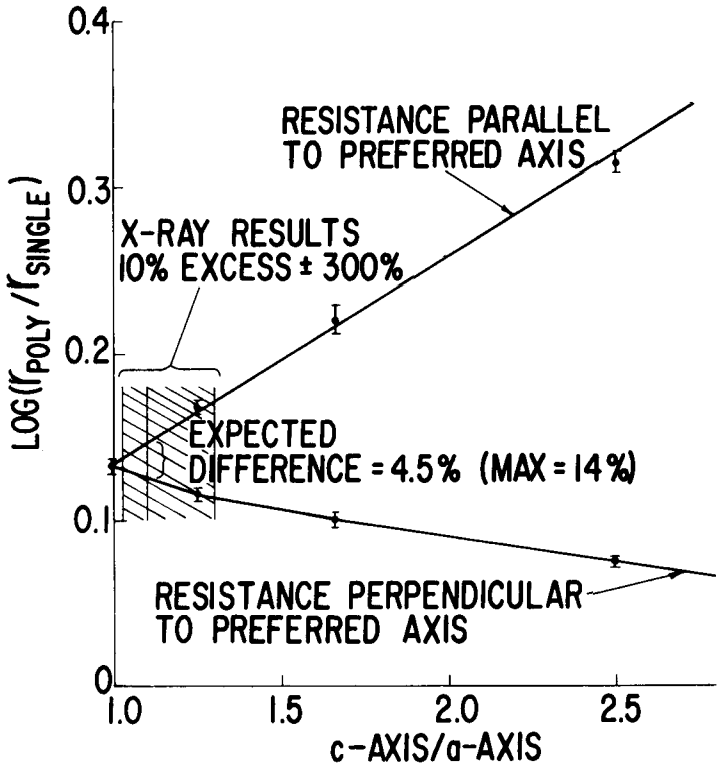

Figure E-18. Plot Showing Effect of Preferred Orientation on Resistivity

bars labeled "x-ray results" are given at the estimated limits of preferred orientation as determined by x-ray diffraction of our beta-alumina tubes.† From the vertical difference between the curves it was calculated that the longitudinal to radial resistivities should likely differ only by 4.5% and at most by 14%.

The effects of large electrical fields near the isolated large crystals which often occur in sintered beta-alumina polycrystalline ware are probably an

†The value of 10% excess (±300%) over random orientation was obtained throughout the thickness of the electrophoretically formed and then fired ceramic tubes. No difference was noted between values specifically obtained by directing the x-rays at the inner surface, or at an internal surface.

important reason for the limited life exhibited by some ceramic electrolyte tubes. More often than not when a conical pit is observed to have penetrated the surface of a failed electrolyte tube, a large grain can be observed by reflected light at the base of this pit.

Figure E-19 represents the simple cubic model used to simulate the effect of exaggerated grain growth in beta-alumina. A 9 x 9 x 9 matrix was used for most of the examples, and most often the computer printout presented potential differences between any two adjacent cubes although the currents between cubes were sometimes also printed out. The figure shows a 5 x 5 slab of crystals oriented with the conductive planes perpendicular to current flow.

On the exploded view of Figure E-20 the potential differences are given between selected cubes. The values have been normalized to 1.0 for the average potential difference between two cubes, or more exactly to the potential difference if all cubes were completely homogeneous. It can be seen from the values obtained that as much as 70% of the voltage applied to the entire sample can appear across the one unit wide exaggerated "grain" in its center portion, which corresponds the point shown to the rear left corner of the 5 x 5 x 1 slab. Relative to a ceramic this would be a very large crystal, with a width approximately equal to the ceramic wall thickness. Although the ceramist tries to avoid such large crystals, they sometimes do exist in not too well controlled beta-alumina ceramics.

The computer approach to examining field effects around large crystals while valuable in one major aspect is nonetheless limited in another. It is noteworthy that examination of the cube-to-cube potentials in the computer printout shows a remarkable uniformity in potential distribution along the face of 5 x 5 x 1 crystal slab in a 9 x 9 x 9 matrix. This is quantitative evidence that the polycrystalline field disturbance caused by the presence of crystals which conduct anisotropically is quite small. However, the method is very limited in studying the potential effects around large crystals because extremely large three dimensional matrices would be required to model the bimodal crystal structures observed in ceramics such as beta-alumina, because the grain size ratio is so large. The deterrent to work is of course the cost

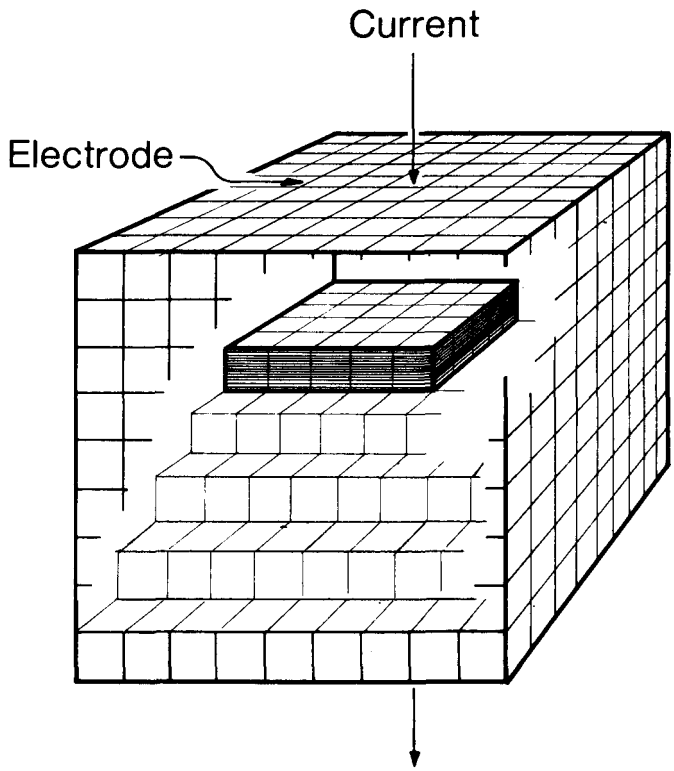

Figure E-19. Drawing Representing a Large, Oriented Thin Crystal in a Randomly Oriented Array of Small Crystals

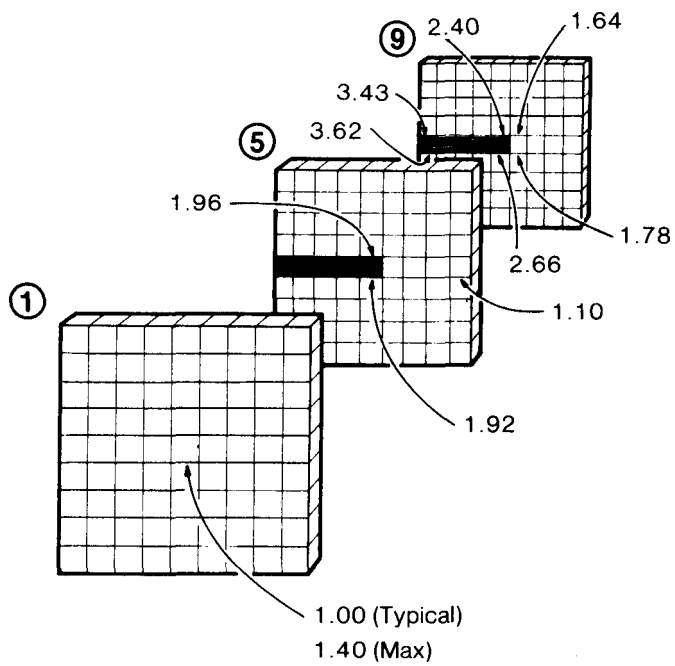

Figure E-20. Exploded View of Figure E-19 Showing Relative Electric Fields at Several Points

and the limited computer capability. However the computer approach does show that other methods are perfectly adequate to handle the field distribution problem. For example the fields along the surface of a large grain oriented as shown in Figure E-20 could be adequately modeled by an insulating slab in a homogeneously conducting media. On the other hand the computer Monte Carlo method is uniquely suited for examining such problems as single to polycrystalline resistivity ratios and the effects of preferred orientation. It is perhaps the only practical approach to solution of these relevant problems.

E-4 STABILITY OF BETA-ALUMINA AT HIGH PRESSURE AND TEMPERATURE

Several years ago exploratory experiments were initiated to synthesize dense compacts of beta-alumina in high pressure "belt" equipment for subjecting materials to very high pressure and temperature. Beta-alumina was expected to be stable since the room temperature conductivity had been measured at Ford Motor Company Research Laboratory and found to be constant up to 4 Kb. It was discovered at that time that beta-alumina decomposed above 600°C at pressures above 10 Kb.

This unexpected decomposition at relatively low pressure and temperature may be important with respect to the stability of beta-alumina at high temperature in an environment of high electric stress. Measurements now have been made which approximately delineate the P-T stability field of beta-alumina and magnesium stabilized beta"-alumina. Comparison of the two common modifications of beta-alumina may help select the optimum composition and structure for application in sodium-sulfur batteries.

Beta-alumina and beta"-alumina were subjected to pressures up to 50 Kb and to temperatures from room temperature to 1200°C. Above 525°C and 10 Kb beta-alumina decomposes into α-Al_2O_3 and $NaAlO_2$. Magnesium stabilized beta"-alumina similarly decomposes under pressure. The products are α-Al_2O_3, $NaAlO_2$, and $MgAlO_4$. The critical temperature for decomposition of beta"-alumina is about 75° higher than beta-alumina.

The driving force for reaction is decrease in molar volume of the reaction products with respect to the reactants, about 22.7 cc $mole^{-1}$ for beta-alumina and 14.3 cc $mole^{-1}$ for magnesium stabilized beta"-alumina.

The pressure dependence of the rate of decomposition of beta-alumina at 600°C was measured. Interpreting the results by the usual theory for thermally activated processes, and assuming the enthalpy of activation independent of pressure, the activation volume is $\Delta V^*=-3.96$ cm^3 $mole^{-1}$. The negative sign is unusual since ΔV^* for most materials is positive. The temperature dependence of the rate of decomposition of beta-alumina at 20 Kb is unusually low, corresponding to enthalpy of activation $\Delta H^*=5000$cal $mole^{-1}$. Within the broad limits of experimental error of these measurements it equals the activation energy, $E=3700$cal $mole^{-1}$, of sodium diffusion in beta-alumina. Above 600°C and 10 Kb the P-T line which defines the critical pressure and temperature for decomposition agrees with the Clausium-Clapeyron equation for change in melting point with pressure.

A proposed model to explain these results is that the rate determining step in decomposition is diffusion of sodium, and the decomposition curve is determined by the pressure dependence of the melting point of the two-dimensional liquid conduction plane. This agrees with neutron diffraction and nuclear magnetic resonance which show the distribution of sodium in the conduction plane is liquid-like at 600°C.

Beta-alumina is metastable at high pressure and temperatures below 600°C. It did not decompose at room temperature, even when held at 50 KB for 6 hours. Specimens subjected to high pressure at low temperature nevertheless underwent structural changes. The x-ray diffraction lines were broadened, which may indicate incipient decomposition. Extrapolation of the P-T decomposition line suggests beta-alumina is metastable at 350°C and pressures above about 8 Kb. This pressure corresponds to critical electric stress of 18^8 V cm^{-1}, comparable to the dielectric strength of most ionic solids. Accordingly, this probably is not an important mechanism for electrochemical decomposition of beta-alumina during cycling sodium-sulfur cells. A precautionary note is that the measurement of pressure below 10 Kb in the belt apparatus is relatively inaccurate and further study would be necessary to establish accurate values of critical pressure for decomposition at moderate temperature.

E-5 COOPERATIVE STUDIES ON BETA-ALUMINA

For several years investigations have been underway to determine the mechanism of sodium transport and the factors which limit conductivity and stability in the beta-aluminas. Some of these are cooperative studies with colleagues at the State University of New York in Albany and at the Brookhaven National Laboratory, carried out with nuclear magnetic resonance and neutron diffraction apparatus not available at Corporate Research and Development. These studies have led to new concepts about the physical properties of beta-alumina, some of which are relevant to sodium-sulfur battery development and are mentioned briefly here. Individuals who have contributed to this research are O. Muller (then CRD), H.S. Story, I. Chung, W. Bailey, S. Glowinkowski, F. Reidinger (SUNYA), S. LaPlaca, J. Axe, L. Corliss, J. Hastings (BNL).

E-5.1 Sodium Motion in Beta-Alumina

Disorder and motion of sodium in beta-alumina crystals have been studied by neutron diffraction and nuclear magnetic resonance. The principal objectives were (1) to determine the preference of sodium atoms for different sites in the conduction plane as a function of temperature, (2) the energy barriers between sites, (3) the mechanism of sodium transport. This information is needed to assess the theoretical limit of conductivity at low temperature, and provide guidance for crystal-chemical modification of properties. There are three sites for sodium: Beevers-Ross (BR), anti Beevers-Ross (aBR), and mid oxygen (mO). The sodium distribution was measured from 80°K to 873°K. The mechanism for sodium transport appears to be thermally activated hopping from BR to mO, then to aBR sites, the last step being rate determining. Above 120°K all sodium ions participate in the motion, at least on a time scale longer than 10^{-5} seconds.

E-5.2 Defects in Beta-Alumina

An unexpected result of the neutron diffraction study of beta-alumina was the discovery of large concentrations of Frenkel defects in the spinel block. These are bound pairs of aluminum vacancies and aluminum interstitials and their importance lies in that they determine sodium disorder and transport in the conduction plane. The defect has the formula

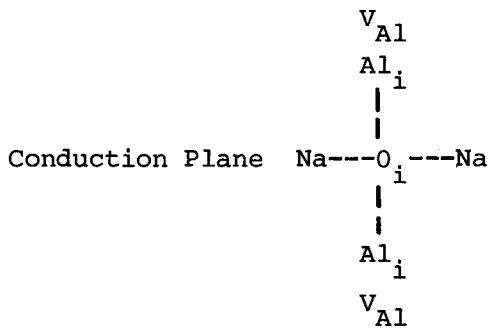

where $V_{Al}Al_i$ is an aluminum vacancy-aluminum interstitial, O_i is an oxygen atom in the conduction plane and two Na atoms are loosely bound to the complex. The presence of interstitial oxygen in the conduction plane resolves the controversy whether non-stoichiometric excess sodium in beta-alumina is compensated by aluminum vacancies or interstitial oxygen. Of great importance are the implications of O_i to sodium ion conduction since it occupies positions which block some channels. A model has been proposed based on this defect which explains the effects of monovalent and divalent additives on conductivity in beta-alumina.

E-5.3 Stabilization of Beta"-Alumina

Beta-alumina and beta"-alumina are both excellent conductors of sodium and both are under active development by different groups for application as solid electrolyte separators in sodium-sulfur batteries. The choice between them depends on their relative conductivity, stability, and ease of fabrication. An unusual feature of beta"-alumina is that binary compositions are unstable and ceramics made from them are mixtures of beta-alumina and beta"-alumina. The addition of Mg^{2+} stabilizes the beta" structure and an objective of this research was to establish the reason for stabilization. It was found by neutron diffraction that magnesium substitutes for aluminum in only one of four kinds of sites. The principal reason for stabilization appears to be reduction of local strain by ion substitution. This relates directly to the decomposition of beta-alumina and beta"-alumina at high pressure, and could lead to the development of compositions with superior stability.

E-5.4 Rotation Diffusion of NH_4^+ Ions in Beta-Alumina

This research had its origin in an unsuccessful attempt to measure sodium diffusion in beta-alumina by inelastic neutron scattering. Inelastic neutron scattering can be used to observe diffusion in solids, and to estimate diffusion coefficients in favorable cases. The incoherent neutron scattering cross-section of hydrogen is extremely large and since NH_4^+ contains four hydrogen atoms, it is a unique ion for study by inelastic scattering techniques. Accordingly the sodium in beta-alumina was ion exchanged with ammonium ions and the inelastic scattering measured. The experimental results show that the NH_4^+ group executes 120° jumps at random about the four 3-fold axes of the tetrahedron. The residence time between translational diffusion jumps places an upper limit to the NH_4^+ diffusion coefficient between 2.5×10^{-6} and 10^{-5} at 200°C. This technique could provide information about sodium in beta-alumina if inelastic neutron scattering was measured on large crystals or with a higher flux reactor.

E-6 FUNDAMENTAL STUDY OF BETA-ALUMINA SINTERING

General Electric Company is supporting a study of the fundamentals of beta-alumina sintering in the Ceramics Division at the Massachusetts Institute of Technology. This project is under the direction of Professor R.M. Cannon with experimental work carried out by Mrs. Umma Choudhury, a post doctoral research associate. It has as its objective an understanding of the basic kinetic processes involved in the sintering and microstructural development of beta-alumina. An indication of the diffusivities which control the solid state sintering rate will be sought. Systematic studies of the effects of controlled additions on the sintering rate and on grain growth will be carried out. Both beta and beta"-alumina are under study. Pre-reacted powders are used to eliminate complexities associated with liquid phase sintering.

Work up to this time has been concerned mainly with the preparation of reactive beta-alumina powder which will not give rise to liquid phase sintering. A number of methods have been examined: reaction of alum with sodium oxalate, reaction of high purity alpha-alumina with sodium carbonate, freeze-drying, and centrifuging of stable suspensions of XB-2 beta-alumina. The

last has been the most successful. The finest size particles, the last to settle from suspension, sinter to nearly full density in a short period of time at temperatures less than 1600°C.

E-7 SUPERIONIC CONDUCTOR CONFERENCE

An international conference, "Superionic Conductors: Chemistry, Physics, and Applications", was held at the General Electric Corporate Research and Development, Schenectady, New York, May 10-12, 1976. Members of the team that is developing sodium-sulfur batteries made major contributions to this Conference by planning, organizing, running, and presiding at the meetings. The staff also contributed important technical papers to the Conference on conductivity, stability, structure, and physical properties of beta-alumina. The Conference Proceedings will be published by Plenum Press, probably in late 1976.

The Conference was supported and co-sponsored by the Air Force Office of Scientific Research, American Physical Society, Electric Power Research Institute, Electrochemical Society, General Electric Company, and National Science Foundation. It was conceived in response to rapidly growing world wide interest in the topic of superionic conductivity in solids. The subject has become a popular area of research in the scientific community. This is due largely to the recognition of the exceptional high ionic conductivity in beta-alumina, and its implication to high energy and high power density electrochemical systems. A primary objective of the Conference was to bring together engineers, experimental solid state scientists, and theorists for critical discussions of the factors that determine and limit ion conduction in solids.

The sessions were attended by about 250 people, of whom 185 were registrants. The balance were visitors from the Research and Development Center, State University of New York at Albany, and Rensselaer Polytechnic Institute. There were 77 papers presented in a three day meeting. Approximately 21% were in technology, 56% in experimental solid state chemistry and physics, and 23% in theory. Principal sessions were devoted to the beta-aluminas, silver conductors, oxygen conductors, and new superionic conductors.

The Conference was uniformly judged successful. Novel features of the meeting that contributed to its success were encouragement of:

(a) interdisciplinary discussion by not having concurrent sessions,

(b) identification of critical problem areas that could benefit from solid state experimental and theoretical research by having invited papers on technology and utilization of superionic conductors,

(c) presentation of some papers in "poster sessions" where they could be viewed and extensively discussed during intermissions and regular sessions.

Several overall impressions that were obtained from discussions at the Conference are:

(a) rapid advances are being made determining the scientific and technological factors that now limit ionic conduction in solids,

(b) the gap between empiricism and fundamental knowledge is closing,

(c) theory and solid state science probably will soon make significant contributions to new technology utilizing solid ionic conductors.

E-8 REFERENCES

E-1 Prochazka, S. "The Role of Boron and Carbon in The Sintering of Silicon Carbide", Report No. 74CRD186, General Electric Co., Schenectady, NY August 1974.

E-2 Hillig, W.B., et al, "Silicon/Silicon Carbide Composites", Report No. 74CRD282, General Electric Co., Schenectady, NY November 1974.

E-3 Singh, Tuohig, Journal of the American Ceramic Society, Vol. 58, No. 1-2, pg. 70.

E-4 Mitoff, S.P., Powers, R.W., Breiter, M.W., "Battery Casing and Hermetically Sealed Sodium-Sulfur Battery", U.S. Patent No. 3,960,596.

E-5 Navias, L. unpublished.

E-6 Powers, R.W. and Mitoff, S.P., J. Electrochem. Soc. 122, 226, 1975.

Section F

AREAS FOR FUTURE WORK

The overall objectives of the 1976-1978 phase of the program are (1) to establish the design and performance of a cell of a multi-tube or a multi-channel configuration which will serve as the building block for larger modules, and (2) to provide engineering basis for subsequent production of a 1 to 10 mWh battery for the BEST Facility. To achieve these objectives, the following programs are needed:

- Program to further improve the performance of prototype cells through material and design innovations.
- Program of ceramic electrolyte material and process development.
- Program to evaluate alternative designs for, and to undertake construction and testing of cells which will ultimately be used as the fundamental building blocks for the BEST battery.
- Program to design multicell modules for the BEST battery, and initiate construction and testing of modules of optimized design.
- Program on systems engineering aspects of the BEST battery system.
- Program on particular fundamental aspects of the chemistry and physics of cell materials and reactions.

Appendix I

DETAILS OF CELL/MODULE/SYSTEM DESIGN

In this appendix a more detailed description of the cell design is given, first with respect to the components required of the cell for thermal purposes, then with respect to the module and system components. Finally the basis, results, and conclusions of the thermal analysis are given.

I-1 CONCEPTUAL DESIGN OF THE COMPONENTS FOR COOLING AND HEATING THE CELLS

I-1.1 Description of the Arrangement of the Tubes of a Cell

The sodium-filled beta-alumina tubes, embedded in the matrix of sulfur-sulfide material, are to be arranged in an array of 10 tubes by 10 tubes, as explained and discussed previously, and shown in Figure I-1.

I-1.2 Components Provided with Each Cell for Thermal Purposes

I-1.2.1 Objectives of the features. One objective of the set of components here described is to provide heat removal (when needed) from the top (horizontal) surface of the cell. This is done by provision for forced flow of air (at a low but constant flow rate) in a horizontal direction in the region above the upper ends of the tubes. The system for supplying and removing this air (and for shutting it off when it is not needed) and the details of the heat transfer surface of the air duct, are described later.

A second objective of the present design concepts is to provide heat conduction in a horizontal direction, sufficient to limit the horizontal non-uniformity of temperature, from tube to tube (of the 10 x 10 array of tubes), in spite of the large variation (from room temperature to over 300°C) in the cooling air as it flows above to the cell. This heat conduction metal (aluminum alloy 6061), is described later in detail. The thermal conductivity of the sulfur-sulfide matrix of the cell is so low that heat conduction horizontally through that material is quite inadequate for the 10 x 10 tube array, although adequate for the previously considered (I-1) array of 2 x 50 tubes. This is the main reason why heat removal from the sides of the cell has been abandoned as a concept for multi-tube cells.

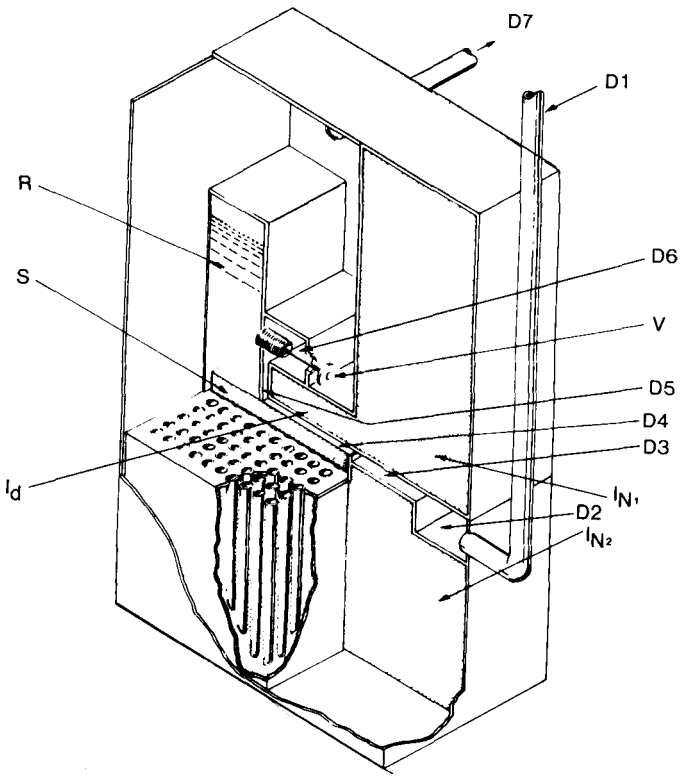

Figure I-1. Cut-away View of a Cell

Heat conduction in the vertical direction is provided mainly by the liquid sodium in the tubes. This is found, by calculation, to be adequate, even with the conservative assumptions of negligible benefit from vertical electrical conductors in the matrix, negligible benefit from free convection in the sodium, and negligible increase of conductivity by the presence of the graphite fibers in the sulfur-sulfide matrix. But the vertical non-uniformity of temperature, although acceptable, is appreciable and is the largest component of the total non-uniformity of temperature. It is of the order of 20°C for the maximum heat-generation rate during normal (not emergency) operation of the cell (76 watts per cell). Accordingly, the already authorized tests to establish the benefit in heat flow contributions, of free convection of the sodium, and of heat conductivity (in the vertical direction) added by the graphite fibers in the sulfur-sulfide matrix remain of practical interest.

I-1.2.2 The Horizontal Flat Duct for Forced-Convection Heat Transfer. The horizontal flat duct provided for forced-convection heat transfer is indicated in Figure I-1, where it is identified as "D_4.) Only the lower surface of this duct serves as the heat transfer surface. The upper surface is thermally insulated, for reasons explained later. The vertical dimension, here called the "gap," of this duct is very small (a value of .050 inch is here proposed). The smallness of this gap yields, for the laminar type of flow expected, a relatively large heat transfer coefficient. This, combined with the chosen low flow rate (about 0.74 ft^3/min per cell measured at 70°F), heats the gas from its initial room temperature, to a temperature only a few degrees below the surface temperature of the duct at the outlet end. For a given surface temperature, the heat removed is, therefore, proportional, approximately, to the flow rate. The flow rate is, therefore, to be chosen such as to be just a little greater than the value which will remove heat at the maximum rate generated in the cell (by normal operation of the cell), minus the small heat loss through the cell walls. The excess of heat removal over that needed for equilibrium will cause the temperature to fall slowly, until the air flow is shut off by a thermostatic valve (as discussed later). The surface temperature will then increase slowly until the thermostatic valve opens, and the air again flows, and the cycle repeats. The temperature spread between the closing and the full opening of the valve can probably be set at only 2°C.

I-1.2.3 The "Heat-Sink" Slab for Horizontal Heat Conduction. The thick slab which is provided for horizontal heat conduction, as mentioned above, is illustrated in Figure I-1, identified as "S." This slab here is called a "heat sink," by analogy with the metal elements, known as "heat sinks," commonly used with semi-conductor power-control devices.

The thickness of this slab is chosen sufficient (0.75 inch in the present design) to limit the calculated maximum temperature non-uniformity over the slab to a value compatible with the chosen allowable range of temperatures for the entire heat cell assembly. In the present design, this non-uniformity of the slab is about 20°C.

I-1.2.4 Thermostatic Control of Air-Flow Rate. It is proposed that the thermostatically-controlled air flow valve be placed in the air flow path in

a convenient location downstream of the outlet of air from the heat-sink duct, as indicated in Figure I-1, where the valve is identified by the symbol "V." Before reaching the valve, however, the air flow is to be collected in an "outlet manifold" (identified as "D_6"), after passing through a short vertical-flow duct "D_5" which carries the air through the layer of duct insulation, "I_d."

One form of thermostatically controlled valve which seems likely to be suitable, and of relatively low cost, is the flexible metal bellows type, commonly used in the cooling system of liquid-cooled automobiles. The bellows contains a charge of volatile liquid plus vapor, the pressure of which varies greatly with temperature. Appropriate choice of the chemical composition of this charge can make the vapor pressure reach a convenient value, to move one end of the bellows against a spring resistance, at the desired temperature. Suitable design of the spring can make the temperature difference between "fully open" and "completely shut" either a small difference, yielding an approximation to "on-or-off" control, or a larger difference, yielding a "proportional" type of control. The time lag of the response of the temperature at the thermostat to the change of air-flow rate will be involved in the choice between these alternatives.

The temperature of the fluid in the bellows will be close to the temperature of the sodium at the bottom of the sodium reservoir, where the bellows is to be mounted, which will be at a temperature close to that of the outlet and of the heat sink. The outlet air is also close to that temperature, since there will be negligible heat flux between the air and the adjacent surfaces in that region.

I-1.2.5 The Other Components of the Air Flow System of a Cell. The various elements of the air flow path through a cell are indicated in Figure I-1, and comprise the following:

- D_1, the inlet duct which carries the air (provided by a fan as discussed later) from an inlet manifold (also considered later) to
- D_2, the distributing chamber, from which the air flows into

D_3, the flat duct, through the thermal insulation, into

D_4, the heat-transfer duct, and then through the vertical duct, D_5, and the manifold D_6, through the valve V (these last four elements have been already discussed above) into the large open space, P. This space may be useful for location of the electrical connections for the sulfur-side electrodes of the next layer of cells above.

From this space, which serves as a plenum or manifold for the set of cells in a row, the hot air can flow horizontally from one cell into the corresponding space of the next cell in the horizontal row of cells, (or for the end cell of a row into a discharge duct D_7). The heat loss to the room which would occur with an external manifold is thereby eliminated.

The discharge duct can lead to a chimney, or, if the recirculation of the hot air or innert gas (for additional safety purposes) through a heat exchanger is desired, to the heat exchanger and then to a fan, and thence back to the inlet duct, D_1.

It is desirable that the cross-section area of each of the ducts or other elements in the air flow circuit for a cell be large enough to keep the pressure drop in that duct or element, to a value relatively low compared to the pressure drop in the heat transfer duct, D_4, with the pressure variation in the supply manifold low enough to yield uniform flow distribution to the cells in a row. Such a limitation will tend to promote uniformity of flow across each heat transfer duct, and avoid unnecessary loss of energy for the system pressure drop. The dimensions illustrated in Figure I-1 are reasonable first approximations but deserve reconsideration for the final design.

I-1.2.6 Thermal Insulation. The loss of heat to the room, through the thermally insulated walls of a cell, during long time intervals of zero or low electrical current, is to be supplied by thermostatically controlled auxiliary heaters (in order to maintain the desired cell temperature). The amount of this loss, and hence the average efficiency of the cell, is of course dependent on the thickness and conductivity of the thermal insulation, and on the area of the insulated surfaces exposed to room air.

In the presently proposed arrangements of cells in a module, the cells will be arranged, "back-to-back" in pairs, in two rows as indicated in Figure I-2. Furthermore, many pairs will be assembled in a row, and these rows will be "stacked" in a column of several (for example, five) "layers" vertically. The only exposed insulated surfaces of most cells will, therefore, be just one vertical wall. The insulation for this wall is indicated as "I_{N1}" and "I_{N2}" in Figure I-1.

In order to keep the energy loss to the room at about 16 watts per cell, the following insulation specifications are required:

- Insulation thickness: ΔL = 5 inches = 0.42 ft
- Insulation material: commercially-available fibrous quartz, known as "Refrasil" (suitable for temperatures well above 400°C)
- Density chosen for this material: 9 lbs/ft^3 in order to keep the conductivity low (lower density increases conductivity);
- Thermal conductivity: k = 0.32 Btu/hr ft deg F, for an <u>average</u> temperature of 180°C (from GE Heat Transfer Design Data Book(I-2), Section 515.24, page 3);
- Height of the insulated wall of one cell, in a column of cells; y_1 = 1.5 ft.
- Width of the insulated wall of one cell, in a row of cells: 0.52 ft.

These values yield an exposed area, A = 0.78 sq. ft per cell for those cells not at the ends of a row nor on the top or bottom layers.

The corresponding heat loss for a temperature difference of 576°F or 320°C (340°C to 20°C) is $q_1 = kA\Delta t/L$ = 34 Btu/hr, which is 10 watts.

The heat losses through the insulated top and bottom surfaces of a "stack" of cells, and through the vertical end walls of a set of many such stacks in the insulated set will increase the <u>average</u> loss per cell, so that the earlier estimate of 15 watts per cell remains a conservative approximation for the present arrangement. The specific value now calculated is 11.2 watts per cell if all 500 cells of a string are located in a single stack as described later.

In addition to the thermal insulation on the external surfaces of all the cells of a module, some thermal insulation, probably of similar material, is now proposed for the upper surface of the heat-transfer duct, as indicated by "I_d" in Figure I-1. Its purpose is to prevent appreciable heat transfer, from the hot "exhaust" air in the "empty" space above this duct, into the cool air flowing in the duct. Such heat would tend to make the air temperature rise at a greater rate as it flowed through the duct, and thereby reduce the ability of this air to absorb heat from the heat sink surface. A thickness of one inch for this duct insulation has been estimated as sufficient for this purpose.

A convenient advantage of the proposed arrangement of components in a cell, illustrated in Figure I-1, is as follows: Access, for adjustment or inspection purposes to the space in which are mounted the thermostatic flow valve, the thermostatic control for the auxiliary heater and the bottom surface of the cell above the space, can readily be provided just by removing the panel of thermal insulation (I_{N1}), located just above the air supply duct, without interferring with that duct.

I-1.2.7 Auxiliary Heating Units, Thermostatically Controlled. A separate electrical heating unit for each cell is proposed, rather than a single heating unit per module. This unit will be located in the relatively empty space, P, above the top of the cooling duct. The heat losses will differ for the end cells of a row, the cells in the top row and the bottom row, and the other cells. The heat flow from cell to cell is almost negligible, so a separate heater for each cell seems essential for providing adequate temperature among all the cells, within the allowable small range of operating temperature. Each heater can be relatively simple, such as heaters used in domestic ovens, or a ceramic-insulated resistor.

Temperature uniformity within the cell during use of the heaters is facilitated by the same heat conducting elements as are provided for the effect of heat from the electrical losses during operation of the cells. The temperature non-uniformities will be less, since the heat rate is less. The temperature sensor for the heater should be located close to the air-flow-control bellows so that there can be no inconsistency in the response of heater and bellows.

In any case, the temperature setting at which a heater is switched "on" should be lower than the temperature below which the air flow thermostat turns the air flow "off," to avoid unnecessary loss of energy by loss of auxiliary heat to cooling air.

The cells at the ends of a row, and the cells in the top or bottom layer which have greater heat losses than the other cells, should have their own thermostatic switches, and a larger wattage output (when "on") than the other cells. Whether a single thermostatic switch to control all the other similar cells will suffice, or whether a separate thermostatic switch for each cell is advisable, remains to be decided. Probably the first tests should be made with separate thermostatic switches in each cell.

I-1.2.8 Reservoir for Storage of Liquid Sodium. The volume of sodium liquid in a cell for the fully-charged condition in the cathode compartment exceeds the volume of the sodium liquid in the fully-discharged condition (Na_2S_3 in the cathode compartment) by about 78 cubic inches. But to start with, an additional 25% for sodium volume is required.

A "reservoir," denoted as "R" in Figure I-1, is here proposed to accommodate this variation in sodium volume. The suggested horizontal cross-section dimensions are 6 inches by 2 inches with a liquid height of 7.9 inches to start with, and 6.3 inches at full charge during operation.

The entire horizontal cross-section area above the cell is not available for the storage volume, as it was in the previously proposed[I-1] arrangement, because the heat removal surface is now located on the top surface of the cell, not on the sides. The lower surface of the heat-sink slab must always be in contact with liquid sodium, regardless of the level of the sodium in the storage volume.

The present cell design has a horizontal dimension of 6.2 inches in one direction on the top surface of which two inches is now allocated to the reservoir, leaving about four inches for the heat transfer surface.

The heat originating in the two-inch wide portion of the cell located under the reservoir is conducted to the heat transfer surface by an extension of the heat-sink slab into the reservoir region, as is shown in Figure I-1. A small gap is left beyond the tip end of this heat sink to allow sodium flow between the reservoir and the flat manifold at the top of the sodium-filled tubes directly under the heat-sink slab. The vertical dimension of this manifold may be, say, 1/8 inch, or whatever seems reasonable.

An option remains of a trade-off between the horizontal width of the reservoir tank (two inches as proposed above) and the initial sodium height (7.9 inches as proposed above). The width may be decreased if the height is increased enough to keep volume constant.

Internal ribs must be provided in the reservoir tank to prevent it from collapsing under vacuum when empty. Such vacuum will occur if the space above the sodium is charged with gas at (or below) atmospheric pressure when the reservoir is full of sodium (as is desirable to prevent bulging of the tank).

A space above the sodium for vapor is desirable, a height of 1.5 inches at the start, which becomes 3.1 inches at full charge in operation is here suggested. This yields a reservoir height, above the heat sink, of 9.3 inches.

I-2 CONCEPTUAL DESIGN WITH RESPECT TO THE SYSTEM OF MODULES, STACKS, FANS, ETC.

I-2.1 Modules and Sets of Modules

The design provides for a "module" comprising a set of 20 cells, arranged as a vertical stack of five layers, each layer containing two pairs of cells, the cells of each pair being arranged back to back, as indicated in Figure I-2. Enough such modules, namely 25, can be placed side-by-side in a row, to form a "string" of 500 cells. All may be connected in series electrically, as proposed in Reference I-1 giving a 1000 volt string, or various parallel connections may be considered. The resulting dimensions will be about 27 ft long by 8 ft high by 2 ft wide.

The hot "exhaust" air from all the cells in one layer will, after flowing horizontally through the spaces inside the cells, half to one end, half to

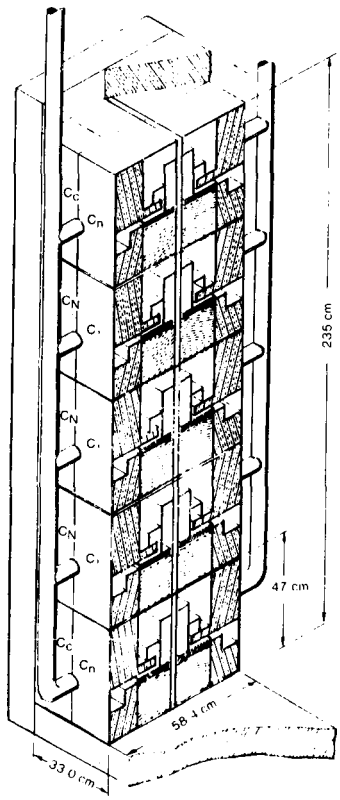

Figure I-2. Twenty Cell Module

the other end of the layer, will be drawn off by two vertical manifold pipes (one at each end), leading either to a chimney, or else to a heat exchanger and thence back to the inlet manifolds. The inlet manifolds and fans are discussed later.

A frame structure can presumably be provided to support the cells in the manner that a vertical structure with brackets for the shelves of a bookcase supports the books. Provisions could be made so that a single cell can be pulled out and replaced by another "spare" cell in case of trouble, or else so that an entire module (20 cells) can be pulled out and replaced. The weight of one cell will be of the order of 20 pounds. The weight of one module of 20 cells will be of the order of 400 pounds (which could be handled by a "forklift" truck).

The use of many modules in one row results in relatively little heat loss through the insulation at the ends of a row, since the area of the ends per cell, is then relatively small compared to the area of the insulated side of each cell.

I-2.2 System for Supply of Coolant Air

I-2.2.1 Air System for a Single Row of Module Stacks, Comprising 500 Cells in the row.

A single fan for the entire 27 feet long, "string" of module stacks may be appropriate.

It would supply air to a large horizontal manifold pipe, probably located above the "string." This pipe would supply air, in turn, to branch manifolds, each running vertically downward to feed the various layers, with one set of branch manifolds on one side and one row on the other side of the "string" of modules, as indicated in Figure I-2. Removal of a single module, for replacement, would then require removal of only one of the branch manifolds.

The fan for this arrangement would be chosen to supply a flow of about 370 ft^3/min, at a pressure of at least 0.4 inch of water at this flow, and somewhat greater pressure when the flow is reduced (by operation of one or more of the thermostatic valves which control the air flow through each of the cells). The fan should be selected so as to have a pressure vs flow characteristic which is relatively flat, for flow below the maximum design flow, since pressure higher than that at the maximum flow serves no useful purpose.

The above value of 0.4 inch of water represents a minimum value assuming negligible pressure drop through all the ducting of the flow system, except for the heat-transfer duct in the cell. These neglected pressure drops will increase with decrease of the cross-section area of each duct concerned. A trade-off between size of each duct and pressure drop of the system can be made later when more detailed study is made. But the sizes of the main manifold, and of the branch manifolds, must be large enough to limit the non-uniformity of pressure along each manifold to a small enough value to avoid significant non-uniformity of flow among the manifold outlets.

The above value of 0.4 inch water required for the fan would be reduced if appreciable draft from the hot air, were obtained by use of a chimney, a subject discussed later. Furthermore, the fan pressure requirement will be increased if a heat exchanger, with its pressure drop increment, is to be included in the air flow circuit.

I-2.2.2 Alternative Fan Arrangements to Eliminate some Manifold Piping. The manifold piping from the fan to each cell could be eliminated by provision of a separate, tiny, fan for each cell, each delivering only about 0.7 ft^3/min. This option is at present rejected because of judgement that the cost of so many fans, even though tiny, would be excessive. It would also be difficult to obtain the desired pressure from such tiny fans. For the arrangement of all cells of a module in a single layer, a separate fan for each side of each module, to supply each row of 14 cells with about 10 ft^3/min also seems undesirable for similar, though less overwhelming, reasons.

Manifolds for the supply of coolant air could be eliminated also by placing the fan or fans in the hot exhaust air instead of using them for the cool air. The coolant air would then be drawn into each cell directly from the room. This option has been rejected for the present because of the expectation of greater cost for fan impellers made of material capable of operating in air as hot as 340°C or so. Furthermore, the fan motors would have to be protected against heat flow from the impeller to the bearings and motor windings, by use of a long "overhung" shaft, with no bearing on the outer end (beyond the impeller).

I-2.2.3 Power Required for the Fans. The power required for the fans will be trivial. For example, for a system pressure drop of 0.6 inch water, the estimated flow of 370 ft^3/min for a string of 500 cells, with a fan efficiency of 50 percent would require only about 52 watts, which is only 0.10 watts per cell, compared with electrical loss of up to 76 watts per cell in normal operation.

I-2.2.4 Non-Uniformity of Air Flow Rate with Respect to Vertical Location of a Module in a Stack. The density of the hot air in the exhaust piping will be about half the density of the room temperature air in the inlet manifolds.

This density difference adds, to the fan pressure, a "chimney effect" which increases the pressure drop over the lower layer of modules in a stack, compared to the top layer of modules since the lower layer will have a greater height of hot air in its exhaust pipe. This causes a proportional non-uniformity of flow among the different layers, since the flow is low enough to make the flow of laminar nature (not turbulent, for which flow would be proportional to the square root of pressure difference).

For example, for a fan pressure of 0.41 inch of water for the top layer, the pressure difference across lower layers will increase by about 1.7% per foot of decrease of elevation of the layer. For a stack of five layers, spaced at intervals of 1.5 feet, vertically, the lowest layer will be six feet lower than the top layer, so that pressure difference, and hence the flow rate, will be greater by about 10 percent.

This flow difference among layers can be tolerated, however, by selecting a fan which will provide enough additional flow, so that the top layer will get what it needs, and the lower layers will get a greater amount than the top layer. This excess will do no harm, since the thermostatic valve can close sooner for the lower layers, during the "air-on" part of the flow cycle, to yield an appropriately shorter time interval of air flow, and thereby keep the cell temperature within the desired range. The values for fan air flow requirements specified in this report include allowance for this excess flow for the layers below the top layer.

I-2.3 Chimney

The natural draft produced by hot air in a chimney would have the advantage, when used with a set of modules, that it would produce a slightly subatmospheric pressure (vacuum) in the hot air filled space inside each cell. This would prevent leakage of hot air into the room through any inadvertent cracks in the module walls or in the exhaust air piping.

The draft produced by a well-insulated chimney with air at 300°C will be about 0.07 inch of water per foot of vertical height. Hence a 60-foot chimney would produce the entire required pressure heat of 0.41 inch when the air is hot. It may be determined that fans are still required for reliability so the

pressure chosen for the fan output during operation of the flow system during normal electrical load cycles should be chosen to take account of whatever chimney draft could be relied on, in spite of disturbances caused by effect of winds, for the particular chimney chosen. Unfortunately, the effect of wind may be relatively uncertain.

The uncertainty of chimney draft would be eliminated by use of a "closed" air system, with a heat exchanger instead of a chimney.

I-2.4 Heat Exchanger

Use of a heat exchanger would have an advantage (in addition to the advantage mentioned immediately above), of saving energy if there will be a practical use for the heat obtainable from the hot exhaust air from the system of modules. Economic trade-off between the value of such energy and the cost of the heat exchanger and associated piping would deserve study to justify a decision on the choice between heat exchanger and chimney.

If an inert gas, rather than air, is desired as the coolant medium, a heat exchanger would, of course, be essential.

If a heat exchanger is indeed to be used, the closed loop of air flow should be open to the room air pressure at such a point (such as the fan outlet) that the pressure of the exhaust hot air will be subatmospheric, in order to prevent leakage of hot air into the room.

I-3 THERMAL ANALYSIS: BASIS, RESULTS, AND CONCLUSIONS

I-3.1 Purpose

The purpose of the analysis here reported is to provide results for answering the following questions?

(a) Can the temperature within the cell be thermostatically controlled, with suitable flow of coolant air when required, to confine the temperature within the presently-desired range of 310 to 365°C?

(b) What flow rate for an "on-and off" flow of coolant air is appropriate, what pressure drop and power consumption will it require, and what will the air outlet temperature be for the appropriate controlled temperature of the heat-transfer duct (at the outlet end)?

(c) How much increase in energy loss will be required for auxiliary heat (when the inherent electrical losses are insufficient to maintain the desired temperature)?

(d) How quickly does the temperature profile, vertically, in the cell material respond to a sudden change in electrical current or to a sudden change in air flow?

(e) Is the rate of decrease of cell temperature, due to heat losses during the idle periods, sufficiently small so that response of the thermostat will prevent excessive temperature fluctuation?

I-3.2 Nature of the Problems Considered

I-3.2.1 Temperature Non-Uniformities. Non-uniformity of temperature in the vertical direction occurs because the heat is removed, by the coolant air, at the top of the cell, whereas the electrical losses are, of course, distributed, nearly uniformly, throughout the cell. The sodium in the tubes, the tube material itself, and the sulfide and sulfur in the "matrix" outside the tubes act as three parallel paths for heat conduction vertically. The variation in rate of electrical loss with temperature (1% per °C, at 300°C) is accounted for in the calculations.

Non-uniformity of temperature in the horizontal direction occurs because the required air flow is so low that the air temperature achieves most of its temperature rise close to the air-inlet and the heat transfer duct. The heat, which is fed into the heat sink nearly uniformly, is conducted to the inlet-end portion by the heat-sink material. The thickness of the heat-sink slab has been chosen large enough to yield an acceptably low temperature variation horizontally. The conductance horizontally through the sulfide and sulfur material is only about four percent that through the heat-sink material.

The temperature non-uniformities, which exist during charge or discharge periods when the cooling air flow is "on," disappear during the idle periods when the air flow is "off," so that there is then no heat flow vertically. The time for substantial achievement of this state of uniformity is one of

the quantities calculated in the analysis. The resulting mean temperature, in the uniform state, is found to be higher than the temperature at the outlet end of the heat sink (where the temperature control sensor will be located). The air flow will not, therefore, become "off" at the start of an "idle" period, unless there is an "over-ride" control which shuts off the fan during the idle period, in order to save heat, and allow less auxiliary heat to be required. The auxiliary heat here calculated is based on the assumption that this "over-ride" is provided.

I-3.2.2 Heat Loss Differences from Cell to Cell, Due to Location. The heat loss, through the insulation, from a cell to the ambient room air, depends on the location of the cell in the stack. The cells at the corners of a stack, identified as "C_c" in Figure I-2, have the greatest heat loss (calculated as 33 watts), since they have two walls and a ceiling of "floor" surface exposed to heat loss. The cells on the vertical edges, having an edge length of 1.5 ft, have a loss of 23 watts. The cells on the horizontal edges having an edge length of 6.2 inches, have a loss of 15 watts. The other cells, each with only one wall exposed, have a loss of 10 watts.

A consequence of these differences is that the auxiliary heat needed (to prevent drop below 310°C during idle periods) differs from cell to cell, and is, indeed, zero for the more favorably located cells, for the conditions here considered.

I-3.3 Assumptions Regarding Temperature Control

I-3.3.1 Thermostatic Control of Air Flow. The thermostatic valve which controls the air flow (by, for example, a flexible bellows, as mentioned above) is here assumed, for simplicity of analysis, to provide full flow for temperature, at the sensor, above 339°C and zero flow for temperature below 339°C. The valve will be alternately open and shut when the average heat removal is less than can be removed by full air flow. This temperature of 339°C is the value calculated for the outlet end of the heat sink when the hot spot (at the bottom of the cell) is at the chosen 360°C for the maximum heat generation (76 watts at the end of the charge period). If the temperature sensor is located above the heat sink, in the air collection manifold, the temperature setting

for the sensor will be less than 339°C, since the outlet air temperature is less (calculated as 310°C).

I-3.3.2 Thermostat Control for Auxiliary Heat. No one single value is assumed in the analysis for the lower temperature limit below which the auxiliary heat will be kept turned "on" by the thermostatic switch for this purpose. Instead, trial values of the amount of auxiliary heat, different values for each of the four types of cell location, are assumed in the analysis, and values are chosen which yield minimum temperatures, during the 24-hour operating cycle, which lie close to, but not below, the chosen allowable minimum of 310°C. More elaborate analysis could establish slightly lower values for the auxiliary heat which would yield a minimum of just 310°C.

I-3.4 Results of Thermal Analysis

I-3.4.1 Minimum and Maximum Temperatures During the 24-hour Operating Cycle: (all temperature values are °C)

	Location of Cell			
	Only 1 Wall Exposed	Horiz. Edge	Vertical Edge	Corner
Location designating symbol:	C_l	C_h	C_v	C_c
5-hour charge period:				
Temp. at outlet end of heat sink:	339	339	339	339
Min. temp. (occurs at inlet end)	319	319	319	319
Mean temp. (volumetric mean)	344	344+	344+	344+
Max. temp. (at bottom of cell)	360	360	360	360
Aux. heat required	0	0	0	0
3-hour idle period after charge:				
Min. temp. (at end of period)	355	330	322	322
Mean temp. is close to the min.				
Aux. heat chosen (per cell) watts	0	0	0	9.2
Aux. heat energy for period, watt-hr	0	0	0	28

	Location of Cell			
Location designating symbol:	Only 1 Wall Exposed C_l	Horiz. Edge C_h	Vertical Edge C_v	Corner C_c
10-hour discharge period (after idle):				
Min. temp (at end of period)	331	331	322	322
Controlled temp., heat sink (outlet)	339	339+	339	339
Max. temp. (at bottom of cell)	347	347-	347-	347-
Aux. heat chosen (per cell), watts	0	0	0	9.2
Aux. heat energy for period, watt-hr	0	0	0	92
6-hour idle period after discharge:				
Min. temp (at end of period)	321	313	323	323
Aux. heat chosen (per cell), watts	0	0	23.5	32.7
Aux. heat energy for period, watt-hr	0	0	141	196
Totals for whole 24-hr. cycle:				
Total aux. heat energy, watt-hr/cell	0	0	141	316
Number of cells in each location	388	92	12	8
Total aux. heat energy per string (watt-hrs	0	0	1692	2528

I-3.4.2 Air Flow and Related Performance Values

m_a = Mass flow rate of air, choice to yield desired heat sink temperature at end of charge period, lbs/hr per cell 3.1

Q_{al} = Volume flow rate, measured at 40C, ft^3/min, per cell 0.74

Δp^*_{hs} = Pressure drop through heat-sink duct, inch water 0.41

p_{hs} = Power loss of air in heat-sink duct = .118 $Q_{hs} \Delta p_{hs}$ .036 watt/cell

$p_{500,fan}$ = Power for fan for 500 cells, if fan efficiency is 50% and pressure losses in flow system outside the heat sink is 50% of that in the heat sink duct = 500 (1.50) Δp^*_{hs}/0.50 = 54 watt/string

I-3.4.3 Time Lag of Response of Vertical Temperature Profile to a Sudden Change in the Heat Removal by the Air, or a Sudden Change in the Heat Generation Rate. Considered here first, for simplicity of concept, is the situation where the temperature is uniformly high, throughout a cell, with zero losses to the surrounding, zero heat generation, and zero air flow, and the air flow is suddenly supplied at a constant rate.

The result will be, eventually, a steady decrease in temperature at the heat sink, and a steady decrease in temperature at the bottom of the cell, but the latter will lag behind, and, therefore, be higher than the former, as indicated in the right-hand portion of the following plot:

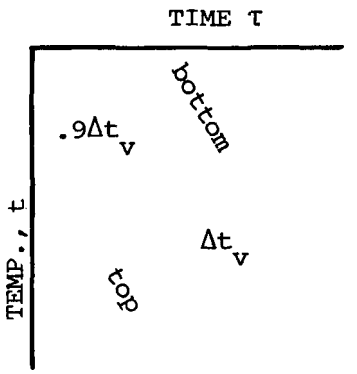

The temperature difference between the top and bottom will start at zero and rise to an asymptotic limit of a constant amount, (called Δt_v here). This assumes that the drop in top temperature is small compared to the difference between top temperature and the inlet-air temperature. The "time lag" as here defined is the time τ_c, required for the top-to-bottom difference to rise to 90% of its final value. The results of the analysis yield a value for this time lag as follows:

When the cell has 100% of full charge : τ_c = 0.14 hours
When the call has 0% of full charge : τ_c = 0.19 hours

Considered next is the related situation where the heat generation is constant, and a constant temperature profile exists, with constant heat removal at the top of the cell, and then both the heat generation and the air flow are suddenly changed to zero. The temperature profile will then gradually change to

a uniform temperature throughout the cell, at the mean temperature which the profile had before the change. By the principal of superposition, the time lag for this change will be the same as for the previously considered situation.

The "time lag" for response of the vertical temperature profile to any sudden change in coolant air flow or in heat generation is, therefore, quite small compared to the duration of three hours or more for each of the intervals, for charge, discharge, or idle, of the operating cycle.

I-3.4.4 Rate of Temperature Decrease During "Idle" Periods, Where No Auxiliary Heat is Provided From the basic definition of specific heat, c, the rate of temperature decrease during "idle" periods, due to a heat loss, q_L from a cell, is as follows:

$$\frac{dt}{d\tau} = \frac{q_L}{\sum_{1}^{n} c_i m_i}$$

where c_i and m_i represent the specific heat and the mass of the i^{th} component of the n components of the cell.

For each cell with only one wall exposed to heat loss, this equation yields, by calculation based on the proposed masses and materials of a cell, the following rates:

For the condition of full charge: 3.0°C per hour
For the condition of full discharge: 2.7°C per hour

For a cell with more than one surface exposed to heat loss, the rates of temperature decrease will be greater than the two above values, in proportion to the increased heat loss. Values for the losses for each type of cell location are listed above in Item I-3.2.2.

The components of mass here taken account of include, in addition to the materials in the sulfide-sulfur region, the tube and the sodium, also the

heat sink, the walls of the reservoir and of the sulfide region, the tube sheet and sodium layer just below the heat sink, and a 0.5 pound allowance for minor components.

I-3.4.5 Rate of Temperature Decrease Due to Excess Air Flow When Heat Generation is Below Maximum Rate, but not Zero. The air flow rate, specified in Item I-3.4.2 above, is chosen to yield a constant temperature for the maximum rate of heat generation. For times when the heat generation rate is below this maximu, but not zero, the air flow remains the same, so that heat removal exceeds the heat generation, and the temperature of the cell decreases until the thermostatic valve shuts off the air flow.

For a cell with only one wall surface losing heat, the maximum heat generation rate is 76 watts and the wall loss is 10 watts, so the air removes 66 watts.

The minimum heat generation rate (for less than 50% charge during the discharge period) is only 22 watts, with the same wall loss, so the heat to be removed by the air is only 12 watts. The consequent excess of 54 watts causes, according to the calculations, using the equation in Item I-3.4.4, a rate of temperature decrease of 16°C per hour.

For a cell with the largest loss through the insulation, namely a cell at a corner of the stack, the loss is 33 watts instead of the 10 watts loss considered above, so the excess cooling is 77 watts instead of 54 watts, and the rates of temperature decrease are proportionally greater than those above, namely 21°C per hour.

The thermostatic valve should be able to respond to a change in temperature of the heat sink within a few minutes, so its temperature lag, consistent with the above temperature change rates, should not exceed a few degrees C.

I-3.5 Conclusions from Thermal Analysis

I-3.5.1 Satisfactory Temperature Range. The chosen limits (which are relatively conservative), 310 to 365°C, for the temperature range of the cell materials are indeed complied with by the proposed design and chosen data, which yield a range of 313 to 360°C under conservative assumptions.

I-3.5.2 High Outlet Temperature of the Coolant Air. The air-cooled surface of the heat sink and of the lower part of the sodium reservoir is so designed that the outlet air temperature is 310°C for the full charge, charging, condition of the cell. This is high enough so that the effect of the outlet air on the temperature of the thermostat temperature sensor can be easily accounted for in the setting chosen for the thermostat operation, and so that the sodium in the upper part of the reservoir will not freeze.

I-3.5.3 Low Energy Loss for Auxiliary Heat. Energy supply for auxiliary heating, during the rated operating cycle of the battery, is required only for those cells which are located on the corners and on the vertical edges of the stack of cells. The consequence is that the energy required for auxiliary heating of the entire battery is gratifyingly low (less than two percent of the energy loss from the electrical losses) during the cycle. But thick (5-inch) insulation is required to achieve this result.

I-3.5.4 Quick Response of Temperature Profile to a "Step" Change of Heat Input or of Cooling Air Flow. The time required for the vertical temperature profile in the cell to approach closely to the new equilibrium profile after a step change of heat input rate or of air flow is small (less than 0.2 hour) compared to the duration of the rated periods of charge, discharge and idle.

I-3.5.5 Slow Rate of Change of Cell Temperature as a Result of Heat Losses Through the Chosen Thermal Insulation. During "idle" periods (zero heat generation), the rate of temperature decrease in the absence of auxiliary heat is relatively slow. For the cells not on an edge or corner of the stack, it is only about 3°C per hour, and for the cells with the greatest heat losses, the corner cells, it is about 10°C per hour.

I-3.5.6 Moderate Rate of Temperature Decrease as a Consequence of Excess Cooling Air Flow for Times when Electrical Losses are Low Since the air flow is to be on full, when not turned off, it will tend to reduce the cell temperature when the heat generation is less than maximum. For the minimum heat generation rate (during discharge, with less than 50% charge), the rate of temperature decrease is moderate, namely 16 to 21°C per hour,

depending on cell location. It is expected that these rates of temperature change will cause only acceptably small temperature fluctuations in the temperature cycle provided by the thermostats. But this conclusion is only tentative, based only on judgment, since the detailed designs for the thermostats have not yet been selected.

I-4 REFERENCES

I-1 "Sodium-Sulfur Battery Development for Bulk Power Storage," Report SRD-74-130, by Electrochemistry Branch, General Electric Corporate Research and Development, December 27, 1974.

I-2 "Heat Transfer Data Book," General Electric Corporate Research and Development, particularly Sections 515.22 and 515.24 or as specified where cited.

I-3 "Thermal Conductivity of Three Sodium Polysulfide and Sulfur-saturated Carbon-felt Specimens," Dynatech Reports dated October 6, 1975 and December 17, 1975.

Appendix II

SODIUM-SULFUR BATTERY SYSTEM RELIABILITY AND PERFORMANCE

In this appendix charts are given for the relationships between system performance and module reliability for various system configurations. In each section the configuration and reliability factor to be considered are described, the use of the chart is explained, and the mathematical derivation of the chart is given.

II-1 ASSUMPTIONS ABOUT MODULES

The analyses in this study employ a number of simplifying assumptions concerning modules. These assumptions and their consequences are listed below.

(1) All modules have identical performance. This means that they all have the same capacity (energy) C_1, voltage, internal resistance r, and failure probability p per (daily) cycle. In reality, modules differ with respect to each such characteristic. In a particular analysis, one can use a typical best, worst, or other value for a performance characteristic; this yields typical, best, worst, or other values for battery system performance.

(2) Module performance does not change with age. In reality, modules age, and their properties change at different rates. As in (1), one can use a typical best, worst, or other value for a module performance characteristic.

(3) In most analyses, "ir" loss is ignored. This means that the value of capacity or voltage used in an analysis should take the ir loss into account. An exception is the analysis of system resistance, which cannot ignore module resistance, of course.

(4) Module voltage has a constant value from 0 to 100% discharge. As before a typical best, worst, or other value of voltage can be used.

(5) In most analyses, the possibility of overcurrent through modules is ignored. Of course, the calculation of the distribution of overcurrent in a crossover system (Section II-12) does not ignore this.

(6) Module performance (capacity, voltage, failure probability, power, etc.) does not depend on how the modules are operated.

(7) A failed module is an open circuit and passes no current. In reality, a module may fail slowly and its performance degrades slowly. Also, a failing module may continue to pass current.

(8) Failure of a module is treated as if the failure occurred at the start of a cycle and is not fixed during the cycle. This assumption means that all performance analyses involving module failures yield results based on low performance.

(9) How one module performs does not affect how another module performs. In particular, failure of a module is (statistically) independent of failure of any other module. An exception to this is the analysis of overcurrent in crossover systems (Section II-12).

II-2 ASSUMPTIONS ABOUT SYSTEMS

The analyses in this study employ a number of simplifying assumptions concerning systems. Such assumptions applying to both crossover and parallel string systems are listed below.

(1) All modules are good at the start of a cycle. If some failed modules have not been replaced (or are replaced by failed modules), system performance will be below that given by the following analyses.

(2) Redundant modules in a system are operating; however, they could be on standby and switched into the system as needed. The assumption of operating redundant modules yields a lower value of system reliability than does standby redundant modules.

II-2.1 Parallel String Systems

A parallel string system consists of modules that are connected in series to form strings, and the strings are connected in parallel as shown below.

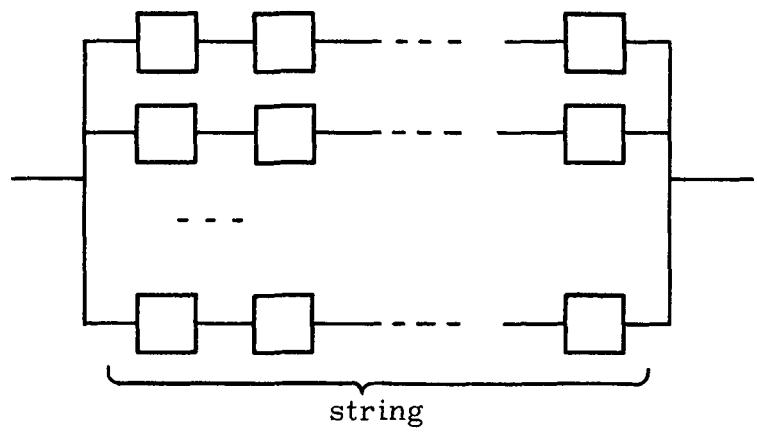

Assumptions that apply only to parallel string systems follow.

Detection and bypassing of failed modules is 100% reliable. Unreliability of such equipment for detection and bypassing lowers system performance below that given by analyses in this report. Also, detection and bypassing does not affect the performance of other modules in the system. The practical problems of detecting and bypassing failed modules are not considered here. Early detection of incipient module failures and replacement of such modules will prevent many actual module failures. Only actual failures during system operation are considered in the following.

II-2.2 Crossover Systems

A crossover system consists of modules that are connected in parallel to form layers, and the layers are connected in series as shown below.

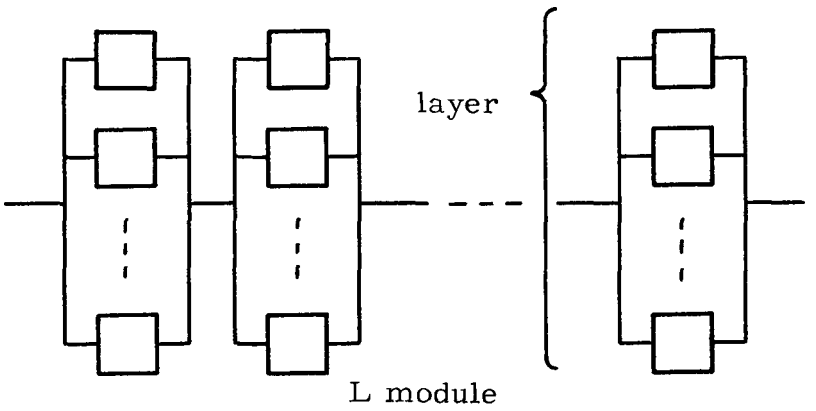

Assumptions that apply only to crossover systems follow.

The possibility of overcurrent in some modules is neglected. In a crossover system, replacement of failed modules should follow a scheme that maximizes system reliability if some failed modules are not replaced. For example, layers with the greatest number of failed modules should have modules replaced first. If the worst number is three failures in a layer, it may be best to replace only two and come back later for the third one if there is time.

II-3 TERMINOLOGY

Various terms are defined in this section.

The reliability of a system is the probability that the system performance exceeds a specified value during a cycle. In certain analyses, satisfactory performance of a system means that while in use, it must have at least eight working strings, each of which must contain at least 500 working cells (other definitions could be used). A daily cycle consists of charging and discharging. A specified period could also be the charging period, the discharging period, or a given number of complete cycles.

The reliability of a module is the probability that it performs satisfactorily for a specified period of time. The time period used for a component is the same time period used for the system reliability, typically one cycle.

Redundant modules in a system are extra modules that improve system performance. Such modules help the system perform adequately even when modules fail. Various redundant configurations are analyzed to determine system performance for a range of module reliabilities. In particular, for parallel string systems, eight, nine, and ten string configurations are analyzed; these contain zero, one, and two extra strings. Also, extra modules per string are analyzed, where the extra number ranges from 1 module through 20% of the minimum number of modules allowed in a string. In addition, different numbers of cells per module will be considered in addition to the current 25 cells, for example, 50, 20, 10 and 1 (this extreme case produces the greatest reliability for a given number of redundant modules).

II-4 CAPACITY OF A CROSSOVER SYSTEM

II-4.1 Effect of Module Failure

This section provides charts for the relationship between module failure probability per cycle and crossover system capacity -- deliverable energy.

II-4.2 Background

Suppose a crossover system has L layers each with M modules as shown here.

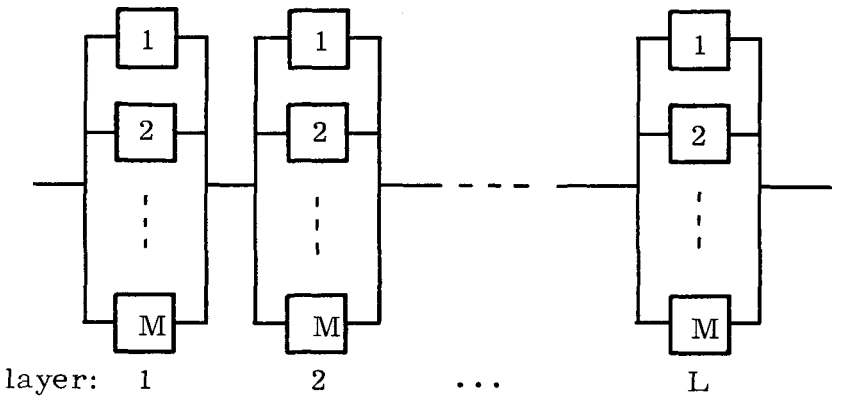

The capacity of the system drops as modules fail. The layer with the fewest operating modules determines the system capacity. If the fewest number of operating modules in a layer is M*, then the system capacity is $C = M^* L C_1$ where C_1 is the capacity of a single module, assumed to be the same for all modules. So the possible values of system capacity are MLC_1 $(M-1) LC_1$, etc., C_1, 0.

This simple view of system capacity involves the assumptions in Sections II-1 and II-2.

In addition, the statistical assumptions are:

- Module failures are statistically independent of each other.
- Each module has the same failure probability p during a cycle. The p value is an "average" for the mix of module ages in a system.

Crossover systems lose much capacity when two or more modules in a layer fail. The capacity loss can be reduced if there is an ability to switch a good module from a layer with all good modules to a layer with two or more failed modules.

II-4.2.1 The Charts and their Use. The following explains charts for different crossover system configurations. Figure II-1 shows the relationship between the module failure probability per cycle and the probability per cycle that the loss of system capacity is M^*LC_1 or greater. The charts can be used two ways:

(1) To determine the probability of a specified loss (or more) of system capacity from a specified module failure probability p;

(2) To determine the module failure probability that gives a specified small probability of a specified loss (or more) of system capacity.

Accomplish Choice (1): a) enter the chart for the system configuration (L layers, M modules) on the horizontal axis at the module failure probability p per cycle; b) go up to the curve labeled with a system capacity loss of M^*LC_1 or more; c) go horizontally to the vertical axis to read the probability that the system capacity loss is M^*LC_1 or more. For example, for a system with L = 18 layers, each with M = 8 modules with failure probability $p = 10^{-3}$, the probability that the system capacity loss is $2 \times 18C_1$ or more ($M^* = 2$) is 5×10^{-4}, that is, one out of $1/(5 \times 10^{-4}) = 2{,}000$ cycles.

Accomplish Choice (2): a) enter the chart for the system configuration on the vertical axis at the specified probability of system capacity loss; b) go horizontally to the curve for the specified capacity loss of M^*LC_1 or more; c) go down to the horizontal scale and read p. For example, for a system with L = 18 layers, each with M = 8 modules, the module failure probability that yields a probability of 10^{-4} that the system capacity loss is C_1 or more ($M^* = 1$) is $p = 4.5 \times 10^{-4}$.

II-4.2.2 Derivation of the Charts. The probability that the "most failed" layer has M* or more failed modules is

$$
\begin{aligned}
P(\text{worst layer has} \geq M^* \text{ failures}) &= 1 - P(\text{worst layer has} < M^* \text{ failures}) \\
&= 1 - P(\text{layer 1 has} < M^* \text{ failures } \underline{\&} \ldots \underline{\&} \text{ layer L has} < M^* \text{ failures}) \\
&= 1 - [P(\text{layer 1 has} < M^* \text{ failures})]^L \\
&= 1 - \left[\sum_{m=0}^{M^*-1} \frac{M!}{m!\,(M-m)!}\, p^m\, (1-p)^{M-m} \right]^L
\end{aligned}
$$

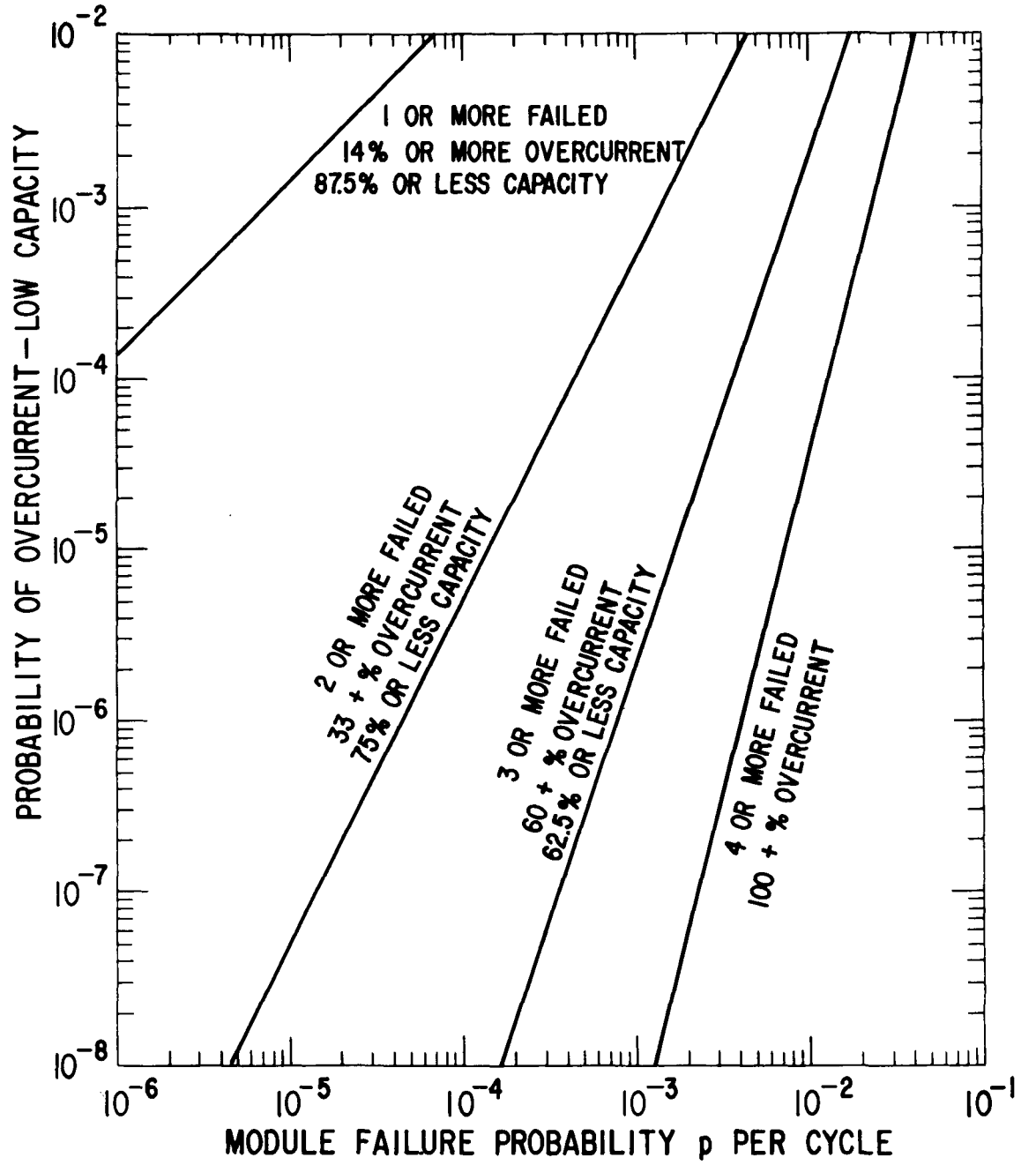

Figure II-1. Probability of Overcurrent or Low Capacity as a Function of Module Failure for a Crossover System

which is in terms of a cumulative binomial probability. This is the probability that the system capacity loss is M^*LC_1 or greater.

The probability that the most failed layer has exactly M* failed modules is

$$P(\text{worst layer has } M^* \text{ failures}) = P(\text{worst layer has} > M^* \text{ failures}) - P(\text{worst layer has} > M^* + 1 \text{ failures})$$

$$= \left[\sum_{m=0}^{M^*-1} \frac{M!}{m!\,(M-m)!}\, p^m\, (1-p)^{M-m}\right]^L - \left[\sum_{m=0}^{M^*} \frac{M!}{m!\,(M-m)!}\, p^m (1-p)^{M-m}\right]^L$$

This is also the probability that the system capacity is $C = M^*LC_1$.

We can view capacity in terms of the fraction of maximum capacity $c_{max} = MLC_1$. Then the fraction is $f = M^*/M$. If the system has extra (redundant) strings, it may be better to view the capacity in terms of the base number M_o of strings. Then the fraction is $f_o = M^*/M_o$, and this may exceed 1. Of course, a redundant system should have $f_o > 1$ with high probability.

It is also possible to calculate the average system capacity

$$EC = LC \sum_{M^*=0}^{M} M^* P(\text{worst has } M^* \text{ good modules})$$

This value and the variance of capacity would be useful to a utility that has a number of battery systems.

II-4.3 Effect of the Distribution of Cell Capacity

This section provides charts for the relationship between cell capacity spread (standard deviation) and system capacity.

II-4.3.1 Background. Assume a crossover system has L layers each with M modules in parallel and where each module contains N cells in series. Suppose all modules work, and the capacity of the $n^{\underline{th}}$ cell in the $m^{\underline{th}}$ module in the $\ell^{\underline{th}}$ layer is $C_{nm\ell}$. Then the capacity of the system is

$$C = NL \min_{\ell} \left[\min_{n} (C_{n1\ell}) + \ldots + \min_{n} (C_{nM\ell}) \right]$$

This equation assumes that the capacity of a parallel connection of units is the sum of the unit capacities and that the capacity of a series of connection of units is the smallest capacity of those units. As modules age or are replaced, their capacities vary. Thus, the system capacity varies and has a statistical distribution.

Suppose the distribution of cell capacity has a mean μ and standard deviation σ. For calculations σ may be expressed as a fraction of μ, that is, as μ/σ, which may also be expressed as a percentage.

This section presents charts for the relationship between the distribution of system capacity and the percent variability 100 σ/μ of cells.

Suppose the capacity of individual cells has a normal distribution. Then about 67% of the cells have capacities in the range $\mu \pm \sigma$, about 95% in the range $\mu \pm 2\sigma$, and about 99.7% in the range $\mu \pm 3\sigma$. For example if 100 σ/μ = 2%, then 67% of the cell capacities are within 2% of the mean, 95% are within 4% of the mean, and 99.7% are within 6% of the mean. If the distribution is not normal, the percentages differ.

The capacity of a cell changes as the cell ages. The distribution of cell capacity used in the analysis will be that of a steady-state mix of ages. Such a steady-state results after the system has been in service long enough for each cell to have been replaced a few times. It may be simpler to use the distribution of capacity of new cells for one analysis and the distribution of capacity of cells when removed from service for another analysis. These are best and worst cases. Also, such an analysis can be based on an engineering estimate of the distribution of cell capacity. The mean μ and standard deviation σ should take into account the change in capacity as cells age. So the μ and σ represent a mix of module ages.

This simple view of system capacity also involves the assumptions in Sections II-1 and II-2. Also, it is assumed that the capacities of the cells in a module are statistically independent.

II-4.3.2 The Charts and their Use. The following explains the charts for different crossover configurations. Figure II-2 shows the relationship between the distribution of system capacity loss and 100 σ/μ. In particular, Figure II-2 gives the 99% and 50% points of the distribution of system capacity loss as a function of 100 σ/μ . The charts can be used two ways:

(1) to determine the 99% or 50% point of system capacity loss for a specified value of 100 σ/μ;

(2) to determine module variability 100 σ/μ, that will provide a specified 99% or 50% point for system capacity loss.

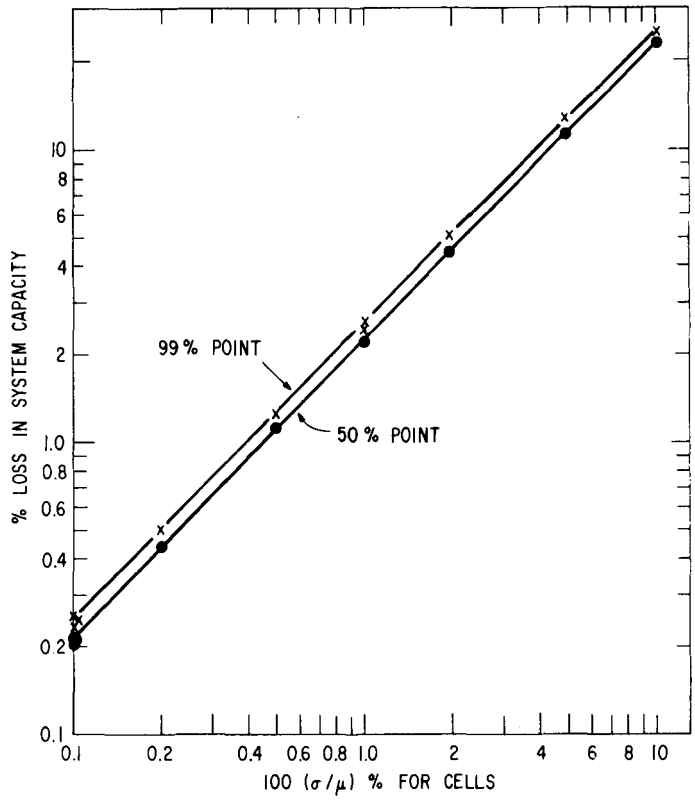

Figure II-2. Loss of System Capacity as a Function of the Percent Variability of Cells

For an example of (1), suppose that a system has L = 25 layers, M = 8 modules/layer, and N = 20 cells/module. Also, suppose that 100 σ/μ = 1% for cells. The chart shows that the corresponding 99% and 50% points of system capacity loss are 2.5% and 2.2%. This means that the system's capacity loss will be

below 2.5% in 99% of the cycles. Also, the median system capacity loss is 2.2%, a typical value.

For an example of (2), consider the same system. Suppose that the typical system capacity loss (50% point) is to be 1%. According to Figure II-2, the design value of 100 σ/μ must be 0.45%.

The lines for the different system configurations are essentially the same for practical purposes.

II-4.3.3 Further Comments. The system capacity loss can be reduced by matching modules in a layer so all layers have nearly the same total capacity. This may be difficult to do since aging changes each module's capacity in a slightly different way.

Module failures reduce the system capacity. Thus, the charts underestimate system capacity loss. It would be difficult to combine the effects of module failures and of capacity differences in an exact analysis. It may be possible to crudely combine the information on both types of charts.

Quite a bit of the capacity goes unused in a crossover system when modules fail. This is less a problem in parallel string systems. However, parallel string systems always lose some capacity since the capacities of individual modules differ; this loss is smaller in a crossover system.

II-4.3.4 Derivation of the Charts. Assume that cell capacity has a normal distribution with mean μ and standard deviation σ. Other distributions would yield different but similar results. Also, assume that the capacities of cells in a module are statistically independent. The following derives the mean and standard deviation of the capacity of modules, layers, and crossover systems.

The capacity of a module of N cells in series is determined by the cell with the lowest capacity. The distribution of the smallest observation among N observations from a normal distribution with a mean μ and standard deviation σ has a mean $\mu - |\alpha_{1/N}|\ \sigma$ and standard deviation $\sqrt{V_{1/N}}\sigma$ where $\alpha_{1/N}$ is the

expectation and $V_{1/N}$ is the variance of the first order statistic in a sample of N observations from a standard normal distribution ($\mu = 0$ & $\sigma = 1$). The $\alpha_{1/N}$ and $V_{1/N}$ are tabled in Contributions to Order Statistics by Sarhan and Greenberg. The mean and standard deviation of the total capacity of the N cells in a module are

$$\mu_M = N(\mu - |\alpha_{1/N}|\alpha),$$

$$\sigma_M = N\sqrt{V_{1/N}}\sigma$$

The capacity of a layer is the sum of the capacities of the M modules in the layer. So the mean and standard deviation of the distribution of layer capacity are

$$\mu_L = M\ \mu_M,$$

$$\sigma_L = \sqrt{M}\ \sigma_M$$

Since the layer capacity is a sum, its distribution is approximately normal, particularly for large M; this is a result of the central limit theorem for sums of independent random variables.

The capacity of a series connection of L layers is determined by the layer with the lowest capacity. The distribution of the lowest layer capacity (the smallest observation among L observations from an approximately normal distribution with mean μ_L and standard deviation σ_L) has a mean $\mu_L - |\alpha_{1/L}|\alpha_L$ and standard deviation $\sqrt{V_{1/L}}\ \sigma_L$. The α and V notation have the same meaning as before. The total system capacity of the L layers then has a distribution with mean and standard deviation

$$\mu_S = L(\mu_L - |\alpha_{1/L}|\sigma_L),$$

$$\sigma_S = L\sqrt{V_{1/L}}\ \sigma_L$$

The system capacity is determined by the least layer capacity. Since it is the smallest observation in a sample of L, its distribution is approximately extreme in value with scale and location parameters

$$b = (\sqrt{6}/\pi)\ \sigma_S,$$

$$a = \mu_S + 0.5772\ b$$

The $100P^{\text{th}}$ percentile of this distribution is

$$y_P = a + b\ \ln[-\ln(1-P)]$$

The system capacity loss can be expressed as percentage. The $100P^{\text{th}}$ percentile of this "percentage" loss distribution is

$$y'_P = (LMN\mu - y_P)/(LMN\mu) = 1 - [y_P/(LMN\mu)]$$

This is plotted in the chart for P = 0.50 and 0.99, (Figure II-2).

II-5 CAPACITY OF A PARALLEL-STRING SYSTEM

II-5.1 Effect of Module Failures

This section provides charts for the relationship between the capacity (deliverable energy) of parallel-string systems and the module failure probability per cycle.

II-5.1.1 Background. Suppose a parallel-string system has M strings each with L modules as shown here.

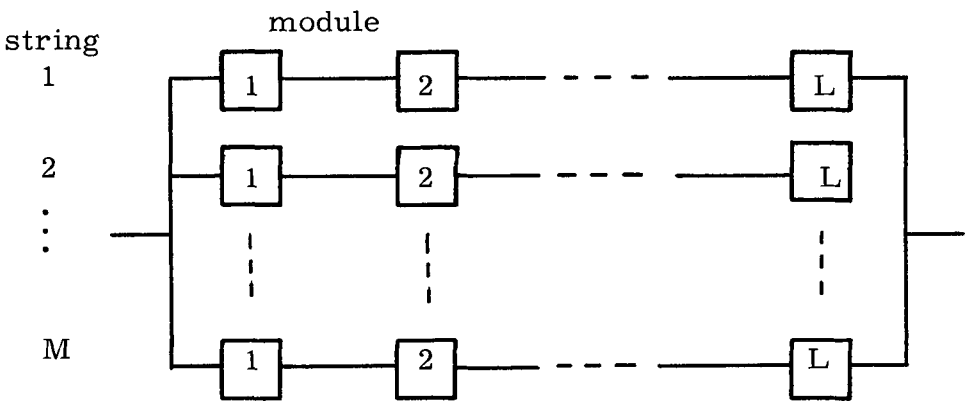

The capacity (energy delivered) of the system drops as modules fail. The number of operating modules determines the capacity as shown below. The maximum system occurs when no modules fail and has the value $C^* = LMC_1$ where C_1 is the capacity of a single module. The following charts give the distribution of capacity as a function of the failure probability p per cycle.

The simple model for the system capacity involves the assumptions in Sections II-1 and II-2.

Additional assumptions are: Strings with different numbers of good modules can operate in parallel, and each string will give all the energy in the good modules. There is no minimum required number of good modules on a string.

Each module has the same failure probability p during a cycle. The p value is an "average" for the mix of module ages in a system.

II-5.1.2 The Charts and their Use. The following explains the charts for parallel-string systems. Figure II-3 shows the relationship between the

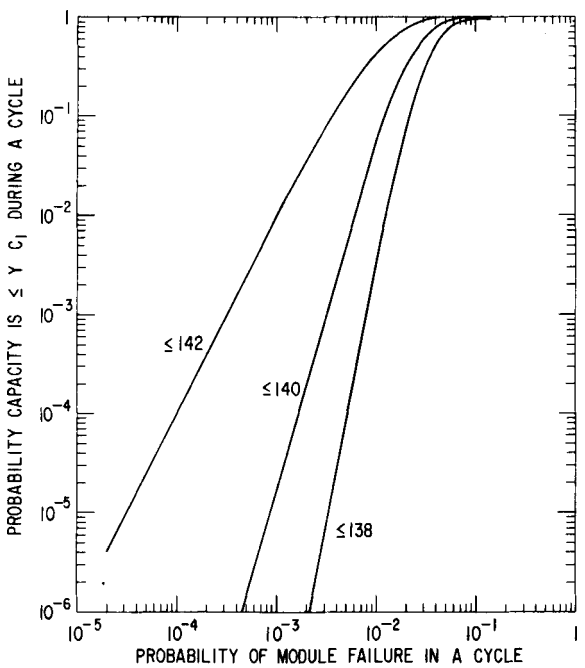

Figure II-3. Probability that System Capacity Falls Below a Certain Value as a Function of Module Failure Probabilities

distribution of system capacity and the module failure probability p, per cycle. In particular, the charts give the probability that the system capacity is less than or equal to yC_1, where C_1 is the capacity of a module.

The charts can be used two ways:

(1) To determine the probability per cycle that the system capacity is yC_1 or less for a specified value of p, the module failure probability per cycle;

(2) To determine p so the system has a specified small probability per cycle that the system capacity is yC_1 or less.

For an example of (1), suppose that a system has M = 8 strings and L = 18 modules per string (a total of 144 modules). Also, suppose that $p = 10^{-3}$. The chart for this configuration shows that the probability per cycle that 140 or fewer modules operate is 1.6×10^{-4}. Thus, such an event occurs in one cycle out of $1/(1.6 \times 10^{-4}) = 6000$ cycles on the average.

For an example of (2), consider the same system. Suppose that the probability per cycle that the system capacity is 142 C_1 or less is to be 10^{-4}. According to the chart, p must be 1.7×10^{-2}.

II-5.1.3 Further Comments. The charts also give the distribution of the number of failed modules that must be replaced in each cycle. This may help in determining needed manpower and supplies of replacement modules. For the above example, of a system with 144 modules for $p = 10^{-3}$, the probability of 140 or fewer good modules is 1.6×10^{-4}. This means there will be 144-140 = 4 or fewer needed replacements with probability $1 - 1.6 \times 10^{-4} = .99984$. The expected number of failures per cycle for a system of L x M modules is LMp where p is the failure probability per cycle for a module of "average" age.

System reliability is higher if failed modules can be replaced at two points in the daily cycle, both before charging and before discharging. Current plans allow for replacement only before discharging.

II-5.1.4 Derivation of the Charts. Under the preceding assumptions, the capacity of a parallel string system is the number of good modules times

C_1. The number Y of good modules has a binomial distribution with sample size LM, the number of modules in the system. So, for y = 0, 1, 2, ..., LM,

$$P[C = yC_1] = \frac{(LM)!}{y!\,(LM-y)!}\,(1-p)^y\,p^{LM-y}.$$

The probability that the capacity is yC_1 or less is the binomial cumulative probability

$$P\,[C \leq yC_1] = \sum_{x=0}^{y} \frac{(LM)!}{x!\,(LM-x)!}\,(1-p)^x\,p^{LM-x}$$

$$= 1 - \sum_{x=y+1}^{LM} \frac{(LM)!}{x!\,(LM-x)!}\,(1-p)^x\,p^{LM-x}$$

$$= 1 - \sum_{x=0}^{LM-y-1} \frac{(LM)!}{x!\,(LM-x)!}\,p^x\,(1-p)^{LM-x}$$

The probability that all modules are good is $P[C = LMC_1] = (1-p)^{LM}$.

Another model for parallel system capacity says that the system capacity equals the capacity of the string with the smallest number of good modules times the number of strings. The most appropriate model must be determined from power engineering considerations.

II-5.2 Minimum-System Reliability

This section provides charts for parallel-string system reliability as a function of the module failure probability p per cycle. The definition of satisfactory performance of a minimum system is simple and perhaps overly so for many purposes. Here, a system is defined to be a satisfactory minimum system if it contains at least 500 working cells per string and at least eight working strings. The system (un)reliability is the probability per cycle that a minimum system is (not) satisfactory. The charts apply to system capacity, power, and other measures of system performance.

II-5.2.1 Background. Suppose a parallel-string system has M strings, each with L modules.

The simple model for system reliability involves the assumptions in Sections II-1 and II-2.

II-5.2.2 The Charts and their Use. The following explains the reliability charts for parallel-string systems. Figure II-4 shows the relationship between system unreliability and the module failure probability p per cycle. Each chart corresponds to a string length which is expressed, for example, as 25/30, which means that (at least) 25 of the 30 modules in each string must work. Each curve in a chart is labeled the number of strings in the system; for example, 8/11 indicates the system has 11 strings of which (at least) 8 must work, that is, each have at least 25 working modules.

The charts can be used two ways:

(1) To determine the unreliability per cycle for a specified value of p, the module failure probability per cycle;

(2) To determine p so the system has a specified small unreliability per cycle.

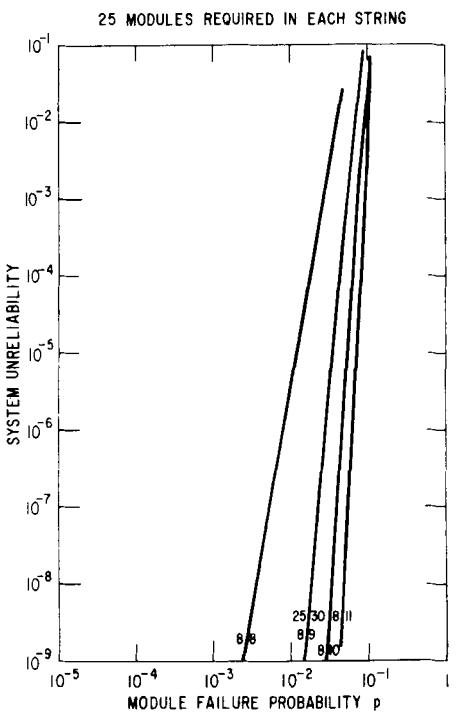

Figure II-4. System Unreliability as a Function of Module Failure Probability in a Parallel String System

For an example of (1), suppose that a system has M = 9 strings and L = 30 modules per string. Also, suppose that $p = 2 \times 10^{-2}$. The system unreliability per cycle comes from the corresponding chart and is 2.2×10^{-8}.

For an example of (2), consider the same system. Suppose that the system unreliability per cycle is to be 10^{-6}. According to the chart, p must be 2.0×10^{-2}.

II-5.2.3 Derivation of the Charts. The following derivation gives the theoretical basis for the reliability charts. First, the reliability of a string is derived and then the reliability of a parallel combination of strings. Suppose that at least L* of the L modules in a string must work for the string to be satisfactory, and suppose that at least M* of the M strings in a system must be satisfactory for the system to be satisfactory.

The L modules in a string are assumed to fail independently, each with the same probability p. So the number of failed modules has a binomial distribution. The string is unsatisfactory if the number of good modules is below L*; the probability of this is the string unreliability

$$Q = \sum_{\ell=0}^{L^*-1} \frac{L!}{\ell!\,(L-\ell)!}\,(1-p)^{\ell}\,p^{L-\ell}$$

$$= 1 - \sum_{\ell=L^*}^{L} \frac{L!}{\ell!\,(L-\ell)!}\,(1-p)^{\ell}\,p^{L-\ell}$$

The string reliability is P = 1 - Q. In reliability terminology, a string is called an L*-out-of-L system, since L* out of the L components must work for the string to be satisfactory; otherwise, the string "fails."

The M strings in a system are assumed to fail independently, each with the same probability Q above. So the number of failed strings has a binomial distribution. The system "fails" if the number of good strings is below M*; the probability of this is the system unreliability

$$\bar{R} = \sum_{m=M^*}^{M} \frac{M!}{m!\,(M-m)!}\, Q^m\, (1-Q)^{M-m}$$

$$= 1 - \sum_{m=0}^{M^*-1} \frac{M!}{m!\,(M-m)!}\, Q^m\, (1-Q)^{M-m}$$

where Q is given above.

The system reliability is $R = 1 - \bar{R}$. The system is an M*-out-of-M system of L*-out-of-L components (strings).

II-6 RESISTANCE OF A CROSSOVER SYSTEM

This section presents results on how system resistance is effected (1) by module failure and (2) by the variability of module resistance.

II-6.1 Effect of Module Failure

The following describes analyses that yield the relationship between system resistance and the module failure probability per cycle.

II-6.1.1 Background. Suppose a crossover system has L layers each with M modules in parallel where the module resistance is r.

The resistance of a system with all modules good is

$$R_o^* = L\ y/M$$

As modules fail, the resistance of the system increases. The following derives the distribution of system resistance as a function of the module failure probability p per cycle.

The analysis involves the assumptions in Sections II-1 and II-2 and the following assumptions.

- All modules have the same resistance, r. Thus, there are no manufacturing or age variations in r. In practice, use a "typical" value for r.

- Failure of a module does not affect the resistance of other modules.
- The possibility of overcurrent through some modules is ignored.

As before, the statistical assumptions are:

- Module failures are statistically independent of each other.
- Each module has the same failure probability p during a cycle. The p value is an "average" for the mix of ages.

The resistance of the system depends on the numbers N_m of layers with m good modules, m = 0, 1, ..., M. Then,

$$R = N_0\ (r/0) + N_1\ (r/1) + \ldots + N_M\ (r/M)$$

where the first term is 0 if $N_0 = 0$ and the system is "open" if $N_0 > 1$. Of course, $N_0 + N_1 + \ldots + N_m = L$.

The N_m have a multinomial distribution

$$P[N_0 = n_0, \ldots, N_M = n_M] = \frac{L!}{n_0!n_1!\ldots n_M!}\ p_0^{n_0}\ p_1^{n_1}\ \ldots\ p_M^{n_M}$$

where

$$p_0 = \binom{M}{0}\ (1-p)^0\ p^M,$$

$$p_1 = \binom{M}{1}\ (1-p)^1\ p^{M-1},$$

$$p_M = \binom{M}{M}\ (1-p)^M\ p^0$$

The probability that the system is open is

$$\begin{aligned} P[\text{open}] &= 1 - P[\text{system not open}] \\ &= 1 - P[\text{layer 1 not open \& } \ldots \text{ \& layer L not open}] \\ &= 1 - [1-P(\text{layer 1 open})]\ x\ \ldots\ x\ [1-P(\text{layer L open})] \\ &= 1 - [1 - p^M]^L \end{aligned}$$

Given that the system is not open, the mean system resistance is

$$ER = \frac{1}{P[\text{open}]} \left[0\ p_0 + \frac{r}{1}\ p_1 + \frac{r}{2}\ p_2 + \cdots + \frac{r}{M}\ p_M\right]$$

$$= \frac{1}{P[\text{open}]} \left[\frac{1}{1}\binom{M}{1}(1-p)^1\ p^{M-1} + \frac{1}{2}\binom{M}{2}(1-p)^2\ p^{M-2} + \cdots + \frac{1}{M}\binom{M}{M}(1-p)^M\ p^0\right]$$

An approach to calculating the distribution of system resistance involves calculating every possible multinomial probability

$$P[N_0 = n_0, \ldots, N_M = n_m]$$

and the corresponding system resistance $R = N_0(r/0) + N_1(r/1) + \ldots N_M\ (r/M)$. The following shows that the number of such probabilities is so large that complete enumeration is out of the question.

The number of possible values of $N_0, N_1, \ldots, N_M$ is the binomial coefficient

$$\binom{M+L}{L} = \frac{(M+L)!}{M!\ L!}$$

Feller[II-3] gives this formula. For example, for M = 8 and L = 25,

$$\binom{8+25}{8} = \frac{33!}{8!\ 25!} \cong 13.88 \times 10^6$$

This is too big for complete enumeration of all possible values of $N_0, N_1, \ldots, N_M$. Even for a smaller system with M = 8 and L = 18,

$$\binom{8+18}{8} = \frac{26!}{8!\ 18!} \cong 1.56 \times 10^6$$

Still too big to evaluate all possible values of R.

The most likely values of N_0, N_1, ..., N_M are

$$\hat{N}_0 = L\, p_o = L\binom{M}{0}(1-p)^0\, p^M$$

$$\hat{N}_1 = L\, p_1 = L\binom{M}{1}(1-p)^1\, p^{M-1}$$

$$\hat{N}_M = L\, p_M = L\binom{M}{M}(1-p)^M\, p^0$$

These would have to be rounded to integers.

Instead of enumerating all N_0, N_1, ..., N_M values, one could enumerate only those with high values of N_M, N_{M-1}, N_{M-2}, and all others lumped together. This will yield the highest resistance values, and their total probability may be high when p is small. Then for L = 25 the number of such "outcomes" is

$$\binom{3+25}{3} = \frac{28!}{3!\ 25!} = \frac{28 \cdot 27 \cdot 26}{6} = 3{,}276$$

This is a feasible number.

An alternative approach is to do a Monte Carlo simulation to empirically determine the distribution of R as a function of p.

II-6.2 Effect of the Distribution of Module Resistance

This section provides equations for the relationship between the distribution of system resistance and the distribution of module resistance.

II-6.2.1 Background. Assume a crossover system has L layers, each with M modules in parallel. Suppose all modules work and the resistance of the m^{th} module in the ℓ^{th} layer is $r_{\ell m}$. Then the resistance R of the system is

$$R = \frac{1}{\frac{1}{r_{11}} + \ldots + \frac{1}{r_{1M}}} + \ldots + \frac{1}{\frac{1}{r_{L1}} + \ldots + \frac{1}{r_{LM}}}$$

As modules age or are replaced, their resistances vary. So the system resistance varies and has a statistical distribution which depends on the

distribution of module resistance. Suppose the distribution of module resistance has a mean r_o and standard deviation σ_r.

II-6.2.2 System Resistance Distribution. The following gives formulas for the mean R_o, the standard deviation σ_R, and percentiles of the distribution of crossover system resistance. This distribution is approximately normal; so it is completely specified by R_o and σ_R. The formulas can be used two ways

1) to determine any percentile of the distribution of system resistance for a specified value of $100\ \sigma_r/r_o$;
2) to determine module variability $100\ \sigma_r/r_o$ that will provide a specified percentile for system resistance.

The mean system resistance is approximately

$$R_o \simeq r_o(L/M)[1-(\sigma_r/r_o)^2[(M-1)/M]]$$

The ratio σ_r/r_o is the standard deviation of module resistance expressed as a fraction of the mean; it is a useful way of describing the distribution spread and is often expressed as a percentage. If $\sigma_r = 0$, all module resistances are the same and $R_o = r_o(L/M)$, simply the resistance of a series parallel connection of identical resistances.

The standard deviation of system resistance is approximately

$$\sigma_R \simeq (L/M^3)^{1/2}\ \sigma_r$$

Of course, this formula shows that $\sigma_R = 0$ if $\sigma_r = 0$.

The $100P^{\text{th}}$ percentile of the distribution of system resistance is approximately

$$y_P \simeq R_o + z_P\ \sigma_R$$

where z_P is the $100P^{\text{th}}$ standard normal percentile. Selected values are listed below.

100P:	0.1	1	10	50	90	99	99.9
z_P :	-3.09	-2.33	-1.28	0	1.28	2.33	3.09

The approximate equations above are based on the assumption that σ_r/r_o is small, say, less than 0.10. The approximations are more accurate the smaller σ_r/r_o is.

The preceding formulas are correct for a system consisting entirely of good modules. When modules fail in a crossover system, the system resistance goes up. Thus, the distribution of system resistance tends to be higher than that given by the formulas above.

II-6.2.3 Derivation of the Formulas. The formulas for the mean and standard deviation of system resistance are derived by the propagation of error method. This involves a Taylor-series expansion of the function for system resistance in terms of the module resistances. Hahn and Shapiro[II-2] give the general equations for the approximate mean and variance of a function of statistically independent random variables, for example,

$$R(r_{11}, \ldots, r_{LM}) = \frac{1}{\frac{1}{r_{11}} + \ldots + \frac{1}{r_{1M}}} + \ldots + \frac{1}{\frac{1}{r_{L1}} + \ldots + \frac{1}{r_{LM}}}$$

which is the system resistance in terms of the module resistances. The mean and standard deviation of a general function are approximately

$$R_o \simeq R(r_o, \ldots, r_o) + (1/2) \sum_{\ell} \sum_{m} (\partial^2 R/\partial r_{\ell m}^2) \, \mathrm{Var}(r_{\ell m}),$$

$$\sigma_R \cong \left[\sum_{\ell} \sum_{m} (\partial R/\partial r_{\ell m})^2 \, \mathrm{Var}(r_{\ell m}) \right]^{1/2}$$

where all the partial derivatives are evaluated at the means of the $r_{\ell m}$.

For the system resistance function,

$$\partial R/\partial r_{\ell m} = (1/r_{\ell m})^2/[(1/r_{\ell 1}) + \ldots + (1/r_{\ell M})]^2 = 1/M^2$$

$$\partial^2 R/\partial r_{\ell m}^2 = -2[(1/r_{\ell 1}) + \ldots + (1/r_{\ell,m-1}) + (1/r_{\ell,m+1}) + \ldots + (1/r_{1M})]/$$

$$\left[1 + r_{\ell m}\left(\frac{1}{r_{\ell 1}} + \ldots + \frac{1}{r_{\ell,m-1}} + \frac{1}{r_{\ell,m+1}} + \ldots + \frac{1}{r_{\ell M}}\right)\right]$$

$$= -2(M-1)/(M^3 r_o)$$

Using these derivatives and $\mathrm{Var}(r_{\ell m}) = \sigma_r^2$ in the above general formulas, we get the system mean and the standard deviation in the previous subsection.

The distribution of R is approximately normal for the following reasons. Each module resistance $r_{\ell m}$ makes only a small contribution to R. Also, when σ_r/r_o is small, R is well approximated by a Taylor-series with linear terms in $(r_{\ell m} - r_o)$. Thus, R is approximately the sum of a large number of statistically independent terms with $(r_{\ell m} - r_o)$. By the Central Limit Theorem for sums of independent identically distributed random variables, R, which is approximately such a sum, has approximately a normal distribution. The mean and standard deviations of this distribution are approximately R_o and σ_R above.

II-7 RESISTANCE OF A PARALLEL-STRING SYSTEM

This section presents results on how resistance of a parallel-string system is affected by (1) module failure and (2) by the variability of module resistance.

II-7.1 Effect of Module Failure

The following describes analyses that yield the relationship between system resistance and the module failure probability per cycle.

II-7.1.1 Background. Suppose a parallel-string system has M strings each with L modules in series where the module resistance is r. The resistance of a string with all modules good is

$$R^* = rL/M$$

As modules fail and are bypassed, the resistance of the system decreases. The following discusses the derivation of the distribution of system resistance as a function of the module failure probability p per cycle. The derivation is based on the assumptions in Sections II-1, II-2, and II-6.

The derivation is essentially the same as that in Section II-6 and the derivation runs into the same difficulty as the one in Section II-6. In particular, it is too laborious to enumerate all patterns of module failure and the corresponding resistances and multinomial probabilities. A Monte Carlo simulation or some approximation would be needed to evaluate the distribution of system resistance.

II-7.2 Effect of the Distribution of Module Resistance

This section provides equations for the relationship between the distribution of system resistance and the distribution of module resistance.

II-7.2.1 Background. Assume a parallel-string system has M strings, each with L modules in series. Suppose all modules work and the resistance of the ℓ^{th} module in the m^{th} string is $r_{\ell m}$. Then the resistance of the system is

$$R = \left[\frac{1}{r_{11} + \ldots + r_{1M}} + \ldots + \frac{1}{r_{L1} + \ldots + r_{LM}} \right]^{-1}$$

As modules age or are replaced, their resistances vary. So the system resistance varies with a statistical distribution which depends on the distribution of module resistance. Suppose the distribution of module resistance has a mean r_o and standard deviation σ_r.

II-7.2.2 System Resistance Distribution. The following gives formulas for the mean R_o, standard deviation σ_R, and percentiles of the distribution of parallel-string system resistance. This distribution is approximately normal; so it is completely specified by R_o and σ_R. The formulas can be used two ways:

(1) to determine any percentile of the distribution of system resistance for a specified 100 σ_r/ir_o;

(2) to determine module variability 100 σ_r/r_o that will provide a specified percentile for system resistance.

The mean system resistance is approximately

$$R_o \simeq r_o(L/M)\left[1-(\sigma_r/r_o)^2\,\frac{(M-1)}{ML}\right]$$

As before the ratio σ_r/r_o, as a percentage 100 σ_r/r_o, usefully expresses the spread in the module distribution. If $\sigma_r = 0$, all module resistances are the same and $R_o = r_o\,L/M$, simply the resistance of a parallel-series connection of identical resistances.

The standard deviation of system resistance is approximately

$$\sigma_R \simeq (L/M^3)^{1/2}\,\sigma_r$$

Of course, $\sigma_R = 0$ if $\sigma_r = 0$.

The $100P^{\text{th}}$ percentile of the distribution of system resistance is approximately

$$y_P \tilde{=} R_o + z_P\,\sigma_R$$

where z_P is the $100P^{\text{th}}$ standard normal percentile.

The approximate equations are based on the assumption that σ_r/r_o is small, say, less than 0.10. The approximations are more accurate the smaller σ_r/r_o is.

The preceding formulas are correct for a system consisting entirely of good modules. When modules fail in a series-parallel system and are bypassed, the system resistance goes down. Thus, the distribution of system resistance tends to be lower than that given by the formulas above.

II-7.2.3 Derivation of the Formulas. The mean and standard deviations of system resistance are derived by the propagation of error method described in Section II-6. The distribution of R is approximately normal for the reasons given in Section II-6.

II-8 VOLTAGE OF A CROSSOVER SYSTEM

This section describes how system voltage is affected (1, by module failure and (2) by the variability of module voltage.

II-8.1 Effect of Module Failure

Suppose a crossover system has L layers each with M modules in parallel where the module voltage is v. The system voltage V when all modules are good is

$$V = L\ v$$

As modules fail, the system voltage does not change much unless all modules in a layer fail. Then the system voltage drops to zero. The chance that all modules in a layer fail is quite small. If overcurrent in modules is taken into account, the system voltage drops to zero when the current through any modules exceeds 50% overcurrent. Charts for the probability of overcurrent appear in Section II-12.

Slight changes in the system voltage depends on the constraints on the system, e.g., constant power, constant current, or whatever. A detailed analysis of such slight voltage changes would be much like that in Section II-6 on resistance of a crossover system. This problem requires further definition and work.

II-8.2 Effect of the Variability of Module Voltage

The distribution of system voltage can be approximated by the propagation of error method described in Section II-6. Such an analysis would take into account the distributions of module voltage and resistance. The analysis would be carried out for a system with all good modules. As above, the system voltage depends on the system constraints, e.g., constant power, constant current, or whatever. This problem requires further definition and work.

II-9 VOLTAGE OF A PARALLEL-STRING SYSTEM

This section describes how system voltage is affected (1) by module failure and (2) by the variability of module voltage and resistance.

II-9.1 Effect of Module Failure

Suppose a parallel-string system has M strings each with L modules in series where the module voltage is v. The system voltage V when all modules are good is

$$V = L\ v$$

As modules fail, the system voltage decreases. The voltage of a string to a first approximation is the number of good modules in the string times v. The system voltage is determined by the string voltages; the way this is to be done must be determined from electrical engineering considerations. A refined analysis would also take into account the effect of the "ir" drop when modules fail.

The charts of Section II-5 can also be used to determine the unreliability of a minimum system consisting of (at least) eight strings each with (at least) 25 modules in series. Each minimum system provides a system voltage of (at least) 25 v. These problems require further definition and work.

II-9.2 Effect of the Variability of Modules

The distribution of system voltage can be approximated by the propagation of error method described in Section II-6. Such an analysis would take into account the distributions of module voltage and resistance. The analysis would be carried out for a system with all good modules. The system voltage depends on the system constraints, e.g., constant power, constant current, or whatever, which are determined by electrical engineering consideration. This problem requires further definition and work.

II-10 POWER OF A CROSSOVER SYSTEM

This section describes how system power output is affected (1) by module failure and (2) by the variability of module voltage and resistance.

II-10.1 Effect of Module Failure

Suppose a crossover system has L layers each with M modules in parallel where the module voltage is v and the design current through a module is i. The system power output P when all modules are good is

$$P = LM\ iv$$

As modules fail, the system power output is affected. The effect is determined by the system constraints, e.g., constant power, constant current, or whatever, which are determined by electrical engineering considerations.

The system will fail to provide a desired power output if overcurrent in some modules is too high; charts for the probability of overcurrent appear in Section II-12. These problems require further definition and work.

II-10.2 Effect of the Variability of Modules

The distribution of system power output can be approximated by the propagation of error methods described in Section II-6. The analysis would be carried out for a system with all good modules. As above, the system power depends on the system constraints, which are determined by electrical engineering considerations. This problem requires further definition and work.

II-11 POWER OF A PARALLEL-STRING SYSTEM

This section describes how system power output is affected (1) by module failure and (2) by the variability of module voltage and resistance.

II-11.1 Effect of Module Failure

Suppose a parallel-string system has M strings each with L modules in series where the module voltage is v and the design current through a module is i. The system power P when all modules are good is

$$P = LM\ iv$$

As modules fail and are bypassed, the system power output decreases. To a first approximation the system power output is the number of good modules times iv. The charts of Section II-5 (system capacity) can also be used to obtain the probability that the system power output falls below a specified value. A more refined analysis would take into account ir losses and constraints on system operation, e.g., constant power, constant current, or whatever. This problem may merit further definition and work.

The charts of Section II-5 can also be used to determine the unreliability of a minimum system consisting of (at least) eight strings each with (at least) 25 modules in series. Such a minimum system provides a power output of (at least) 8·25 iv.

II-11.2 Effect of the Variability of Modules

The distribution of system power output can be approximated by the propagation of error method described in Section II-6. Such an analysis would take into account the distributions of module voltage and resistance. The analysis would be carried out for a system with all good modules. As above, the system power depends on engineering constraints. This problem requires further definition and work.

II-12 OVERCURRENT IN A CROSSOVER SYSTEM

This section describes charts for the relationship between the probability of overcurrent in modules and the module failure probability per cycle.

II-12.1 Background

Suppose a crossover system has L layers each with M modules in parallel. As modules in a layer fail, the current through the system must pass through the remaining good modules in that layer. If the current through them becomes too high, the good modules will fail. Typically, 50% overcurrent (or more) will cause module failure. Failure of all modules in a layer causes failure of a crossover system.

The following presents charts for the relationship between the probability of overcurrent and the module failure probability per cycle. The charts are based on the assumptions in Section II-1 and II-2.

II-12.2 The Charts and their Use

The following explains how to use the charts for the different crossover system configurations. The charts, for example Figure II-1 which appears in Section II-4, show the relationship between the probability the worst overcurrent in any layer results from m* or more module failures. The charts can be used two ways:

(1) to determine the probability that the worst overcurrent results from a specified m* or more failed modules in a layer from a specified module failure probability p per cycle;

(2) to determine the module failure probability p that gives a specified small probability of a given m* or more module failures in the worst layer.

To accomplish choice (1): a) enter the chart in Section II-4 for the system configuration (L layers, M modules) on the horizontal axis at the module failure probability p per cycle; b) go up to the curve labeled with a loss of m* or more modules; c) go horizontally to the vertical axis to read the probability that the worst overcurrent results from failure of m* or more modules in a layer. For example, for a system with L = 18 layers, each with M = 8 modules with failure probability $p = 10^{-3}$, the probability that the worst overcurrent results from m* = 2 or more failures in a layer is 5×10^{-4}; that is, one out of $1/(5 \times 10^{-4}) = 2{,}000$ cycles.

To accomplish choice (2): use the charts in reverse. For example, for the same system, the module failure probability that yields a probability of 10^{-4} that the worst overcurrent results from m* = 2 or more module failures is $p = 4.5 \times 10^{-4}$.

II-12.3 Further Comments

If the number of good modules in a layer gets too small, they can all be bypassed to avoid passing too large a current through the remaining modules in the layer. This means that the series strings must contain extra modules. Such bypassing would entail appropriate monitors and bypass equipment. However, such equipment would reduce the probability of damaging overcurrent and increase system capacity.

II-12.4 Derivation of the Charts

The derivation and basis for the charts are given in Section II-5.

II-13 SUMMARY

This study has established a statistical methodology for determining system reliability in terms of component reliability, appropriate to sodium sulfur batteries for a load-leveling system. When component reliability and performance variables are established in the future, charts of the specific types illustrated and explained in the text will be used to determine optimum configurations for obtaining the required system reliability. This work will be expanded in following contract periods.

II-14 REFERENCES

II-1 Shooman, M.L. (1968), Probabilistic Reliability: An Engineering Approach, McGraw-Hill, New York. Chapter 6, for calculation of system reliability from component reliabilities.

II-2 Hahn, G.J. and Shapiro, S.S. (1967), Statistical Models in Engineering, Wiley, New York. Chapter 7 for propagation of error methods.

II-3 Feller, W.G. (1957), Probability Theory - With Applications, 2nd. ed., Wiley, New York.